

UNIVERSITY OF CALIFORNIA

SANTA BARBARA

**Transition Metal Doped Semiconductor Quantum Dot Alloys**

A dissertation submitted in partial satisfaction of  
the requirements for the degree of  
Doctor of Philosophy in Chemistry

by

Khalid M. Hanif

Committee in charge:

Professor Steven K. Buratto

Professor Peter C. Ford

Professor William C. Kaska

Professor Geoffrey F. Strouse, Advisor

March 2004

The dissertation of Khalid M. Hanif is approved

---

Steven K. Buratto

---

Peter C. Ford

---

William C. Kaska

---

Geoffrey F. Strouse, Advisor

March 2004

**Transition Metal Doped Semiconductor Quantum Dot Alloys**

Copyright ©2004

By

Khalid M. Hanif

## ACKNOWLEDGEMENTS

I would like to thank first and foremost GOD Almighty for having blessed me with a wonderful family, friends and also for the health he has given me.

I would like to thank my wonderful parents for their unwavering support and all the sacrifice they have made for me throughout their lives. I would like to thank my little brother and sister for bringing joy and happiness into my life.

I would like to thank my advisor, Geoff Strouse, for all the support he has given me throughout my graduate education helping me prepare for future obstacle and challenges.

My tenure here would not have been as enjoyable without the many friends that I have had and made here. I especially would like to thank Robert Meulenberg, Donny Magana, Greg Khitrov, and Jeff Gerbec for being very good friends and good colleagues.

## ABSTRACT

Synthesis and Characterization of Transition Metal Doped Semiconductor

Alloys

by

Khalid M. Hanif

Semiconductor Quantum Dots have been the focus of intense research throughout the past two decades. It is the size dependant optical properties, and enhanced magnetic properties of these materials that have brought forth such interest in them. In this dissertation the synthesis of monodisperse, crystalline,  $Cd_{1-x}Co_xSe$  and  $Cd_{1-x}Cu_xSe$  quantum dots will be discussed. The precursors required for the synthesis will also be studied and discussed in detail. A question that arises often when doping nanomaterials is the location of the dopant ion. Effective analytical techniques for studying the location of the impurity atoms have been implemented and are discussed here (EXAFS, XANES, XPS, pXRD, ICP-AE). Using these methods the oxidation states of the dopants have been determined and it the site of the dopant can be assigned to the core of the quantum dot.

## TABLE OF CONTENTS

### **CHAPTER 1: Introduction to Doped Semiconductor Quantum Dots**

1.1	Introduction	2
1.2	Synthesis of Doped Nanocrystals	5
1.2.1	Reverse Micelle Synthesis	6
1.2.2	Lyothermal, TOP/TOPO Synthesis	7
1.2.3	Synthesis of Nanocrystals using metal-carbamato complexes	9
1.2.4	Synthesis of Quantum Dots using Inorganic Cluster precursors	10
1.3	Structural and Elemental Analysis	11
1.3.1	Elemental Analysis	12
1.3.2	Extended X-ray Absorption Fine Structure (EXAFS)	13
1.3.3	X-ray Absorption Near Edge Spectroscopy (XANES)	15
1.3.4	X-ray Photoelectron Spectroscopy (XPS)	16
1.3.5	Powder X-ray Diffraction (pXRD)	16
1.4	Magnetic Studies of Doped Nanocrystals	17
1.4.1	Magnetocircular Dichroism (MCD)	19
1.4.2	Superconducting Quantum Interference Devices (SQUID)	20
	Magnetometry	
1.4.3	Electron Paramagnetic Resonance (EPR) Spectroscopy	20
1.5	Conclusion	21

1.6	References	22
-----	------------	----

## **Chapter 2: Synthesis and Characterization of Inorganic Clusters as Single**

### **Source precursors.**

2.1	Introduction	26
2.2	Experimental	28
2.2.1.1	Materials	28
2.2.1.2	Synthesis of $\text{Li}_2[\text{Cd}_4(\text{SPh})_{10}]$	28
2.2.1.3	Synthesis of $\text{Li}_4[\text{Cd}_{10}\text{Se}_4(\text{SPh})_{16}]$	31
2.2.1.4	Synthesis of $(\text{TMA})_2[\text{Cu}_4(\text{SPh})_6]$	35
2.2.1.5	Synthesis of $(\text{TMA})_2[\text{Co}_4(\text{SPh})_{10}]$	35
2.2.1.6	Synthesis of $(\text{TMA})_4[\text{Cd}_4\text{Co}_6(\text{SPh})_{16}]$	39
2.2.2	Characterization	39
2.2.2.1	Mass Spectrometry	39
2.2.2.2	Superconducting Quantum Interference Devices (SQUID)	43
2.2.2.3	X-ray Absorption Near Edge Spectroscopy (XANES)	44
2.2.2.4	UV-Vis absorption spectroscopy	44
2.3	Results and Discussion	44
2.3.1	$\text{Li}_2[\text{Cd}_4(\text{SPh})_{10}]$ and $\text{Li}_4[\text{Cd}_{10}\text{Se}_4(\text{SPh})_{16}]$ clusters	44
2.3.2	$(\text{TMA})_2[\text{Co}_4(\text{SPh})_{10}]$ cluster	45
2.3.3	$(\text{TMA})_2[\text{Cu}_4(\text{SPh})_6]$ cluster	50

2.3.4	(TMA) <sub>4</sub> [Cd <sub>4</sub> Co <sub>6</sub> (SPh) <sub>16</sub> ] cluster	55
2.3.4.1	Mass spectra analysis of (TMA) <sub>4</sub> [Cd <sub>4</sub> Co <sub>6</sub> (SPh) <sub>16</sub> ]	55
2.3.4.2	Optical absorption of (TMA) <sub>4</sub> [Cd <sub>4</sub> Co <sub>6</sub> (SPh) <sub>16</sub> ]	56
2.3.4.3	XANES of (TMA) <sub>4</sub> [Cd <sub>4</sub> Co <sub>6</sub> (SPh) <sub>16</sub> ]	60
2.4	Conclusion	66
2.5	References	67

### **Chapter 3: Cd<sub>1-x</sub>Co<sub>x</sub>Se Semiconductor Quantum Dot Alloys**

3.1	Introduction	70
3.2	Experimental	81
3.2.1.1	Materials	81
3.2.2.2	Synthesis of Cd <sub>1-x</sub> Co <sub>x</sub> Se Quantum Dots	82
3.2.3	Materials Characterization	83
3.2.3.1	Transmission electron microscopy (TEM)	83
3.2.3.2	Powder X-ray diffraction (pXRD)	84
3.2.3.3	UV-Visible absorption	84
3.2.3.4	Photoluminescence and Resonance Raman Spectroscopy	85
3.2.3.5	ICP-AE	85
3.2.3.6	Superconducting Quantum Interference Devices (SQUID)	86
3.2.3.7	Extended X-ray Absorption Fine Structure (EXAFS)	86
3.2.3.8	X-ray Absorption Near Edge Structure (XANES)	87

3.3	Results and Discussion	87
3.3.1	Size Analysis	88
3.3.2	Measuring Co concentrations in Co: CdSe	91
3.3.3	pXRD Vegard's law analysis of site occupation	95
3.3.4	Raman Studies of Cd <sub>1-x</sub> Co <sub>x</sub> Se	105
3.3.5	Electron-phonon coupling in Cd <sub>1-x</sub> Co <sub>x</sub> Se	110
3.3.6	Determination of oxidation state of Co using XANES	112
3.3.7	Site specific analysis using EXAFS	114
3.3.8	Magnetic properties of Cd <sub>1-x</sub> Co <sub>x</sub> Se	123
3.4	Other Co: CdSe synthesis	137
3.4.1	Doping CdSe with Co(NO) <sub>3</sub> • 6H <sub>2</sub> O	137
3.4.2	Doping CdSe with (TMA) <sub>2</sub> [Co(SPh) <sub>4</sub> ]	137
3.5	Conclusion	141
3.6	References	145

## **Chapter 4: Synthesis and Characterization of Cd<sub>1-x</sub>Cu<sub>x</sub>Se Quantum Dots and Quantum Rods**

4.1	Introduction	152
4.2	Experimental Details	155
4.2.1.1	Materials	155
4.2.1.2	Synthesis of (TMA) <sub>2</sub> [Cu <sub>4</sub> (SPh) <sub>6</sub> ]	155

4.2.1.3 Synthesis of Cd <sub>1-x</sub> Cu <sub>x</sub> Se Quantum Dots	156
4.2.1.4 Synthesis of Cd <sub>1-x</sub> Cu <sub>x</sub> Se Nanorods	158
4.2.2 Materials Characterization	159
4.2.2.1 Transmission Electron Microscopy (TEM)	159
4.2.2.2 Powder X-ray Diffraction (pXRD)	159
4.2.2.3 UV-Vis absorption spectroscopy	159
4.2.2.4 Photoluminescence spectroscopy	160
4.2.2.5 ICP-AE	160
4.2.2.6 X-ray photoelectron spectroscopy (XPS)	160
4.2.2.7 X-ray absorption near edge spectroscopy (XANES)	161
4.3 Results and Discussion	161
4.3.1 Size analysis	161
4.3.2 Elemental analysis of nano-dot alloys by ICP-AE	167
4.3.3 Oxidation state of Cu in Cu:CdSe	171
4.3.4 X-ray powder diffraction (pXRD)	181
4.4 Part II: Cd <sub>1-x</sub> Cu <sub>x</sub> Se Nanorods	183
4.5 Conclusions	190
4.6 References	197

**Chapter 5: Structural determination and vibrational study for hexagonal  
elpolites Cs<sub>2</sub>NaGaF<sub>6</sub>:Cr<sup>3+</sup> and Cs<sub>2</sub>NaAlF<sub>6</sub>:Cr<sup>3+</sup>**

5.1	Introduction	200
5.2	Experimental	203
5.3	Results	206
5.3.1	Vibrational Analysis	214
5.4	Discussion	222
5.5	Conclusion	229
5.6	References	231
	<b>APENDIX I</b>	234

## THESIS SUMMARY

This thesis has been divided into 5 chapters. The first chapter consists of an introduction into the field of doped nanomaterials. The second chapter focuses on the synthesis and characterization of inorganic clusters that serve as excellent precursors for the synthesis of quantum dots. The third chapter focuses on the synthesis and characterization of  $\text{Cd}_{1-x}\text{Co}_x\text{Se}$ . In chapter three optical, magnetic and structural properties of  $\text{Cd}_{1-x}\text{Co}_x\text{Se}$  quantum dots will be discussed. Chapter 4, will focus on  $\text{Cd}_{1-x}\text{Cu}_x\text{Se}$ . Once again both the synthetic method and the subsequent characterization of the material (XANES, XPS, pXRD, photoluminescence, UV-vis absorption) will be covered in this chapter. The final chapter (chapter 5) will discuss neutron, single crystal XRD and Raman studies that have been performed on a series of elpasolite single crystals.

## Chapter 1: Introduction to Doped Semiconductor Quantum Dots

## 1.1 INTRODUCTION

Semiconductors quantum dots have been an area of increasing interest over the past 15 years due to the observation of size dependant properties in these materials. As a class of materials, quantum dots provide a bridge between chemistry at the molecular level and physics in bulk materials. Figure 1.1 shows a diagram of the change in the effective band structure for a direct band gap semiconductor as the particle size decreases from the bulk to the individual molecular unit. As can be seen in the figure, the band gap increases and discrete energy levels are formed as the particle size decreases below the effective Bohr radius, or volume occupied by the electron-hole pair (exciton) in the bulk solid. The change in the band gap of these materials with size was described by Brus, et al according to the equation below<sup>1</sup>.

$$E = \frac{\hbar^2 \pi^2}{2R^2} \left[ \frac{1}{m_e} + \frac{1}{m_h} \right] - \frac{1.8e^2}{\epsilon_2 R} + \frac{e^2}{R} \sum_{n=1}^{\infty} \alpha_n \left( \frac{S}{R} \right)^{2n}$$

where E is the energy gap,  $\hbar$  is Planck's constant, R is the particle radius,  $m_e$  and  $m_h$  are the effective masses of the electron and hole,  $\epsilon_2$  is the dielectric constant of the material, S is the distance between the solvent and exciton, and  $\alpha$  is the polarizability. Due to inherent tunability of these materials, they have found a wide range of possible applications in solar cells, spintronics, laser, displays, and biological tags.<sup>2-7</sup>

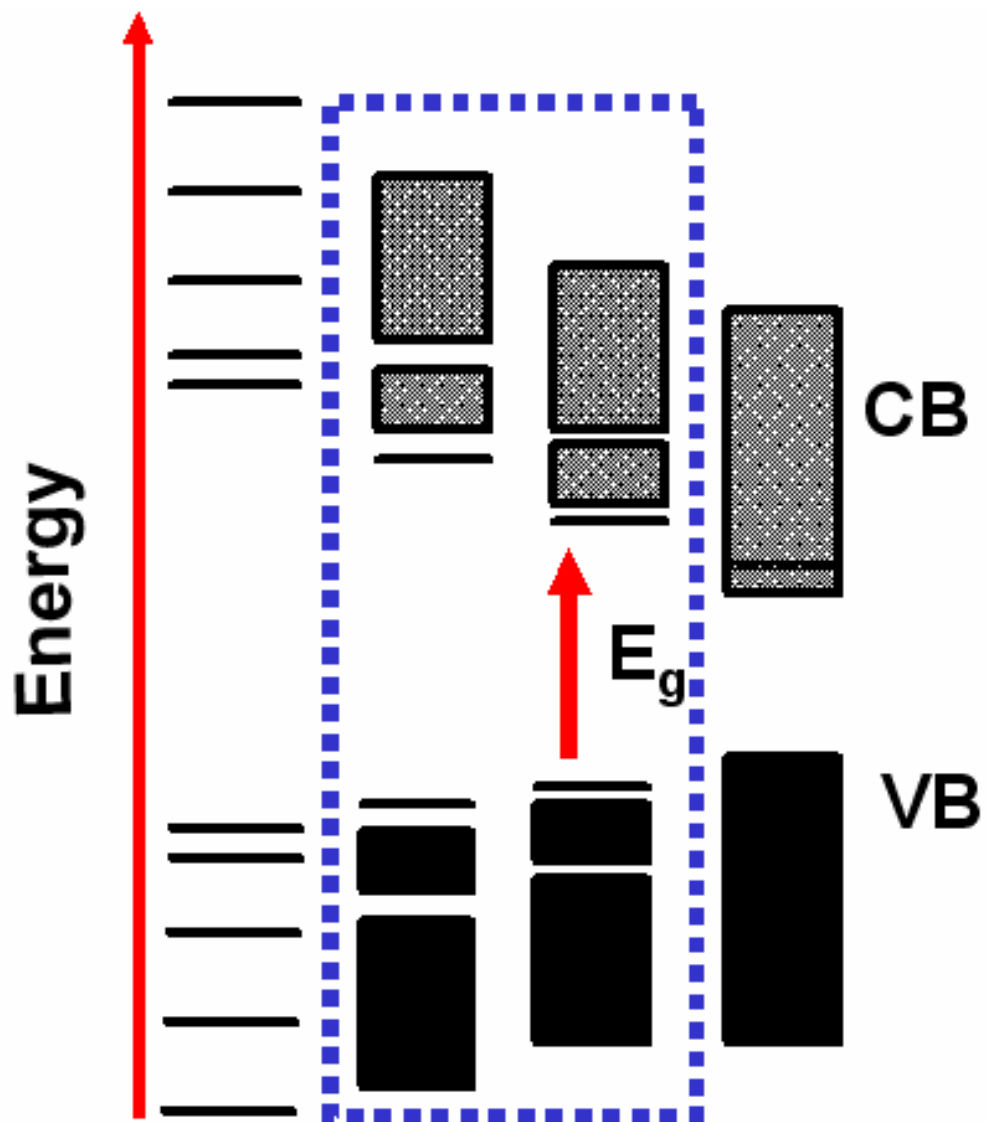


**Figure 1.1.** Band diagram of molecules (left) to bulk (right).

As the fundamental physics of binary nanomaterials became better understood and the synthetic capabilities to produce semiconductor quantum dots improved, a natural progression towards the development of methods to prepare ternary alloys developed in the field of nanomaterials. The push toward development of nanoscale ternary alloys or doped nanomaterials originated from the interesting properties observed in bulk diluted magnetic semiconductors (DMS) over the past two decades. Bulk DMS materials exhibit large g-factors, large Zeeman splitting and large Faraday rotations, which are important properties for applications in magnetic and magneto-optical device technologies.<sup>8</sup> Possible applications of DMS quantum dots extend to the area of spintronics where harnessing the spin degrees of freedom and the carrier mobility are critical to spin-electronic applications. Realization of a bottom-up method to prepare ternary alloys possessing spin and high carrier densities may lead to products such as nonvolatile, high speed, high density random access memory and also quantum computing. Already, recent publications on chemically and molecular beam epitaxy (MBE) prepared magnetic ternary alloys have demonstrated enhanced magnetic properties at the nanoscale with respect to the bulk.<sup>9,10</sup> These enhanced magnetic properties include larger exchange interactions,  $J_{NN}$ .<sup>10</sup>

Initially the development of ternary alloys met with repeated failure, primarily due to limitations of the existing synthetic techniques and the lack of

appropriate single source precursors for alloy formation. The synthetic limitations coupled to a lack of a convenient analytical technique to probe site-occupation (core, near surface, or surface) and dopant concentration led to speculation that ternary alloys were nearly-impossible to chemically prepare at the nanoscale, although countless examples exist based on MBE grown materials. The recent developments as described in this thesis provide the framework for opening the field of nanoscale ternary alloys and lay a foundation for a series of investigations on the unique properties generated by confinement effects in this new class of materials.

This chapter will be divided into three sections. The first section will focus on various doped nanomaterials that have been synthesized and the some of the most successful and widely used synthetic methodologies that have been implemented in making these particles. The second section will focus on structural and elemental analysis of doped systems employed to determine the location of the dopant ion. The third section will focus on the magnetic properties (SQUID, EPR, etc) of these systems.

## **1.2 SYNTHESIS OF DOPED NANOCRYSTALS.**

A wide range of doped quantum dots have been synthesized to date which include inverse micelle, lyothermal, and aqueous preparative methods.<sup>9,11-15</sup> One of the earliest methods employed in the synthesis of doped

quantum dots is that of co-precipitation (Mn:ZnS).<sup>16</sup> However, this method does not match those that have recently been used therefore it will not be discussed. Every method has its advantageous and disadvantageous. However, for future industrial-level nanomaterial applications several key issues must be considered when developing a synthetic methodology:

- I. Ease of synthesis
- II. Quality of materials produced using the synthesis
- III. Cost
- IV. Toxicity and danger involved in the synthesis.

Ideally you would want a synthetic method that is cheap, simple, non toxic and would produce the highest quality of materials.

*1.2.1 Reverse Micelle Synthesis.* Some of the earliest work on doped nanomaterials utilized a room temperature, reverse micelle synthetic methodology. Pileni and co-workers were able to dope  $\text{Mn}^{2+}$  into CdS using this method.<sup>17</sup> Doping levels of up to 30% with  $\text{Mn}^{2+}$  were reported.<sup>17</sup> The precursors used in this synthesis are Cd di(ethyl-2-hexyl) sulfosuccinate ( $\text{Cd}(\text{AOT})_2$ ),  $\text{Mn}(\text{AOT})_2$ ,  $\text{Na}_2\text{S}$ , water, and isooctane. Varying the ratio of water to isooctane provided nanoparticle size control by systematically varying the micelle size. This method is advantageous, in that literature methods exist for the synthesis of  $\text{Cd}(\text{AOT})_2$  and  $\text{Mn}(\text{AOT})_2$ , and the AOT forms the inverted

micelle for the synthesis.<sup>18</sup> Particle sizes of 1.9 – 3.5 nm were synthesized by varying  $w$  ( $w=[\text{H}_2\text{O}]/[\text{AOT}]$ ) from 5 to 40. This is a fairly simple synthesis, however the drawbacks of this method are that it is difficult to prepare monodisperse nanoparticles and the crystallinity of the particles does not match that of materials prepared using high temperature synthetic methods. Gamelin, et al recently modified this technique to synthesize  $\text{Ni}^{2+}$ ,  $\text{Fe}^{2+}$ , and  $\text{Co}^{2+}$  doped ZnO.<sup>11,19</sup> They concluded that this method results in essentially no core doping of the ZnO quantum dots. The only way that the dopant could be incorporated inside the quantum dot was by growing an isocrystalline core shell structure in which a shell of ZnO is grown over a surface doped quantum dot.<sup>11</sup>

*1.2.2 Lyothermal, TOP/TOPO Synthesis.* A number of doped systems have been synthesized using TOP/TOPO as a solvent using organometallic precursors combined under elevated thermal conditions (>200 °C). The materials that have been made using this synthetic method include the following:  $\text{Cd}_{1-x}\text{Mn}_x\text{Se}$ ,  $\text{Cd}_{1-x}\text{Mn}_x\text{S}$ ,  $\text{Zn}_{1-x}\text{Mn}_x\text{Se}$ ,  $\text{Zn}_{1-x}\text{Cd}_x\text{Se}$ ,  $\text{Zn}_{1-x}\text{Cd}_x\text{S}$ , and  $\text{Pb}_{1-x}\text{Mn}_x\text{Se}$ .<sup>6,12,13,15,20</sup> The synthesis of all of these materials is quite similar with the only difference being the dopant ion and the metal precursor.

These reactions in general are performed by injection of TOPSe and Dimethyl Cadmium, Diethyl Zinc, or lead(II) 2-ethylhexanoate. The Mn dopant precursor used for the  $\text{Cd}_{1-x}\text{Mn}_x\text{Se}$  and  $\text{Pb}_{1-x}\text{Mn}_x\text{Se}$  was  $\text{Mn}_2-(\mu-$

$\text{SeMe}_2(\text{CO})_8$  and  $\text{MnMe}_2$  was used in the  $\text{Zn}_{1-x}\text{Mn}_x\text{Se}$  reaction. These reactions require temperatures as high as  $300^\circ\text{C}$ . In the  $\text{Cd}_{1-x}\text{Mn}_x\text{Se}$  reaction doping concentration below 1% were achieved in quantum dots with diameters  $< 4$  nm. Most of the dopant ions were shown to reside on the surface of the quantum dot with little core doping. In the  $\text{Pb}_{1-x}\text{Mn}_x\text{Se}$  reaction doping concentrations as high as 4.7% were observed in particles that were 10 nm in diameter. In the  $\text{Zn}_{1-x}\text{Mn}_x\text{Se}$  reaction doping concentrations as high as 2.5% were achieved with particle sizes as large as 5.75 nm.

Recently,  $\text{Zn}_{1-x}\text{Cd}_x\text{Se}$ , and  $\text{Zn}_{1-x}\text{Cd}_x\text{S}$  alloys have been synthesized using this route. The precursors used in these reactions are TOPS or TOPSe for the chalcogenide source and the metal source used is CdO and diethyl Zinc. In these reactions a small nanoparticles of CdS or CdSe was grown. Once the reaction temperature reached  $\sim 290^\circ\text{C}$  diethyl Zinc and either TOPS or TOPSe was added to the reaction mixture. The reaction was allowed to heat for 3 – 6 minutes and afterwards the reaction was halted by removing it from heat. Usually, when a CdSe is grown, addition of ZnS or ZnSe to the reaction mixture will create a shell around the CdSe quantum dots. However, in this reaction an alloy was formed. The experiments showed that heating the reaction to temperatures in excess of  $270^\circ\text{C}$  leads to migration of the ions in the lattice and formation of an alloy. Had the reaction mixture been heated less than  $270^\circ\text{C}$  then the ZnSe or ZnS would simply have formed a shell around the

CdSe or CdS quantum dots respectively. This observation confirmed earlier speculation that doping using a high temperature lyothermal methods tends to lead to ion migration, and in the case of Mn doped CdSe and ZnS migration of the defect ion towards the nanomaterial surface through an apparent self-annealing process.

The lyothermal method has two major Achilles heels, the reactions are very air sensitive and the precursors also are expensive. In general these reactions yield less than 100 mg of material and controlling the site of doping is complicated by the high temperature of the reaction conditions. The advantages of this method are that it yields very crystalline quantum dots, has short reaction times, and produces monodisperse quantum dots.

*1.2.3 Synthesis of Nanocrystals using Metal-carbamato complexes.* The use of metal carbamato complexes has been widely used for the synthesis of a wide range of quantum dots (CdSe, CdS, PbS, PbSe, ZnSe, ZnS).<sup>21-25</sup> This method uses a single precursor for the synthesis of undoped quantum dots. Recently, this method was adapted to synthesize Mn:CdS by Cheon et al.<sup>26</sup> The manganese source used in the reaction was Manganese bisdithiocarbamate ( $\text{Mn}(\text{S}_2\text{CNET}_2)_2$ ). The reaction was performed by injecting a solution of octylamine containing both  $\text{Mn}(\text{S}_2\text{CNET}_2)_2$  and  $\text{Cd}(\text{S}_2\text{CNET}_2)_2$  into a hot solution ( $\sim 120^\circ\text{C}$ ) of hexadecylamine (HDA). The reaction only required  $\sim 10$

minutes to grow quantum rods with a width of 7 nm and a length of 25 nm.

Mn<sup>2+</sup> doping concentration as high as 12% were achieved using this method.

The advantage of this method is that the precursor used in the synthesis is air stable and is a single source precursor for the reaction, in other words both the metal and chalcogenide are generated from the initial reactant.

Furthermore, carbamate complexes with many different transition metals can be synthesized allowing this method to be used to potentially synthesize a wide variety of doped materials. The disadvantage of this method is that the size distributions obtained using carbamate complexes do not quite compete with the TOP/TOPO grown quantum dots described in the previous section.

#### *1.2.4 Synthesis of Quantum Dots using Inorganic Cluster precursors.* Inorganic

cluster precursors have proven to be very effective in the synthesis of doped quantum dots. Clusters with the formula Li<sub>4</sub>[M<sub>10</sub>X<sub>4</sub>(SPh)<sub>16</sub>] where (M= Cd or Zn and X= S or Se) have been used to synthesize undoped quantum dots.

These clusters are known to exchange their metal ions at room temperature in solution, making them ideal starting points for single source precursor nanomaterial alloy growth. This is the technique fully described in the following chapters of this thesis. To date, a number of different doped quantum dots by our group and others have been synthesized using this method (Cd<sub>1-x</sub>Co<sub>x</sub>Se, Cd<sub>1-x</sub>Eu<sub>x</sub>Se, Cd<sub>1-x</sub>Cu<sub>x</sub>Se, Cd<sub>1-x</sub>Mn<sub>x</sub>Se, Zn<sub>1-x</sub>Mn<sub>x</sub>Se).<sup>10,14,27-29</sup>

The dopant sources for the Eu and Co doped materials were  $\text{EuCl}_2$  and  $(\text{Me}_4\text{N})_2[\text{Co}_4(\text{SPh})_{10}]$ . The synthesis of Mn doped II-VI quantum dots was slightly different. The synthesis was performed by using a doped precursor cluster to grow the doped quantum dots having the formula  $\text{Li}_4[\text{M}_{10-x}\text{Mn}_x\text{Se}_4(\text{SPh})_{16}]$ . The reactions were performed in hexadylamine (HDA) under  $\text{N}_2$  at  $\sim 260^\circ\text{C}$  for 30 minutes - 3 hours to grow quantum dots. Doping concentrations as high as 30, 37, 20, and 10% were achieved for the  $\text{Cd}_{1-x}\text{Co}_x\text{Se}$ ,  $\text{Cd}_{1-x}\text{Eu}_x\text{Se}$ ,  $\text{Cd}_{1-x}\text{Cu}_x\text{Se}$ , and  $\text{Cd}_{1-x}\text{Mn}_x\text{Se}$  quantum dots respectively.

The advantages of this synthesis is that the synthesis can be scaled up to make gram batches of quantum dots, the precursors are air stable, the chemicals required are relatively inexpensive and less reactive, and high quality crystalline, monodisperse materials can be isolated. More detailed descriptions of this method appear in Chapter 2-4.

### **1.3 STRUCTURAL & ELEMENTAL ANALYSIS**

A fundamental question that needs to be answered when synthesizing doped quantum dots is the location of the impurity atom, it could be located at the core of the nanoparticle either as a random ion substitutional element or as an interstitial atom. To address the site of the defect ion in the ternary alloy, three techniques when correlated can be used to answer this question:

elemental analysis, Extended X-ray Absorption Fine Structure (EXAFS), and p-XRD.

*1.3.1 Elemental Analysis.* A simple method for determining core doping concentration is elemental analysis using inductively-coupled plasma atomic emission (ICP-AE) spectroscopy. This technique does not differentiate between core, surface and unbound dopant ions, because it measures the absolute ion concentration of materials dissolved in acid regardless of the ion position and should be considered an ensemble measurement providing an average doping level. The accuracy of AE-ICP methods for determining site of doping can be improved by chemically stripping the quantum dot surfaces repeatedly with pyridine. Bawendi, et al demonstrated chemical stripping was an effective means of removing contamination of the nanoparticle surface in Mn doped  $\text{Cd}_{1-x}\text{Mn}_x\text{Se}$ . In this study, Mikulec et al used tripyrrolidinophosphine to etch the surface of  $\text{Cd}_{1-x}\text{Mn}_x\text{Se}$  quantum dots grown by lyothermal techniques.<sup>12</sup> Analysis of the quantum dots after etching showed that the amount of manganese decreased 6 fold providing evidence that most of the manganese was unbound or isolated at the surface. In  $\text{Cd}_{1-x}\text{Co}_x\text{Se}$  and  $\text{Cd}_{1-x}\text{Cu}_x\text{Se}$  quantum dots prepared in the thesis, pyridine stripping of the quantum dots was used to eliminate contributions arising from surface bound metal ions during AE-ICP elemental analysis.<sup>10</sup>

*1.3.2 Extended X-ray Absorption Fine Structure (EXAFS).* An alternative technique that provides evidence for ion incorporation into the quantum dot core by inspection of the site-occupation and not concentration is EXAFS. EXAFS is an element specific technique that provides information on the surroundings, including the type and number of next nearest neighbors around a specific element within a material. The details of this technique are discussed in detail in the  $\text{Cd}_{1-x}\text{Co}_x\text{Se}$  chapter (Chapter 3).

One of the most important pieces of information that can be obtained using this method is the distance between the element of interest and the shells of atoms surrounding this atom within a material. Information on the coordination number can also be obtained using this method. Using this method the first shell of Eu in  $\text{Cd}_{1-x}\text{Eu}_x\text{Se}$  was shown to be  $\sim 227$  pm from the Eu ion with a pseudo-octahedral coordination geometry.<sup>27</sup> In  $\text{Cd}_{1-x}\text{Co}_x\text{Se}$  it has been shown that the first shell surrounding the Co(II) cations is  $\sim 228$  pm with a  $T_d$  site occupation. The information that this method provides is crucial in understanding the location of the guest ion and the local lattice perturbations caused by the inclusion of the guest ion.

If the guest ion is located within the host then it is expected to contain the same coordination as the host (Fig. 1.2). Using calculated and experimental data from the literature, approximations can be made as to what the bond

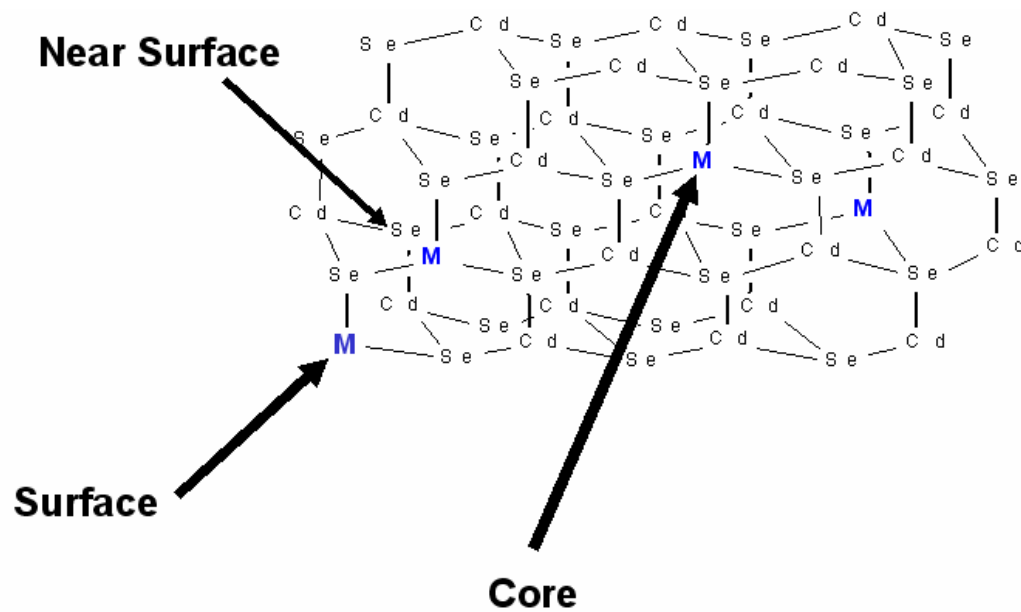


**Figure 1.2.** Location of dopant ion within a cluster and the geometry of the dopant ion. Ions within the lattice have tetrahedral coordination and atoms on the surface have pseudo-tetrahedral coordination.

distance between the guest ion and the atom in its first shell would be. If the distance between the guest ion and its first shell based upon EXAFS agrees with what is expected to be observed for the atom in such an environment then this will provide strong evidence for doping of the nanocrystal core on a substitutional site. In the case of  $\text{Cd}_{1-x}\text{Co}_x\text{Se}$  the expected and experimental data agree with Co being on a tetrahedral site and bound to four Se atoms, demonstrating the power of the technique. EXAFS results on Mn doped ZnS by Zhang, et al were used to provide proof of the Mn ion sitting both in the core of the particle and at the surface of the particle, providing further proof of the power of EXAFS analysis for understanding the nature of site-occupation in ternary alloys.<sup>8</sup> Taking the EXAFS results with the AE-ICP results provide a picture of the concentration and location of the dopant ion in the lattice. However, it does not prove a random ion substitutional process directly. For this powder X-ray diffraction is useful.

*1.3.3 X-ray Absorption Near Edge Spectroscopy (XANES)* XANES is a powerful, elemental specific analytical tool that provides information on the oxidation state of elements within materials. This spectroscopic technique allows for the study of powder, crystalline or thin films under vacuum. Generally, a synchrotron source is required to perform these experiments. This technique has been applied in order to study the oxidation state of Co: CdSe and

Cu:CdSe. Based upon the findings from this technique determination of the Cu and Co oxidation states in CdSe were identified as +1 and +2 respectively (Chapter 3, 4).

*1.3.4 X-ray Photoelectron Spectroscopy (XPS)* XPS is also a great tool for the analysis of both oxidation states in a material and also for quantitative analysis. The oxidation state of Cu was very easily determined since XPS spectra of Cu(I) and Cu(II) have dramatic differences. Shake-up peaks are a phenomenon observed in the XPS spectra of first row transition metals if the transition metal is paramagnetic. These peaks occur to slightly higher binding energy of the main peak. Cu(I) and Cu(II) are diamagnetic and paramagnetic respectively. In the case of Cu:CdSe it was determined that the oxidation state of the Cu is +1 due to the lack of observance of shake-up peaks (Chapter 4).

*1.3.5 Powder X-ray Diffraction (pXRD).* Another technique that is vital in the characterization of doped materials is pXRD. PXRD provides direct information about the structure of the lattice, the degree of crystallinity, and more importantly the average lattice parameters. For instance, in  $\text{Cd}_{1-x}\text{Cu}_x\text{Se}$  materials it was shown that incorporation of Cu(I) within CdSe made it more favorable for the material to have a zinc blende structure as opposed to the

wurtzite structure that is typically seen in CdSe synthesized using that method.<sup>29</sup>

Information about the lattice constants can also be extracted from pXRD data. Unlike EXAFS, pXRD measures the average distance between planes in a material. When a guest ion is incorporated into a material, the guest ion bond distance to its nearest neighbor will typically be different than that of the host it replaced. Therefore, depending upon the size of the guest ion the lattice will experience an average contraction or expansion of the lattice. This is referred to as a Vegard's law analysis and has been used extensively to provide definitive proof of random ion substitutional processes in guest: host materials.<sup>30</sup> In fact, more relevant to the thesis studies, bulk doped semiconductors have shown that if the dopant is distributed randomly throughout the lattice then a linear shift with doping concentration should be observed for the lattice parameters. To date only a handful of researchers have been able to show pXRD evidence of doping in nanomaterials however.<sup>10,13,15,20,26,27,29</sup>

#### **1.4 MAGNETIC STUDIES OF DOPED NANOCRYSTALS**

Transition metal doping is convenient, since often the dopant ion has unpaired spins which allow magnetic measurements to be used to probe the lattice properties. The standard methods employed in analysis of quantum dots

include electron paramagnetic resonance (EPR) spectroscopy, SQUID magnetometry and magneto-circular dichroism (MCD). These methods help bring insight onto the oxidation state of the dopant ion and the magnetic exchange interactions that exist in paramagnetically doped material. Each of these methods is different and helps shed light on the magnetic properties of a material.

SQUID experiments are useful in determining what magnetic interactions exist between the magnetic ions. Zero-field cooled, and field-cooled measurements are generally performed in order to get insight on the nature of the magnetic interactions (paramagnetic, ferromagnetic, antiferromagnetic). Hysteresis measurements are also performed using SQUID to determine if a material is ferromagnetic. This measurement is performed by scanning the field from 7T to -7T under a constant temperature. If a hysteresis is observed then the material is said to be ferromagnetic.

MCD provides insight into the magneto-optical properties of a material. Generally, this experiment measures the absorption of left and right circularly polarized light by a material under a magnetic field. The degree of the Zeeman splitting and the effective g-factors can be obtained using this technique.

EPR also provides insight into the magnetic properties of a material. These experiments are performed in a microwave cavity in between two magnets. The sample is usually placed inside a quartz tube, evacuated and

sealed. Transition metal ions generally have weak EPR signals, as a result most of the measurements are performed below 77K. Under a magnetic field the levels of a semiconductor begin to split. As the field is scanned the sample will absorb microwave radiation when the energy of the radiation corresponds to a transition between two levels. From this information about the g-factors of a material can be determined.

*1.4.1 Magnetocircular Dichroism (MCD).* Although not applied in this thesis, MCD is a technique that has been used on a number of doped nanomaterials to help study the magneto-optical properties of the dopant ion.<sup>6,19,31</sup> In  $Zn_{1-x}Mn_xSe$  it was shown that the Zeeman splitting was two orders of magnitude larger than observed in bulk Mn:ZnSe.<sup>6</sup> In this study, the exciton in  $Zn_{1-x}Mn_xSe$  was shown to feel an effective field of >400T under zero applied magnetic field simply due to the presence of the  $Mn^{2+}$  impurity within the core of the nanoparticle. The presence of a giant internal magnetic field in quantum dots due to magnetic ion dopants has also been observed in  $Cd_{1-x}Mn_xS$ .<sup>31</sup> This study showed that the CdS effectively feels the presence of a field that is on the order of 100-1000 T due to the presence of  $Mn^{2+}$ . This phenomenon was attributed to the enhancement of spin interaction of the host electron and hole with that of the  $Mn^{2+}$  dopant ion and suggested that magnetically doped

quantum dots had great potential in device technology if the synthetic difficulties could be overcome.

#### *1.4.2 Superconducting Quantum Interference Devices (SQUID) Magnetometry.*

SQUID magnetometry is a powerful technique that has been used to study the nature of magnetic interaction within doped nanomaterials. Depending on the interactions that exist and the level of doping, the doped quantum dot can exhibit a number of different types of behaviors including paramagnetism, ferromagnetism, antiferromagnetism, and spin glass behaviors. In  $\text{Cd}_{1-x}\text{Co}_x\text{Se}$  it was shown that doping of the quantum dot with Co resulted in an antiferromagnetic spin glass behavior with exchange interactions that were much larger than that of the bulk.<sup>10</sup> In  $\text{Cd}_{1-x}\text{Mn}_x\text{Se}$  it was shown that incorporation of  $\text{Mn}^{2+}$  in CdSe resulted in ferromagnetism with  $T_C \sim 50^\circ\text{C}$ . Studies on  $\text{Mn}^{2+}$  doped PbSe showed paramagnetic behavior down to 2K.<sup>15</sup>

#### *1.4.3 Electron Paramagnetic Resonance (EPR) Spectroscopy.* EPR

spectroscopy has been widely used to determine the oxidation state and site symmetry of paramagnetic metal ions in QD alloys. A good example is  $\text{Mn}^{2+}$  in II-VI quantum dot alloys.<sup>12,15,31</sup> The nuclear spin of  $\text{Mn}^{2+}$  is 5/2 therefore it is expected to exhibit 6 peaks in the EPR spectra.  $\text{Mn}^{2+}$  hyperfine splitting in bulk CdSe has been shown to be  $62 \times 10^{-4} \text{ cm}^{-1}$ .<sup>32</sup> Studies of  $\text{Mn}^{2+}$  doped ZnS have

shown that if the dopant resides in the core and surface,  $\text{Mn}^{2+}$  exhibits hyperfine splittings of  $65 \times 10^{-4} \text{ cm}^{-1}$ , and  $89 \times 10^{-4} \text{ cm}^{-1}$  respectively.<sup>33</sup> In  $\text{Cd}_{1-x}\text{Mn}_x\text{Se}$  prepared by Mikulec et al, the  $\text{Mn}^{2+}$  had a hyperfine splitting of  $83 \times 10^{-4} \text{ cm}^{-1}$  and was therefore attributed to being near the surface. The  $\text{Mn}^{2+}$  doped ZnSe prepared by Norris, et al showed a hyperfine splitting of  $60.4 \times 10^{-4} \text{ cm}^{-1}$ , thereby indicating that the  $\text{Mn}^{2+}$  was core doped. This has proven to be a vital tool in determining the oxidation state of Mn in a host and also the location of the impurity.

## **1.5 CONCLUSION.**

Doped nanomaterials are an exciting area that has only recently been investigated. It has been shown that synthetic methods that have recently been developed allow the synthesis of high quality nanocrystals. EXAFS and pXRD are very important methods that aid in the determination of the location of the impurity ion. EPR, SQUID magnetometry and MCD spectroscopy provide useful information upon the oxidation state of the dopant, location of dopant and the nature of the magnetic interaction in the material.

## 1.6 REFERENCES:

- (1) Brus, L. E. *J Chem Phys* **1984**, *80*, 4403-4409.
- (2) Bhargava, R. N. *J Lumin* **1996**, *70*, 85-94.
- (3) Htoon, H.; Hollingworth, J. A.; Malko, A. V.; Dickerson, R.; Klimov, V. I. *Appl Phys Lett* **2003**, *82*, 4776-4778.
- (4) Huynh, W. U.; Dittmer, J. J.; Alivisatos, A. P. *Science* **2002**, *295*, 2425-2427.
- (5) Mattoussi, H.; Mauro, J. M.; Goldman, E. R.; Anderson, G. P.; Sundar, V. C.; Mikulec, F. V.; Bawendi, M. G. *J Am Chem Soc* **2000**, *122*, 12142-12150.
- (6) Norris, D. J.; Yao, N.; Charnock, F. T.; Kennedy, T. A. *Nano Lett* **2001**, *1*, 3-7.
- (7) Tran, P. T.; Goldman, E. R.; Anderson, G. P.; Mauro, J. M.; Mattoussi, H. *Phys Status Solidi B* **2002**, *229*, 427-432.
- (8) Furdyna, J. K. *J Appl Phys* **1988**, *64*, R29-R64.
- (9) Feltin, N.; Levy, L.; Ingert, D.; Pileni, M. P. *Adv Mater* **1999**, *11*, 398-402.
- (10) Hanif, K. M.; Meulenberg, R. W.; Strouse, G. F. *J Am Chem Soc* **2002**, *124*, 11495-11502.
- (11) Radovanovic, P. V.; Gamelin, D. R. *J Am Chem Soc* **2001**, *123*, 12207-12214.

- (12) Mikulec, F. V.; Kuno, M.; Bennati, M.; Hall, D. A.; Griffin, R. G.; Bawendi, M. G. *J Am Chem Soc* **2000**, *122*, 2532-2540.
- (13) Zhong, X. H.; Feng, Y. Y.; Knoll, W.; Han, M. Y. *J Am Chem Soc* **2003**, *125*, 13559-13563.
- (14) Magana, D.; Hanif, K. M.; Strouse, G. F. *Manuscript in prep.* **2004**.
- (15) Ji, T.; Jian, W. B.; Fang, J. *J Am Chem Soc* **2003**, *125*, 8448-8449.
- (16) Gallagher, D.; Heady, W. E.; Racz, J. M.; Bhargava, R. N. *J Cryst Growth* **1994**, *138*, 970-975.
- (17) Levy, L.; Hochepped, J. F.; Pileni, M. P. *J Phys Chem-Us* **1996**, *100*, 18322-18326.
- (18) Petit, C.; Lixon, P.; Pileni, M. P. *Langmuir* **1991**, *7*, 2620-2625.
- (19) Radovanovic, P. V.; Norberg, N. S.; McNally, K. E.; Gamelin, D. R. *J Am Chem Soc* **2002**, *124*, 15192-15193.
- (20) Zhong, X. H.; Han, M. Y.; Dong, Z. L.; White, T. J.; Knoll, W. *J Am Chem Soc* **2003**, *125*, 8589-8594.
- (21) Ludolph, B.; Malik, M. A.; O'Brien, P.; Revaprasadu, N. *Chem Commun* **1998**, 1849-1850.
- (22) Revaprasadu, N.; Malik, M. A.; O'Brien, P.; Zulu, M. M.; Wakefield, G. *J Mater Chem* **1998**, *8*, 1885-1888.

- (23) Trindade, T.; O'Brien, P. *J Mater Chem* **1996**, *6*, 343-347.
- (24) Trindade, T.; O'Brien, P.; Zhang, X. M. *Chem Mater* **1997**, *9*, 523-530.
- (25) Trindade, T.; O'Brien, P.; Zhang, X. M.; Motevalli, M. *J Mater Chem* **1997**, *7*, 1011-1016.
- (26) Jun, Y. W.; Jung, Y. Y.; Cheon, J. *J Am Chem Soc* **2002**, *124*, 615-619.
- (27) Raola, O. E.; Strouse, G. F. *Nano Lett* **2002**, *2*, 1443-1447.
- (28) Norman, T. J.; Magana, D.; Wilson, T.; Burns, C.; Zhang, J. Z.; Cao, D.; Bridges, F. *J Phys Chem B* **2003**, *107*, 6309-6317.
- (29) Hanif, K. M.; Tracey, J.; Diana, F.; Petrov, P.; Strouse, G. F. *Manuscript in prep.* **2004**.
- (30) Vegard, L.; Schjelderup, H. *Phys. Z.* **1917**, *18*, 93-96.
- (31) Hoffman, D. M.; Meyer, B. K.; Ekimov, A. I.; Merkulov, I. A.; Efros, A. L.; Rosen, M.; Couino, G.; Gacoin, T.; Boilot, J. P. *Solid State Commun* **2000**, *114*, 547-550.
- (32) Ludwig, G. W.; Woodbury, H. H. *Solid State Physics*; Academic Press: New York, 1962; Vol. 13.
- (33) Kennedy, T. A.; Glaser, E. R.; Klein, P. B.; Bhargava, R. N. *Phys Rev B* **1995**, *52*, 14356-14359.

**Chapter 2:** Synthesis and Characterization of  
Inorganic Clusters as Single Source Precursors

## 2.1 INTRODUCTION:

Development of a synthetic strategy for the preparation of nano-materials that cleanly separates the nucleation step from the growth step, thus minimizing the simultaneous competition of kinetics and thermodynamics, has long been a standing goal in nano-material development. This is particularly true for development of ternary materials, where high temperature nucleation events tend to drive self-annealing processes and therefore the elimination of the guest ion from the host lattice. An alternative synthetic method that uses a pre-doped single source precursor may provide a unique opportunity to avoid the high temperature nucleation events by initiating the reaction from preformed nuclei allowing growth of the nanoparticles to be thermodynamically controlled. The use of a single source precursor employing a cluster of known size with a core that is reminiscent of the bulk lattice has been demonstrated to be beneficial in the growth process.<sup>1-3</sup> Clusters that have been demonstrated to be effective for the synthesis of II-VI semiconductor quantum dots for instance,  $\text{Li}_4[\text{Cd}_{10}\text{Se}_4(\text{SPh})_{16}]$ ,  $\text{Li}_4[\text{Cd}_{10}\text{S}_4(\text{SPh})_{16}]$ ,  $\text{TMA}_4[\text{Zn}_{10}\text{Se}_4(\text{SPh})_{16}]$ , and  $\text{TMA}_4[\text{Zn}_{10}\text{Se}_4(\text{SPh})_{16}]$ .<sup>4</sup> This approach is related to the pyrolytic growth of nanoclusters first employed by Wang, et al. for growth of colloidal CdS from inorganic precursors.<sup>5</sup>

A potential single source precursor for the ternary nanomaterials is the diamond lattice metal-chalcogenide family with a core of six metal ions

tetrahedrally coordinated to four trigonally bound chalcogenides and four metal tetra-thiophenolate caps. These single source precursors based on inorganic chalcogenide clusters have long been studied and shown to rapidly rearrange and incorporate guest ions into the core of the cluster in solution at elevated temperature, thus providing a mechanism for nanomaterial growth from a preformed ternary alloy.<sup>6-9</sup> Holm, et al has shown that clusters with the structure  $[M_4(\text{SPh})_{10}]^{2-}$  readily exchanged the following metal ions into the cluster core (Fe(II), Co(II), Zn(II), and Cd(II)) to give the following structure  $[M_{4-n}M'_n(\text{SPh})_{10}]^{2-}$  when mixed together in  $\text{CD}_3\text{CN}$ .<sup>10</sup> Similar studies on Zn and Co doping of  $[M_{10}\text{S}_4(\text{SPh})_{16}]^{4-}$  to generate  $[M_{10-x}M'_x\text{S}_4(\text{SPh})_{16}]^{4-}$  have been demonstrated by Bowmaker, et al and Strouse, et al. This provides literature support of the ability to prepare ternary alloy single source precursors for nanomaterial growth.

In the study below a number of different thiolate clusters were synthesized. We have generated several new clusters that are beneficial for formation of ternary alloy nanomaterials, that include  $\text{TMA}_2[\text{Co}_4(\text{SPh})_{10}]$ ,  $\text{TMA}_2[\text{Co}(\text{SPh})_4]$ , and  $\text{TMA}_2[\text{Cu}_4(\text{SPh})_6]$ . As described above, these clusters are excellent starting materials for the synthesis of quantum dots. The structure of these clusters was determined using ESI-MS. The optical and magnetic properties of some of the clusters were also studied.

## 2.2 EXPERIMENTAL:

**2.2.1.1 Materials.** The clusters were synthesized using  $\text{Cd}(\text{NO}_3)_2 \cdot 6\text{H}_2\text{O}$  (STREM),  $\text{Co}(\text{NO}_3)_2 \cdot 6\text{H}_2\text{O}$  (Allied), elemental sulfur (Fisher),  $\text{CH}_3\text{CN}$  (Fisher), MeOH (Fisher), thiophenol (Aldrich), triethylamine (Fisher), and tetramethylammonium chloride (ACROS). Methanol was dried using molecular sieves (2Å).

**2.2.1.2 Synthesis of  $\text{Li}_2[\text{Cd}_4(\text{SPh})_{10}]$ .**  $\text{Li}_2[\text{Cd}_4(\text{SPh})_{10}]$  (Fig. 2.1) is the precursor required for the preparation of  $\text{Li}_4[\text{Cd}_{10}\text{Se}_4(\text{SPh})_{16}]$  (Fig. 2.2) and was synthesized according to a slightly modified literature method.<sup>8</sup>

$\text{Li}_2[\text{Cd}_4(\text{SPh})_{10}]$  is synthesized by the addition of (18.6 mL, 182 mmol) thiophenol and (25.5 mL, 182 mmol) triethylamine to a stirred solution containing ~ 60 mL methanol at RT under atmospheric conditions. This solution was stirred for a few minutes and then a solution containing (21.0 g, 68 mmol)  $\text{Cd}(\text{NO}_3)_2 \cdot 6\text{H}_2\text{O}$  in 60 mL of methanol was added slowly. Upon addition of the  $\text{Cd}(\text{NO}_3)_2 \cdot 6\text{H}_2\text{O}$  an immediate white precipitate forms, which slowly redissolves. The addition of the  $\text{Cd}(\text{NO}_3)_2 \cdot 6\text{H}_2\text{O}$  solution is suspended until the precipitate redissolves. Following the addition of all the Cd salt, the solution was heated to ~ 60°C to ensure dissolution of the precipitate. To metathesize the anionic cluster salt to a Li salt,

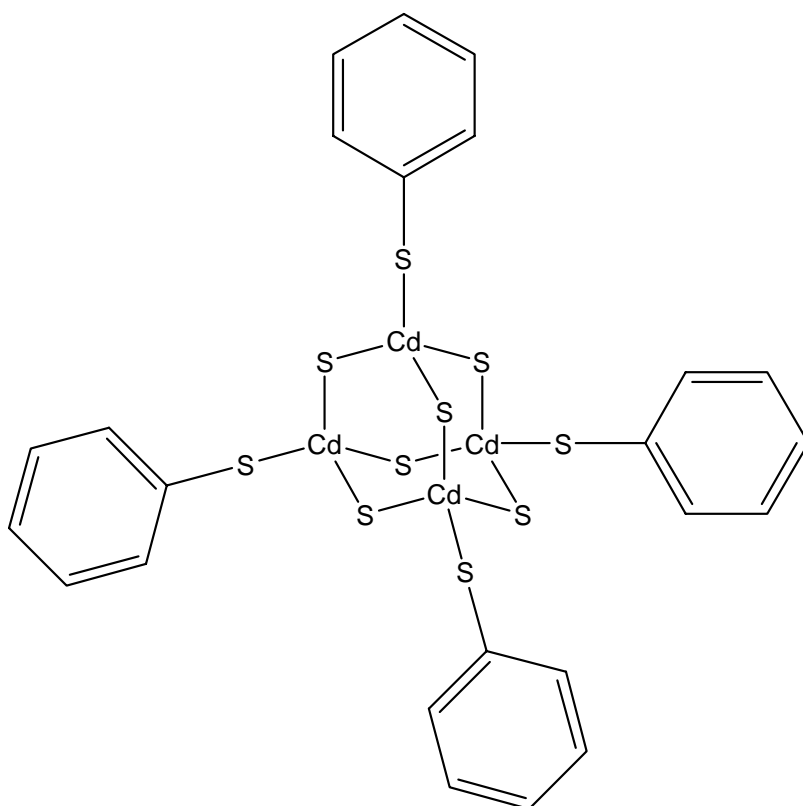


**Figure 2.1.** Structure of  $\text{Li}_2[\text{Cd}_4(\text{SPh})_{10}]$ . All of the sulfurs in this diagram are benzenethiols. In order to allow a better visualization of the molecule the benzene rings were not included in all of the thiophenol molecules.

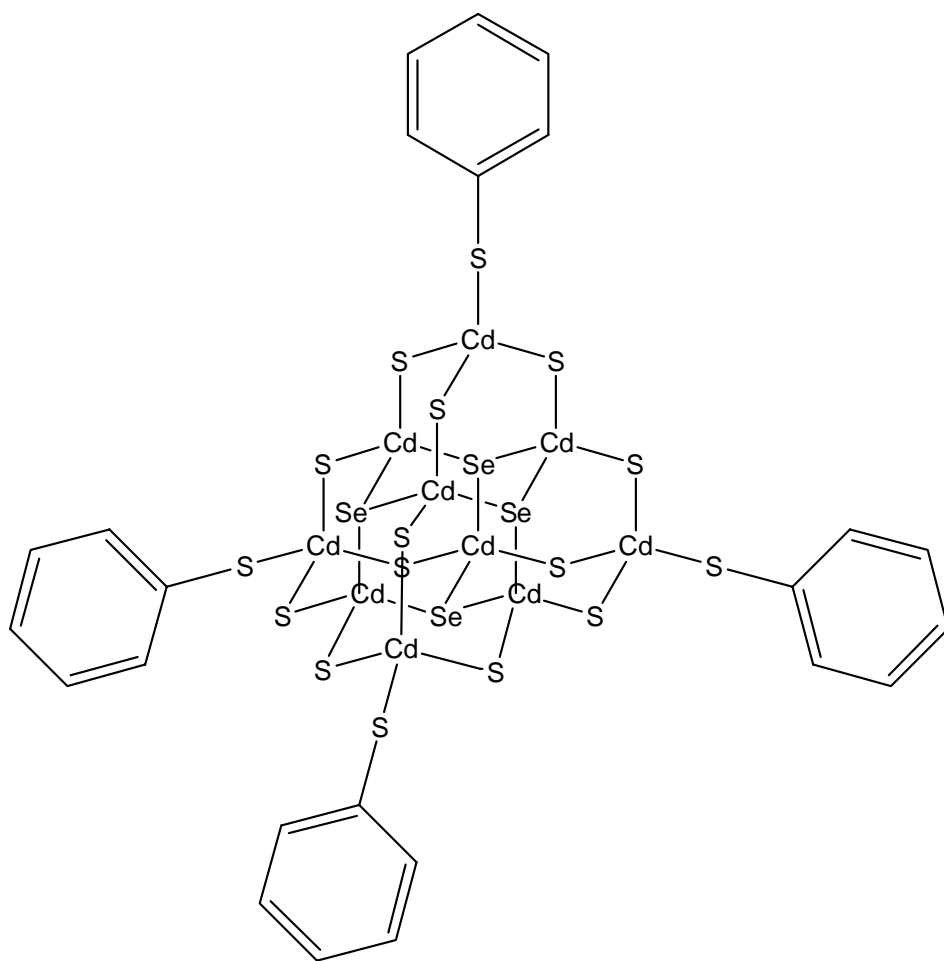


**Figure 2.2.** Structure of  $\text{Li}_4[\text{Cd}_{10}\text{Se}_4(\text{SPh})_{16}]$ . All of the sulfur atoms in this diagram are thiophenol molecules.

LiNO<sub>3</sub> (5.3 g, 80 mmol) in 40 mL methanol is added. This solution is then cooled to ~ 0°C for 1 – 2 hours. The Li<sub>2</sub>[Cd<sub>4</sub>(SPh)<sub>10</sub>] crystallizes as a white solid and is collected and washed with methanol and diethylether. Afterwards the white powder is vacuum dried for 30 minutes to remove remnant thiophenol. This reaction can successfully be scaled up to five times. This reaction has a 75% yield. Approximately, 20 g (~75% yield) of product can be synthesized using this size reaction. The pXRD and ESI-MS of these cluster is shown in figures 2.3 and 2.4.

**2.2.1.3 Synthesis of Li<sub>4</sub>[Cd<sub>10</sub>Se<sub>4</sub>(SPh)<sub>16</sub>].** Li<sub>4</sub>[Cd<sub>10</sub>Se<sub>4</sub>(SPh)<sub>16</sub>] is synthesized by the addition of Li<sub>2</sub>[Cd<sub>4</sub>(SPh)<sub>10</sub>] (13.84 g, 8.9 mmol) and Se (0.701 g, 8.9 mmol) to ~ 40 mL acetonitrile. The solution is allowed to stir at RT under atmospheric conditions for 3-8 hours until it turns creamy white. Afterwards, ~ 300 mL of acetonitrile is added and the solution is heated to 75°C until the precipitate dissolves (20 min). Once all of the white precipitate has dissolved the solution is filtered to remove unreacted Se powder. The filtrate is allowed to sit undisturbed for six hours at 0°C to crystallize as white or yellow Li<sub>4</sub>[Cd<sub>10</sub>Se<sub>4</sub>(SPh)<sub>16</sub>] crystals. This solution is filtered and the crystals are washed with acetonitrile. The reaction yields ~ 5.5 g (~ 76% yield) of Li<sub>4</sub>[Cd<sub>10</sub>Se<sub>4</sub>(SPh)<sub>16</sub>]. This reaction can be scaled up and it has been successfully scaled up to three times as large of a reaction as the one described above. The pXRD of this cluster is shown in figure 2.5

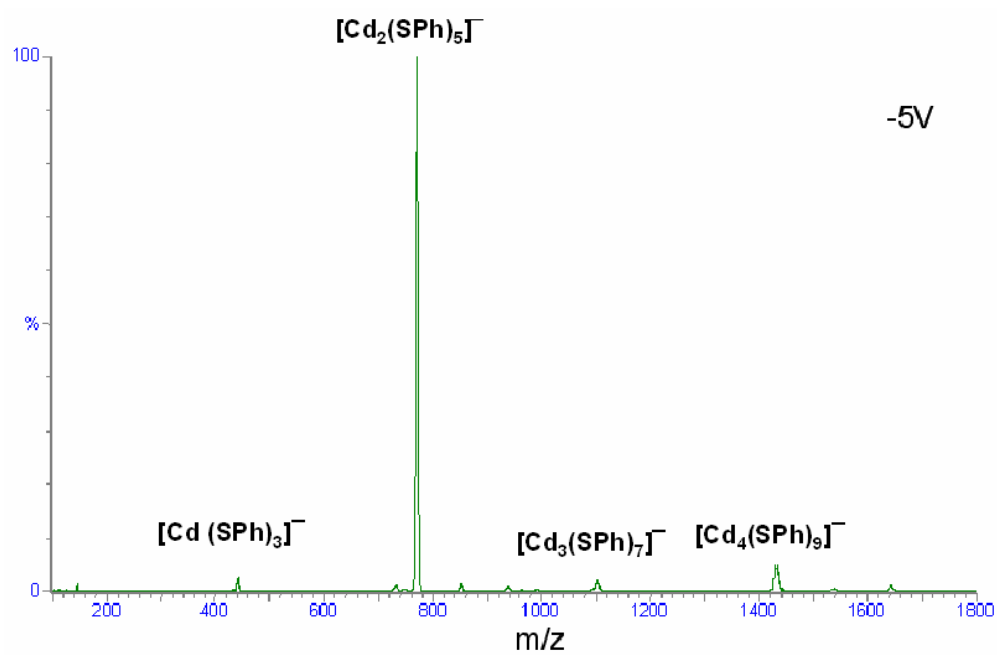


**Figure 2.3.** ESI-MS of  $\text{Li}_2[\text{Cd}_4(\text{SPh})_{10}]$  with a cone voltage of -5V.

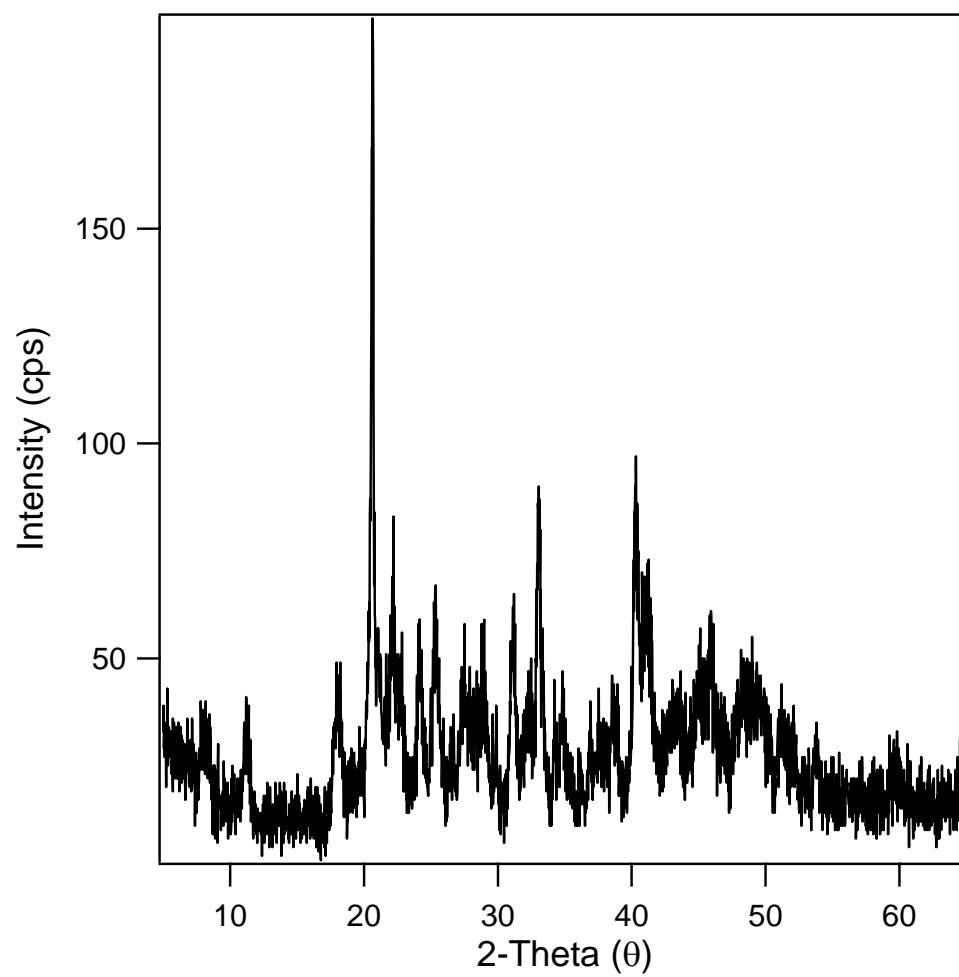


**Figure 2.4.** PXRD spectra of  $\text{Li}_2[\text{Cd}_4(\text{SPh})_{10}]$ .

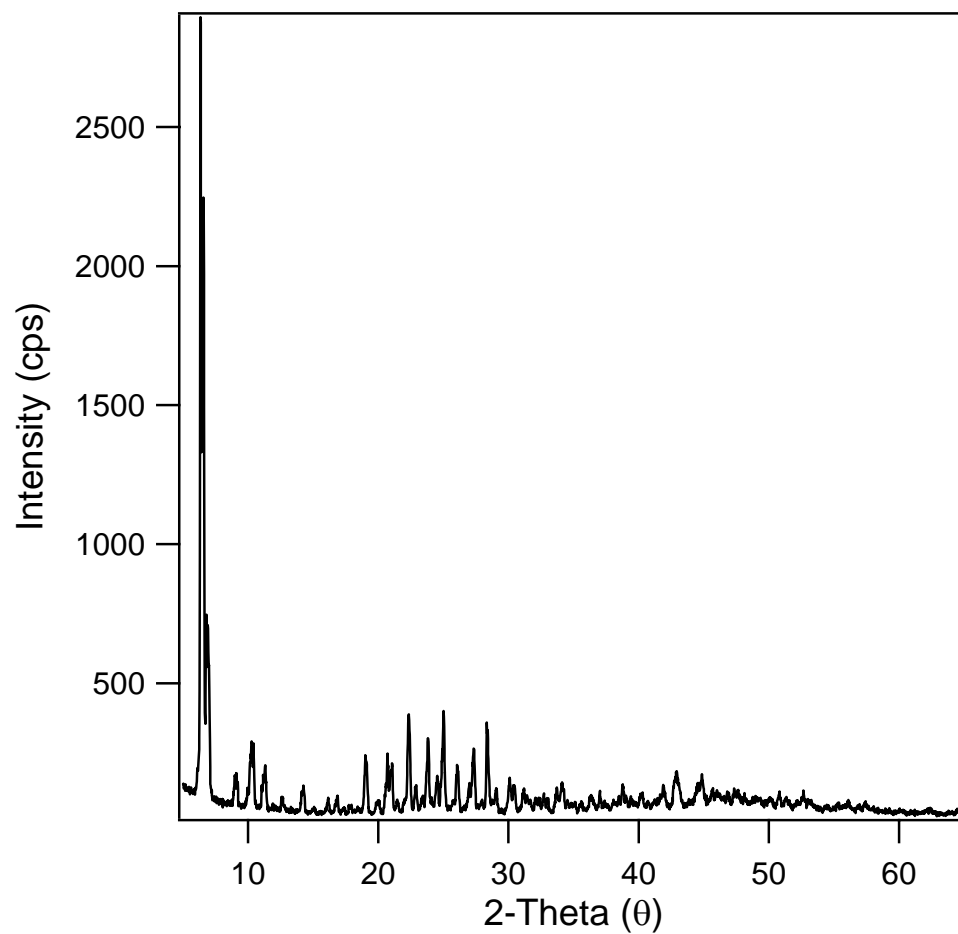


**Figure 2.5.** PXRD spectra of  $\text{Li}_4[\text{Cd}_{10}\text{Se}_4(\text{SPh})_{16}]$ .

**2.2.1.4 Synthesis of  $\text{TMA}_2[\text{Cu}_4(\text{SPh})_6]$**  Synthesis of  $[\text{Cu}_4(\text{SPh})_6]$  (Fig. 2.6) was performed by combining thiophenol (18.7 mL, 182 mmol) and triethylamine (25.5 mL, 182 mmol) in 60 mL of methanol at RT under atmospheric conditions. To this stirred solution,  $\text{Cu}(\text{NO}_3)_2 \cdot 2\frac{1}{2} \text{H}_2\text{O}$  (15.19 g, 68 mmols) in 60 mL methanol was slowly added. Upon the addition of the  $\text{Cu}(\text{NO}_3)_2 \cdot 2\frac{1}{2} \text{H}_2\text{O}$  the solution turned yellow in color. Precipitate formed and then redissolved in solution upon continuous stirring. To metathasize the anionic cluster to a tetramethylammonium counterion, tetramethylammonium chloride (8.2 g, 80 mmol) in 40 mL of methanol was added to the solution and allowed to sit at  $0^\circ\text{C}$  for 6 hours. Yellow crystalline needles formed and the solution was vacuum filtered to collect the crystals. The crystals were washed with cold methanol and diethyl ether. Details on the characterization of these materials are described in the following section. The pXRD of this cluster is shown in figure 2.7.

**2.2.1.5 Synthesis of  $\text{TMA}_2[\text{Co}_4(\text{SPh})_{10}]$ .**  $\text{TMA}_2[\text{Co}_4(\text{SPh})_{10}]$  (Fig. 2.8) was synthesized in a similar manner to  $\text{TMA}_2[\text{Cd}_4(\text{SPh})_{10}]$ .  $\text{Co}(\text{NO}_3)_2 \cdot 6\text{H}_2\text{O}$  (5.8 g, 20 mmol) in 30 mL of methanol was added slowly to a well stirred solution of (5.9 g, 54 mmol) thiophenol, and triethylamine (7.6 mL, 54 mmol) in 30 mL of methanol at RT under ambient conditions. Upon addition of the  $\text{Co}(\text{NO}_3)_2 \cdot 6\text{H}_2\text{O}$  solution the initially clear solution turned pine green and then dark purple. To convert the anionic cluster to a TMA salt, the anionic cluster was

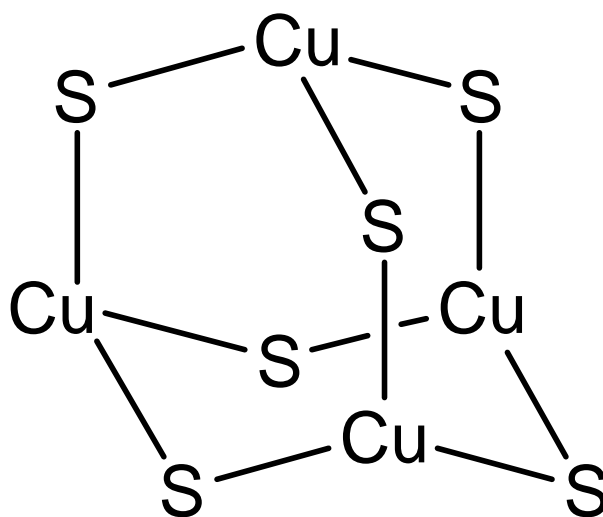


**Figure 2.6.** Structure of  $(\text{Me}_4\text{N})_2[\text{Cu}_4(\text{SPh})_6]$ . The sulfur atoms represent benzenethiols. For clarity the benzene ring was omitted from the benzenethiols in the structure.

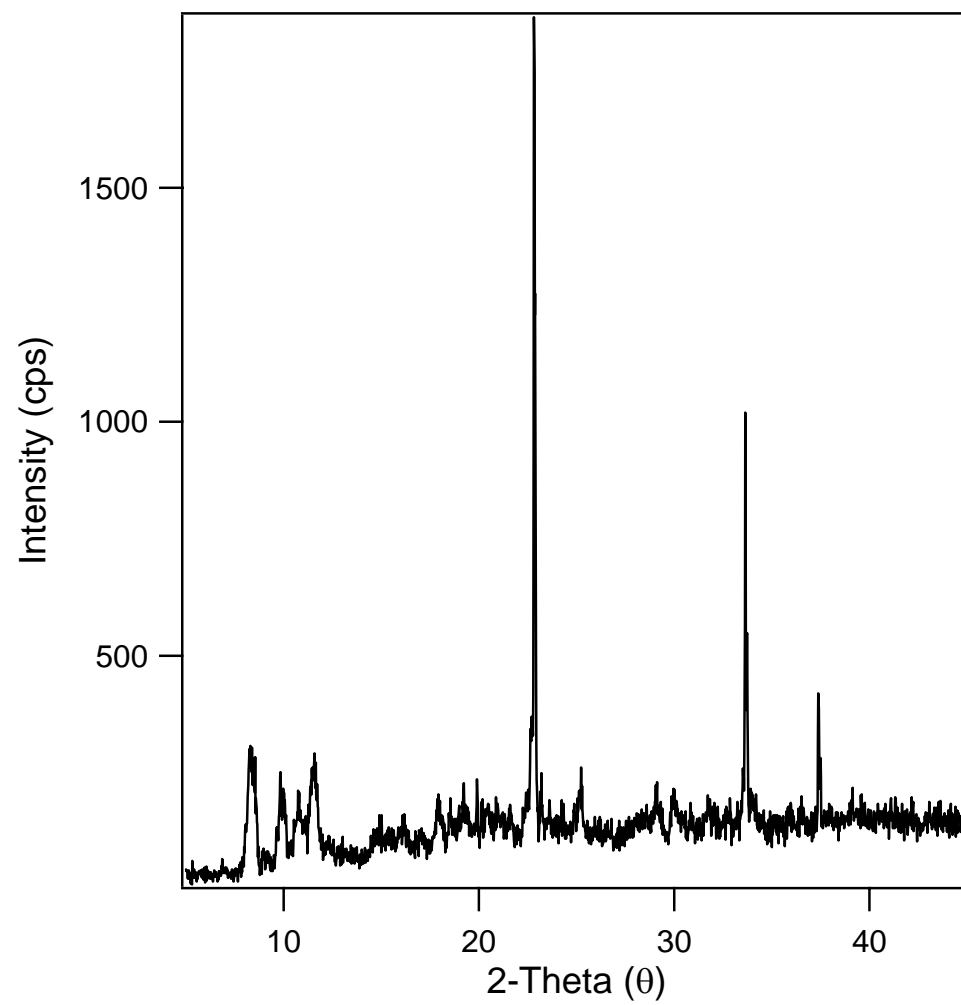


**Figure 2.7.** PXR D spectra of  $(\text{Me}_4\text{N})_2[\text{Cu}_4(\text{SPh})_6]$ .

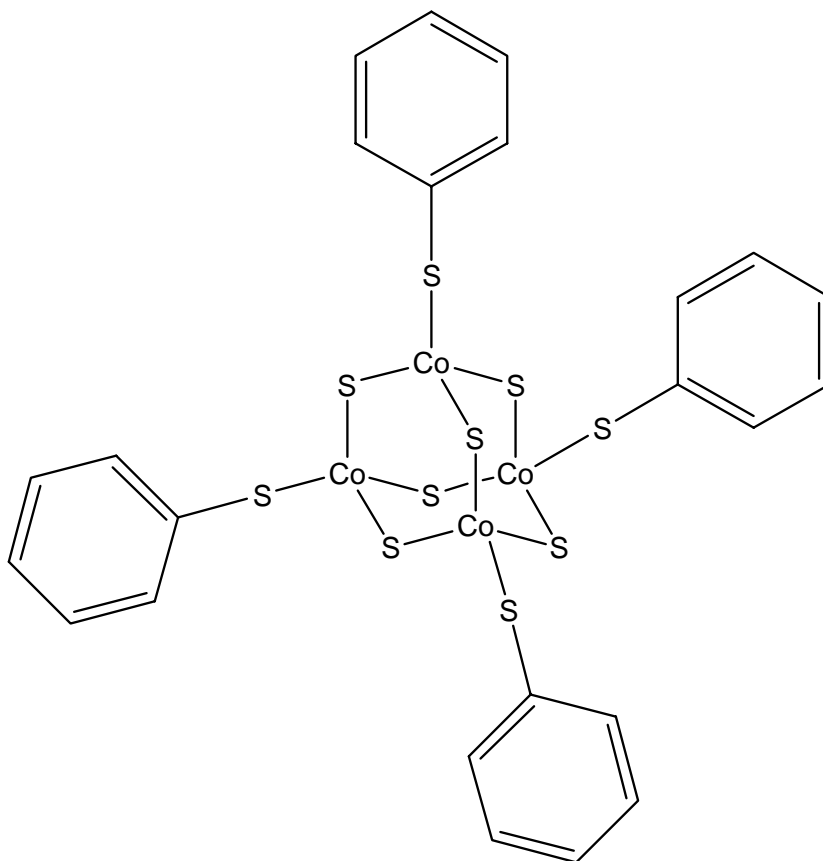


**Figure 2.8.** Structure of  $(\text{Me}_4\text{N})_2[\text{Co}_4(\text{SPh})_{10}]$ . All the sulfur atoms in the structure are benzenethiol. The benzene atoms for most of the benzenethiol have not been included for clarity.

metathasized by addition of tetramethylammonium chloride (2.5g, 23 mmol).

This solution was then allowed to sit at 0°C for 24 hours over which time a dark red precipitate formed and was collected by filtration and washed with (~ 200 mL) methanol and then (~150 mL) diethyl ether.

**2.2.1.6 Synthesis of TMA<sub>4</sub>[Cd<sub>4</sub>Co<sub>6</sub>S<sub>4</sub>(SPh)<sub>16</sub>].** TMA<sub>4</sub>[Cd<sub>4</sub>Co<sub>6</sub>S<sub>4</sub>(SPh)<sub>16</sub>] (Fig. 2.9) was synthesized in a similar manner to literature methods for TMA<sub>4</sub>[Cd<sub>10</sub>S<sub>4</sub>(SPh)<sub>16</sub>].<sup>8</sup> TMA<sub>2</sub>[Cd<sub>4</sub>(SPh)<sub>10</sub>] (2.04 g, 1.31 mmol) was placed in 30 mL CH<sub>3</sub>CN under N<sub>2</sub>. A solution containing 30 mL of CH<sub>3</sub>CN and (50 mg, 0.17 mmol) Co(NO<sub>3</sub>)<sub>2</sub> · 6H<sub>2</sub>O was rapidly added to the first solution. The solution turned green within a few minutes, and then deep purple. This solution was centrifuged yielding a green supernatant and a deep purple precipitate. The supernatant was vacuum evaporated and recrystallized in warm CH<sub>3</sub>CN yielding green TMA<sub>4</sub>[Cd<sub>4</sub>Co<sub>6</sub>S<sub>4</sub>(SPh)<sub>16</sub>] crystals. Large crystals of this compound could not be synthesized to do single crystal xrd analysis. The pXRD spectra of this structure is shown in figure 2.10.

## **2.2.2 Characterization:**

### **2.2.2.1 Mass Spectrometry.**

*Electrospray mass spectrometry.* Mass spectra were performed in negative-ion

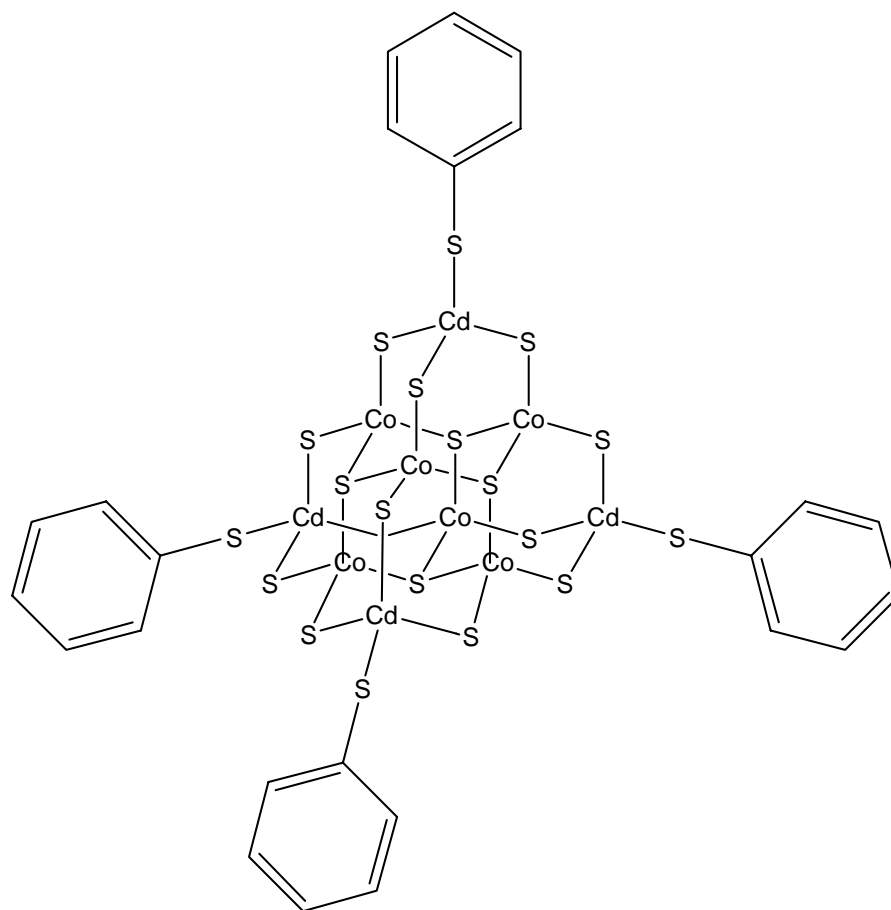


**Figure 2.9.** Structure of  $(\text{Me}_4\text{N})_4[\text{Cd}_4\text{Co}_6\text{S}_4(\text{SPh})_{16}]$ . The Cd-tetrathiophenolate caps have the benzene rings removed from the thiophenol for clarity.

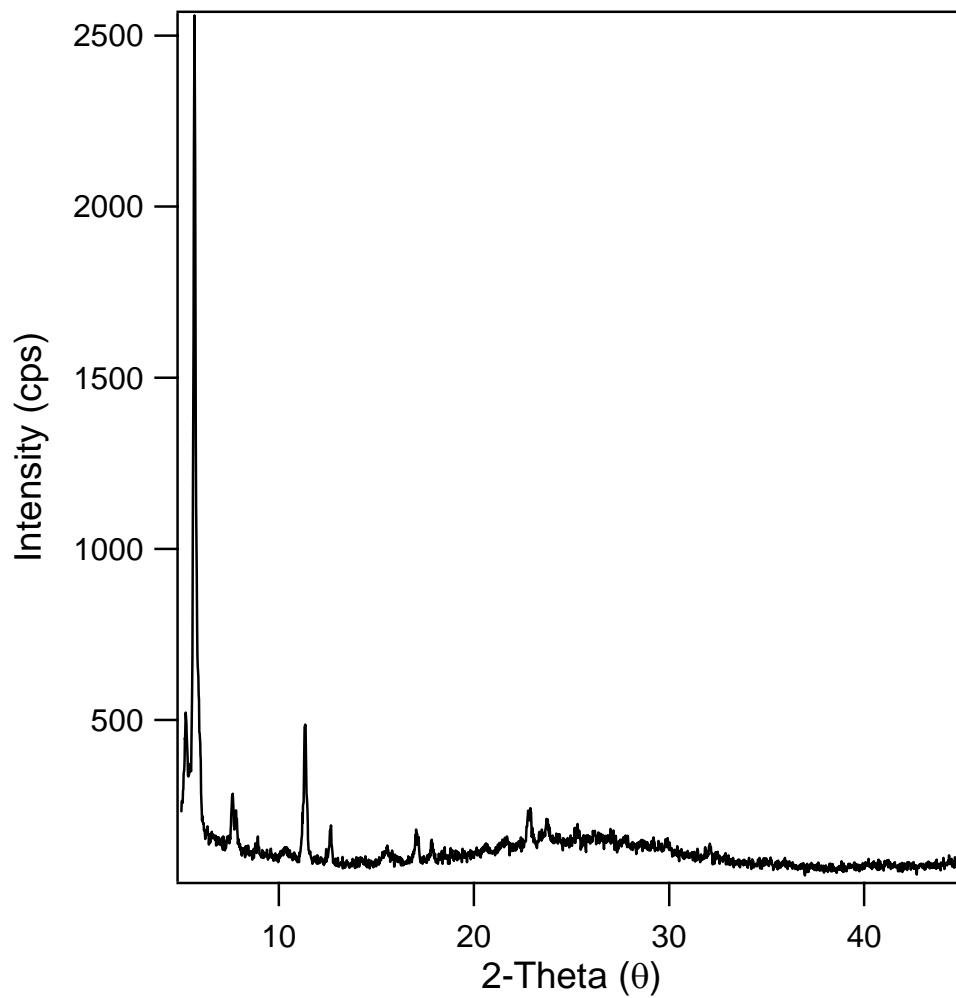


**Figure 2.10.** PXRd spectra of  $\text{TMA}_4[\text{Cd}_4\text{Co}_6\text{S}_4(\text{SPh})_{16}]$ .

using a VG Platform II mass spectrometer (Fisons Instruments) coupled to a quadrupole mass filter with a  $m/z$  ion range from 0 to 3000. The quadrupole mass selector was calibrated using a solution of sodium iodide as a standard. Nitrogen was employed as both the drying and nebulizing gas. Freshly prepared samples [approximate concentration: 0.1 mmol L in dry acetonitrile (4 Å molecular sieve, HPLC Grade)] were injected into the spectrometer at a flow rate of  $20 \text{ L min}^{-1}$  using a syringe infusion pump (Harvard Apparatus). The solutions are delivered to the mass spectrometer source at a temperature of  $67^\circ\text{C}$ . The cone voltage was - 5 V for all samples to minimize induced fragmentation processes. Cone voltages from - 5 to - 190 V were checked for reliability of the ion distribution. All assigned peaks in the presented mass spectra were identified by the most intense  $m/z$  value within the isotopic mass distribution. Although the resolution in the mass spectra is limited, assignments of the ionic species by comparison to the predicted isotope distribution patterns provide further evidence of the cluster fragment assignments.

*Nanospray Mass Spectrometry.* Mass spectrometry was performed using a QSTAR Hybrid MS/MS System (Applied Biosystems Inc.) consisting of a quadrupole mass analyzer followed by a modified quadrupole as a collision cell and a reflectron time-of-flight as the second mass analyzer. The system was equipped with a TurboIonSpray (ESI) source (Applied Biosystems Inc.) and a

nanoelectrospray source (Protana Inc.) which provided minimal sample consumption. The flow rate of the nanospray source was fixed at  $\sim 20 \text{ nl}\cdot\text{min}^{-1}$ . The ion source voltage applied to the flow was between 500 and 1500 V in positive ion mode ( $-500$  and  $-1500$  V in negative ion mode) depending on the compound. The orifice voltage was set at  $\pm 40$  V for all samples to minimize fragmentation. The orifice voltage from  $-100$  to  $+100$  V was checked for reliability of the ion distribution. Nitrogen was employed as both the drying and nebulizing gas. Freshly prepared samples [approximate concentration :  $0.1 \text{ mmol}\cdot\text{L}^{-1}$  in dry acetonitrile ( $4 \text{ \AA}$  molecular sieve, HPLC grade)] were injected in the spectrometer using a syringe infusion pump (Harvard Apparatus Inc.). Mass scans were performed with a dwell time of  $1.0 \text{ ms}$  for a  $m/z$  ion range from 400 to 6000. All assigned peaks in the presented mass spectra were identified by the most intense  $m/z$  value within the isotopic mass distribution. Confirmation of ionic species was made by comparing the experimental with the calculated isotope distribution patterns using Multiview software (Applied Biosystems Inc.).

**2.2.2.2 Superconducting Quantum Interference Devices (SQUID).** SQUID magnetometry was performed on powder samples in gel caps. Approximately  $20 \text{ mg}$  of sample was used for these measurements. The SQUID measurements were performed under a constant applied DC field of  $500 \text{ Oe}$  under a Zero-

field-cooled (ZFC) and Field-cooled (FC). The temperature was ramped between 300 and 2 K under constant applied field.

**2.2.2.3 X-ray Absorption Near Edges Structure (XANES).** XANES was performed on the samples at the undulator beam line 8.0.1 at the Advanced Light Source at Lawrence Berkeley National Labs. Powder samples were pressed onto Indium foil and the sample chamber had a base pressure less than  $8 \times 10^{-9}$  torr.

**2.2.2.4 UV-Vis Absorption spectroscopy.** UV-Vis was taken on an Ocean Optics S2000 CCD fiber optic spectrophotometer (resolution 4 meV). Absorption measurements were performed on  $1 \times 10^{-6}$  M solutions at room temperature in methanol.

## 2.3 RESULTS AND DISCUSSION

### 2.3.1 *Li<sub>2</sub>[Cd<sub>4</sub>(SPh)<sub>10</sub>] and Li<sub>4</sub>[Cd<sub>10</sub>Se<sub>4</sub>(SPh)<sub>16</sub>]clusters.*

Observation of the mass spectra of both the  $M_4$  and  $M_{10}$  clusters shows that all of the fragmentation peaks can be attributed to the parent ion. In the  $M_4$  cluster ( $M = \text{Cd}$  or  $\text{Co}$ ), fragmentation of the parent ion results in a series of peaks with the formula  $[\text{M}_n(\text{SPh})_{2n+1}]^-$  from  $n = 1 - 4$ . In the positive mass

spectra of  $\text{Li}_2[\text{Cd}_4(\text{SPh})_{10}]$  a pseudo-parent ion is seen with the loss of a  $\text{Me}_4\text{N}^+$  with an  $m/z$  of 1615. It has been shown that by increasing the cone-voltage a subsequent increase in the intensity of the fragment peaks should be observed.<sup>11</sup> The most characteristic peak in the  $\text{M}_4$  clusters is  $\text{M}(\text{SPh})_3^-$ . The  $\text{Cd}_{10}$  system also exhibits fragments that are due to loss of  $\text{Cd}(\text{SPh})_2$ , which is consistent with what has been observed in the  $\text{Cd}_4$  system. In the  $\text{Cd}_{10}$  cluster, the  $\text{Cd}(\text{SPh})_3^-$  fragment has been assigned to fragmentation from a corner of the cluster (figure 2.11).<sup>12</sup> Table 2.1 shows the peak assignments for the two clusters.

### ***2.3.2 $[\text{Me}_4\text{N}]_2[\text{Co}_4(\text{SPh})_{10}]$ cluster.***

The  $\text{Co}_4$  cluster seems to be more stable than that of the  $\text{Cd}_4$  cluster that may give rise to the different fragmentation behavior observed in the  $\text{Co}_4$  cluster. A pseudo-parent ion at  $m/z$  1400 is observed corresponding to  $(\text{Me}_4\text{N})[\text{Co}_4(\text{SPh})_{10}]^-$  (figure 2.12). A peak at  $m/z$  1308 is observed which is due to a loss of  $\text{Co}(\text{SPh})^+$  and another peak at  $m/z$  1123 is seen due to a further loss of  $\text{Me}_4\text{N}^+$  and thiophenol. A second series of fragmentation of the parent ion peak at  $m/z$  1400 occurs by loss of one  $\text{Me}_4\text{N}^+$  and thiophenol producing  $[\text{Co}_4(\text{SPh})_9]^-$  with  $m/z$  1216. Peaks at 1049 and 1233 are due to contamination of the product with  $\text{Cl}^-$  substitution of one  $\text{SPh}^-$  at  $m/z$  1123 and 1307. The chloride ion impurities are most likely due to the tetramethylammonium

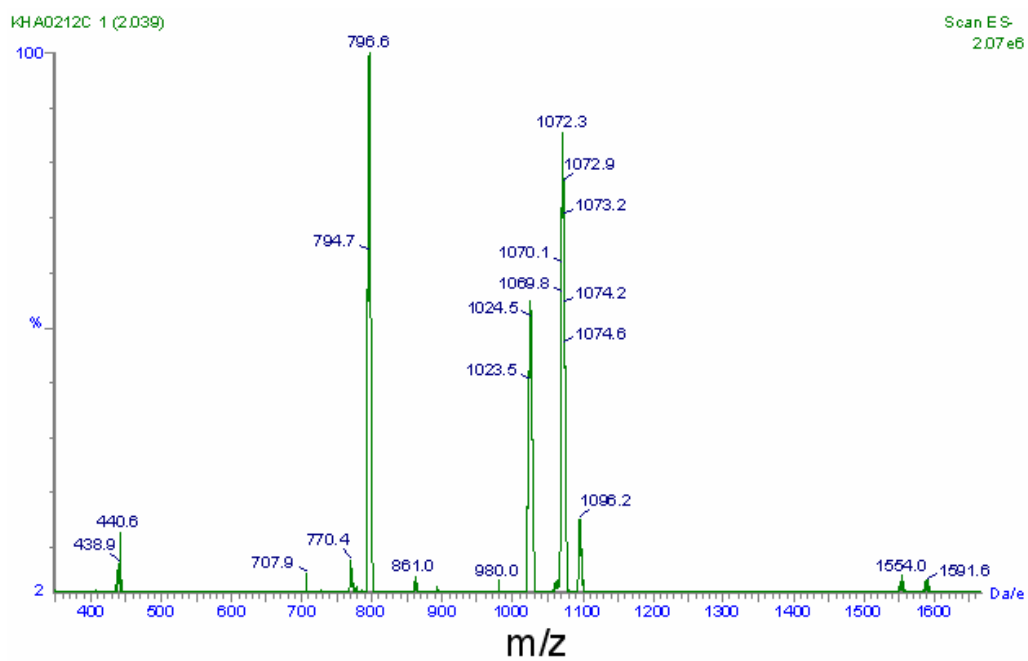


**Figure 2.11.** ESI-MS of  $\text{Li}_4[\text{Cd}_{10}\text{Se}_4(\text{SPh})_{16}]$  with a cone voltage of -5V.

Fragment	Experimental m/z	Calculated m/z
<b>Li<sub>2</sub>[Cd<sub>4</sub>(SPh)<sub>10</sub>]</b>		
[Cd(SPh) <sub>3</sub> ] <sup>-</sup>	441	441
[Cd <sub>2</sub> (SPh) <sub>5</sub> ] <sup>-</sup>	770	772
[Cd <sub>3</sub> (SPh) <sub>7</sub> ] <sup>-</sup>	1101.8	1104.8
[Cd <sub>4</sub> (SPh) <sub>9</sub> ] <sup>-</sup>	1436.7	1432
<b>Li<sub>4</sub>[Cd<sub>10</sub>Se<sub>4</sub>(SPh)<sub>16</sub>]</b>		
[Cd(SPh) <sub>3</sub> ] <sup>-</sup>	441	441
[Cd <sub>2</sub> (SPh) <sub>5</sub> ] <sup>-</sup>	770	772
[Cd <sub>4</sub> Se <sub>3</sub> (SPh) <sub>8</sub> Li <sub>4</sub> ] <sup>2-</sup>	796	797
[Cd <sub>5</sub> Se <sub>2</sub> (SPh) <sub>9</sub> Li] <sup>2-</sup>	861	861
[Cd <sub>6</sub> Se <sub>2</sub> (SPh) <sub>14</sub> Li] <sup>2-</sup>	1024	1025
[Cd <sub>6</sub> Se <sub>3</sub> (SPh) <sub>11</sub> Li <sub>3</sub> ] <sup>2-</sup>	1072	1072
[Cd <sub>2</sub> Se(SPh) <sub>7</sub> Li <sub>4</sub> ] <sup>-</sup>	1096	1096
[Cd <sub>4</sub> (SPh) <sub>10</sub> Li] <sup>-</sup>	1554	1554
[Cd <sub>5</sub> Se <sub>3</sub> (SPh) <sub>7</sub> Li <sub>2</sub> ] <sup>-</sup>	1591	1587

**Table 2.1.** ESI-MS peak assignments for Li<sub>2</sub>[Cd<sub>4</sub>(SPh)<sub>10</sub>] and Li<sub>4</sub>[Cd<sub>10</sub>Se<sub>4</sub>(SPh)<sub>16</sub>].

Fragment	Assignment	Experimental m/z	Calculated m/z
<b>(Me<sub>4</sub>N)<sub>2</sub>[Co<sub>4</sub>(SPh)<sub>10</sub>]</b>			
[Co <sub>n</sub> <sup>II</sup> (SPh) <sub>2n+1</sub> ] <sup>-</sup>			
n=1	(1,3)	386	386
n=2	(2,5)	663	663
n=3	(3,7)	940	940
n=4	(4,9)	1216	1217
[Me <sub>4</sub> N][Co <sub>3</sub> (SPh) <sub>8</sub> ] <sup>-</sup>	B1	1123	1123
[Me <sub>4</sub> N] <sub>2</sub> [Co <sub>3</sub> (SPh) <sub>9</sub> ] <sup>-</sup>	B2	1307	1306
[Me <sub>4</sub> N][Co <sub>4</sub> (SPh) <sub>10</sub> ] <sup>-</sup>	PICo <sub>4</sub>	1400	1400
<b>(Me<sub>4</sub>N)<sub>2</sub>[Cu<sub>4</sub>(SPh)<sub>6</sub>]</b>			
[Cu <sub>n</sub> <sup>I</sup> (SPh) <sub>n+1</sub> ]			
n=1	(1,2)	280	281
n=2	(2,3)	454	453
n=3	(3,4)	626	625
n=4	(4,5)	800	797

**Table 2.2.** Dominant ionic species observed in the ESI-MS (-5V) for (Me<sub>4</sub>N)<sub>2</sub>[Co<sub>4</sub>(SPh)<sub>10</sub>] and (Me<sub>4</sub>N)<sub>2</sub>[Cu<sub>4</sub>(SPh)<sub>6</sub>].

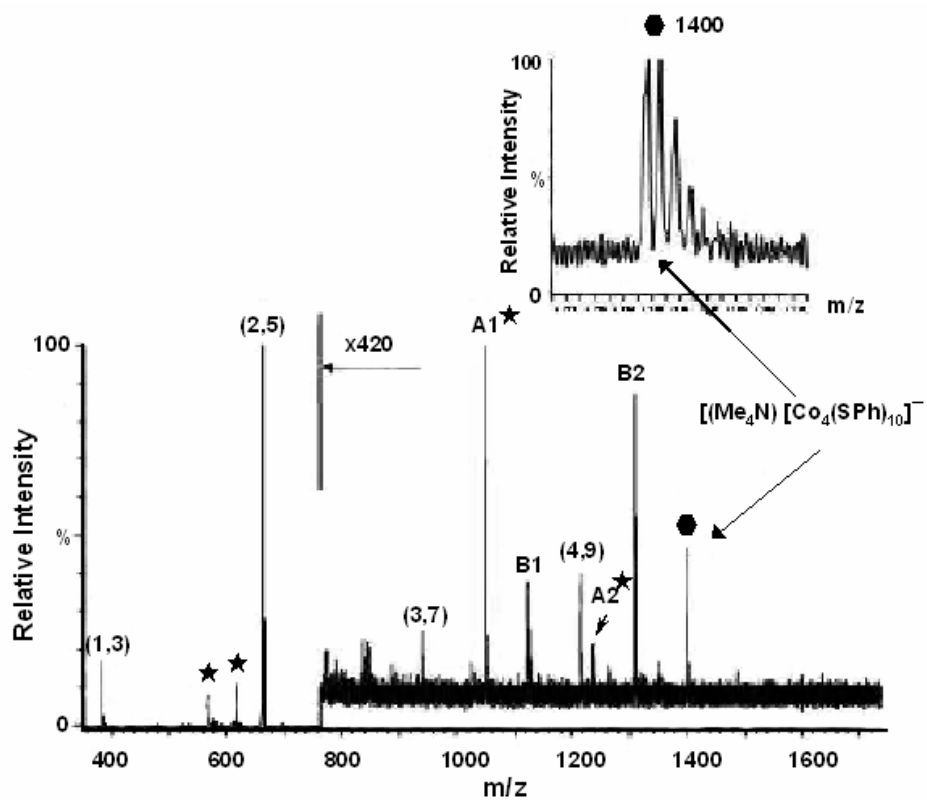


**Figure 2.12.** ESI-MS of  $(\text{Me}_4\text{N})[\text{Co}_4(\text{SPh})_{10}]^-$ .

chloride that was added into the reaction mixture. The peak assignments for this cluster can be found in table 2.2.

Magnetic measurements were also conducted on the cluster  $(\text{Me}_4\text{N})_2[\text{Co}_4(\text{SPh})_{10}]$ . The zero-field cooled and field-cooled magnetic data under a field of 500 Oe is shown in figure 2.13. This cluster exhibits paramagnetic behavior at high temperature and has an antiferromagnetic phase transition at 7K. Magnetism and magnetic properties will be discussed in more detail in Chapter 3.

### 2.3.3 $(\text{Me}_4\text{N})_2[\text{Cu}_4(\text{SPh})_6]$

Mass spectra of the  $(\text{Me}_4\text{N})_2[\text{Cu}_4(\text{SPh})_6]$  cluster is shown in figure 2.14. The pseudo-parent ion peak at  $m/z$  800 has been assigned as  $[\text{Cu}_4(\text{SPh})_5]^-$ . This corresponds to a cluster composed of Cu(I) ions. The pseudo parent ion arises from a loss of two  $\text{Me}_4\text{N}^+$  and one  $\text{SPh}^-$ . Subsequent fragments are formed by loss of  $\text{Cu}(\text{SPh})$ . The peaks at  $m/z$  280, 454, and 626 correspond to  $[\text{Cu}(\text{SPh})_2]^-$ ,  $[\text{Cu}_2(\text{SPh})_3]^-$ , and  $[\text{Cu}_3(\text{SPh})_4]^-$  respectively. The calculated and experimental values of the peak assignments can be seen in table 2.2.

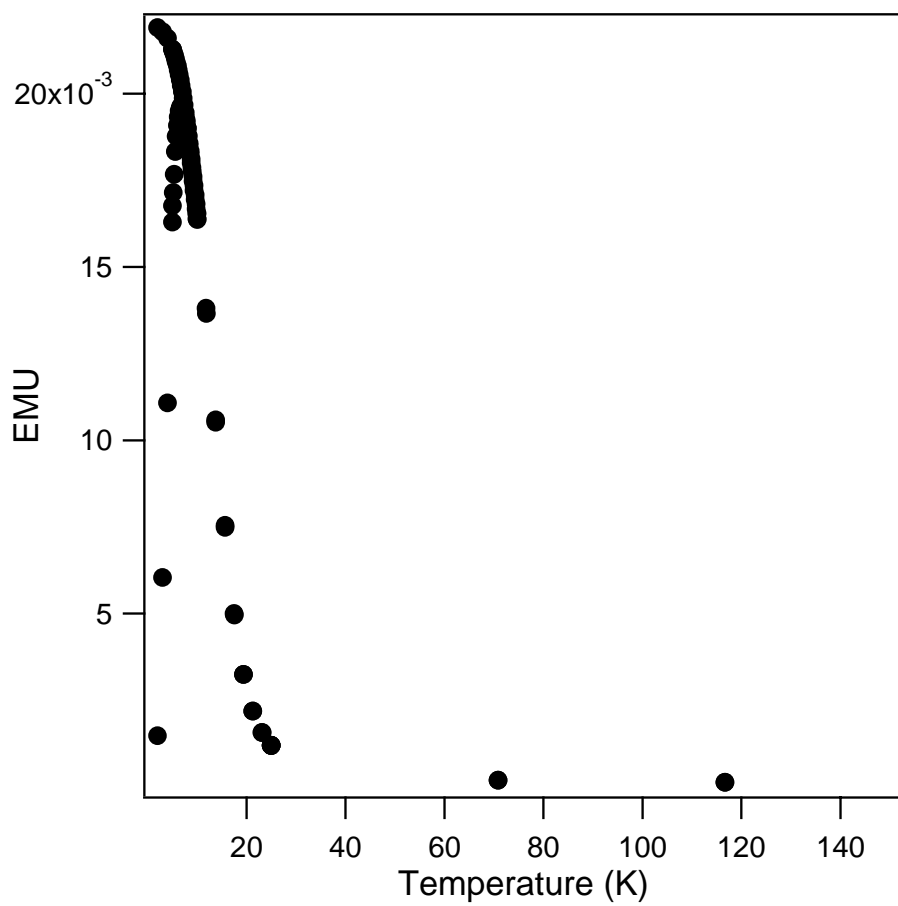


**Figure 2.13.** Zero-field cooled, field-cooled susceptibility measurements of  $(\text{Me}_4\text{N})_2[\text{Co}_4(\text{SPh})_{10}]$  under a field of 500 Oe.

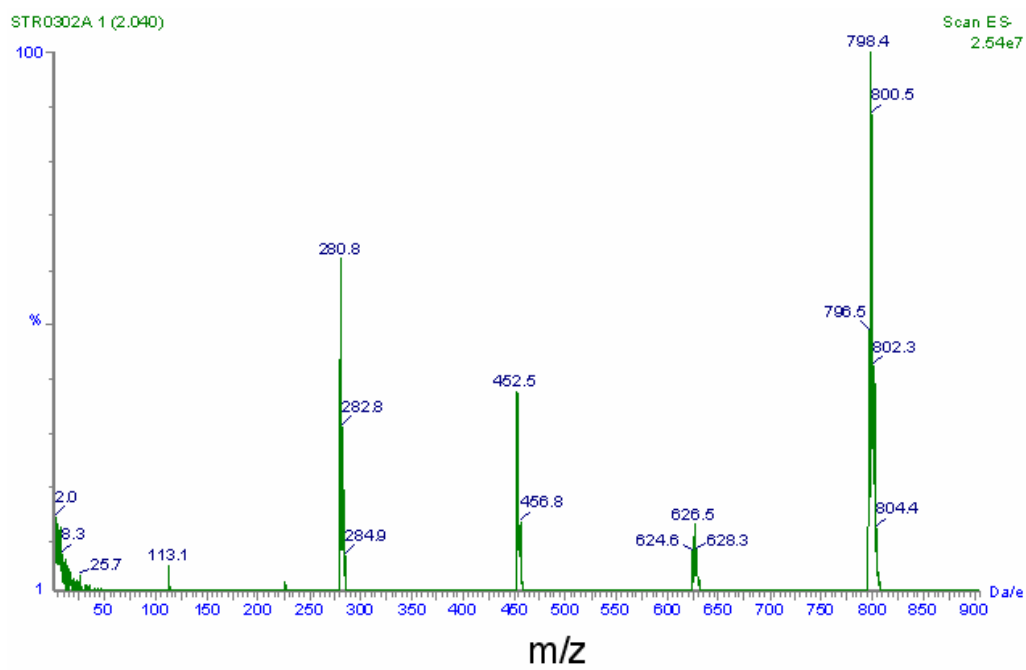


**Figure 2.14.** ESI-MS of  $(\text{TMA})_2[\text{Cu}_4(\text{SPh})_6]$  with a cone voltage of -5V.

XANES and XPS analysis was performed on the  $(\text{Me}_4\text{N})_2[\text{Cu}_4(\text{SPh})_6]$  cluster to verify the oxidation state assignments. Both of these methods are excellent for determination of oxidation states within the material. Since this cluster was used as a dopant precursor in the synthesis of Cu: CdSe in Chapter 4, understanding the oxidation state of the cluster is crucial.<sup>2,3,13-15</sup>

XANES spectroscopy is a very powerful tool for analysis of the oxidation state for a specific ion in the lattice and can be used to provide definitive proof of localized oxidation states in the lattice. In x-ray absorption spectroscopy, we are exciting a core electron to an unoccupied orbital, which allows a mapping of the unoccupied partial density of states on the ion. The oxidation state of a material in XANES is determined by comparison of a sample with that of known standards. We compared the XANES spectra of the  $[\text{Me}_4\text{N}]_2[\text{Cu}_4(\text{SPh})_6]$  with both Cu(I)I and Cu(II)Se, as shown in figure 2.15. It can be seen in the XANES spectra, the Cu edge resembles that of the Cu(I)I and not that of Cu(II)Se. This allows us to conclude that the oxidation state of the cluster is +1, in agreement with the mass spectrum data.

XPS is another tool for determination of oxidation states in materials. XPS spectra of diamagnetic and paramagnetic first row transition metal ions can be distinguished by the appearance of intense satellite peaks for paramagnetic first row transition metals. This is observed as less intense peaks

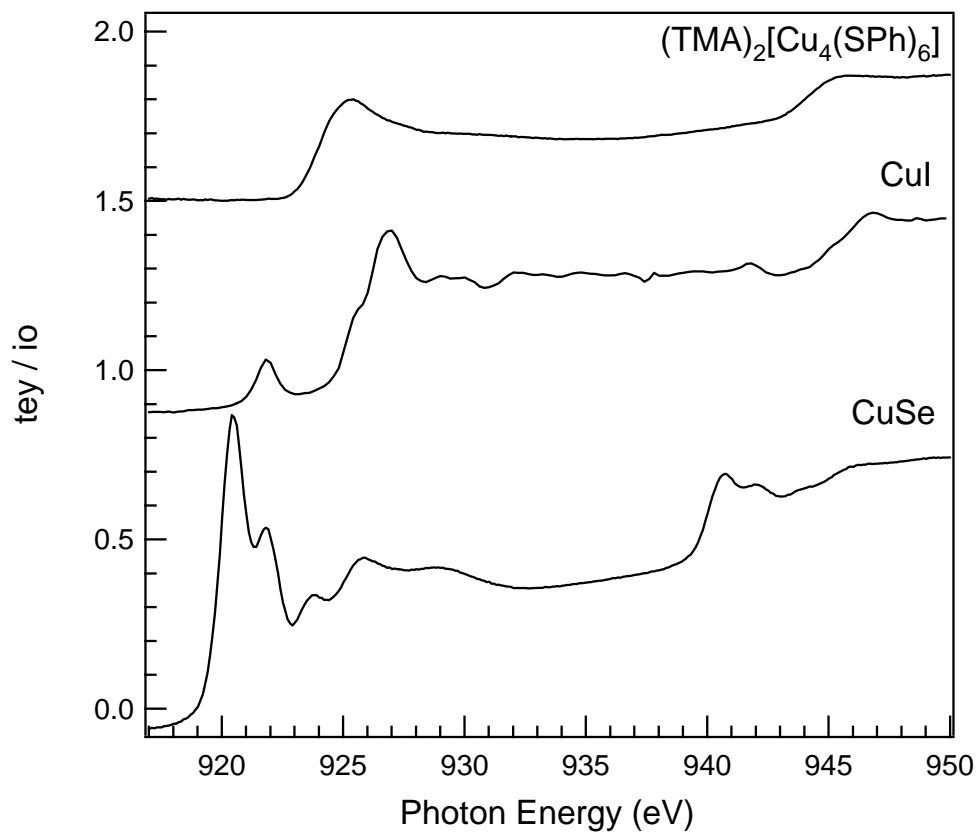


**Figure 2.15.** Cu-edge XANES spectra of  $(Me_4N)_2[Cu_4(SPh)_6]$ , Cu(I)I and Cu(II)Se.

on the high binding energy side of the main peak. In the case of Cu, very intense satellite peaks can be observed for Cu(II), while Cu(I) shows absolutely no satellite peaks thereby making it very simple to determine the oxidation state of Cu ions in a material. The XPS spectra of  $[\text{Me}_4\text{N}]_2[\text{Cu}_4(\text{SPh})_6]$  is shown in figure 2.16. No shake-up peaks (satellite peaks) were observed in the XPS spectra. This allows us to confirm the oxidation state of the Cu ion in the cluster as +1, which would give a cluster composed of a  $3d^{10}$  diamagnetic Cu(I) ion.

### ***2.3.4 $\text{TMA}_4[\text{Cd}_4\text{Co}_6\text{S}_4(\text{SPh})_{16}]$***

#### *2.3.4.1 Mass spectra analysis of $\text{TMA}_4[\text{Cd}_4\text{Co}_6\text{S}_4(\text{SPh})_{16}]$ .*

The pseudo-parent ion peak measured at -50V is observed at  $m/z$  1338 for  $[\text{Cd}_4\text{Co(II)}_4\text{Co(III)}_2\text{S}_4(\text{SPh})_{16}]^{2-}$  and is in good agreement with the isotopic distribution analysis for a cluster composed of two cobalt oxidation states.

When the charge of the pseudo-parent ion peak is balanced only one possible solution can exist where there are 4 Co(II) and 2 Co(III) ions in the core of the cluster. Figure 2.17 shows the low cone voltage mass spectra of the  $\text{TMA}_4[\text{Cd}_4\text{Co}_6\text{S}_4(\text{SPh})_{16}]$  ( $\text{Cd}_4\text{Co}_6$ ) cluster. The spectrum at low cone voltage consists of only 3 major peaks at  $m/z$  440, 771, and 1101 corresponding to  $[\text{Cd}(\text{SPh})_3]^-$ ,  $[\text{Cd}_2(\text{SPh})_5]^-$ , and  $[\text{Cd}_3(\text{SPh})_7]^-$  respectively. In analogy to the

fragmentation behavior in the Cd<sub>10</sub> parent cluster, the lack of [Co(SPh)<sub>3</sub>]<sup>-</sup> fragments suggest the Cd ions are involved with the tetrathiophenolate caps and the Co ions are in the core as a Co<sub>6</sub>Se<sub>4</sub> structure with a mixed valent 4 Co(II) / 2 Co(III) composition. The arrangement of the internal Co(II) is predicted to lie on the equatorial plane relative to the M<sub>6</sub>S<sub>4</sub> structure, and the Co(III) atoms are predicted to lie in an axial geometry. Arrangement of the atoms in such a manner would result in an absence of a Co(SPh)<sub>3</sub><sup>-</sup> fragment observed in the ESI-MS spectra. The proposed structure of this cluster along with the fragmentation of the cluster at cone voltages of -5V and -50V is shown in figure 2.18. A list of the ionic species and assignment of them can be found in table 2.3.

#### 2.3.4.2 Optical absorption of TMA<sub>4</sub>[Cd<sub>4</sub>Co<sub>6</sub>S<sub>4</sub>(SPh)<sub>16</sub>].

Gamelin, et al have previously demonstrated the applicability of ligand field spectroscopy as a probe of site symmetry in doped nanomaterials. In Co:CdS quantum dots, the Co(II) absorption is observed at 693 nm for surface bound Co(II) on a distorted T<sub>d</sub> site and at 728 nm for core Co(II) ions sitting on a T<sub>d</sub> site.<sup>16</sup> The Co(II) absorption is due to the electronic transition that occurs from <sup>4</sup>A<sub>2</sub> → <sup>4</sup>T<sub>1</sub>(P) and the shifts in the peaks were shown to result from ligand field effects. The optical properties of the Co<sup>2+</sup> ion were studied as a function of passivating ligand (pyridine, dodecanthiol) and it was shown that the absorption

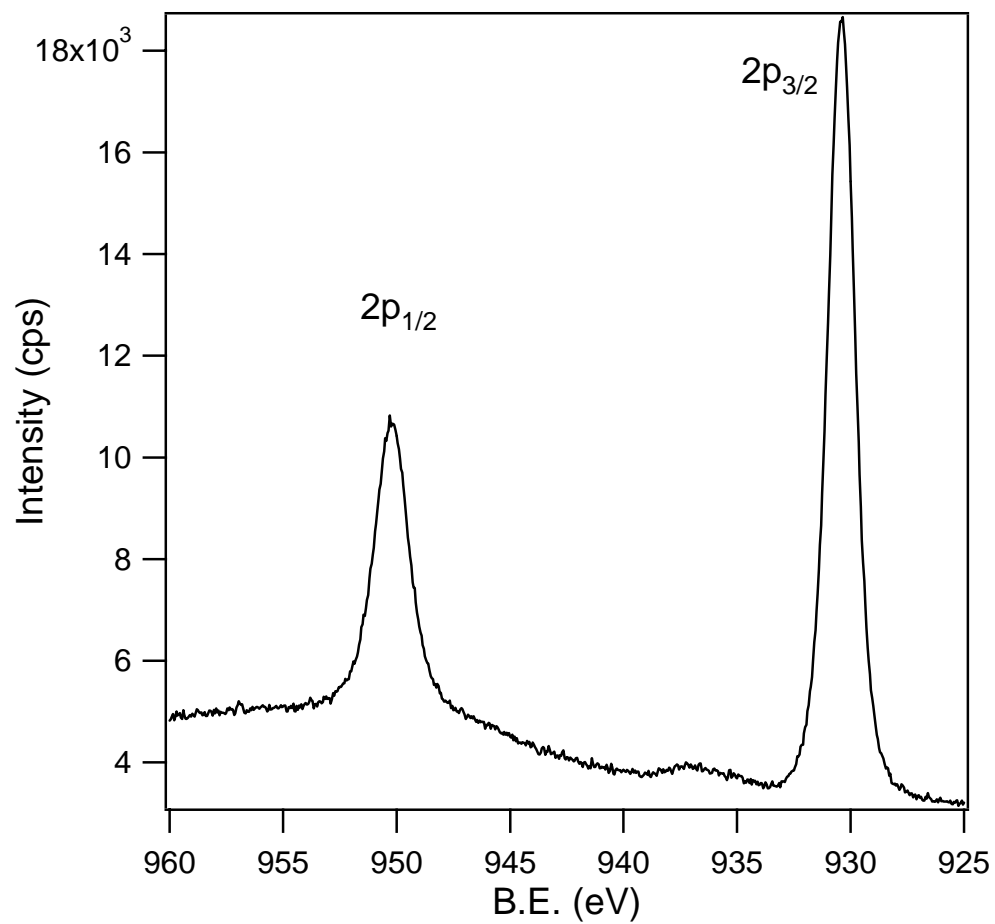


**Figure 2.16.** XPS spectra of  $(\text{Me}_4\text{N})_2[\text{Cu}_4(\text{SPh})_6]$ .

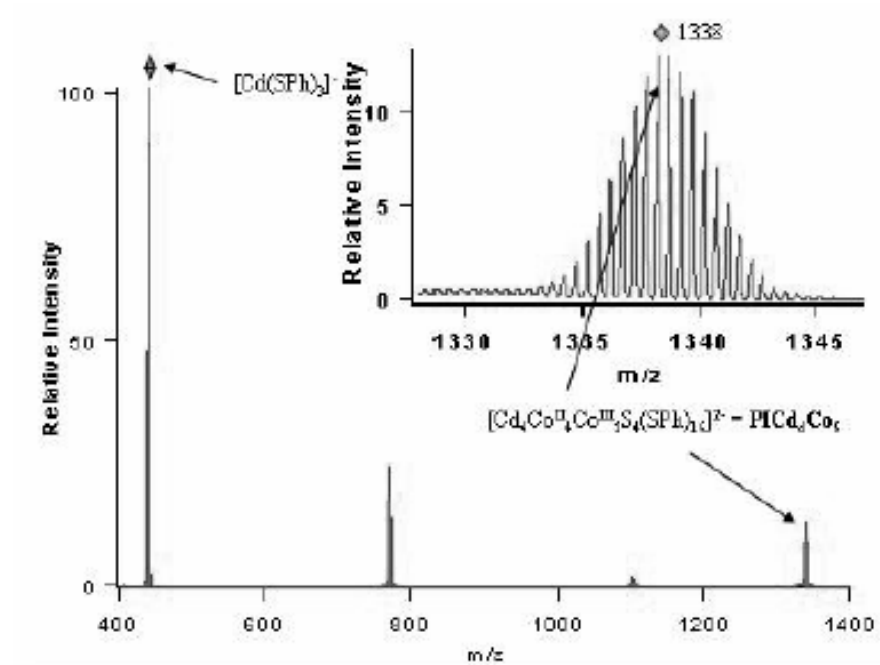


**Figure 2.17.** ESI-MS of  $[\text{Me}_4\text{N}]_4[\text{Cd}_4\text{Co}_6\text{S}_4(\text{SPh})_{16}]$  with a cone voltage of  $-5$

V. The inset shows an the expanded region of the parent ion peak

$[\text{Cd}_4\text{Co}_6\text{S}_4(\text{SPh})_{16}]^{2-}$ .

---

<u>Ionic Species</u>	<u>Assignment</u>	<u>m/z expt.</u>	<u>m/z calc.</u>
$[\text{Cd}_n(\text{SPh})_{2n+1}]^-$			
n=1	(1,3)	441	441
n=2	(2,5)	771	771
n=3	(3,7)	1101	1101
$[\text{Cd}_n(\text{SPh})_{2n-1}\text{S}]^-$			
n=3	C1	916	915
n=4	C2	1246	1246
$[\text{Cd}_4\text{Co}_4^{\text{II}}\text{Co}_2^{\text{III}}\text{S}_4(\text{SPh})_{16}]^{2-}$	PICd <sub>4</sub> Co <sub>6</sub>	1338	1339
$[\text{Cd}_4\text{Co}_4^{\text{II}}\text{Co}_2^{\text{III}}\text{S}_4(\text{SPh})_9]^-$	PICd <sub>4</sub> Co <sub>6</sub> -[Cd <sub>3</sub> (SPh) <sub>7</sub> ] <sup>-</sup>	1576	1576

---

**Table 2.3.** Dominant ionic species observed in ESI-MS of [Me<sub>4</sub>N]<sub>4</sub>[Cd<sub>4</sub>Co<sub>6</sub>S<sub>4</sub>(SPh)<sub>16</sub>] with a cone voltage of -50V.

of  $\text{Co}^{2+}$  assigned to a surface site was affected by the passivating ligand.

Tetrahedrally coordinated Co(III) is also known to have an absorption maximum between 500-600 nm.

The experimentally observable difference in the absorption spectra for Co(II) and Co(III) allows the site – symmetry and the oxidation state of the cobalt in the clusters to be identified by inspection of the optical absorption data, shown in figure 2.19. The absorption spectra for  $\text{TMA}_4[\text{Cd}_4\text{Co}_6\text{S}_4(\text{SPh})_{16}]$  exhibits three features at 608 nm, 716 nm, and 750 nm. The peaks at 716 nm and 750 nm are assignable to a tetrahedral Co(II) center in the cluster. The broad peak at 608 nm can be assigned to an axially distorted pseudo-tetrahedral Co(III) site in the cluster, suggesting the cluster exists in a mixed valent form in solution. This confirms the MS findings that  $\text{TMA}_4[\text{Cd}_4\text{Co}_6\text{S}_4(\text{SPh})_{16}]$  consists of two oxidation states at two specific sites in the cluster.

#### 2.3.4.3 XANES of $\text{TMA}_4[\text{Cd}_4\text{Co}_6\text{S}_4(\text{SPh})_{16}]$ .

Further confirmation of the mixed valent nature of the cluster can be extracted directly from the XANES spectroscopy. For a Co atom, the  $L_{2,3}$  edges are formally electron transitions from the spin-orbit split  $2p_{1/2}$  and  $2p_{3/2}$  orbitals, respectively, to the unoccupied  $3d$  orbitals. The shape of the XANES spectra can provide information on local bonding and the energy of the peak

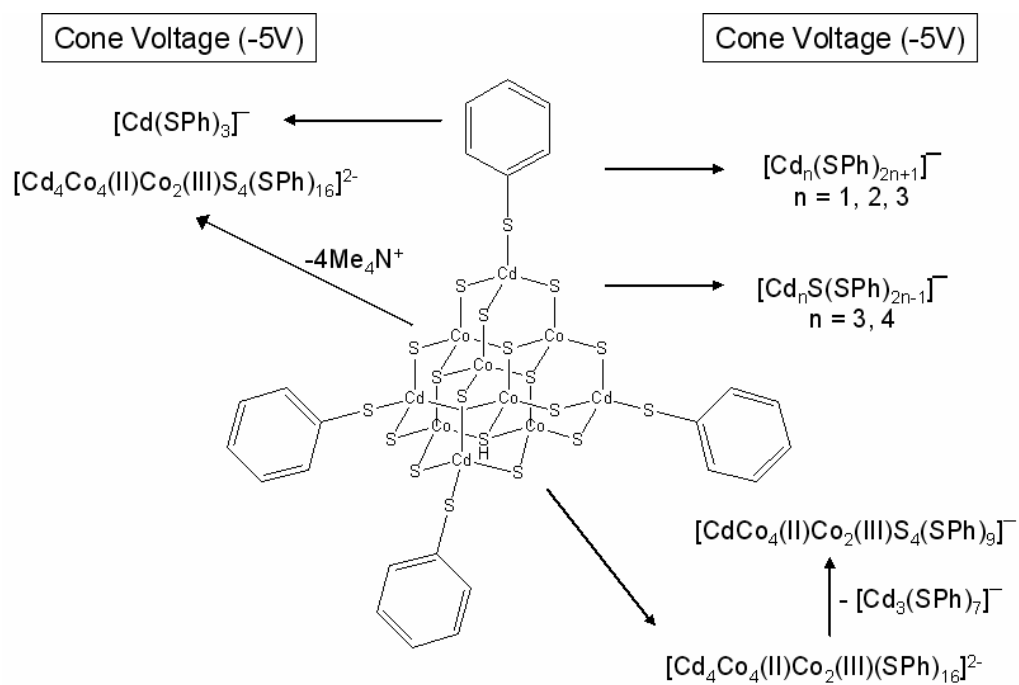


**Figure 2.18.** Proposed cluster structure along with the fragmentation observed in the ESI-MS at cone voltages of -5 V and -50 V,

can provide information on the local oxidation state. For instance, octahedral  $d^7$  metals will exhibit a small pre-edge feature from the  $1s \rightarrow 3d$  transition, due to relaxation of the dipole selection rules because of symmetry considerations. Therefore an analysis of both the shape and energy of the XANES spectra will provide a direct measure of both the Co oxidation states and site symmetry in the cluster. Soft x-ray absorption spectra at the Co  $L_{2,3}$  edge is shown in Figure 2.20, with absorption features appearing at 770 and 785 eV, corresponding to the Co  $L_2$  and  $L_3$  edges. For calibration of the XANES results, the inset of figure 2.20 shows the S  $L_3$  edge can be observed at 162.1, which is very close to the value of 162.4 for elemental sulfur.

To extract further site information from the measured XANES data, the data set can be fit numerically using a non-linear regression analysis to a sum of Voigt functions. Inspection of the fit in figure 2.20, it can be seen that the data will not fit to a single Voigt function ( $\chi^2=0.158$ ). The data set is most likely composed of two sets of peaks, each described by a Voigt function. The two sets of peaks arise from a linear combination of valence charge states of cobalt.

Using no fixed parameters, the best fit to the data set yielded a  $\chi^2=0.045$ . For the  $L_3$  edge, we observe components at  $770.87 \pm 0.03$  and  $772.79 \pm 0.85$  eV, while for the  $L_2$  edge, we observe components at  $785.91 \pm 0.09$  and  $787.57 \pm 0.35$  eV. The difference in the two peaks are 1.6 – 1.9 eV which

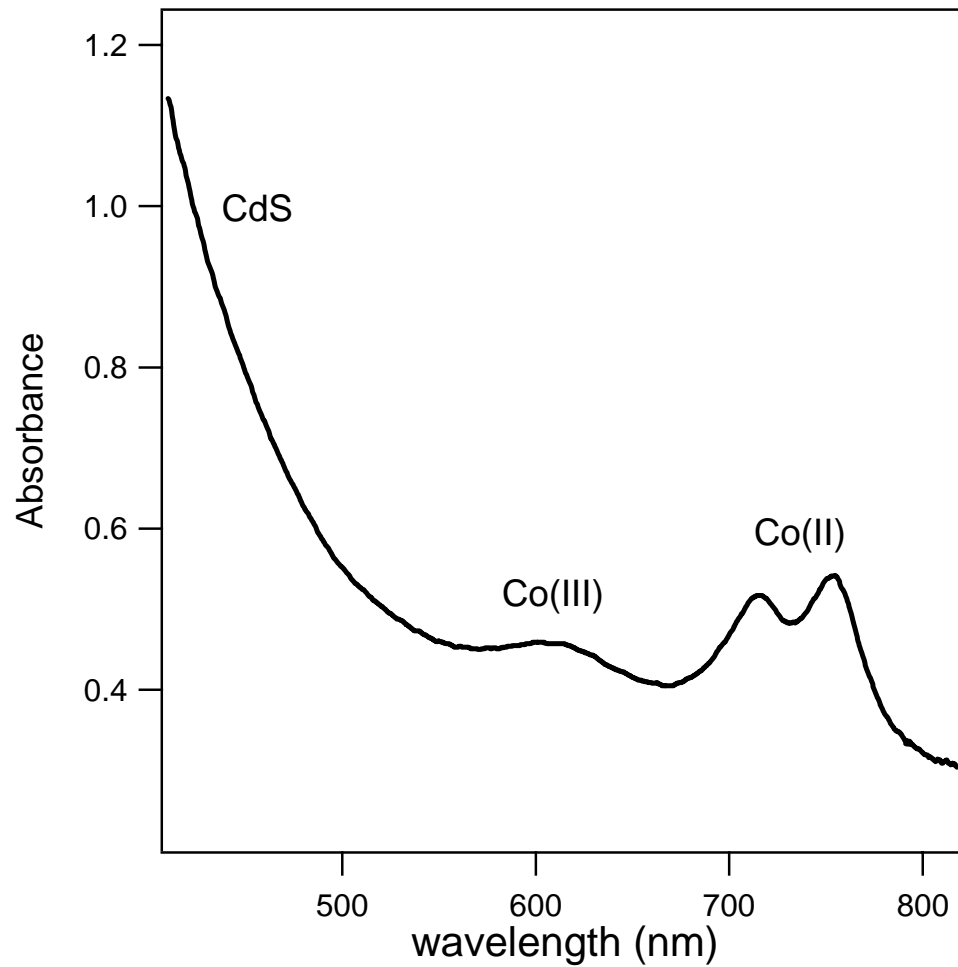


**Figure 2.19.** UV-visible absorption spectra of  $\text{TMA}_4[\text{Cd}_4\text{Co}_6\text{S}_4(\text{SPh})_{16}]$ .

is identical to the 1.5 eV energy difference observed between Co(II) and Co(III) in XANES spectroscopy<sup>17</sup>.

Because the photoabsorption process involves a core  $2p$  electron being excited into an unoccupied  $3d$  state, depleting the  $3d$  valence levels by one electron (i.e. going from Co(II) to Co(III)) will have very little effect on the x-ray absorption cross section (i.e. initial state); therefore, the intensities of the Voigt functions should provide a semi-quantitative estimate of the ratio of Co(II)/Co(III) in the cluster. The observed ratios of the  $L_3$  and  $L_2$  edges are  $I_{\text{Co(II)}}/I_{\text{Co(III)}} = 2.5$  and  $I_{\text{Co(II)}}/I_{\text{Co(III)}} = 2.3$ , respectively, indicating that the average ratio of the two valent states in the cluster are  $I_{\text{Co(II)}}/I_{\text{Co(III)}} = 2.4$ , in good agreement with the MS data which predicts  $I_{\text{Co(II)}}/I_{\text{Co(III)}} = 2.0$ .

Based on analysis of the XANES data in conjunction with the absorption data, the cobalt ions are mixed valent, sit on tetrahedral centers, and they are predominately localized on the Co site. Lack of pre-edge features eliminates the idea of dopant induced rearrangements. This allows the structure of the cluster to be properly described as  $\text{TMA}_4[\text{Cd}_4\text{Co(II)}_4\text{Co(III)}_4\text{S}_4(\text{SPh})_{16}]$ , confirming the MS model for the structure.

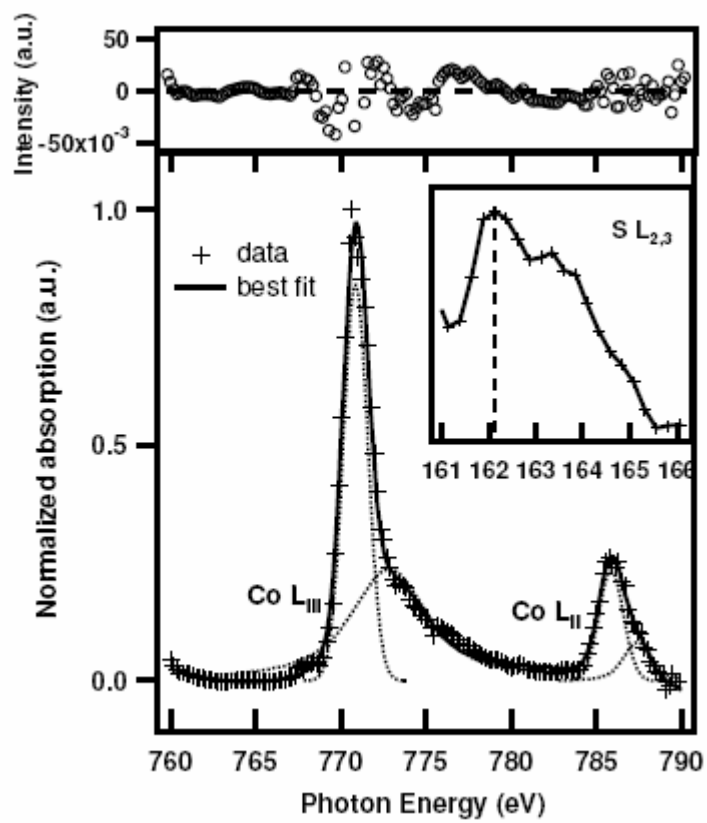


**Figure 2.20.** Co-edge XANES spectra of  $\text{TMA}_4[\text{Cd}_4\text{Co}_6\text{S}_4(\text{SPh})_{16}]$ .

## 2.4 CONCLUSION

Inorganic clusters are excellent building blocks for the synthesis of semiconductor quantum dots. ESI-mass spectrometry has proven to be a simple technique that is useful in identifying the composition of small clusters to both study the fragmentation of the clusters and also as a simple and facile method to perform quality assurance of the products synthesized.<sup>12,18</sup> This technique provides information on the metal ion valence state, fragmentation pattern, and structure of individual clusters. Each of the clusters that have been synthesized and has been characterized by mass spectrometry. XANES and XPS spectroscopy were used to establish the oxidation states of  $(\text{Me}_4\text{N})_2[\text{Cu}_4(\text{SPh})_6]$ . A wide variety of techniques were implemented in the characterization of  $(\text{Me}_4\text{N})_4[\text{Cd}_4\text{Co}_6\text{S}_4(\text{SPh})_{16}]$ . Using ESI-MS, optical absorption spectroscopy, and XANES it was determined that this cluster is mixed valent with the following structure  $(\text{Me}_4\text{N})_4[\text{Cd}_4\text{Cd}_4^{\text{II}}\text{Co}_2^{\text{III}}\text{S}_4(\text{SPh})_{16}]$ .

## 2.5 REFERENCES

- (1) Raola, O. E.; Strouse, G. F. *Nano Letters* **2002**, *2*, 1443-1447.
- (2) Hanif, K. M.; Meulenberg, R. W.; Strouse, G. F. *J Am Chem Soc* **2002**, *124*, 11495-11502.
- (3) Norman, T. J.; Magana, D.; Wilson, T.; Burns, C.; Zhang, J. Z.; Cao, D.; Bridges, F. *Journal of Physical Chemistry B* **2003**, *107*, 6309-6317.
- (4) Cumberland, S. L.; Hanif, K. M.; Javier, A.; Khitrov, G. A.; Strouse, G. F.; Woessner, S. M.; Yun, C. S. *Chemistry of Materials* **2002**, *14*, 1576-1584.
- (5) Herron, N.; Wang, Y.; Eckert, H. *Journal of the American Chemical Society* **1990**, *112*, 1322-1326.
- (6) Banda, R. M. H.; Cusick, J.; Scudder, M. L.; Craig, D. C.; Dance, I. G. *Polyhedron* **1989**, *8*, 1995-1998.
- (7) Dance, I. G.; Isaac, D. *Australian Journal of Chemistry* **1977**, *30*, 2425-2431.
- (8) Dance, I. G.; Choy, A.; Scudder, M. L. *J Am Chem Soc* **1984**, *106*, 6285-6295.
- (9) Elnakat, J.; Fisher, K. J.; Dance, I. G.; Willett, G. D. *Inorganic Chemistry* **1993**, *32*, 1931-1940.

- (10) Hagen, K. S.; Stephan, D. W.; Holm, R. H. *Inorganic Chemistry* **1982**, *21*, 3928-3936.
- (11) Lover, T.; Henderson, W.; Bowmaker, G. A.; Seakins, J. M.; Cooney, R. P. *Chemistry of Materials* **1997**, *9*, 1878-1886.
- (12) Gaumet, J. J.; Strouse, G. F. *Journal of the American Society for Mass Spectrometry* **2000**, *11*, 338-344.
- (13) Jun, Y. W.; Jung, Y. Y.; Cheon, J. *Journal of the American Chemical Society* **2002**, *124*, 615-619.
- (14) Ji, T.; Jian, W. B.; Fang, J. *Journal of the American Chemical Society* **2003**, *125*, 8448-8449.
- (15) Feltin, N.; Levy, L.; Inger, D.; Pileni, M. P. *Advanced Materials* **1999**, *11*, 398-402.
- (16) Radovanovic, P. V.; Gamelin, D. R. *Journal of the American Chemical Society* **2001**, *123*, 12207-12214.
- (17) Sheu, H. S.; Jen, S. H.; Kang, T. W.; Jang, L. Y.; Lee, J. F. *Journal of the Chinese Chemical Society* **2002**, *49*, 813-818.
- (18) Gaumet, J. J.; Khitrov, G. A.; Strouse, G. F. *Nano Letters* **2002**, *2*, 375-379.

### Chapter 3. Cd<sub>1-x</sub>Co<sub>x</sub>Se Semiconductor Quantum Dot Alloys

*Most of this chapter has appeared in print: Hanif, K.M., Meulenberg, R.W.,  
Strouse, G.F. JACS* **124**, 11495-11502 (2002)

### 3.1 Introduction:

Diluted magnetic semiconductors (DMS) in bulk materials have been intensively studied in II-VI lattices (ZnS, ZnSe, CdS, CdSe, CdTe) containing randomly substituted Mn, Co, and Fe at the  $T_d$ -cation site.<sup>1-4</sup> These materials exhibit unique optical and magnetic properties arising from the strong *sp-d* exchange mixing that exists between the valence and conduction band of the host lattice with the d-orbitals of the dopant ion. This leads to large internal magnetic fields in the host lattice.<sup>5</sup>

Alloys are convenient systems, in that magnetic phases and band gap tuning is achievable by control of the doping level in bulk systems, which makes these materials potentially exciting for applications in spintronics. Recent interest in development of DMS alloys at the nanoscale has arisen due to the potential to fine tune not only the bandgap of the alloy through alloy formation, but also the energy of the band positions arising from quantum confinement effects at the nanoscale. This would provide an infinitely tunable material to probe changes in the nature of magnetic exchange arising from coupling between the defect ion spin levels and the valence and conduction band levels in the nanomaterial. Several theorists have predicted that these nano-alloys will possess size dependent magnetic phases coupled with dramatic increases in g-factors, large Zeeman splitting energies and large Faraday rotation constants.<sup>6</sup>

Magnetic phases in a DMS material reflect the bulk property of the material, and is influenced by the spin quantum number of the paramagnetic guest ion and the degree of angular momentum for the ion coupled to the number of nearest PM neighbors in the alloy lattice. At the nanoscale, quantum confinement effects, lattice grain boundaries, and the site of occupation of the guest ion in the lattice will further control the observed magnetic phases in this class of materials. Depending on the nature of exchange coupling between the *s-p-d* orbitals, the dilute magnetic nanoalloys may exhibit paramagnetism, antiferromagnetism, ferromagnetism or spin glass behavior. The observed magnetic properties in DMS alloys is dependant on the lattice orbital energy, covalency, and guest ion concentration. The dopant ion can induce paramagnetic (PM), antiferromagnetic (AFM), spin glass (SG), or ferromagnetic (FM) behavior depending on the magnitude of the d-d ( $J$ ) and sp-d ( $\alpha, \beta$ ) exchange integrals between the dopant and the host lattice.

Paramagnetic materials contain non-interacting or very weakly interacting spins and will typically be observed in DMS alloys that have very low guest ion concentrations ( $x < 1\%$ ) thus limiting the number of nearest neighbor interactions in the alloy. The orientation of the spins is randomized by thermal energy ( $k_B T$ ) and therefore the temperature of the system needs to be lowered or the applied field needs to be increased in order to align the spins with the field. Figure 3.1 shows a typical  $1/\chi$  vs temperature plot of a

paramagnetic material. An ideal paramagnet consists of spins that are spaced sufficiently apart preventing any interactions from taking place in between the spins and thereby will follow Curie Law.

$$\chi = C/T \quad (1)$$

In equation 1,  $\chi$  is the susceptibility and C is the Curie constant. In most paramagnetic materials the spins are close enough to allow weak interaction to take place, therefore they do not behave as Curie paramagnets and the Curie-Weiss law needs to be applied to describe their magnetic behavior (eqn. 2).

$$\chi = \frac{C}{T - \Theta} \quad (2)$$

In equation 2,  $\Theta$  is the Curie temperature. Figure 3.1 shows a  $1/\chi$  versus temperature plot of what a typical Curie magnet would look like and that of a material that deviates from the Curie law. Paramagnetism will dominate for DMS systems at low guest ion concentration (<1%) or when the spin levels of the guest ion do not sufficiently overlap with the *s* or *p* orbital of the host lattice to enhance exchange interactions via a super-exchange mechanism.

In DMS materials antiferromagnetism (AFM) is most common and occurs when the concentration of the PM guest ion reaches a concentration where nearest neighbor interactions become favorable for magnetic exchange. For an AFM alloy the exchange interaction, J, between the materials is negative

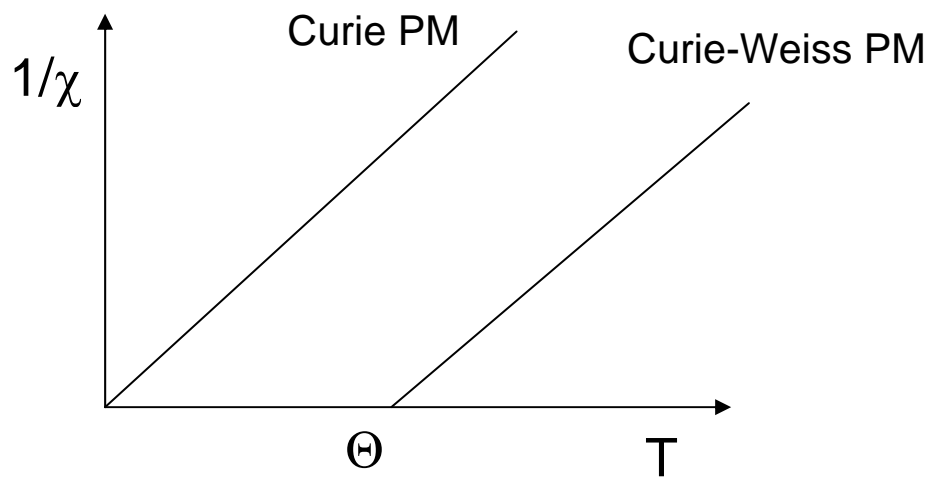


**Figure 3.1** Typical plot of a  $1/\chi$  vs temperature for a Curie and Curie-Weiss paramagnetic material.

in value. At high temperatures the magnetic behavior of AFM materials follows the Curie-Weiss law. As the temperature is lowered to the point when the exchange energy becomes greater than  $k_B T$ , the spins begin to align antiparallel as shown in figure 3.2. A  $1/\chi$  versus temperature plot of a typical AFM material is shown in figure 3.2. The point of inflection in the plot is referred to as the Neel temperature ( $T_N$ ). At the Neel temperature a phase transition occurs between a disordered paramagnetic state and the onset of AFM ordering. Below that point the spins continue to align anti-parallel until all of the spins have aligned resulting in a net 0 magnetic moment ( $\chi \rightarrow 0$ ) from the material.

Ferromagnetic (FM) materials are rare in DMS alloys and have only been observed in systems where free carriers have been induced by the doping process. FM systems exhibit long range order where the spins align parallel under very small magnetic fields. All ferromagnets lose their ferromagnetic behavior above the Curie temperature ( $T_C$ ). Above  $T_C$  they essentially behave like paramagnets because the exchange energy between the atoms is not strong enough to overcome the thermal excitations beyond  $T_C$ . Figure 3.3 shows a  $1/\chi$  versus temperature plot and a cartoon depicting the spins of a typical ferromagnet. Although FM is rarely observed in DMS systems, free carriers in the lattice can promote an overall FM exchange interaction in

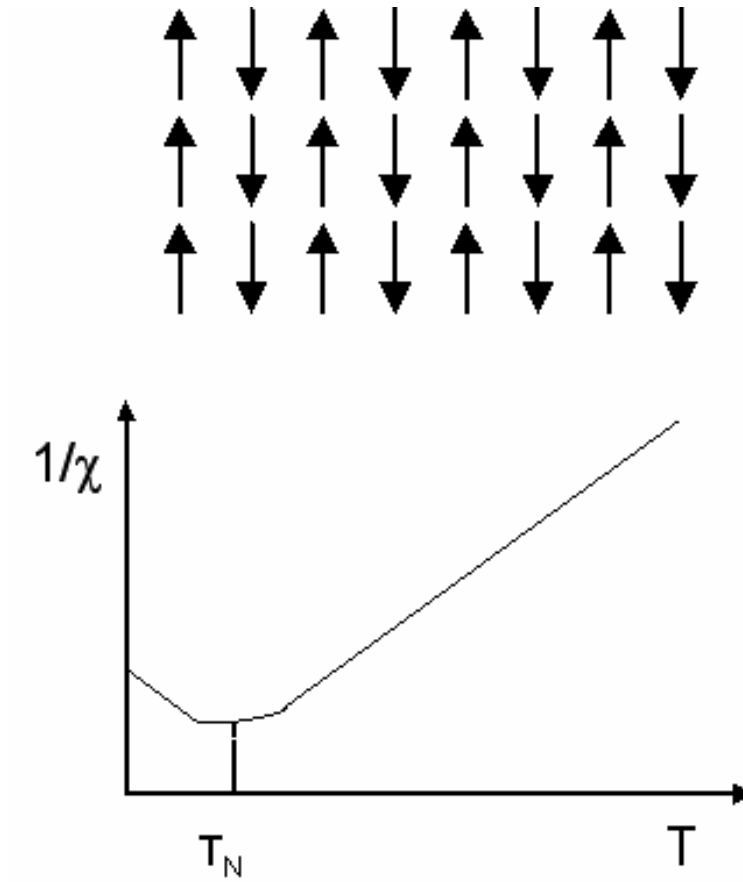


**Figure 3.2.** Typical plot of a  $1/\chi$  vs temperature plot of an antiferromagnetic material and the moments of an AFM material.

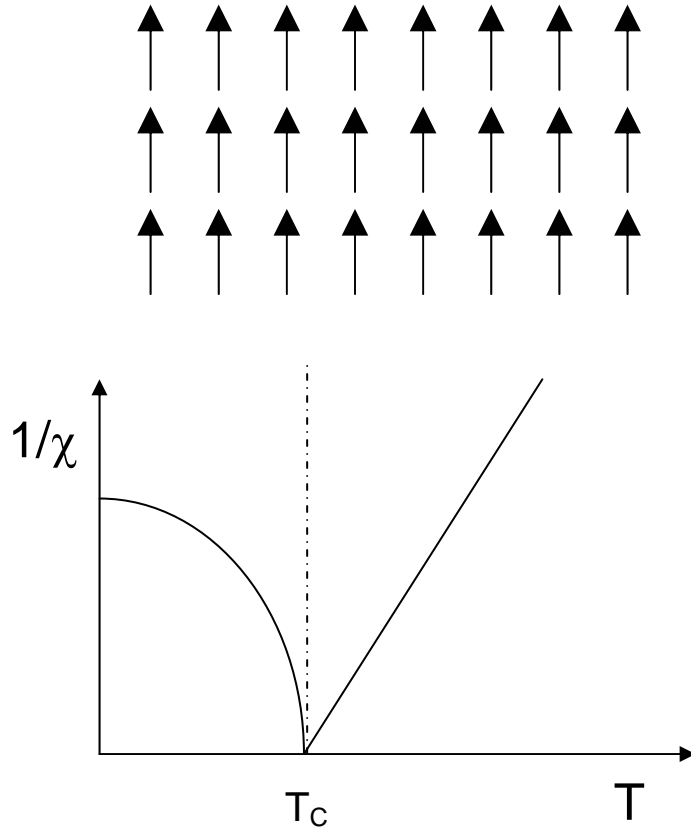


**Figure 3.3.** Typical plot of a  $1/\chi$  vs temperature plot of an ferromagnetic material and the moments of an FM material.

the lattice. Such behavior has been observed in  $\text{Ga}_{1-x}\text{Mn}_x\text{As}$ ,  $\text{Cd}_{1-x}\text{Mn}_x\text{Te}$ , and  $\text{In}_{1-x}\text{Mn}_x\text{As}$ .<sup>7-10</sup>

Spin glass (SG) behavior is very commonly observed in DMS alloys.<sup>11-</sup>

<sup>14</sup> When magnetic atoms are doped in a diamagnetic host to form an alloy the magnetic dopants can interact with one another in the host. Since the concentration of the dopant is usually large enough to have many nearest and next nearest neighbor interactions (typically possessing different exchange strengths), the material will not behave as an ideal paramagnet at low temperatures. A spin glass is a kinetically frozen spin lattice that has not achieved a thermodynamic minimum. The kinetically trapped spin orientations generate domains of spin or in effect an amorphous-glassy spin-lattice. The concentration of dopant ions in these materials usually do not go beyond the percolation threshold (concentration above which there exist nearest neighbor interaction between guest ions spanning from one end to the other end of a crystal), there will not be a AFM or FM ordering throughout the whole lattice, resulting in a spin frustrated system at low temperature. At high temperature such a cluster will behave as a paramagnet and its behavior can be understood through the Curie-Weiss law. At lower temperature below the glass temperature ( $T_g$ ), the material will start to order and exist as a kinetically frozen series of magnetic domains which is commonly referred to as spin glass.

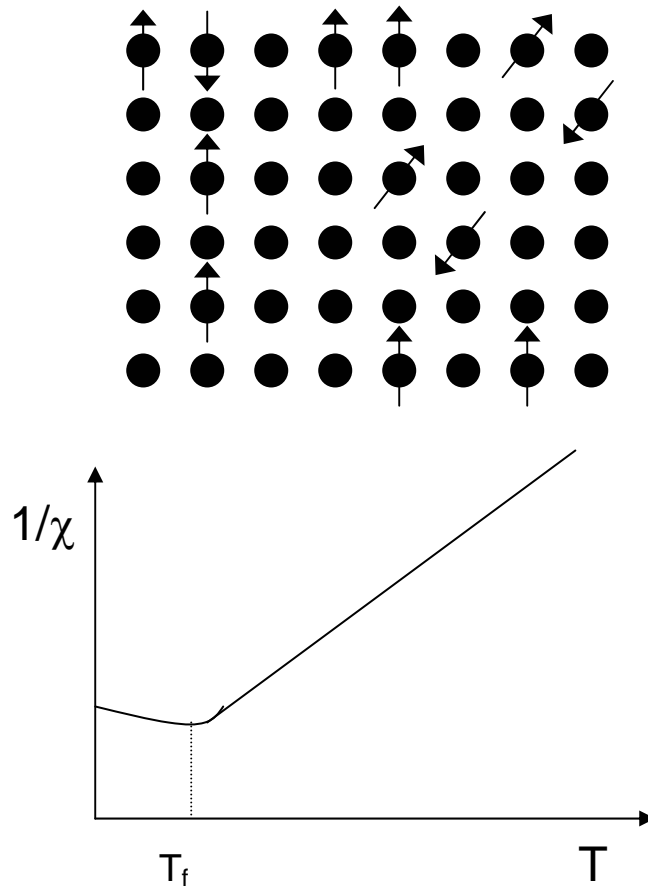


**Figure 3.4.** Typical plot of a  $1/\chi$  vs temperature plot of a spin glass material and the moments of an spin glass material.

Figure 3.4 shows a plot of the  $\chi$  versus temperature and a cartoon of the spins of a typical spin glass material. Since the magnetic atoms are randomly doped in the lattice, the magnetic properties of the spin glass mirror more closely that of an amorphous system. Since the spins are disordered the magnetic interactions between the spins will be a mix of both ferromagnetic and antiferromagnetic interactions.

The observed magnetic behavior in DMS alloys will therefore be strongly dependant upon the guest ion type, the host lattice properties, and in nanoscale materials, the lattice shape and size due to confinement effects. The effect of the guest ion on the properties of the DMS alloy is clearly shown by contrasting the observed behavior of Mn(II), Co(II) and Fe(II) doped into bulk II-VI host lattice. Mn<sup>2+</sup> doped semiconductors are the most extensively studied of the DMS alloys.<sup>5,8</sup> Mn<sup>2+</sup> has been shown to be very soluble in II-VI hosts, in which doping levels of up to 80% Mn<sup>2+</sup> have been achieved. Mn<sup>2+</sup> (S=5/2, T<sub>d</sub> site) has a <sup>6</sup>S<sub>5/2</sub> ground state in a tetrahedral crystal field. The magnetic properties of Mn<sup>2+</sup> are the simplest to understand since this is essentially a spin only case. There are no spin orbit interactions in Mn<sup>2+</sup> and the ground state is not split by the crystal field. II-VI semiconductors doped with low concentrations of manganese exhibit classical PM behavior down to < 1 K consistent with the lack of magnetic coupling to the host lattice due to the low angular momentum contribution of Mn(II).<sup>5</sup>

$\text{Fe}^{2+}$  ( $S = 2$ ) is quite different than  $\text{Mn}^{2+}$  due to its large angular momentum term.  $\text{Fe}^{2+}$  has a  ${}^5\text{D}_{3/2}$  ground state term symbol. The  ${}^5\text{D}$  term is split by a tetrahedral crystal field and then further split by spin orbit interactions, both of which do not exist in  $\text{Mn}^{2+}$ . This splits the  ${}^5\text{D}$  term into an  ${}^5\text{E}$  and  ${}^5\text{T}$  orbital. The magnetic properties of this ion are determined by the  ${}^5\text{E}$  orbitals which is further split into 5 magnetic sub-levels, the ground state being an  $\text{A}_1$ .<sup>15</sup> The symmetric  $\text{A}_1$  ground state will have no permanent magnetic moment being associated with the ground state for  $\text{Fe}^{2+}$  doped onto a  $\text{T}_d$ -site in the II-VI host lattice.

$\text{Co}^{2+}$  ( $S = 3/2$ ) doped semiconductor alloys present a case that falls between that of  $\text{Mn}^{2+}$  and  $\text{Fe}^{2+}$  doped materials.  $\text{Co}^{2+}$  has a  $d^7$  electronic configuration. The 28 fold degenerate  ${}^4\text{F}$  term of  $\text{Co}^{2+}$  is split by both the crystal field into a singlet  ${}^4\text{A}_2$ , and triplet  ${}^4\text{T}_2$  and  ${}^4\text{T}_1$ . The crystal field leaves the  ${}^4\text{A}_2$  level unsplit and further splits the triplet states.<sup>16</sup> The ground state  ${}^4\text{A}_2$  level is  $\sim 474$  meV below the excited state and has no orbital momentum. Therefore, the magnetic properties of  $\text{Co}^{2+}$  end up being similar to that of  $\text{Mn}^{2+}$ , however in this case the system has a ground state with an effective spin of  $3/2$ , with longer range exchange coupling arising from the larger angular momentum contribution in Co.

In this chapter, we present data for 5 nm  $\text{Cd}_{1-x}\text{Co}_x\text{Se}$  samples that have cobalt doping levels  $< 30\%$ . In addition, there were some studies performed on

samples that differed in size (4 nm). Using pXRD, Resonance Raman, and EXAFS, we present structural data supporting core doping of the CdSe host with  $\text{Co}^{2+}$  sitting as a substitutional element on the Cd- $T_d$  site. Inspection of the analytical data provides evidence that  $\text{Co}^{2+}$  is replacing  $\text{Cd}^{2+}$  cations within the lattice through a random ion substitution (RIS) mechanism other than localization at or near the nanoparticle surface. The observance of an order in magnitude higher spin glass temperatures in quantum dots ( $T_g \sim 5$  K) than that of the bulk ( $T_g < 1$  K) indicates that the magnetic interactions between cobalt ions are enhanced in quantum dots. The increase in  $T_g$  temperature for Co:CdSe QDs compared to bulk alloys is believed to be due to enhanced sp-d interactions in quantum dots caused by the shift of the valence band of quantum dots with respect to that of the bulk due to confinement effects in the nanoparticles.

## **3.2 EXPERIMENTAL:**

**3.2.1.1 Materials.** The clusters  $\text{Li}_4[\text{Se}_4\text{Cd}_{10}(\text{SPh})_{16}]$  and  $\text{Li}_2[\text{Co}_4(\text{SPh})_{10}]$  were prepared according to literature methods as is discussed in Chapter 2.<sup>17</sup>

Cobalt(II) nitrate hexahydrate (Allied), elemental selenium (~200 mesh, Aldrich), thiophenol (Aldrich), pyridine (Fisher), hexadecylamine (ACROS),  $\text{LiNO}_3$  (ACROS),  $\text{CH}_3\text{OH}$  (Fisher) were used as supplied.

**3.2.2.1 Synthesis of Cd<sub>1-x</sub>Co<sub>x</sub>Se Quantum Dots.** Cd<sub>1-x</sub>Co<sub>x</sub>Se quantum dots were synthesized by a lyothermal method using an inorganic cluster precursor methodology developed in the Strouse laboratory.<sup>18</sup> Li<sub>4</sub>[Se<sub>4</sub>Cd<sub>10</sub>(SPh)<sub>16</sub>] (1.2g, 0.7 mmol) and Li<sub>2</sub>[Co<sub>4</sub>(SPh)<sub>10</sub>] (400 mg – 1.25g, 0.3 - 0.8 mmol) were combined and heated under a N<sub>2</sub> atmosphere to ~ 210°C in a solution of ~ 40 mL of hexadecylamine (HDA). Control of the doping level is achieved by altering the ratio of Cd to Co in the reaction mixture. The final ratio is not equivalent to the initial stoichiometry, but is correlated to the initial ratio. Growth of the quantum dots was monitored by UV-VIS absorption spectroscopy of the first excitonic transition in CdSe. When the first exciton absorbance was ~ 590 nm, corresponding to ~ 5 nm particles, the quantum dots were isolated from the reaction mixture according to the following procedures. The solution was first cooled to ~ 60°C (solution is cooled to prevent boiling of MeOH when the reaction is added to it) and then it was poured into a beaker containing 100 -150 mL of MeOH. This solution was centrifuged, and the resultant green supernatant that contained unreacted cobalt was removed. MeOH was added (3x) to the precipitate and centrifuged to wash the sample. By the third methanol wash the supernatant solution became clear after centrifugation indicating removal of nearly all unreacted cobalt ions.

Following isolation of the QD particles, the QD particles were stripped and recapped with pyridine three times to ensure removal of any adventitious

cobalt that was not doped within the quantum dot. This process has been demonstrated by Norris et al to remove surface adsorbed guest ions from the doped QD samples.<sup>6</sup> This was performed by placing ~ 50 mg of isolated QDs in a vial and adding a few mL of pyridine until the solution became clear. The vial is heated in a hot water bath to ~ 80°C for 30 minutes. Afterwards hexanes were added to precipitate the QDs from pyridine, and centrifuged to isolate the QDs. The precipitate was vacuum dried and the above procedure was repeated twice. The resulting pyridine capped QDs appeared as very fine glossy flakes. The average concentration of Co<sup>2+</sup> in the quantum dots was measured by Inductively Coupled Plasma Atomic Emission (ICP-AE) spectroscopy and the size distribution (< 5%) of the materials was determined using transmission electron microscopy (TEM).

### **3.2.3 Materials Characterization**

**3.2.3.1 Transmission electron microscopy (TEM).** Transmission electron microscope measurements were performed on a JEOL 2010 Microscope operated at 200 kV in bright-field mode. Samples were dissolved in toluene and deposited on Nickel holey carbon grids (SPI) with Formvar removed. The size and size distributions of the quantum dots were determined by digitizing micrograph negatives and manually measuring sizes of the quantum dots on a single TEM image. Comparison between the lattice spacing from the TEM to

that of the pXRD is obtained by measuring the lattice fringe spacing in the TEM. Since the error in measuring the distance between two lattices is rather large using TEM, the lattice spacing was determined by taking an average between the lattice spacing of 12 consecutive lattices.

**3.2.3.2 Powder X-ray diffraction (PXRD)** Powder x-ray diffraction measurements on pre-pyridine etched samples were performed on a Scintag X2 diffractometer with a Cu K $\alpha$  source ( $\lambda = 1.5418 \text{ \AA}$ ). In general approximately 20-30 mg of QDs and  $\sim 3$  mg of Si were used for the pXRD measurements. The sharp peaks in the p-XRD spectra at 1.638, 1.920 and 3.136  $\text{\AA}$  arise from Si powder which is added as an internal standard. Peaks that are due to excess hexadecylamine (HDA) in the samples are identified by (●) in figure 3a. HDA impurity signatures arise from differences in nanocrystal cleaning from batch to batch, but should not influence the nanocrystal properties since pyridine stripping removes excess HDA from the samples used for all other analysis. The lattice parameters for the samples are extracted by fitting the pXRD data to a wurtzite model.

**3.2.3.3 Ultraviolet-Visible Absorption (UV-Vis Absorption).** UV-Visible absorption measurements were performed on an Ocean Optics S2000 CCD fiber-optic spectrophotometer (resolution 4 meV). Measurements were taken at room temperature in toluene.

**3.2.3.4 Photoluminescence and Resonance Raman Spectroscopy.** The photoluminescence (PL) and resonance Raman spectra (resonant with the high energy  $1p_h-1p_e$  transition) were collected in backscattering configuration using the 488.0 nm (2.54 eV) line of either a 10 W Spectra Physics 2200 (Raman, 80 mW) or a 100 mW American Laser Corp. (PL; 10 mW) Ar ion laser as a pump source. A 0.5 M ARC single spectrograph (1800 lines  $\text{mm}^{-1}$ , blaze = 500 nm) coupled to a Princeton Instruments 512 x 512 liquid nitrogen cooled charge coupled device (CCD) was used to measure the Raman spectra. The PL experiments were measured on a 0.5 M CVI single spectrograph (150 lines  $\text{mm}^{-1}$ , blaze = 500 nm) coupled to an air cooled 375 x 242 CCD array (Santa Barbara Instrument Group). Laser plasma lines in the Raman spectra are indicated with an asterisk (\*). A Kaiser Optical Supernotch plus filter was used to reject the fundamental lines of the laser in both the Raman and PL experiments.

**3.2.3.5 Inductively-Coupled Plasma Atomic Emission Spectroscopy (ICP-AE)** Elemental analysis was performed using a Thermo-Jarrell Ash IRIS ICP-AE Spectrophotometer. All the samples were dissolved in hot  $\text{HNO}_3$  (~ 10-15 mg QD in ~1 mL  $\text{HNO}_3$ ) and then diluted using deionized water to ~ 50 mL. This mixture was heated until the solution turned clear and was used without filtering. The Cd and Co standards used in these measurements were purchased from High Purity Standards. The Cd concentration was monitored using the

average concentration measured at 214.438 and 226.502 nm atomic emission lines. The Co concentration was determined using the average of the 228.616, 237.862 and 238.892 nm atomic emission lines of Co. An average of 3-5 runs were taken for each element with an error of < 5%.

**3.2.3.6 Superconducting Quantum Interference Devices (SQUID).** Direct current (DC) and alternating current (AC) susceptibility measurements were performed on (6 – 30 mg) powder QD samples encased in a gelatin capsule by a SQUID magnetometer (Quantum Design, model 1802) at magnetic field  $H < 7$  T. Plastic capsules were used for the AC measurement and yield better results because they do not absorb moisture and have a smaller diamagnetic signal. Field dependant magnetization measurements (hysteresis loops) were performed at 2 K from -7 to 7 T. AC susceptibility measurements were performed under a DC field of 100 Oe with an AC field of 5 Oe.

**3.2.3.7 Extended X-ray Absorption Fine Structure (EXAFS).** EXAFS measurements were performed on powders (~ 10 mg) on Capton tape at the Stanford Linear Accelerator on beamline 7-3. It was suggested that the samples be mixed in with Boron Nitride in order to have the samples spread more uniformly in the sample holder. Measurements of Co (7709 eV) edge EXAFS were performed on the samples. The signals were detected using a germanium detector in x-ray fluorescence mode.

**3.2.3.8 X-ray Absorption Near Edge Spectroscopy (XANES).** The XANES experiments were performed at the undulator beamline 8.0.1 at the Advanced Light Source at Lawrence Berkeley National Labs. XANES experiments were performed using the total electron yield method. Soft X-rays were used to eject electrons from the L-shell of Co. Approximately 10 mg of samples was pressed onto indium foil with dimensions of 3 mm x 3 mm. All spectra were recorded at room temperature in at base pressures of less than  $8 \times 10^{-9}$  torr.

### **3.3 RESULTS AND DISCUSSIONS:**

Doping of quantum dots with cobalt has proven to be especially difficult. In the case of  $\text{Cd}_{1-x}\text{Co}_x\text{S}$  it was determined that the cobalt covered the surface of the quantum dot and essentially no core cobalt substitution on Cd-T<sub>d</sub> sites occurred.<sup>19</sup> The apparent lack of success may arise from the doping methodology employed. Recent efforts have produced  $\text{Co}^{2+}$  and  $\text{Mn}^{2+}$  quantum dots with doping levels from 1 – 12%.<sup>20,21</sup> However, these doping levels are quite low compared to what has been achieved in bulk II-VI semiconductors  $\text{Mn}^{2+}$  (80%),  $\text{Co}^{2+}$  (40%), and  $\text{Fe}^{2+}$  (20%).<sup>6,19,22-25</sup>

While bulk DMS alloys have readily been prepared for a range of II-VI and III-V materials, few examples exist in the literature of nanoscale materials. The lack of successful alloy formation can be traced to inappropriate doping

strategies applied in the literature and the high reaction temperatures typically employed. In this chapter we present a method for controlled doping by applying a single source precursor technology. We find that we can exchange up to 30% of the Cd(II) centers by Co(II) ions in 5 nm Co:CdSe alloys. The Co doping occurs by a random ion substitution process which results in Co(II) uniformly distributed throughout the core and surface of the nanocrystal. The resultant materials are highly crystalline and uniform. The successful synthesis of materials doped as high as 30% using this method supports the fact that the single source precursor methodology is very effective in doping of II-VI semiconductor quantum dots.

**3.3.1 Size Analysis.** TEM images and UV-VIS absorption were used to determine both the size and size distribution of the quantum dots prepared in this chapter. In figures 3.5 the TEM image for the  $\text{Cd}_{0.88}\text{Co}_{0.12}\text{Se}$  sample is shown. It can be seen in the TEM image that this sample is  $\sim 5\text{nm}$  in size and that the size distributions are  $< 5\%$ . The plot in figure 3.6 shows a size-distribution histogram for the 12% Co doped CdSe alloy. Two important things are observed in the TEM image. The first is the observation of a hexagonal packing which is suggestive of a hexagonal wurtzite structure of the sample, as confirmed by the powder XRD pattern of the same sample (see below). The second observation is that of lattice fringes arising from Bragg scattering of the

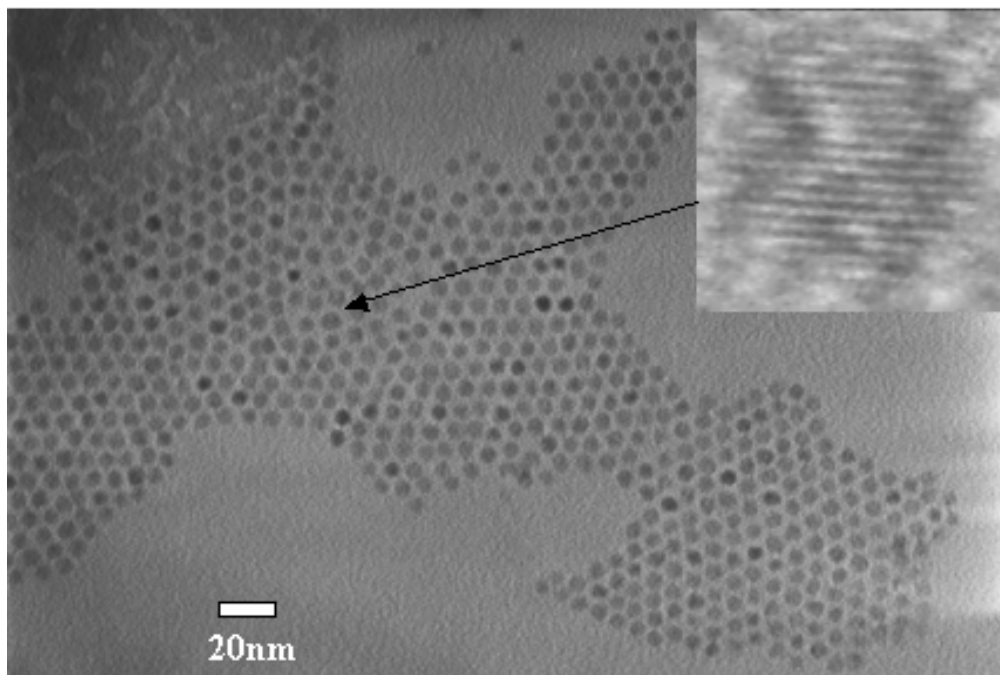


**Figure 3.5.** TEM image of Cd<sub>0.88</sub>Co<sub>0.12</sub>Se.

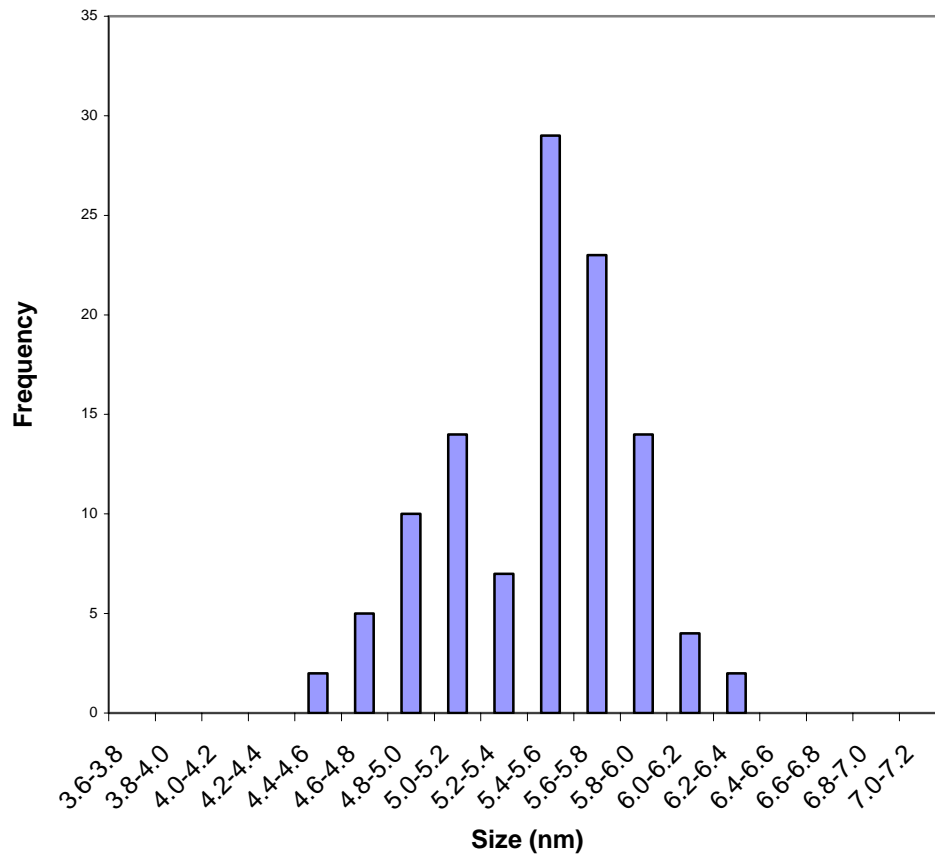


**Figure 3.6.** Histogram showing the size distribution of the quantum dots from the TEM image of  $\text{Cd}_{0.88}\text{Co}_{0.12}\text{Se}$ .

electron beam, which implies that the individual nanocrystals are crystalline and of hexagonal symmetry.

The exciton absorption at 590 nm in the absorption data shown in figure 3.7 is consistent with the TEM measurement of particles being ~ 5 nm in diameter. The absorption spectra of the Co:CdSe alloys exhibit well defined excitonic features (FWHM ~ 25 nm), but no absorption for Co is readily observed in any of the spectra due to the overlap of the ligand field transitions with the QD exciton edge. The photoluminescence data exhibits a small Stokes shift (30-40 meV) with respect to the band edge exciton absorption. The full width at half-maximum for the PL is very narrow being only 90 – 100 meV which is similar to that observed for pure 5.0 nm CdSe. The quantum yields for these samples were 0.10, 0.19, 0.03, and 0.14 for the  $x = 0.004$ , 0.12, 0.17, and 0.30 samples, respectively.

**3.3.2 Measuring Co concentrations in Co:CdSe.** Inductively-Coupled plasma atomic emission (ICP-AE) spectroscopy provides a very accurate method for determining the average concentrations of Cd and Co in a sample, although it is important to note that it can not distinguish free Co from incorporated Co. The ratio of Cd:Co should be a reflection of the doping level if both ions sit on the same lattice site as 2+ metal centers. Exclusion of free Co or Co bound electrostatically to the QDs is possible by extensive washing with CH<sub>3</sub>OH as demonstrated for Cu:CdSe alloys (Chapter 4). MeOH washing

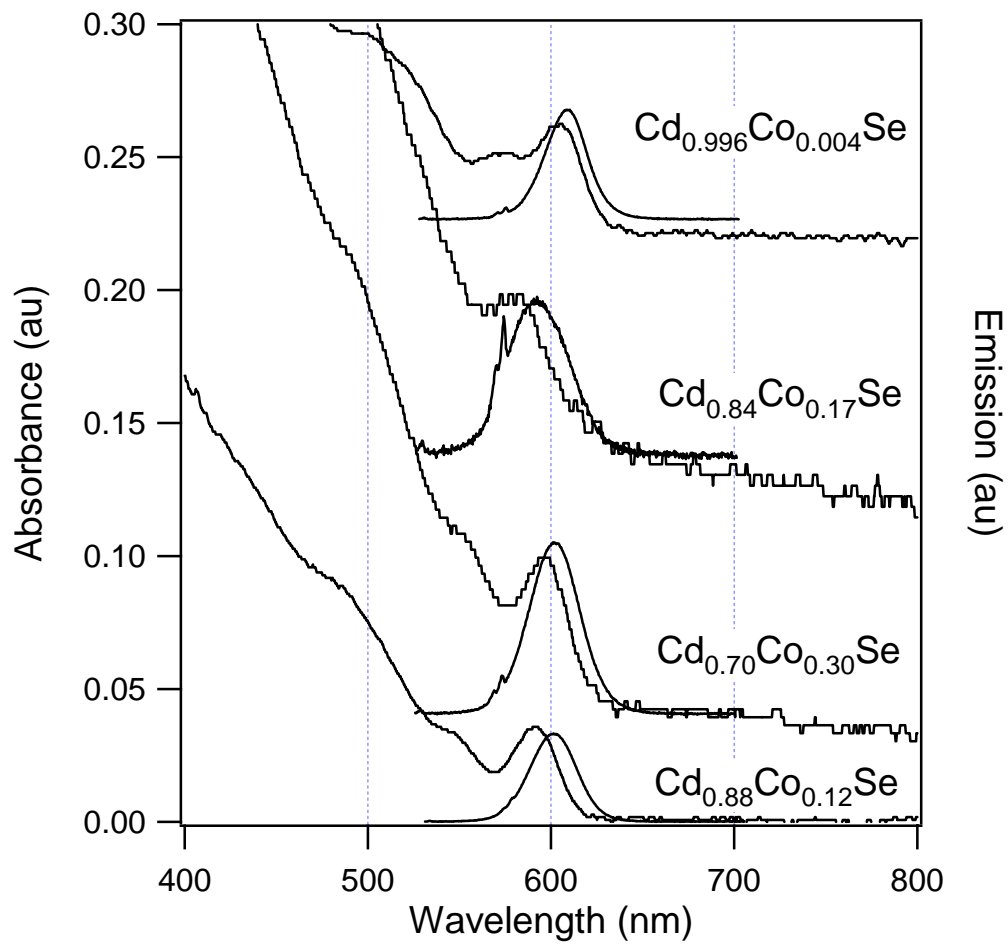


**Figure 3.7.** Absorption and Emission spectra of Co:CdSe with cobalt doping concentration of 0.4, 12, 16 and 30%.

removes unreacted  $\text{Co}^{2+}$ , which is soluble in the  $\text{CH}_3\text{OH}$ , as evidenced by the green supernatant. Electrostatically bound Co can be removed by stripping the QDs with pyridine to coordinate the Co ions, thus allowing the Co concentration in the alloy to be determined. In order to test this hypothesis elemental analysis was performed on a series of cobalt doped quantum dots prior to and after recapping with pyridine. Table 1 shows that there is essentially no difference in doping concentrations prior to and after recapping. This provides strong evidence that the unreacted cobalt ions are removed during workup. It is important to note that this is only true if the excess HDA has been removed from the quantum dot. Otherwise, there may be dramatic changes prior to and after pyridine recapping due to trapping of Co ions in the HDA layer.

Using the values for the  $\text{Co}^{2+}$  mole percent obtained from the ICP-AE elemental analysis, the number of  $\text{Co}^{2+}$  ions per dot can be estimated. Assuming a spherical particle, a 5 nm quantum dot contains  $\sim 3368$  atoms, of which  $\sim 1684$  are Cd atoms. Therefore, it can be predicted that these quantum dots contain anywhere from 7 to 505  $\text{Co}^{2+}$  atoms randomly distributed between the core and surface of the QD corresponding to doping levels of 0.4 – 30% Co in CdSe. A 5 nm QD has approximately 20% surface-to-volume ratio. Assuming that the doping is random, a quantum dot with 12% doping would then have  $\sim 40$  of its 202 cobalt atoms on the surface, and the remaining

---

Cobalt Doping concentration prior to and after pyridine stripping

---

<u>% Cobalt Out of Batch</u>	<u>% Cobalt After Pyridine Stripping</u>
0.53 ±0.025	0.50 ±0.025
1.62 ±0.081	1.15 ±0.058
1.45 ±0.073	1.25 ±0.063
2.80 ±0.14	2.75 ±0.14

---

**Table 1.** Doping concentration of 5 Co: CdSe QD samples prior to and after pyridine stripping.

number of  $\text{Co}^{2+}$  ions are at least one layer below the surface or randomly doped throughout the nanoparticle (both core and surface) if doping arises from a random ion substitution (RIS) mechanism. The observed concentration of  $\text{Co(II)}$  ions in the samples is consistent with a RIS mechanism, and is too high to support a localization of the Co ions only at or near the surface of the nanoalloy.

**3.3.3 pXRD Vegard's Law analysis of site occupation.** Structural analysis can provide concrete evidence for the random ion substitution (RIS) doping in these materials. When a crystal is doped only one set of diffraction peaks is expected to be observed for an alloyed material that reflects the average lattice spacing of the new material. The only time a second set of diffraction peaks would be observed is if the dopant ion were to segregate forming a mixed phase material.<sup>26</sup> Since pXRD is an ensemble macroscopic measurement, and not an atomistic level analytical technique, as a smaller ion is substituted onto a single site in a material, the lattice on average will contract. The opposite will be observed for a larger substitutional element. This empirical method was shown by Vegard, etc to produce a linear lattice change with increasing ion substitution only if the substitution is on a lattice site and more importantly random.<sup>27</sup>

Using Vegard's law analysis, it can be determined if the Co ion is statistically distributed within the host lattice, in that if the doping is random

then the lattice parameters will shift linearly with doping concentration. The tetrahedral covalent radii of Co and Cd are 1.20 pm and 1.48 pm respectively. Therefore it is expected for the lattice spacing to shift towards smaller d-spacing with increasing  $\text{Co}^{2+}$  levels for a RIS processes. Each lattice reflection therefore provides correlated evidence of a RIS process for an alloyed material. This does not mean that all the cation-anion bond distances are identical. For example, the lattice spacing shift towards larger d-spacing with increasing Mn concentration in Mn:ZnSe was shown to arise from the increase of Mn-Se content in the lattice, which has a larger bond distance than that of ZnSe. This was experimentally verified by EXAFS analysis.<sup>5</sup>

Below in figure 3.8 we show the pXRD data for a series of  $\text{Cd}_{1-x}\text{Co}_x\text{Se}$  ( $x=0.004 - 0.30$ ). The structure of these materials is wurtzite. Figure 3.9 shows the lattice parameters extracted from the XRD data of these materials as a function of doping concentration. The experimentally observed linear compression provides strong evidence of the RIS process, for doping of Co in CdSe as an alloy material. The equation below describes the relation between the position of the diffraction peak and that of the lattice parameters.

$$1/(d_{hkl})^2 = (h/a)^2 + (k/b)^2 + (l/c)^2$$

In this equation  $hkl$  represent the Miller indices of the diffraction peaks and  $a$ ,  $b$ , and  $c$  represent the crystal axes. The shift in lattice parameters is linear until the  $x=0.30$  sample, which indicates that phase segregation may be occurring at

this doping concentration. The same phenomenon has been observed in bulk samples with doping levels over  $x=0.20$ .<sup>28</sup>

Table 2 shows the average M-Se bond distance extracted from the p-XRD. The average M-Se bond distance is calculated using the unit cell parameters. This can be shown by inspection of the structural projection of CdSe (wurtzite) in Figures 3.10 and 3.11. Looking down the  $\langle 001 \rangle$  axis it can be seen that the Cd and Se atoms form a hexagonal structure. If the atoms were in the same plane, then the distance between the Cd and Se would be 2.42 Å (Figure 3.11). However, it is shown in figure 3.13 that the Se atoms lay below the Cd atoms. Therefore the distance between the metal and selenium atoms is 2.67 Å taking into account the geometrical relationship. Figure 3.12 shows that the distance between the Cd and the point in the same plane as the Cd just above the selenium atom is 2.48 Å, with an angle of  $x = 21.7^\circ$ . In order to extract the M-Se bond distance from the pXRD data, the following steps need to be followed. First the position of the (110) peak needs to be extracted in d-spacing from the pXRD plot. This value needs to be multiplied by 2 in order to give the  $a$  lattice parameter. The average distance between the M atom and the point in space above the Se atom in the same plane as the M atom is determined by taking the  $a$  lattice parameter and dividing it by  $\cos(30)$ . This value is then divided by  $\cos(21.7^\circ)$  to provide the average M-Se

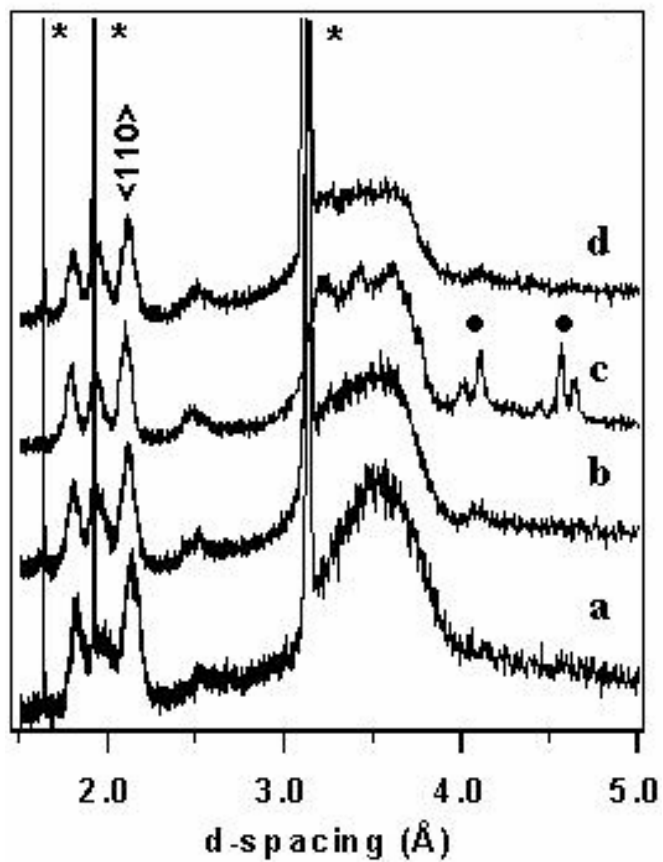


**Figure 3.8.** XRD spectra of a)  $\text{Cd}_{0.996}\text{Co}_{0.004}\text{Se}$  b)  $\text{Cd}_{0.88}\text{Co}_{0.12}\text{Se}$  c)  $\text{Cd}_{0.83}\text{Co}_{0.17}\text{Se}$  d)  $\text{Cd}_{0.70}\text{Co}_{0.30}\text{Se}$ . The asterisk (\*) and circle (●) represent the Si standar and hexadecylamine diffraction peaks, respectively.

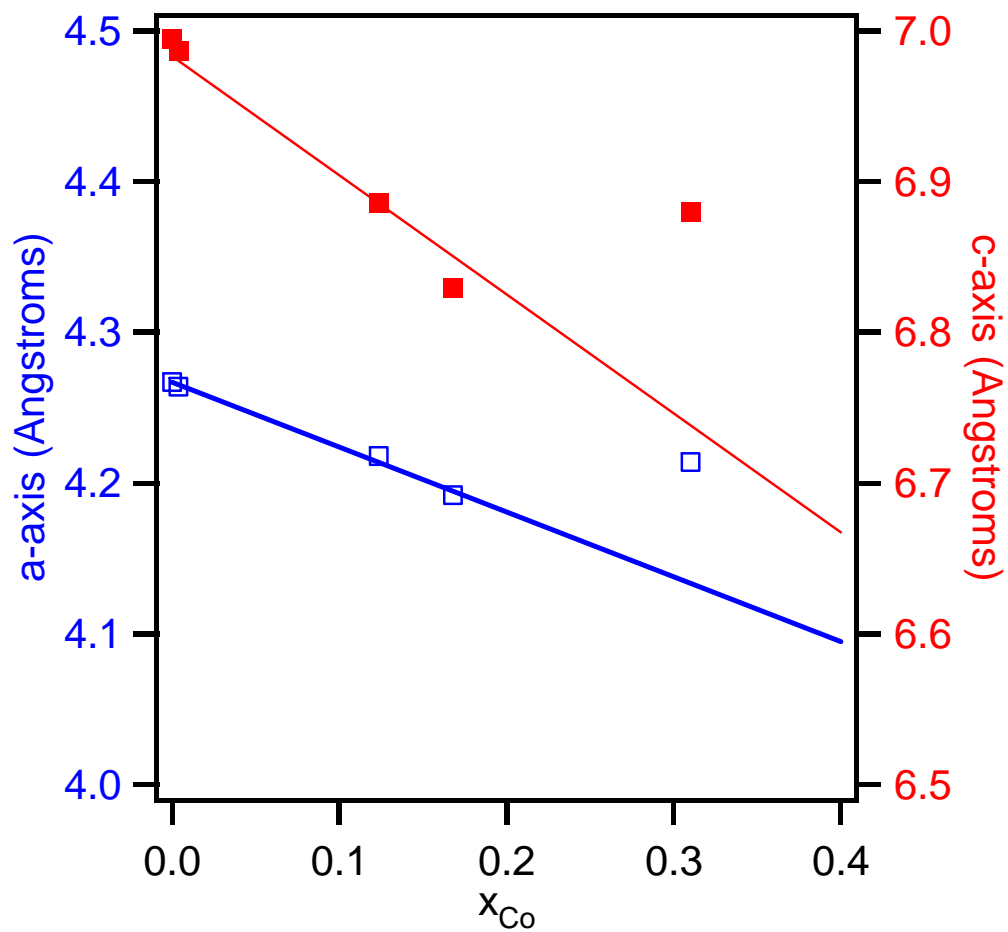


**Figure 3.9.** Plot of the lattice parameters of Co:CdSe as a function of doping concentration.

x	Average M-Se bond distance
0	2.621
0.004 ±0.0002	2.608
0.12 ±0.006	2.585
0.17 ±0.009	2.566
0.30 ±0.015	2.583
1	2.28*

**Table 2.** Average Metal-Se bond distance in  $\text{Cd}_{1-x}\text{Co}_x\text{Se}$  samples based upon pXRD data. (\*) signifies extrapolation of the M-Se bond distance vs. concentration plot to estimate the distance that would be expected to be observed for pure CoSe with a wurtzite structure.

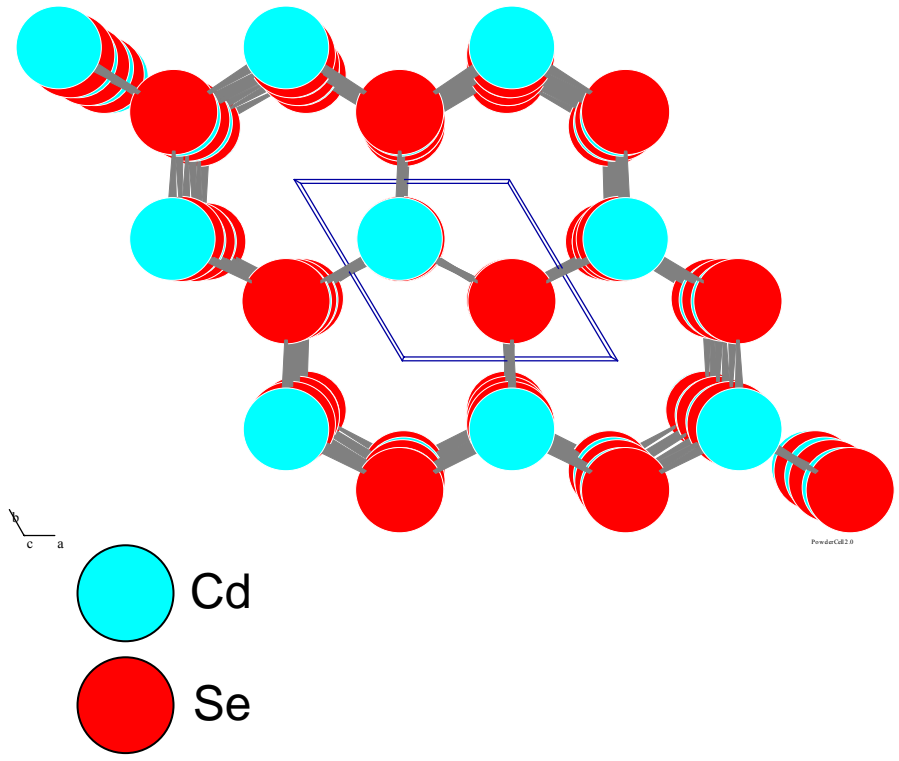


**Figure 3.10.** Structure of CdSe looking down the  $\langle 001 \rangle$  (c-axis).



bond distance in the quantum dot based on the pXRD measurements. As the doping concentration increases the average M-Se bond distance decreases. When this is extrapolated to  $x = 1$ , a Co-Se bond distance of 2.28 Å is predicted for a wurtzite lattice. This is smaller than the theoretical Co-Se bond distance (2.43 Å) based on ionic radii, however this is not abnormal since it is known that quantum dots exhibit a contraction in the lattice relative to that of the bulk AND Co-Se typically adopts an  $O_h$  lattice in bulk.<sup>29</sup>

TEM provides further support of an RIS process at a single dot level by measuring the average lattice spacing in the TEM image for an individual nanomaterial. Measurement of the array of dots allows an approximate measure of the uniformity of doping within the sample. A thermodynamically driven RIS process should produce a statistical distribution with a gaussian histogram, while a sample that tends towards phase segregation or a non-RIS process will show a very wide distribution of doping levels. Although the error of measuring TEM fringe patterns is large (~6 - 10%), it can provide strong support of a RIS process existing that is thermodynamically driven. For the Co:CdSe samples, the lattice spacing observed in the pXRD and the TEM correlate with one another. For the  $x=0.12$  sample, the average  $\langle 100 \rangle$  lattice spacing observed in the TEM images from the fringe spacing is  $\sim 37 \pm 2$  pm which is in agreement with the 36.5 pm observed in the pXRD for the  $\langle 100 \rangle$ . This is surprisingly good agreement for the two and inspection of a large

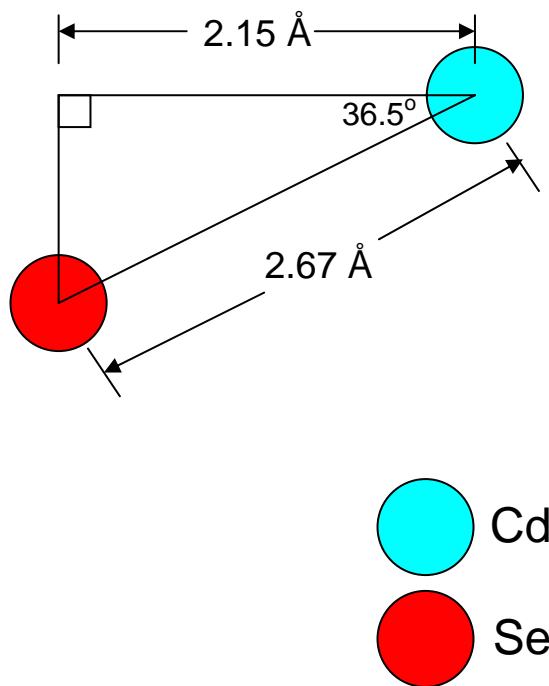


**Figure 3.12.** Diagram showing the distance between Se and Cd in a wurtzite lattice and the position of the two atoms relative to one another assuming that you are looking down the  $\langle 100 \rangle$  axis.

number of QDs of the TEM confirms that the pXRD values reflect a narrow distribution in the average concentration in the ensemble of QDs. This allows the conclusion of a uniform doping level across the QD sample.

**3.3.4 Raman Studies of  $\text{Cd}_{1-x}\text{Co}_x\text{Se}$ .** Observation of a shift in the longitudinal optical phonon mode (LO) for CdSe corroborates the RIS model for doping achieved by a single source precursor growth technology. The shift in the Raman LO reflects the observed contraction in the lattice by pXRD (figure 3.13). Using a Hooke's law analysis, it is expected that a change at the  $\Gamma$  point in the Brillouin center ( $k = 0$ ) LO mode will reflect the random displacement of Cd by Co in the host lattice, as long as the process is random and no superlattice is formed. A hardening of the LO mode is observed with increasing doping concentration due to the average lattice contraction. This can not be due to phonon confinement effects because phonon confinement results from a relaxation of the  $k = 0$  selection rule resulting in a softening of the LO mode relative to that of the bulk, which is opposite to what is observed.<sup>28</sup>

Along with the change in the LO mode, appearance of local vibrational modes (LVM) also occur in these alloy samples resulting from the substitution of Cd with Co. The LVM modes are believed to arise from local symmetry breaking in the Brillouin zone, which can induce zone folding or the appearance of infrared, and silent modes, overtones, and combination modes in the resonant Raman spectra. The LVM modes in the Co:CdSe alloy are observed

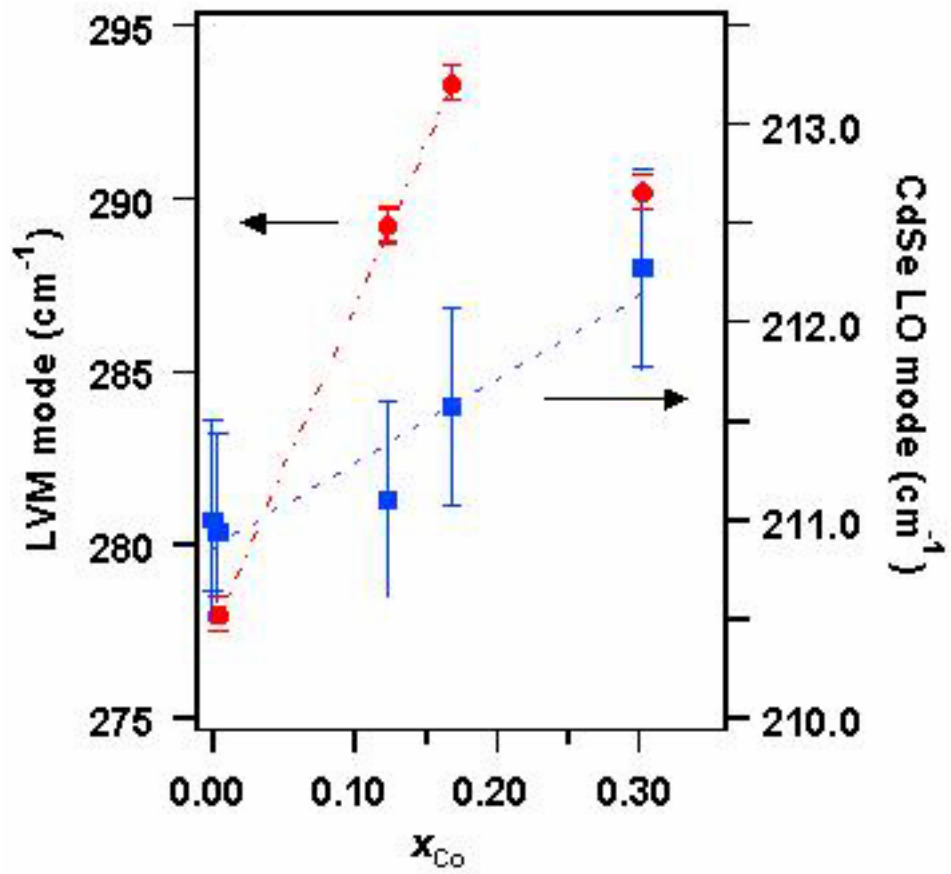


**Figure 3.13.** Position of LVM and CdSe LO mode as a function of doping concentration  $x$ . The LVM is represented by (●) and the CdSe LO mode is represented by (■).

at 275 cm<sup>-1</sup> and 490 cm<sup>-1</sup> (figure 3.14). The LVM modes show a linear shift with increasing Co concentration up to x = 0.18 in intensity and position. At x > 0.18 a softening of the LVM is observed along with a decrease in intensity of this mode. This is in agreement with the pXRD data, which suggests that there may be a phase transition due to segregation of CoSe in the alloy lattice at these extreme doping levels.

We can not assign the LVM at 275 cm<sup>-1</sup> to a pure Co-Se vibrational mode based on a modified Mazur, Montroll, and Potts (MMP) model which predicts that the value of a cobalt ion in a CdSe lattice would be at 198 cm<sup>-1</sup>.<sup>30</sup> This frequency is calculated according to the following equation.

$$\omega_{lm}^2(\varepsilon_2) = \frac{2\omega_2 + (1 - \varepsilon_2^2)\omega_1^2 + [4\varepsilon_2^2\omega_2^4 + (1 - \varepsilon_2^2)\omega_1^4]^{1/2}}{2(1 - \varepsilon_2^2)} \quad (3)$$

In the equation above  $\varepsilon_2$  is the mass defect parameter,

$$\varepsilon_2 = 1 - M / M_2 \quad (4)$$

where  $M$  is the mass of the impurity (Co) and  $M_2$  is the mass of the host atom (Cd). The value for  $\omega_j$  is calculated according to the following equation.

$$\omega_j^2 = 2f_{12} / M_j \quad (5)$$

where  $f_{12}$  represents the force constant of the Cd and Se bond. The value of  $j$  is either 1 or 2 where 1 represents the lighter atom (Se) and 2 represents the heavier atom. (Cd). The calculated MP frequency may give rise to increased

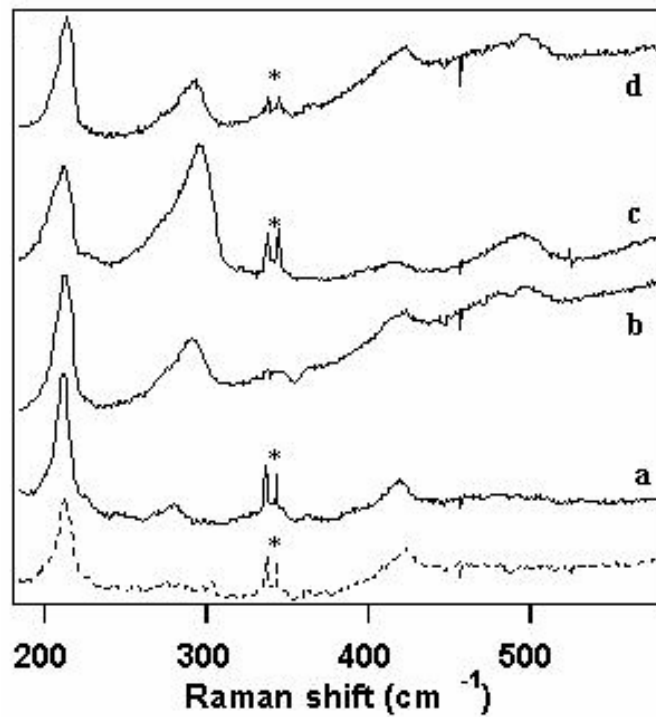


**Figure 3.14.** Raman spectra of a)  $\text{Cd}_{0.996}\text{Co}_{0.004}\text{Se}$  b)  $\text{Cd}_{0.88}\text{Co}_{0.12}\text{Se}$  c)  $\text{Cd}_{0.83}\text{Co}_{0.17}\text{Se}$  d)  $\text{Cd}_{0.70}\text{Co}_{0.30}\text{Se}$ . The dashed lines represent the spectra of CdSe and the (\*) represents laser plasma lines.

asymmetry observed in the CdSe LO mode.<sup>31</sup> This also can not be assigned to a strain induced softening of the LO mode, as has been observed in  $Zn_{1-x}Be_xSe$ <sup>32</sup> since this is not in agreement with the modified random ion isodisplacement<sup>33</sup> for the LO mode. Using a calculated force constant for  $Cd_{1-x}Co_xSe$  for  $x=1$ , a strain inducted shift of the optical phonon branch would predict a shift in the frequency toward  $\sim 215 \text{ cm}^{-1}$  with increasing concentration, which is not observed experimentally.

The LVM mode may be due to either an anharmonic lattice<sup>34</sup> or an electron-LO phonon coupled mode. Appearance of an electron-phonon coupled mode has been seen in rare earth doped  $CaF_2$ ,<sup>35</sup> with n-type dopants inducing excess electrons coupled to a resultant mode softening. The existence of el-ph coupling has also been observed in a one dimensional MX crystal.<sup>36</sup> If the LVM at  $\sim 275 \text{ cm}^{-1}$  arises from enhanced el-ph coupling in the lattice, this may be due to p-doping arising when  $Co^{2+}$  is doped into CdSe. This creates excess holes in the valence band which would therefore lead to the observation of el-LO phonon coupled mode arising in the vibrational spectrum.

The mode at  $\sim 490 \text{ cm}^{-1}$  is assignable to a combination mode based upon the CdSe LO mode ( $\sim 210 \text{ cm}^{-1}$ ) and the LVM mode ( $\sim 275 \text{ cm}^{-1}$ ). This suggests both modes have  $A_1$  symmetry since they can combine to give a new mode at  $\nu_{\text{comb}} = \nu_{\text{LO}} + \nu_{\text{LVM}} \approx 485 \text{ cm}^{-1}$ . It is important to note that the term

LVM may not be correct for the 275 cm<sup>-1</sup> mode due to the observance of the combination mode.

**3.3.5 Electron-phonon coupling in Cd<sub>1-x</sub>Co<sub>x</sub>Se.** The possibility for enhanced el-ph interaction in these materials can be determined by analysis of the overtone modes in the Raman data shown in figure 3.14. The Huang-Rhys parameter,  $S$ , measures the distortion between the ground and excited state thus indirectly measuring the degree of el-ph coupling. Assuming that the intensities of the LO phonon and LO phonon replicas can be used in place of the transition probabilities, then  $S$  can be directly calculated from the vibrational data.<sup>28</sup>  $S$  is given by

$$\frac{P_{a \rightarrow b}}{P_{ab}} = \frac{S^i e^{-S}}{i!} \quad (6)$$

where  $P_{a \rightarrow b} / P_{ab}$  is the relative transition probability for the  $i$ th phonon replica.<sup>37</sup>

The intensity of the Raman modes are given by<sup>38</sup>

$$I_{a \rightarrow b} = c(\nu_o \pm \nu_{ab})^4 \sum_{\rho\sigma} |(P_{\rho\sigma})_{ab}|^2 \quad (7)$$

which is indirectly proportional to  $P_{ab}$ . Assuming that  $I \propto P$  (i.e., low-power condition), the calculation of  $S$  will be given by  $I_{LO}/I_{2LO}=2/S$ .<sup>34</sup> Table 3 contains a list of  $S_n$  ( $n = \text{CdSe LO mode or LVM mode}$ ) vs concentration. The values of  $S_n$  for all the doped samples were higher than that of the undoped CdSe samples indicating that greater el-phonon coupling exists in the doped

x	$S_{\text{CdSe}}$	$S_{\text{LVM}}$
0	2.36	
0.004 ±0.0002	4.72	3.06
0.12 ±0.006	4.67	1.76
0.17 ±0.009	3.33	1.27
0.30 ±0.015	2.73	1.25

**Table 3.** Calculated Huang-Rhys constants from the Raman spectra.

samples.<sup>39</sup> For the  $x = 0.004$  sample,  $S_{LO}$  increases by a factor of 2 relative to that of the undoped sample while the  $x = 0.30$  sample increases by a factor of only 1.16 to that of the undoped sample. The observed decrease in  $S_{LO}$  is correlated with a decrease in  $S_{LVM}$  at  $275\text{ cm}^{-1}$ . The value of  $S_{LVM}$  decreases by a factor of 2.5 between  $x = 0.004$  and  $x = 0.30$  indicating a decrease in el-ph coupling from the lowest to highest doped sample. This could suggest the formation of a ternary lattice in the highest doped samples. While this study does not clearly explain the identity of the LVM mode, it does suggest that changes in el-ph coupling are consistent with the appearance of a LVM mode. The observance of similar LVM modes in both wurtzite and zinc blende II-VI semiconductors have been observed.<sup>40</sup>

**3.3.6 Determination of oxidation state of Co using XANES.** XANES is an effective method for determining oxidation states of guest ions in a host lattice. The XANES region in X-ray absorption is 50 eV from the absorption edge. Most elements show significant shifts in binding energy as a function of oxidation state thereby making this technique ideal for the determination of the oxidation states of elements within a material. This is done by comparing the x-ray absorption of the materials of interest with standards. Figure 3.15 shows Co-edge XANES data for  $\text{Cd}_{1-x}\text{Co}_x\text{Se}$  and  $\text{CoSe}$ . It can be seen that the two have similar XANES spectra and the energy of the absorption peaks are at

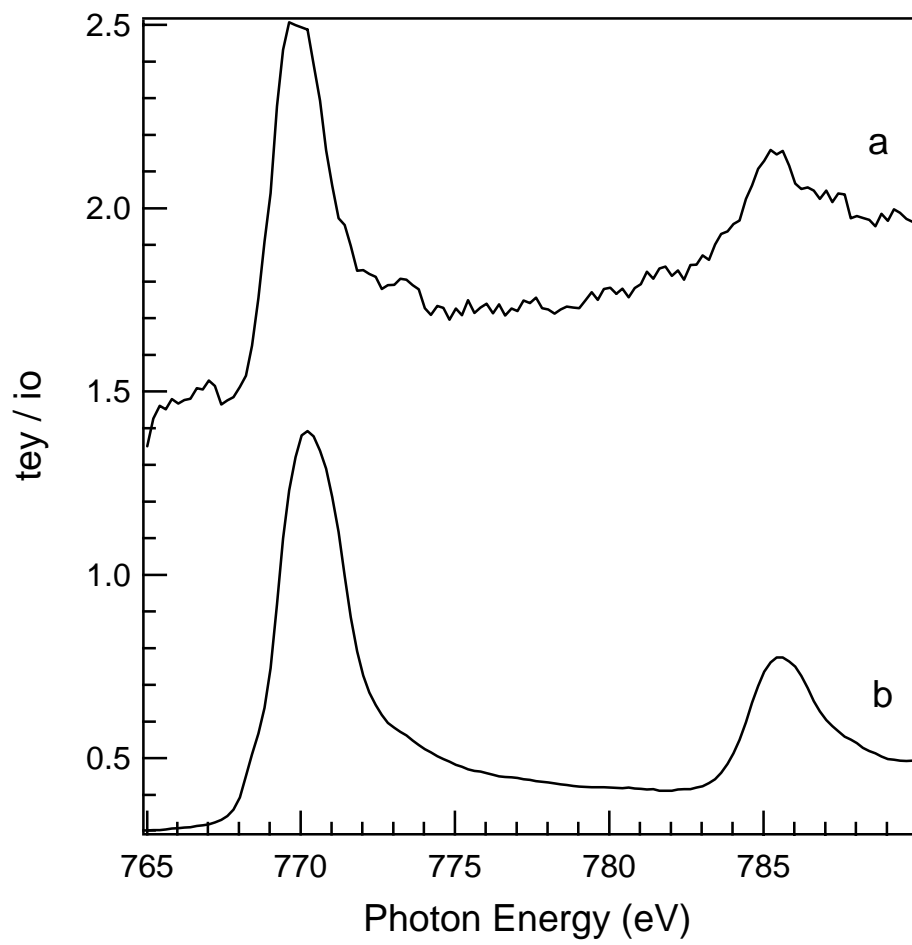


**Figure 3.15.** XANES spectra of a)  $\text{Cd}_{0.975}\text{Co}_{2.5}\text{Se}$  and b)  $\text{CoSe}$ .

approximately the same energy. This provides evidence for the cobalt having an oxidation state of +2 in Co:CdSe.

**3.3.7 Site specific analysis using EXAFS.** EXAFS is a non-destructive, element specific, technique that provides information on the distance between the atom of choice and the shells of atoms surrounding that atom, thus providing direct insight into the guest ion site occupation in the lattice. A synchrotron source is required to perform these measurements. The elements that were studied in our EXAFS experiments were cobalt and cadmium. The electron binding energies of the K 1s electrons in cobalt is 7709 eV.<sup>41</sup> When these samples are exposed to X-ray radiation of 7709 eV, K 1s electrons from the cobalt atoms are ejected. These electrons travel as waves away from the cobalt atoms as they are ejected. Once they come into contact with the selenium atoms surrounding the cobalt atoms a certain number of these electrons is backscattered. When the wave of backscattered electrons comes into contact with the wave of electrons being ejected from the cobalt the appearance of fine structure is observed in the EXAFS. Figure 3.16 shows a picture of this phenomenon. Appropriate background corrections are performed on this data set and the Fourier transform of this data is then worked up using EXAFS Pak to provide information on the distance between the cobalt atoms and the selenium atoms making up the 1<sup>st</sup> shell of the cobalt atoms. We performed EXAFS measurements on a

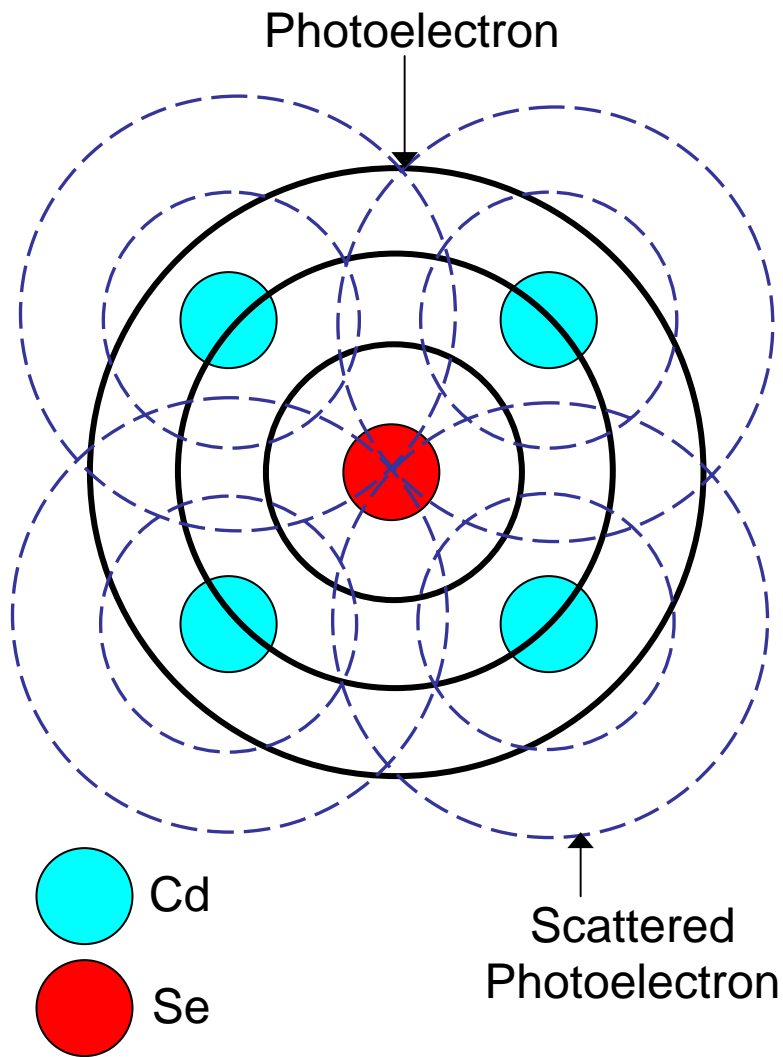
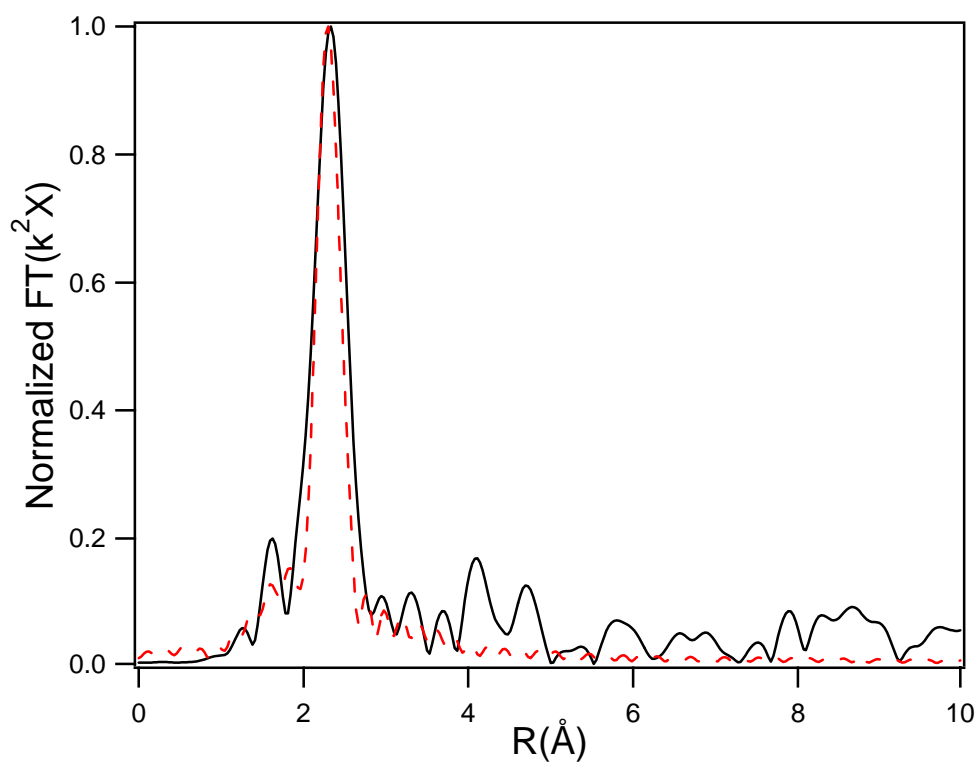


Figure 3.16. Diagram depicting the emission and

backscattering of electrons in EXAFS experiments.

number of  $\text{Cd}_{1-x}\text{Co}_x\text{Se}$  samples. For the Se and Co edge EXAFS the data was fit using models created by FEFF 8.20 in conjunction with IFEFFIT. The clusters used for generating the theoretical spectra consisted of a 50 atom cluster created by ATOMS. Using FEFF 8.20 the electron path files were created. The path files were then imported into ARTEMIS to generate the theoretical spectra of the data.

Figure 3.17 – 3.20 shows the Cobalt K-shell EXAFS and the fits for three  $\text{Cd}_{1-x}\text{Co}_x\text{Se}$  samples and CoSe. The distance between the Co and the first shell are approximately 2.28 – 2.29 Å. This is in good agreement with a  $T_d$  site in which Co is bound to 4 Se atoms at a Cd- $T_d$  substitutional site, and consistent with the extrapolated data from the Co-Se bond distance obtained from the pXRD measurement. Regardless of the doping concentration the bond distance between the Co-Se does not change. This behavior is expected for a localized guest ion in a crystalline host lattice, and has been observed previously for substitutional defect ions in bulk alloy lattices.<sup>42-44</sup> Figure 3.22 shows the Se K-shell EXAFS for a set of  $\text{Cd}_{1-x}\text{Co}_x\text{Se}$  samples and bulk CdSe. The first shell of Se is ~ 2.61 – 2.67 Å corresponding to the Cd-Se bond distance obtained in the bulk of 2.67 Å. If cobalt substituted as a phase segregated CoSe then another peak corresponding to Co-Se at ~ 2.28 Å would be present.



**Figure 3.17.** The solid line is the Co-edge EXAFS of CoSe and the dashed line represents the fit for the data.

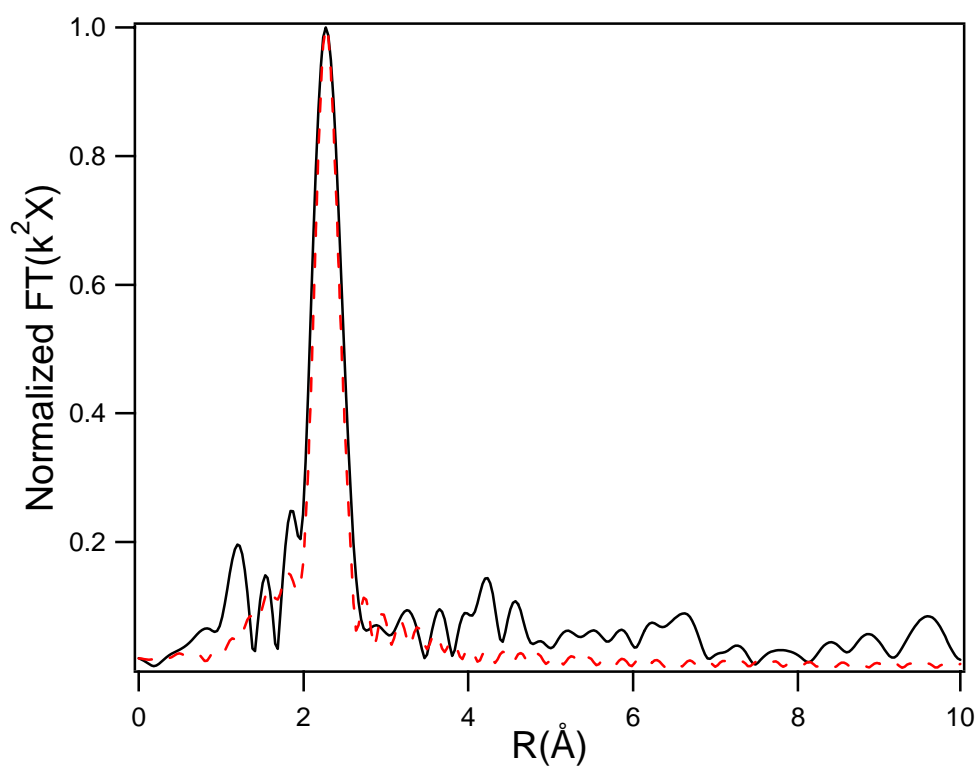


**Figure 3.18.** The solid line is the Co-edge EXAFS of Cd<sub>0.978</sub>Co<sub>0.022</sub>Se and the dashed line represents the fit for the data.

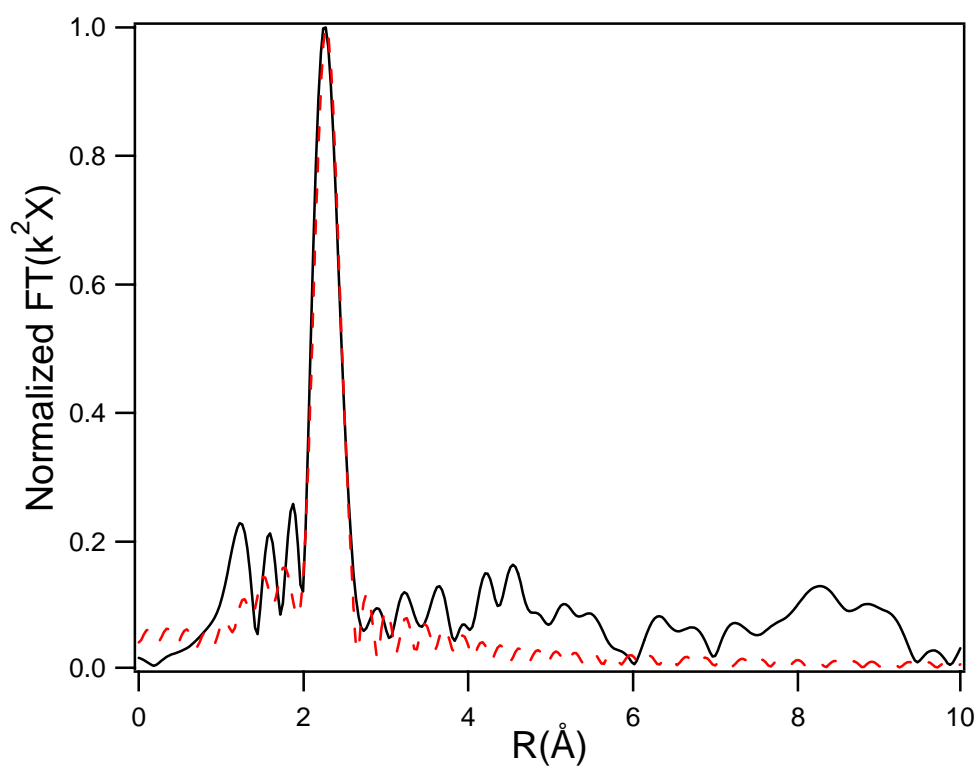


**Figure 3.19.** The solid line is the Co-edge EXAFS of  $\text{Cd}_{0.971}\text{Co}_{0.029}\text{Se}$  and the dashed line represents the fit for the data.

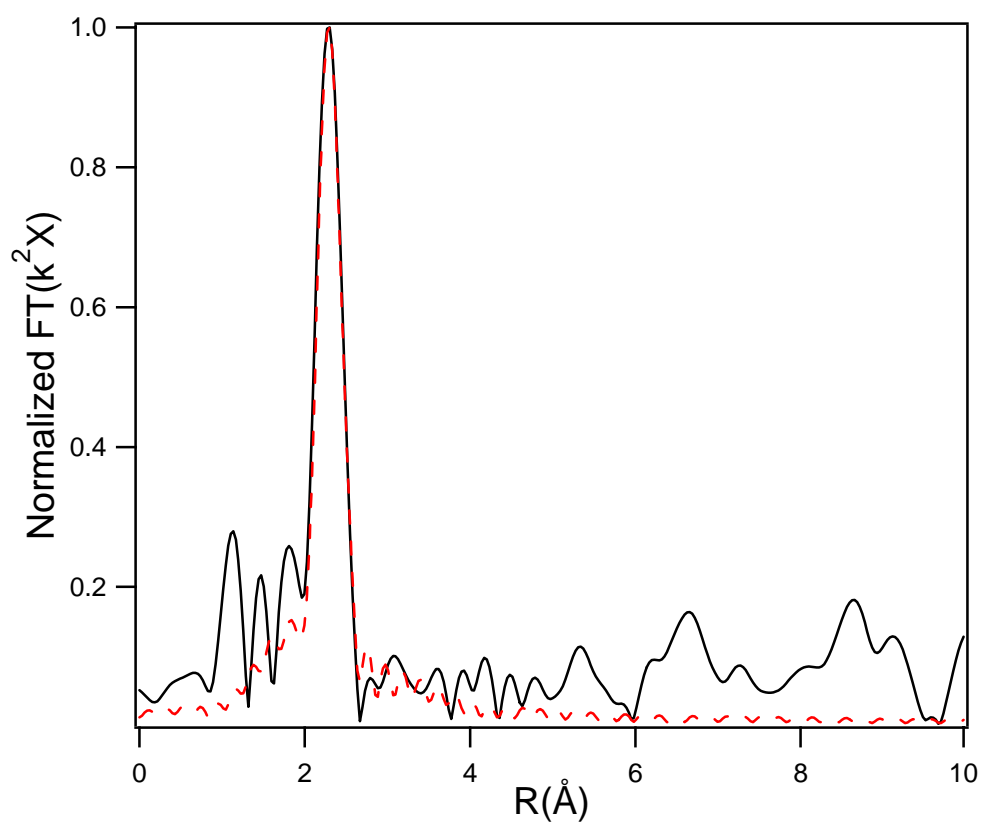


**Figure 3.20.** The solid line is the Co-edge EXAFS of  $\text{Cd}_{0.895}\text{Co}_{0.105}\text{Se}$  and the dashed line represents the fit for the data.

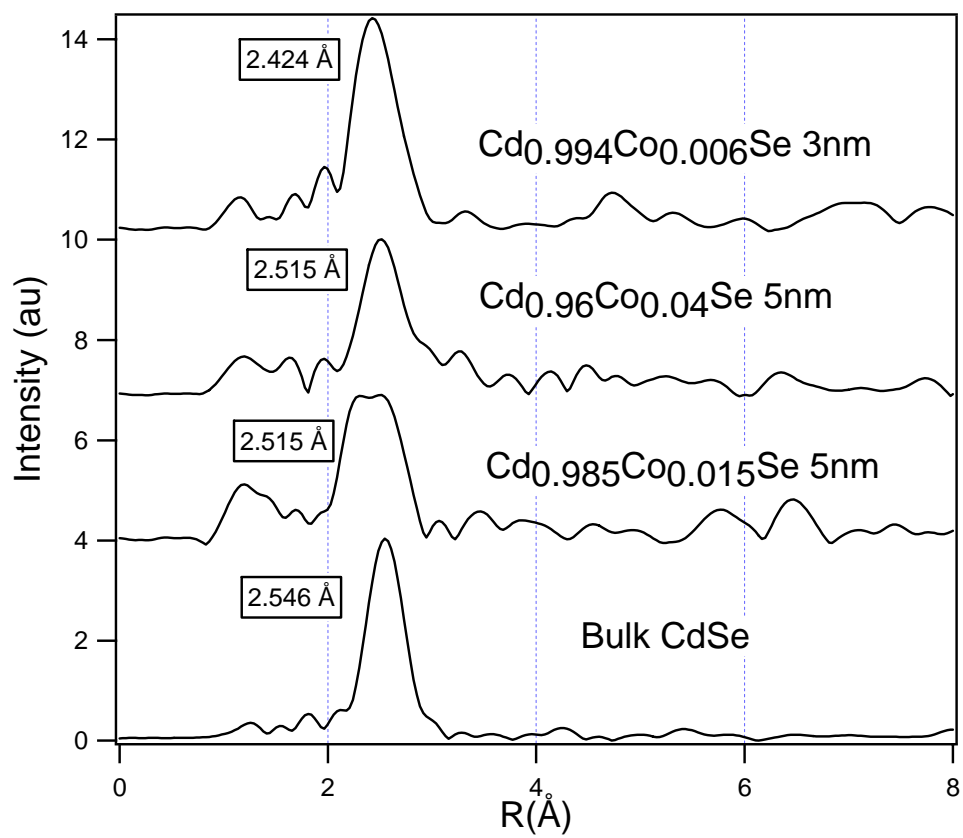


**Figure 3.21.** Cd-edge EXAFS on three Co: CdSe samples and bulk CdSe.

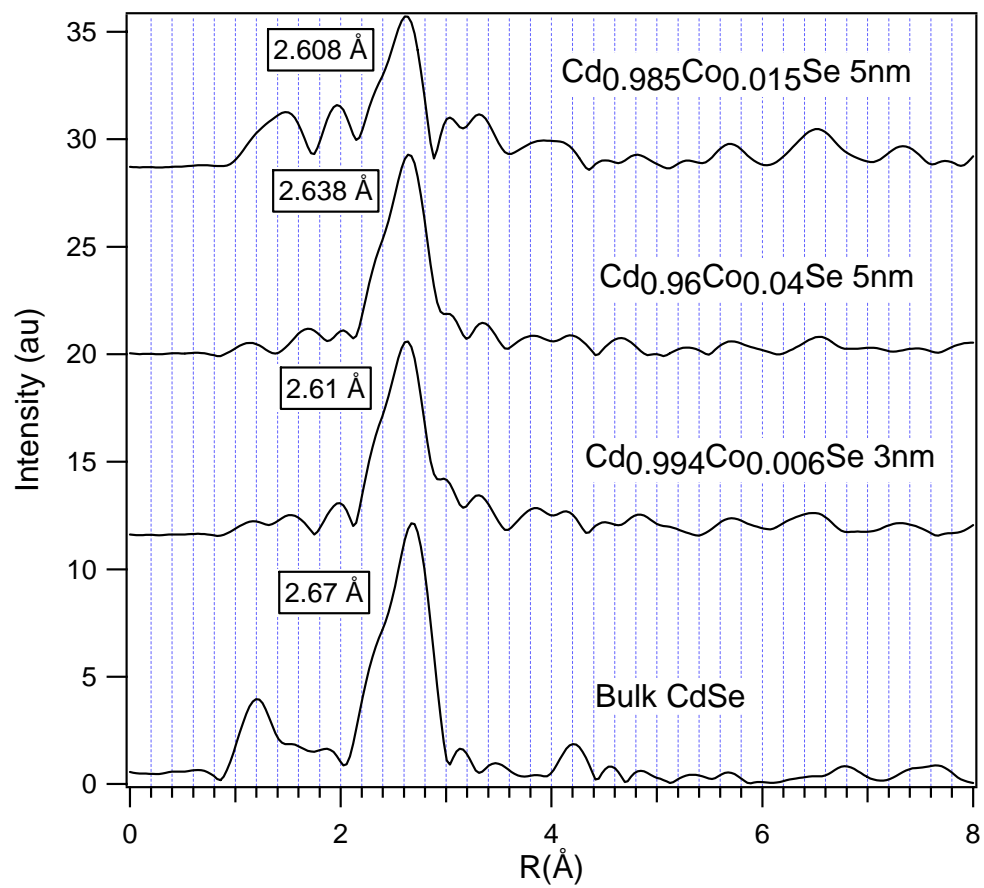


**Figure 3.22.** Se-edge EXAFS of a series of Cd<sub>1-x</sub>Co<sub>x</sub>Se samples and CdSe bulk.

**3.3.8 Magnetic Properties in Cd<sub>1-x</sub>Co<sub>x</sub>Se.** Magnetic properties of II-VI semiconductors depend upon the degree of coupling of the transition metal ion dopant with that of the II-VI semiconductor electronic levels. The magnitude of the mixing is directly dependant upon the magnitude of mixing between the d-orbitals of the dopant and the s and p electrons in the valence band (VB) and conduction band (CB) of the II-VI host. Values of el-ph coupling constants, which can modulate the sp-d mixing in II-VI materials, suggest that significant perturbation of the QD properties may yield unique magnetic properties. Bulk Co: CdSe shows evidence for two different magnetic regimes: a high temperature PM regime and a low temperature (< 1K) SG-AFM regime.<sup>5</sup> Curie-Weiss behavior in the high temperature region is observed followed by the onset of AFM coupling at low temperature due to a superexchange (SE) mechanism between nearest neighbors (NN). The superexchange integral  $J_{NN}$  of Co pairs is large due to a strong radial exchange interaction ( $J(R)$ ) of the spin  $S = 3/2$  system.<sup>22</sup>

A plot of  $\chi(T)$  versus temperature is shown in figure 3.23 for Cd<sub>1-x</sub>Co<sub>x</sub>Se ( $x = 0.004 - 0.30$ ). The direct current (DC) susceptibility exhibits a phase transition at low temperature evident by the cusp in the DC susceptibility. Figure 3.24 shows a plot of  $1/\chi(T)$  indicating classical PM Curie-Weiss behavior occurs at high temperatures followed by deviation at lower temperature (<50 K), due to strong coupling between the cobalt ions. The

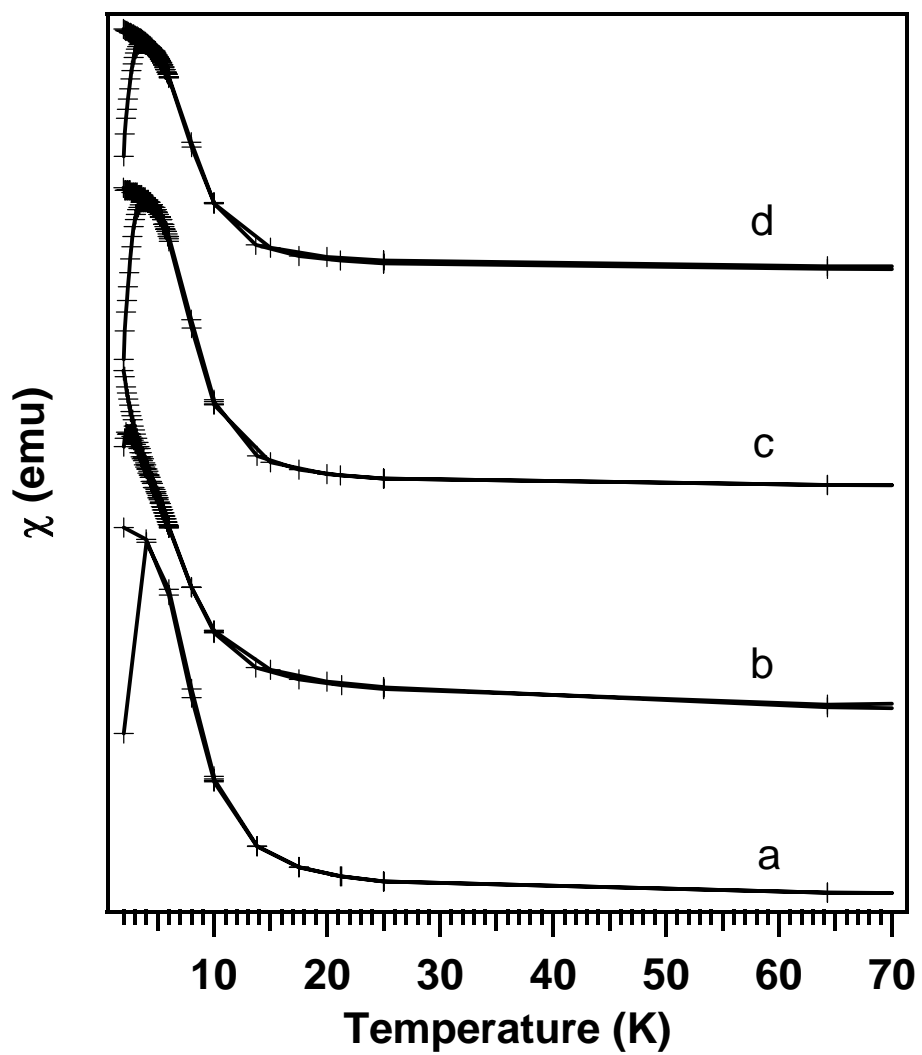


**Figure 3.23.** ZFC/FC data for a)  $\text{Cd}_{0.996}\text{Co}_{0.004}\text{Se}$  b)  $\text{Cd}_{0.88}\text{Co}_{0.12}\text{Se}$  c)  $\text{Cd}_{0.83}\text{Co}_{0.17}\text{Se}$  d)  $\text{Cd}_{0.70}\text{Co}_{0.30}\text{Se}$ .

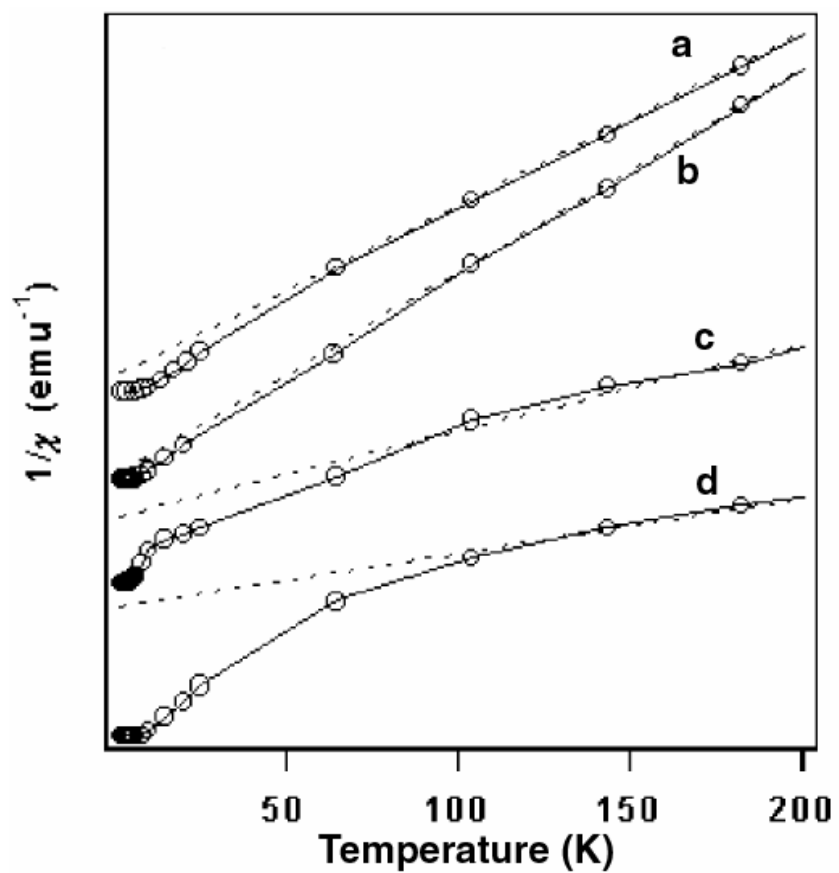


**Figure 3.24.**  $1/\chi$  vs. temperature data for a)  $\text{Cd}_{0.996}\text{Co}_{0.004}\text{Se}$  b)  $\text{Cd}_{0.88}\text{Co}_{0.12}\text{Se}$   
 c)  $\text{Cd}_{0.83}\text{Co}_{0.17}\text{Se}$  d)  $\text{Cd}_{0.70}\text{Co}_{0.30}\text{Se}$ .

magnitude of deviation increases with increasing Co concentration. This anomaly can be assigned to an AFM-SG transition and is confirmed by comparison of the zero-field-cooled (ZFC) and field-cooled (FC) data in figure 3.23. The glass temperature ( $T_g$ ) occurs at the “cusp” of the ZFC data. The  $T_g$  in Co: CdSe QDs is an order of magnitude greater than that observed in bulk Co-DMS systems ( $T_g \approx 100 - 900$  mK) of equivalent doping concentrations.<sup>12,45</sup> The observed increase in  $T_g$  in these systems is believed to be due to an enhancement in the long-range coupling between the cobalt ions.

The high temperature magnetic susceptibility,  $\chi(T)$ , can be fit by the Curie-Weiss law shown in the equation below.

$$\chi(T) = C / (T - \Theta) \quad (8)$$

In the equation above, C is the Curie constant, T is the temperature in Kelvin, and  $\Theta$  is the Curie temperature. The Curie temperature is obtained by fitting the high temperature  $1/\chi(T)$  data. The point at which the fitted line crosses the x-axis is the Curie temperature. Fits of the high temperature  $1/\chi(T)$  data for the four samples resulted in a positive Curie temperature in the  $x = 0.004$  and  $0.12$  case, and a negative Curie temperature in the  $x = 0.17$  and  $0.30$  case the values of which can be listed in table 4. This is significant in that a positive Curie high doped samples implies the presence of AFM interactions. The observation of an AFM-SG phase suggests that the Co(II) cations are interacting strongly.

x	$\Theta$ (K)	$J_{NN}$ (K)
0.004 $\pm$ 0.0002	3	0.1
0.12 $\pm$ 0.006	6	0.2
0.17 $\pm$ 0.009	-168	-5.6
0.30 $\pm$ 0.015	-3660	-122

**Table 4.** Nearest-Neighbor  $\text{Co}^{2+}$ - $\text{Co}^{2+}$  Curie Temperatures ( $\Theta$ ), and Exchange Integrals ( $J_{NN}$ ) for  $\text{Cd}_{1-x}\text{Co}_x\text{Se}$  Quantum Dots.

This is similar to the observation of strong superexchange interactions in bulk Co: CdSe, where the interactions arise primarily from nearest neighbor interactions between Co(II) ions. Further support for an AFM-SG phase in the highly doped sample is shown in the magnetization data,  $M(H)$ , where no evidence for a hysteresis is observed. AFM interactions can occur between Co spins in the same particle (intraparticle) or Co spins in neighboring particles (interparticle). The organic passivating layer is believed to provide a large enough distance ( $d \sim 2$  nm) between the particles making it highly unlikely that the AFM interactions could occur from interparticle interactions.

Further support for the SG behavior is provided in the alternating current (ac) susceptibility measurements. AC susceptibility is performed by applying a small ac field ( $\sim 5$  Oe) while applying a dc field. The frequency of the ac field can be changed which has an effect upon the freezing temperature ( $T_f$ ) of a material. It is through this dependence that the nature of the magnetic properties can be determined. Depending on the value obtained from the equation below, it can be determined whether a material is spin glass or superparamagnetic.

$$x = \Delta T_f / [T_f \Delta(\log \omega)] \quad (9)$$

Here  $T_f$  is the freezing temperature and  $\omega$  is the frequency of the ac field. If the value obtained from the above equation is on the order of 0.10 then the material is spin glass. If the value is on the order of 0.28 then the material is a

superparamagnet.<sup>46</sup> Figure 3.25 shows a plot of the ac susceptibility of Cd<sub>0.96</sub>Co<sub>0.04</sub>Se at 10 and 1000 Hz. The value for x obtained in the Cd<sub>0.96</sub>Co<sub>0.04</sub>Se sample is 0.06 thus providing evidence for spin glass behavior in Co: CdSe.

The magnetization of the x=0.12 is shown in the inset of figure 3.26. It exhibits high field saturation, the behavior of which can be described by a Langevin function,

$$\frac{M}{M_s} = \coth\left(a \frac{H}{T}\right) - \frac{T}{aH} \quad (10)$$

where  $M/M_s$  is the relative magnetization and  $a = \mu/k$ . Equation 11 is obtained from the classical limit ( $J = \infty$ ) of the Brillouin function,

$$\frac{M}{M_s} = \frac{2J+1}{2J} \coth\left(\frac{2J+1}{2J} a \frac{H}{T}\right) - \frac{1}{2J} \coth\left(\frac{aH}{2JT}\right) \quad (11)$$

where  $J$  is the total angular momentum. An effective Bohr magneton,  $\mu_{\text{eff}}$ , of  $3.52 \mu_B$  can be obtained from the data, very close to the spin-only value of  $3.87 \mu_B$ , indicative of paramagnetic spin domains in the low-doped samples. This supports the susceptibility measurements in that the low doped samples exhibit high temperature paramagnetic behavior with weak FM interactions at low temperatures.

The value of  $\Theta$  as a function of concentration can be used to estimate the overall exchange integral for cobalt interactions and it can be used to

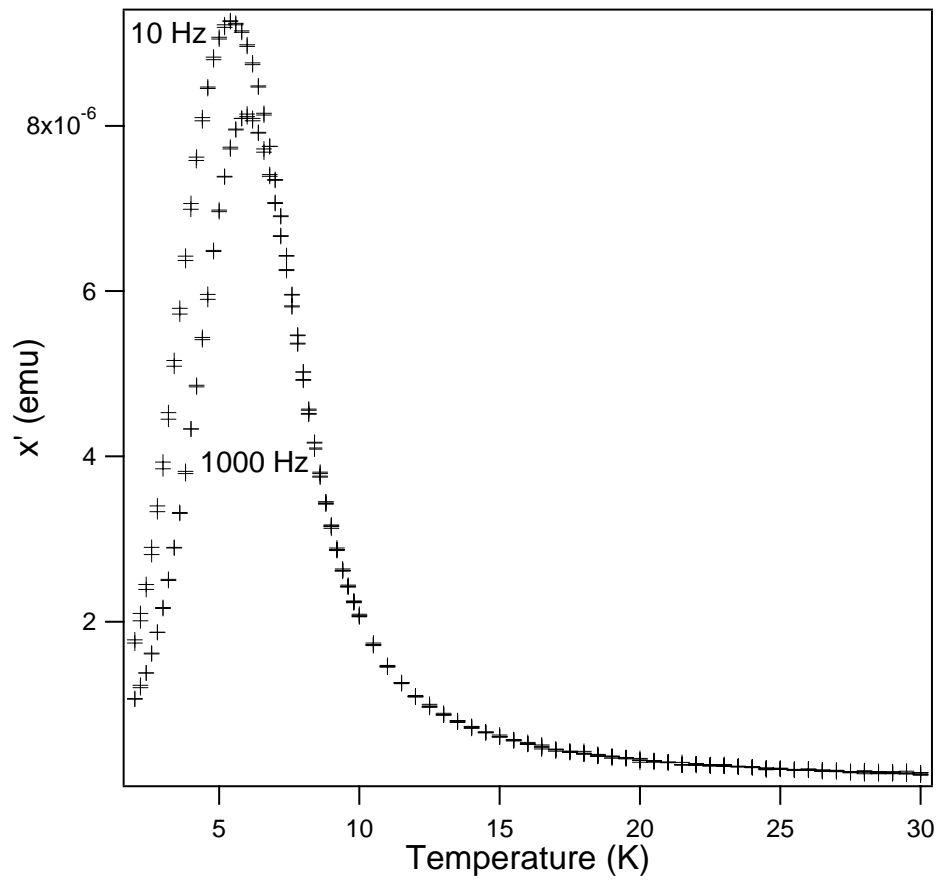


**Figure 3.25.** AC susceptibility of  $\text{Cd}_{0.96}\text{Co}_{0.04}\text{Se}$  at frequencies of 10 and 1000 Hz.

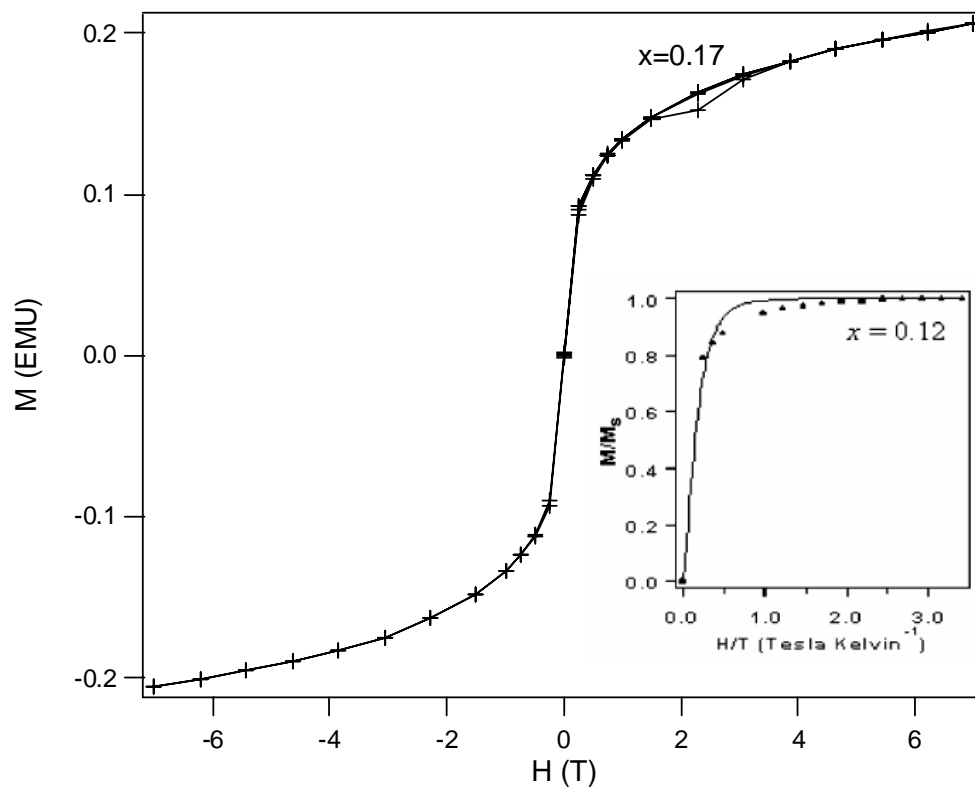


**Figure 3.26.** Field-dependent magnetization,  $M(H)$ , for  $x=0.17$  Co: CdSe.

Inset:  $M(H)$  for  $x=0.12$  Co: CdSe.

estimate the strength of the superexchange interaction in these materials. The magnitude of the SE interaction can be obtained by fitting the concentration dependence of  $T_g$ .<sup>22</sup> It has been shown that DMS systems typically follow a power law behavior governed by  $T_g \sim Bx^{n/3}$ , where B is a constant and  $n$  represents the radial extent of the superexchange interaction (figure 3.27). For these systems fitting  $T_g$  to a SE model yield  $n = 0.38$ , which is an order in magnitude smaller than that observed in the bulk. The values of  $n$  for Co, Mn and Fe bulk DMS materials are 6.3, 6.8 and 12 respectively.<sup>22</sup> Assuming that the coupling is dominated by NN interactions, the smaller value can be understood by expressing the radial extent of the exchange interaction  $n$ , in terms of  $J_1 \sim J_{NN}R^n$ . It can therefore be implied that longer range coupling exists for lower values of  $n$ . The value of the nearest neighbor exchange integral,  $J_{NN}$ , can be calculated using the equation 12.

$$J_{NN} = -\frac{3\Theta(x)k_b}{2S(S+1)Z} \quad (12)$$

Equation x assumes that the  $J_{NN}$  is much larger than  $J_{NNN}$ . In equation x  $k_b$  is boltzmann's constant,  $x$  is the doping concentration,  $\Theta$  is the Curie temperature,  $Z$  is the number of nearest neighbors ( $Z = 12$  for wurtzite and zinc blende) and  $S$  is the spin number.

The values of  $J_{NN}$  correlate with doping concentration, suggesting enhanced SE interaction with increasing  $\text{Co}^{2+}$  concentration. This is similar to

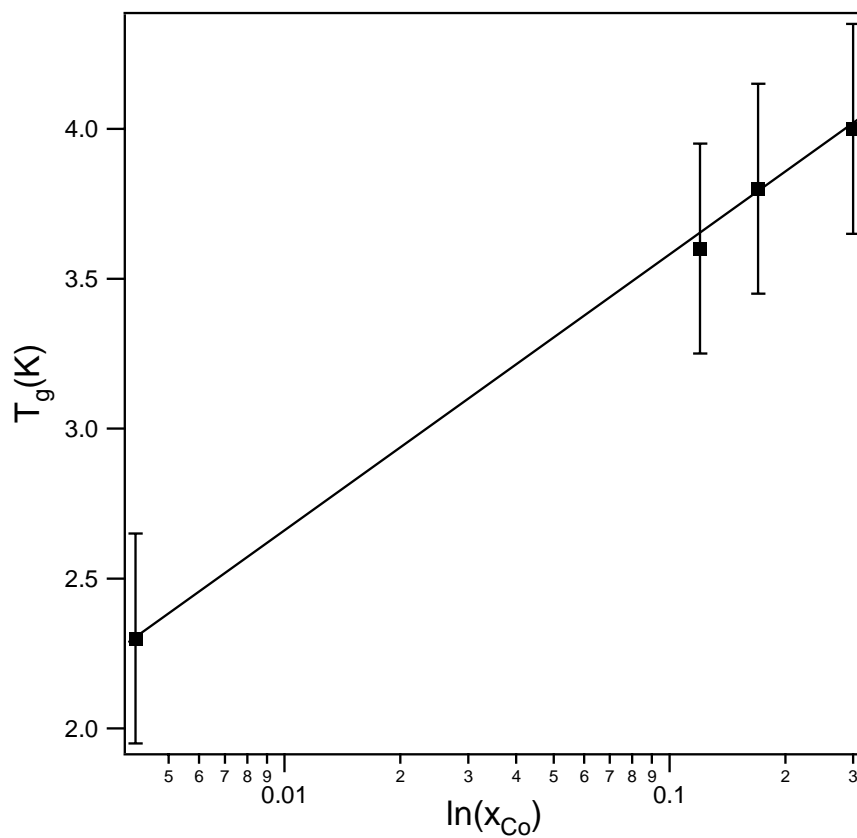


**Figure 3.27.** Plot of  $\ln(x_{Co})$  vs  $T_g$ .

what has been observed in Mn<sup>2+</sup> doped CdS nanoparticles.<sup>47</sup> The increased values of  $J_{NN}$  are believed to be due to stronger hybridization between the d-orbitals of Co<sup>2+</sup> with that of the CdSe QD valence band in comparison to that of the bulk. Figure 3.28 shows that in bulk CdSe the occupied  $e_+$  and  $t_+$  orbitals lie 4 eV below the valence band while the occupied  $e_-$  orbital lies 800 meV below the valence band. The valence and conduction bands shift as the particle size becomes smaller in accordance to the following scaling laws:  $E_{VB} \sim r^{-1.24}$  and  $E_{CB} \sim r^{-1.37}$ .<sup>48</sup> Therefore a 50 Å particle would exhibit a CB shift of ~ 210 meV and a VB shift of ~ 190 meV. The shift of the VB increases the orbital overlap integral between Co<sup>2+</sup> d-orbitals and the CdSe VB and could explain the observed increase in  $J_{NN}$  for Co:CdSe quantum dots.

Contribution of the cobalt d-orbital hybridization with that of the VB of the host materials can be calculated for a 50 Å Cd<sub>1-x</sub>Co<sub>x</sub>Se QDs (eqn. 13)

$$N_0\beta_{hyb} = 32V_{pd}^2 \left( \frac{U_{eff}}{(e_- + U_{eff} - E_{VB})(E_{VB} - e_-)} \right) \quad (13)$$

where  $V_{pd}$  is the hybridization parameter (~1 eV),  $e_-$  is the occupied Co<sup>2+</sup> levels,  $E_{VB}$  is the valence band energy, and  $U_{eff}$  is defined as the energy difference between the occupied ( $e_-$ ) and the unoccupied ( $t_-$ ) Co orbitals. For bulk CdSe, assuming that  $E_{VB} = 0$  eV,  $e_- \approx 0.8$  eV, and  $U_{eff} \approx 2.8$  eV, the estimated value for  $N_0\beta_{hyb} \approx -31.1$  eV.<sup>49</sup> For a 50 Å CdSe QD, assuming size dependent shift in the VB energy is  $E_{VB}(QD) \approx [E_{VB}(bulk) - 0.19 \text{ eV}]$ , the  $N_0\beta_{hyb} \approx -43.1$  eV. There is

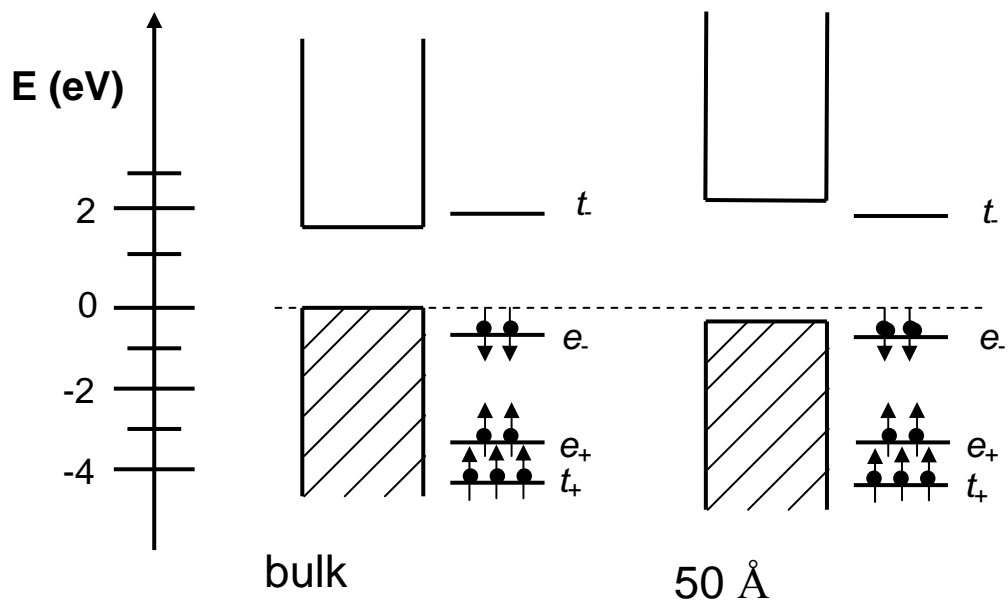


**Figure 3.28.** Schematic illustration of the  $\text{Co}^{2+}$  energy levels in bulk CdSe and in 50 Å.

approximately 30% greater overlap with the d-orbitals of the dopant ion in the quantum dots compared to that of bulk CdSe. This can account for the observed increase in NN exchange interaction in the quantum dots.

Another possibility for the increased coupling can potentially be due to increased contribution from longer range interactions arising from next-nearest-neighbors (NNN) and next-next-nearest-neighbors(NNNN). The values of  $J_{NN}$ ,  $J_{NNN}$ , and  $J_{NNNN}$  for bulk Co: CdSe and 50 Å Co: CdSe QDs are shown in figure 3.27. The line in figure 3.27 is an empirical fit to the SE model, and it was assumed that the  $J_{NNN}$  and  $J_{NNNN}$  interactions would occur at the same distance in quantum dots as that of the bulk. The model shows that the values of  $J_{NNN}$  and  $J_{NNNN}$  are an order of magnitude greater in QDs than the bulk and it is believed that this could potentially be due to the changes in el-ph coupling with increasing doping concentration, which may cause an increase in  $T_g$  consistent with recent calculations.<sup>50</sup> This could result in spin domains forming in the lattice thereby influencing coupling. The large values of  $\Theta$  imply that a simple least-squares application of the Curie-Weiss law to the high temperature susceptibility may not be adequate in explaining the interactions in these materials.<sup>51</sup> This has been observed in materials that show longer range magnetic coupling from NNN and NNNN.<sup>52</sup>

### 3.4 Other Co:CdSe synthesis

Although a full analysis of the following attempts for the formation of Co:CSe alloys has not been carried out, other synthesis approaches to forming alloys will be described in this section. Doping of CdSe was attempted with both  $\text{Co}(\text{NO})_3 \bullet 6\text{H}_2\text{O}$  and  $\text{TMA}[\text{Co}(\text{SPh})_4]$ .

**3.4.1 Doping CdSe with  $\text{Co}(\text{NO})_3 \bullet 6\text{H}_2\text{O}$ .** Doping with  $\text{Co}(\text{NO})_3 \bullet 6\text{H}_2\text{O}$  proved to be unsuccessful due to the water that complexes to  $\text{Co}(\text{NO})_3$ . This reaction was carried out by placing 750 mg of  $\text{Co}(\text{NO})_3 \bullet 6\text{H}_2\text{O}$ , 2.0 g of  $\text{Li}_2[\text{Se}_4\text{Cd}_{10}(\text{SPh})_{16}]$ , and 140 g HDA in a 250 mL three neck round bottom flask. The reaction was heated to  $\sim 120^\circ\text{C}$  under vacuum. At  $\sim 180^\circ\text{C}$  popping noises were heard in the reaction mixture most likely due to the hydrate  $\text{Co}(\text{NO})_3 \bullet 6\text{H}_2\text{O}$ . The bandedge absorption of the quantum dots stayed narrow until  $\sim 524$  nm. Within  $\sim 30$  minutes of hearing the popping noise the absorption spectra of the reaction became very broad. This reaction was attempted one more times resulting in the same behavior.

**3.4.2 Doping CdSe with  $\text{TMA}_2[\text{Co}(\text{SPh})_4]$ .** Doping with  $\text{TMA}_2[\text{Co}(\text{SPh})_4]$  was attempted using the parallel plate synthetic methodology. This cluster proved to be a good precursor for doping of CdSe. The  $\text{TMA}_2[\text{Co}(\text{SPh})_4]$  coordination compound was prepared according to literature methods.<sup>53</sup> The reaction was performed by placing 1.2 g  $\text{Li}_4[\text{Cd}_{10}\text{Se}_4(\text{SPh})_{16}]$  in each vial along

with 100 mg, 200 mg, 400 mg and 600 mg of  $\text{TMA}_2[\text{Co}(\text{SPh})_4]$ . A septa was placed on the vial and the vials were evacuated. In a separate 250 mL flask hexadecylamine was heated to  $\sim 120^\circ\text{C}$  under vacuum. After thirty minutes of being under vacuum 35 mL aliquots were removed with a glass syringe and transferred to the reaction vials containing the clusters. A needle was attached to the vacuum line and Argon was transferred to each of the vials. Afterwards these reactions were heated under the same condition and the absorption spectra were measured to monitor the growth. These materials were isolated in the same manner as all the other syntheses. These particles were grown to  $\sim 4.5 - 5$  nm and doping concentrations as high as 10.8% was achieved. The absorption spectra of these particles is shown in figure 3.29. Table 5 shows the amount of precursors added and the resulting Co concentrations of each of the reactions.

This dopant is preferred over the  $\text{TMA}_2[\text{Co}_4(\text{SPh})_{10}]$  in that the  $\text{TMA}_2[\text{Co}(\text{SPh})_4]$  coordination compound is more stable in air than the  $\text{TMA}_2[\text{Co}_4(\text{SPh})_{10}]$ . This allows for greater control over the doping level in that there is no real way of determining what percentage of the  $\text{TMA}_2[\text{Co}_4(\text{SPh})_{10}]$  that has oxidized. When the  $\text{TMA}_2[\text{Co}_4(\text{SPh})_{10}]$  is oxidized it becomes insoluble in most solvents. On the other hand the  $\text{TMA}_2[\text{Co}(\text{SPh})_4]$  is very soluble in solvents such as

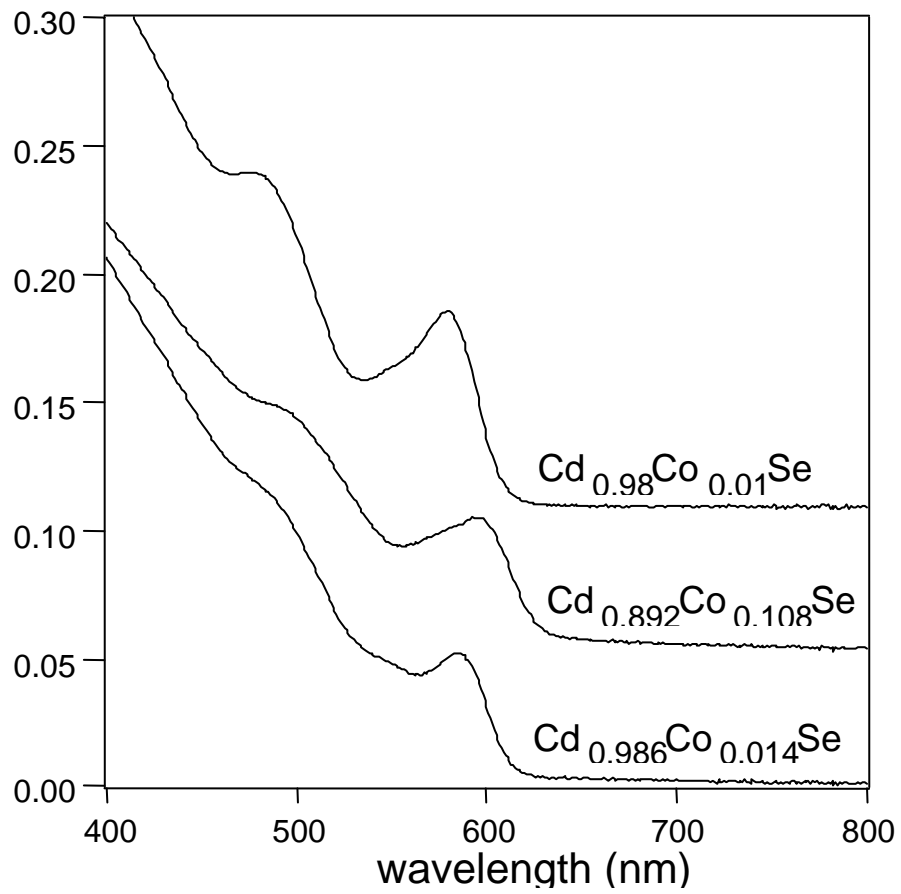


**Figure 3.29.** Absorption of 3 Co: CdSe samples.

$\text{Li}_4[\text{Cd}_{10}\text{Se}_4(\text{SPh})_{16}]$	$(\text{Me}_4\text{N})_2[\text{Co}(\text{SPh})_4]$	%Co doping
1.2 g	100 mg	1.0% $\pm$ 0.05
1.2 g	200 mg	1.43% $\pm$ 0.07
1.2 g	400 mg	2.7% $\pm$ 0.14
1.2 g	600 mg	10.8% $\pm$ 0.54

**Table 5.** List of the resulting cobalt doping concentration in CdSe and the amount of precursor initially added.

MeOH and acetonitrile. Using this methodology the doping concentration correlated closer to the initial precursor concentrations.

The magnetic properties of this dopant are also peculiar (Fig. 3.30 & 3.31). The  $T_g$  (4.7 K) measured using this precursor was slightly higher than that of any Co:CdSe samples that were synthesized to this point. The highest  $T_g$  measured to this point was  $\sim 4$  K. The exact nature of the dopant within the quantum dot is not very well understood. Since each of the cobalt precursor clusters contains only one cobalt it is unlikely that the dopant enters the quantum dot as small preformed clusters. It is also not understood at this point as to why the  $T_g$  of Co:CdSe with doping concentrations  $< 1.4\%$  is greater than that of Co:CdSe samples with 18% cobalt using  $\text{TMA}_2[\text{Co}_4(\text{SPh})_{10}]$ .

### **3.5 Conclusion:**

In conclusion we have developed an effective synthetic method that yields  $\text{Co}^{2+}$  doping levels in quantum dots that have not yet achieved by any other method. Elemental analysis has provided evidence for doping levels as high as 30%. Structural evidence using pXRD shows that random doping of the CdSe host lattice is achieved by  $\text{Co}^{2+}$  ions. The EXAFS data correlates with the Co-Se bond distance of 2.28 Å by extrapolation of the M-Se bond distance vs concentration plot to  $x=1$ . Raman spectroscopy shows evidence for a LVM that

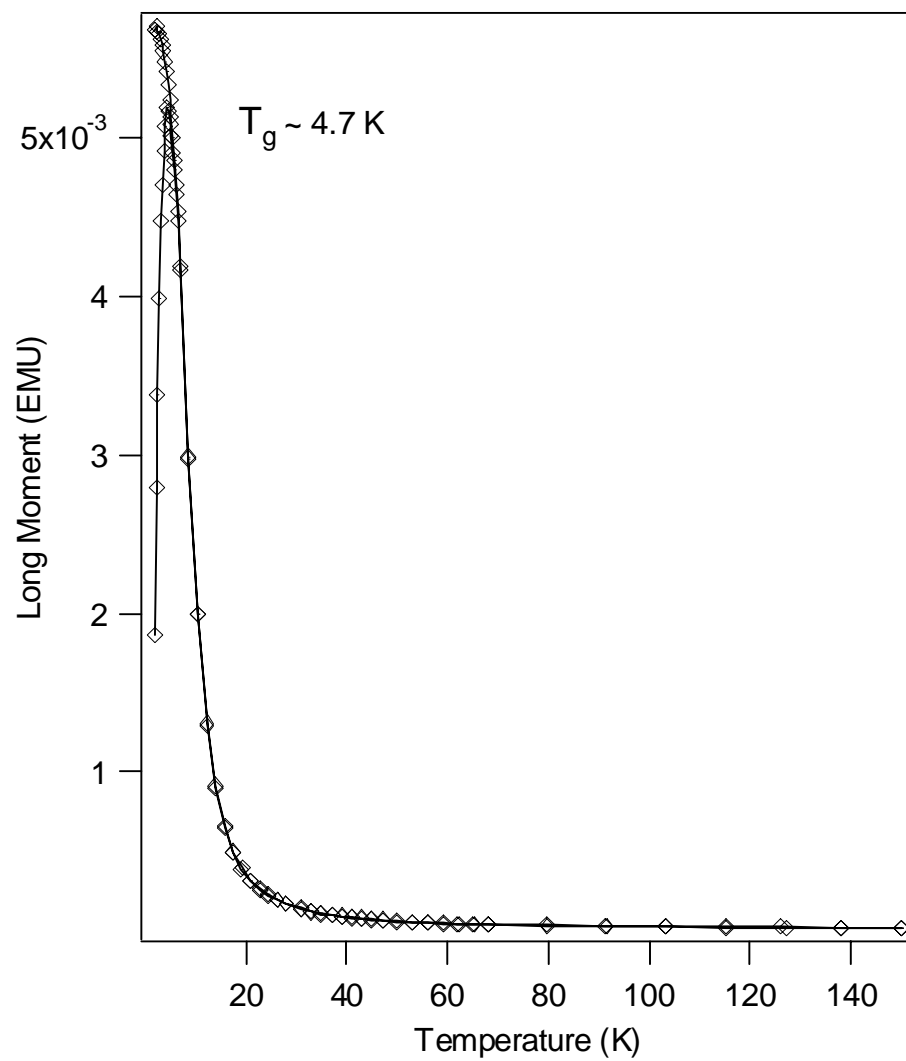


**Figure 3.30.** ZFC/FC data of  $\text{Cd}_{0.986}\text{Co}_{0.014}\text{Se}$ .

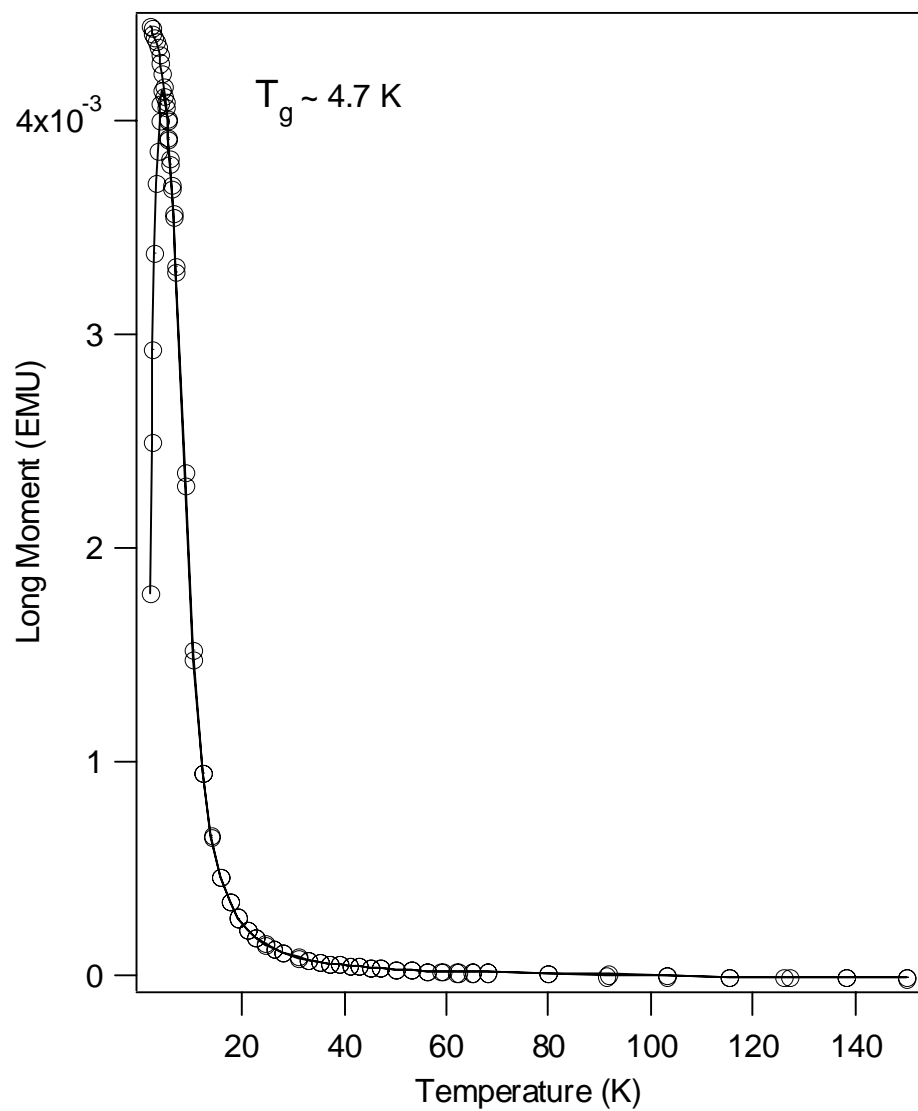


**Figure 3.31.** ZFC/FC data of Cd<sub>0.99</sub>Co<sub>0.01</sub>Se.

is attributed to the cobalt in the lattice. The CdSe LO vibrational mode shifts linearly as a function of doping concentration which also correlates with the pXRD data indicating a hardening of the lattice with increased doping concentration. The hardening of the LO phonon along with the observance of the LVM at  $\sim 275 \text{ cm}^{-1}$  suggests that changes in el-ph coupling may arise in these materials with increasing  $\text{Co}^{2+}$  concentration. The oxidation of the cobalt is confirmed to be +2 in CdSe by XANES measurements. A surprising increase in  $J_{\text{NN}}$  by an order in magnitude in QD compared to the bulk is observed. This is believed to be due to greater overlap between d-orbitals of  $\text{Co}^{2+}$  in QDs with that of the CdSe valence band minimum. We have also shown that doping of CdSe is achievable using a coordination compound ( $\text{TMA}_2[\text{Co}(\text{SPh})_4]$ ) which yield  $T_g$  values in the SQUID measurements that are higher than that using the  $\text{TMA}_2[\text{Co}_4(\text{SPh})_{10}]$  precursor.

### 3.6 References:

- (1) Dolling, G.; Holden, T. M.; Sears, V. F.; Furdyna, J. K.; Girit, W. *J Appl Phys* **1982**, *53*, 7644-7648.
- (2) Ansaldo, E. J.; Noakes, D. R.; Keitel, R.; Kreitzman, S. R.; Brewer, J. H.; Furdyna, J. K. *Phys Lett A* **1987**, *120*, 483-485.
- (3) Giebultowicz, T. M.; Klosowski, P.; Rhyne, J. J.; Udovic, T. J.; Furdyna, J. K.; Girit, W. *Phys Rev B* **1990**, *41*, 504-513.
- (4) Dobrowolska, M.; Luo, H.; Furdyna, J. K. *Acta Phys Pol A* **1995**, *87*, 95-106.
- (5) Furdyna, J. K. *J Appl Phys* **1988**, *64*, R29-R64.
- (6) Norris, D. J.; Yao, N.; Charnock, F. T.; Kennedy, T. A. *Nano Lett* **2001**, *1*, 3-7.
- (7) Akai, H. *Phys Rev Lett* **1998**, *81*, 3002-3005.
- (8) Kossacki, P.; Kudelski, A.; Gaj, J. A.; Cibert, J.; Tatarenko, S.; Ferrand, D.; Wasiela, A.; Deveaud, B.; Dietl, T. *Physica E* **2002**, *12*, 344-350.
- (9) Dietl, T.; Sawicki, M.; Khoi, L. v.; Jaroszynski, J.; Kossacki, P.; Cibert, J.; Ferrand, D.; Tatarenko, S.; Wasiela, A. *Phys Status Solidi B* **2002**, *229*, 665-672.
- (10) Matsukura, F.; Ohno, H.; Shen, A.; Sugawara, Y. *Phys Rev B* **1998**, *57*, R2037-R2040.

- (11) Lewicki, A.; Schindler, A. I.; Miotkowski, I.; Crooker, B. C.; Furdyna, J. K. *Phys Rev B* **1991**, *43*, 5713-5718.
- (12) Shand, P. M.; Lewicki, A.; Crooker, B. C.; Giriat, W.; Furdyna, J. K. *J Appl Phys* **1990**, *67*, 5246-5248.
- (13) Sawicki, M.; Furdyna, J. K.; Luo, H. *Acta Phys Pol A* **1996**, *90*, 923-926.
- (14) Nagata, S.; Galazka, R. R.; Mullin, D. P.; Akbarzadeh, H.; Khattak, G. D.; Furdyna, J. K.; Keesom, P. H. *Phys Rev B* **1980**, *22*, 3331-3343.
- (15) Low, W.; Weger, M. *Phys Rev* **1960**, *118*, 1119-1130.
- (16) Weakliem, H. A. *J Chem Phys* **1962**, *36*, 2117-&.
- (17) Dance, I. G.; Choy, A.; Scudder, M. L. *J Am Chem Soc* **1984**, *106*, 6285-6295.
- (18) Cumberland, S. L.; Hanif, K. M.; Javier, A.; Khitrov, G. A.; Strouse, G. F.; Woessner, S. M.; Yun, C. S. *Chem Mater* **2002**, *14*, 1576-1584.
- (19) Radovanovic, P. V.; Gamelin, D. R. *J Am Chem Soc* **2001**, *123*, 12207-12214.
- (20) Jun, Y. W.; Jung, Y. Y.; Cheon, J. *J Am Chem Soc* **2002**, *124*, 615-619.
- (21) Radovanovic, P. V.; Norberg, N. S.; McNally, K. E.; Gamelin, D. R. *J Am Chem Soc* **2002**, *124*, 15192-15193.

- (22) Twardowski, A.; Swagten, H. J. M.; Dejonge, W. J. M. *Cobalt-based II-VI semimagnetic semiconductors*; World Scientific: Singapore, 1993.
- (23) Swagten, H. J. M.; Twardowski, A.; Dejonge, W. J. M.; Demianiuk, M. *Phys Rev B* **1989**, *39*, 2568-2577.
- (24) Mikulec, F. V.; Kuno, M.; Bennati, M.; Hall, D. A.; Griffin, R. G.; Bawendi, M. G. *J Am Chem Soc* **2000**, *122*, 2532-2540.
- (25) Ladizhansky, V.; Vega, S. *J Phys Chem B* **2000**, *104*, 5237-5241.
- (26) Afify, H. H.; El Zawawi, I. K.; Battisha, I. K. *J Mater Sci-Mater El* **1999**, *10*, 497-502.
- (27) Vegard, L.; Schjelderup, H. *Phys. Z.* **1917**, *18*, 93-96.
- (28) Shiang, J. J.; Risbud, S. H.; Alivisatos, A. P. *J Chem Phys* **1993**, *98*, 8432-8442.
- (29) Norman, T. J.; Magana, D.; Wilson, T.; Burns, C.; Zhang, J. Z.; Cao, D.; Bridges, F. *J Phys Chem B* **2003**, *107*, 6309-6317.
- (30) Lucovsky, G.; Brodsky, M. H.; Burstein, E. *Phys. Rev. B* **1970**, *2*, 3295-3302.
- (31) Mak, C. J.; Bak, J.; Sooryakumar, R.; Steiner, M. M.; Jonker, B. T. *J Appl Phys* **1994**, *75*, 5719-5724.
- (32) Pages, O.; Ajjoun, M.; Laurenti, J. P.; Bormann, D.; Chauvet, C.; Tournie, E.; Faurie, J. P. *Appl Phys Lett* **2000**, *77*, 519-521.

- (33) Chang, I. F.; Mitra, S. S. *Phys Rev* **1968**, *172*, 924-&.
- (34) Sievers, A. J.; Takeno, S. *Phys Rev Lett* **1988**, *61*, 970-973.
- (35) Eisenber.P; Adlerste.Mg *Phys Rev B* **1970**, *1*, 1787-&.
- (36) Swanson, B. I.; Brozik, J. A.; Love, S. P.; Strouse, G. F.; Shreve, A. P.; Bishop, A. R.; Wang, W. Z.; Salkola, M. I. *Phys Rev Lett* **1999**, *82*, 3288-3291.
- (37) Hehlen, M. P.; Kuditcher, A.; Rand, S. C.; Tischler, M. A. *J Chem Phys* **1997**, *107*, 4886-4892.
- (38) Nakamoto, K. *Infrared and Raman spectra of inorganic and coordination compounds*; 5th ed.; Wiley: New York, 1997.
- (39) Meulenberg, R. W.; Strouse, G. F. *Phys Rev B* **2002**, *66*, -.
- (40) Mayur, A. J.; Sciacca, M. D.; Kim, H. J.; Miotkowski, I.; Ramdas, A. K.; Rodriguez, S. *Phys Rev B* **1996**, *53*, 12884-12888.
- (41) Thompson, A.; Atwood, D.; Gullikson, E.; Howells, M.; Kim, K. W.; Kirz, J.; Kortright, J.; Winick, H.; Lindau, I.; Pianetta, P.; Robinson, A.; Scofield, J.; Underwood, J.; Vaughan, D.; Williams, G. *X-ray Data Booklet* Berkeley, 2001.
- (42) Bunker, B. A.; Pong, W. F.; Debska, V.; Yoder-Short, D. R.; Furdyna, J. K.; Aggarwal, R. L., Furdyna, J. K., von Molna, S., Eds.; Materials Research Society: Pittsburgh, 1987; Vol. 89.
- (43) Bunker, B. A. *J Vac Sci Technol A* **1987**, *5*, 3003-3008.

- (44) Balzarotti, A.; Czyzyk, M.; Kisiel, A.; Motta, N.; Podgorny, M.; Zimnalstarnawska, M. *Phys Rev B* **1984**, *30*, 2295-2298.
- (45) Shand, P. M.; Lewicki, A.; Miotkowski, I.; Crooker, B. C.; Furdyna, J. K. *Phys Rev B* **1991**, *44*, 6152-6157.
- (46) Mydosh, J. A. *Spin Glasses: An Experimental Introduction*; Taylor & Francis: Washington D.C., 1993.
- (47) Feltin, N.; Levy, L.; Ingert, D.; Pileni, M. P. *Adv Mater* **1999**, *11*, 398-402.
- (48) Williamson, A. J.; Zunger, A. *Phys Rev B* **2000**, *61*, 1978-1991.
- (49) The difference between our calculated coupling term (-31.1 eV) and the experimental coupling term (-1.87 eV) may come from the use of  $E_v = 0$ , from  $V_{pd}$  changing with dopant ion, or from  $U_{eff}$  not reflecting the true values of the dopant ions in the nanocrystal. Although the calculated values may not be rigorously correct, the observed trends from the calculations, however are important.
- (50) Li, M. Z.; Zou, L. J.; Zheng, Q. Q. *J. Appl. Phys.* **1998**, *83*, 6596-6598.
- (51) Srdanov, V. I.; Stucky, G. D.; Lippmaa, E.; Englehardt, G. *Phys. Rev. Lett.* **1998**, *80*, 2449-2452.
- (52) Rushbrooke, G. S.; Baker, G. A.; Wood, P. J. *Heisenberg Model*; Academic: London, 1974; Vol. 3.

(53) Dance, I. G. *J Am Chem Soc* **1979**, *101*, 6264-6273.

## **Chapter 4. Synthesis and Characterization of Cd<sub>1-x</sub>Cu<sub>x</sub>Se Quantum Dots and Quantum Rods**

Portions of this chapter have been submitted to be published in the proceeding of the MRS. Hanif, K.M., Strouse, G.F. *Synthesis and Characterization of Cd<sub>1-x</sub>Cu<sub>x</sub>Se Quantum Dots*. Vol. 724, (2004)

## 4.1 INTRODUCTION

Solar cells are rarely made of nanoscale inorganic compounds due to the high cost of synthesizing inorganic compounds as compared to the more traditional amorphous Si based solar cells. Organic polymers have been suggested as alternatives to Si, however the drawback to using organic polymers is that efficiencies of only 2.5% have been achieved. On the other hand nanoscale inorganic solar cells can easily achieve efficiencies of ~ 15% with a maximum of ~ 30% in GaInP/GaAs based systems.<sup>1</sup> CdS and CdSe are known to be an excellent photoconductive material because its absorption covers the whole visible spectrum. Unfortunately, it is not useful in photovoltaic applications due to its low carrier concentration. In order for CdSe to be used as an absorber layer for solar cell applications it must be p-doped.

In a quest to develop alternatives to Si based photovoltaics, limited work has been carried out on inducing p-type carriers in bulk II-VI semiconductors by introduction of Cu(I). Cu(I) doping leads to p-doping of the lattice making these materials of interest for solar cell applications.<sup>2</sup> The observation of p-type carriers in bulk lattices has led researchers to speculate that Cu(I) doping in quantum dot alloys may allow the optical bandgap and carrier concentrations to be systematically controlled.<sup>3</sup> Developing methods to introduce guest ions into nanoscale semiconductor host lattices to form nano-alloys has attracted considerable attention due to the potential to control the carrier concentrations

and physical properties in these materials.<sup>4-7</sup> Although CuSe, Cu<sub>2</sub>Se and CuInSe<sub>2</sub> has been prepared at the nanoscale, a robust methodology for controlled inclusion of Cu(I) into II-VI semiconductor quantum dots has not yet been investigated.<sup>8</sup>

Increasing carrier concentrations by doping with a guest ion has proved important for more than just photovoltaic applications.<sup>2,9-11</sup> It is believed that a major contributor to the ferromagnetic behavior observed in diluted magnetic semiconductors is traceable to p-doping.<sup>9,10</sup> Co-doping of Cu along with Fe in ZnO has been used to increase the carrier concentration of the material. The effect of co-doping with Cu induces ferromagnetism in Fe:ZnO.<sup>2</sup> The reason that Cu is ideal for co-doping along with another transition metal is due to the high diffusivity of copper within semiconductors.<sup>12,13</sup>

Until recently, the only synthetic methods for formation of nanoalloys that were capable of achieving high doping levels were low temperature methods.<sup>14</sup> The low temperature reaction led to concern over guest ion segregation and lattice crystallinity problems limiting the usefulness of these materials. Only within the past few years has successful doping of semiconductor quantum dots with guest ions on substitutional sites within the nanoparticle core been accomplished using high temperature techniques.<sup>7,15-21</sup> High temperature synthetic techniques are favored over room temperature methods because they tend to yield materials that are more crystalline and that

have less defects, such as vacancies and glide plane defects. Although the materials are of high quality, to date studies have shown that it has been very difficult to reliably dope the core of nanoparticles with impurities.<sup>21</sup> In most cases only one or two ions were doped in the core of each nanoparticles, which equates to a core doping level of approximately <0.2%, with the bulk of the guest ion isolating on the QD surface or near the QD surface.<sup>21</sup> Due to the self-annealing effects occurring at elevated temperatures, one of the most important issues that exist in nanoalloys is the location of the impurity. The impurity can exist either on a lattice point in the core, at interstitial sites, or localized at the surface of the quantum dot. It is critical to prove not only the level of doping but also the site of doping and the lattice perturbation arising from the guest ion occupation of the host lattice. Elemental analysis on Cu(I) substitution into II-VI semiconductors has shown self compensation effects that occur by formation of group VI vacancies in the alloyed material.<sup>3,12,13</sup>

Here we report up to 20% core doping of Cu(I) into CdSe. In this chapter the effect of doping Cu(I) into CdSe will be discussed. In these materials the lattice parameters shift linearly as a function of doping. This provides evidence for statistical doping of the core with Cu(I) ions. XPS and XANES analysis of the nano-alloy samples provide evidence for Cu existing as Cu(I) within the lattice, and only trace amounts of Cu(II). In addition qualitative analysis of the ratio of Cd + Cu to Se in these alloys indicate an increasing degree of Se

vacancies are created as a direct result of doping to compensate for charge imbalance effects arising from  $\text{Cu}^+$  substituting for  $\text{Cd}^{2+}$  inducing  $\text{Se}^{2-}$  vacancies.

## **4.2 EXPERIMENTAL DETAILS**

### **4.2.1.1 Materials.**

The  $(\text{Li}_4)[\text{Se}_4\text{Cd}_{10}(\text{SPh})_{16}]$  clusters were prepared according to literature methods and are described in detail in Chapter 2.  $\text{Cd}(\text{NO}_3)_2 \cdot 4\text{H}_2\text{O}$  (STREM),  $\text{Cu}(\text{NO}_3)_2 \cdot 2\frac{1}{2} \text{H}_2\text{O}$  (Fisher), selenium powder (~ 200 mesh, Aldrich), thiophenol (Aldrich), triethylamine (Fisher), Methanol (ACS Grade), Acetonitrile (HPLC Grade), hexadecylamine (90%, ACROS), pyridine (EM Science), and hexanes (Fisher) were used as supplied.

### **4.2.1.2 Synthesis of $[\text{Cu}_4(\text{SPh})_6] (\text{TMA})_2$ .**

$[\text{Cu}_4(\text{SPh})_6] (\text{TMA})_2$  was synthesized by adding  $\text{Cu}(\text{NO}_3)_2 \cdot \text{H}_2\text{O}$  (15.8 g, 68 mmols) dissolved in 70 ml MeOH to a room temperature solution of benzenethiol (20.0 g, 182 mmols) and triethylamine (18.5g, 182 mmols) in 40 mL MeOH. To this mixture, a solution of tetramethylammonium chloride (TMACl) (8.4g, 77 mmols) in 40mL MeOH was added to methasize the anionic cluster to a TMA salt. The resultant cluster was allowed to crystallize at  $0^\circ\text{C}$  producing a yellow solid. The solution was filtered, washed with cold MeOH and vacuum dried. The sample was characterized by ESI-MS and the parent ion

peak for  $[\text{Cu}_4(\text{SPh})_6]^{2-}$  containing four Cu(I) centers was observed at 454.7 m/z.

The ESI-MS of this cluster is shown in Chapter 2.

#### **4.2.1.3 Synthesis of $\text{Cd}_{1-x}\text{Cu}_x\text{Se}$ Quantum Dots.**

Synthesis of  $\text{Cd}_{1-x}\text{Cu}_x\text{Se}$  quantum dots was performed using a parallel plate methodology (Figure 4.1) developed by Jeff Gerbec, by adding ~1.200 g of  $(\text{Li}_4)[\text{Se}_4\text{Cd}_{10}(\text{SPh})_{16}]$  and various concentrations of  $(\text{TMA}_2)[\text{Cu}_4(\text{SPh})_6]$ , [0.100g, 0.200 g, 0.300 g, 0.400g, 0.500g, 0.600g, 0.700g, and 0.900g] in 9 reaction vials. The materials were placed under vacuum and to these flasks about 35mL of n-hexadecylamine (HDA) at ~100°C was added. Growth of the doped nanomaterials was accomplished by heating the cluster precursor solution to ~250°C at a rate of ~ 20°C/hour under  $\text{N}_2$ . Nanomaterial growth is followed by monitoring aliquots removed by syringes from the reaction vial using absorption spectroscopy. The shape and energy of the exciton was monitored to allow the growth conditions to be controlled to ensure that that the band edge absorption stays narrow. Growth of the doped quantum dots was halted when the nanoalloy size approached 4 nm corresponding to a band edge absorbance of ~ 550 nm.

The quantum dots were isolated from the HDA and recapped with pyridine according to literature methods.<sup>17</sup> This was performed by addition ~ 7



**Figure 4.1.** Picture of the setup for a parallel plate reaction. 9 vials are placed inside an aluminum block with holes drilled out to fit the vials snugly. The aluminum block is then placed onto a hot plate.

mL of pyridine to ~ 50 mg of the QD sample. The solution was heated for ~30 minutes in a hot water bath at ~ 80°C. Afterwards the quantum dots were precipitated by addition of hexanes. This step was repeated three times to ensure that all the free Cu ions have been removed from the surface of the QD. Similar stripping strategies have been demonstrated to be effective in removing adventitious guest ions from the surface of the nano-alloy.<sup>16</sup>

#### **4.2.1.4 Synthesis of Cd<sub>1-x</sub>Cu<sub>x</sub>Se Quantum Nanorods.**

Nano-rod alloys can be prepared by a similar reaction condition to the dots. 1.8 g of (TMA)[Se<sub>4</sub>Cd<sub>10</sub>(SPh)<sub>16</sub>] was placed in a flask containing ~ 50g of hexadecylamine. The solution was heated to ~ 120°C on a parallel plate reactor, and three solutions of octylamine (5 mL) containing 300 mg, 600 mg, and 900mg of (TMA)<sub>2</sub>[Cu<sub>4</sub>(SPh)<sub>6</sub>] were added to the reaction vials containing hexadecylamine. The (TMA)<sub>2</sub>[Cu<sub>4</sub>(SPh)<sub>6</sub>] requires sonication for dissolution in octylamine. The reaction temperature of the vials was raised to 250°C over 3 hours. The reactions were stopped when their band edge absorbance was 590nm, roughly corresponding to a ~5 nm particle.

Isolation of these particles were performed by cooling the reaction mixture to ~ 80°C, adding it to methanol (100 mL), and collection of the precipitate by centrifugation. The centrifuge plug was resuspended in MeOH, and centrifuged again. A final cleanup was performed by dissolution of the plug

in chloroform, addition of MeOH to incipient precipitation, and centrifugation to isolate the nanoparticles as plug. The solid was dried under vacuum.

## **4.2.2 Materials Characterization**

**4.2.2.1 Transmission electron microscopy (TEM).** Transmission electron microscope measurements were performed on a JEOL 2010 High Resolution microscope. Samples were dissolved in toluene and deposited on Nickel holey carbon grids. The TEM has a resolution of 2 Å at 200 kV. TEM images were used to determine the size and size distributions of the particles.

**4.2.2.2 Powder X-ray diffraction (PXRD)** Powder x-ray diffraction measurements were performed on a Scintag X2 diffractometer with a Cu K $\alpha$  source ( $\lambda = 1.5418$  Å). Si powder was used as an internal standard ( $\sim 25$  mg QD,  $\sim 5$  mg Si). The sharp peaks in the p-XRD at 1.638, 1.920 and 3.136 Å are due to the Si. Peaks that are due to excess hexadecylamine (HDA) not removed by the washings are identified by (\*). Not all the spectra show peaks due to HAD, and is dependant on how well the materials has been cleaned during the isolation process.

**4.2.2.3 Ultraviolet-Visible Absorption (UV-Vis Absorption).** UV-Visible absorption measurements were performed on a CARY 50 Bio UV-VIS spectrophotometer. Absorption of the quantum dots was performed during growth to monitor the reaction. Small aliquots of the reaction mixture were

diluted in toluene. The resolution of the UV-Vis is 2 nm. Measurements were performed at room temperature.

**4.2.2.4 Photoluminescence Spectroscopy.** Photoluminescence measurements were performed on a CARY Eclipse Fluorescence Spectrophotometer using an excitation energy of 490 nm. The photoluminescence experiments were performed on samples of  $\text{Cd}_{1-x}\text{Cu}_x\text{Se}$  dissolved in toluene.

**4.2.2.5 Inductively-Coupled Plasma Atomic Emission Spectroscopy (ICP-AE)** Elemental analysis was performed using a Thermo-Jarrell Ash IRIS ICP-AE Spectrophotometer. All samples (~ 10 mg) were dissolved in a hot solution of fuming  $\text{HNO}_3$  (2mL). Once the solution turned clear water (~ 50mL) was added to dilute the solution. The Cd and Cu standards used in these measurements were purchased from High Purity Standards. The Cd concentration was determined using the average concentration measured at 214.438 and 226.5 nm atomic emission lines. The Cu concentration was determined using the average value obtained at 223.008, 224.700, and 327.396 nm atomic emission lines of Cu. An average of three runs were taken for each element with an error of < 5%.

**4.2.2.6 X-ray Photoelectron Spectroscopy (XPS).** X-ray photoelectron spectroscopy measurements were performed on a Kratos Axis Ultra X-ray photoelectron Spectrometer. Samples were dissolved in Hexane and drop cast on glass slides. Survey scans were performed using a pass energy of 180 keV and a

step size of 0.5 eV. Regional scans were performed using a pass energy of 20 keV and a step size of 0.05 eV. The Al-K $\alpha$  source was used for these measurements and calibration of the peak XPS data was accomplished by referencing the C 1s peak. All measurements were performed below  $1 \times 10^{-8}$  Torr. A flood gun was used to minimize charging effects.

**4.2.2.7 X-ray Absorption Near Edge Spectroscopy (XANES).** The XANES experiments were performed at the Advanced Light Source at Lawrence Berkeley National Labs. Soft X-rays were used to eject electron from the L-shell of Co. Approximately 10 mg of samples was pressed onto indium foil with dimensions of 3 mm x 3 mm.

## **4.3 RESULTS and DISCUSSION**

### **Cd<sub>1-x</sub>Cu<sub>x</sub>Se Quantum Dots**

**4.3.1 Size Analysis.** The quantum dots have a band edge absorption that ranges from ~540 – 560 nm consistent with the absorption of 3.8-4.2 nm particles, as can be seen in figure 4.2. TEM images corroborate that these particles are ~ 4 +/- 0.2 nm in size and have small size distributions (<7%) based on a size histogram of a single TEM grid image. Lattice fringes can be observed in the TEM images of these materials indicating that the materials are crystalline (Fig. 4.3 & 4.4). The stacking of the unit cells in the TEM images shows an ABCAB stacking that is consistent with that of a cubic structure, which is confirmed by

the pXRD pattern (see below). Stacking faults are observed in the TEM images of some of the quantum dots. The TEM images show that the vast majority of quantum dots have no stacking faults or glide plane defects.

The band edge absorption was narrow ( $\sim 35\text{nm}$ ), consistent with materials that exhibit narrow size distributions. All of the Cu doped quantum dots exhibited practically no band edge luminescence, as can be seen in figure 4.5. A broad defect emission was observed in the red for all the samples. We attribute the lack of an exciton emission to selenium vacancy formation in the alloy lattice arising from charge compensation due to Cu(I) inclusion on a Cd(II) lattice site in the alloy, as discussed below. The Se vacancies would create trap sites for electrons thereby hindering the recombination of electrons with holes in the quantum dots, resulting in the observed loss of photoluminescence from these samples. The low energy defect observed in the PL data has been attributed to trap centers formed by Se vacancies in bulk Cu:CdSe materials. The optically induced trap centers are believed to generate a p-type lattice following photoexcitation, important for applications in solid state photovoltaic applications.

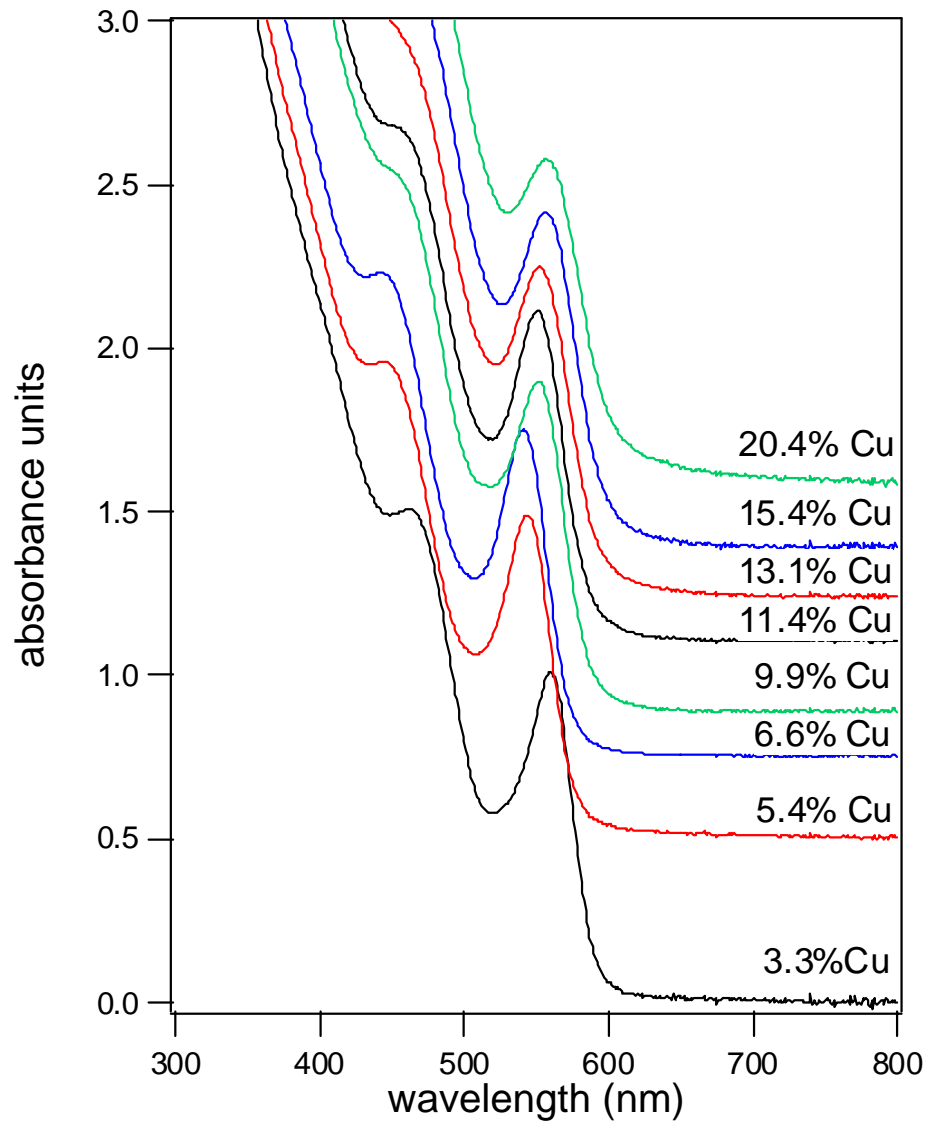


**Figure 4.2.** Absorption spectra of 8 different Cd<sub>1-x</sub>Cu<sub>x</sub>Se samples with the %Cu doping concentration indicated in the graph.

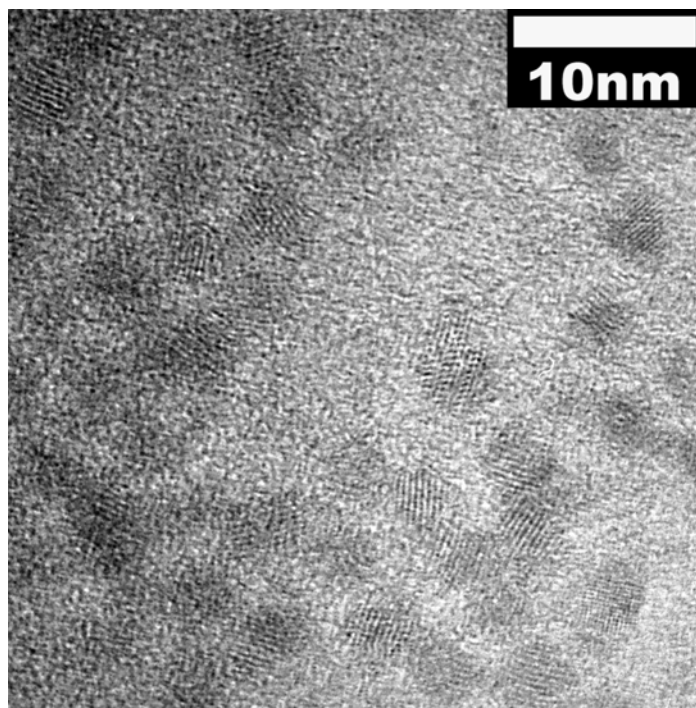


**Figure 4.3.** TEM image of Cd<sub>0.911</sub>Cu<sub>0.099</sub>Se.

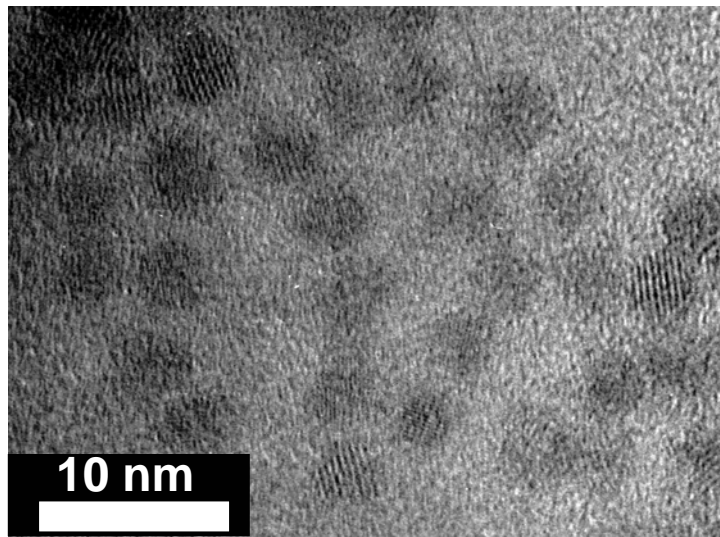


**Figure 4.4.** TEM image of Cd<sub>0.946</sub>Cu<sub>0.054</sub>Se.

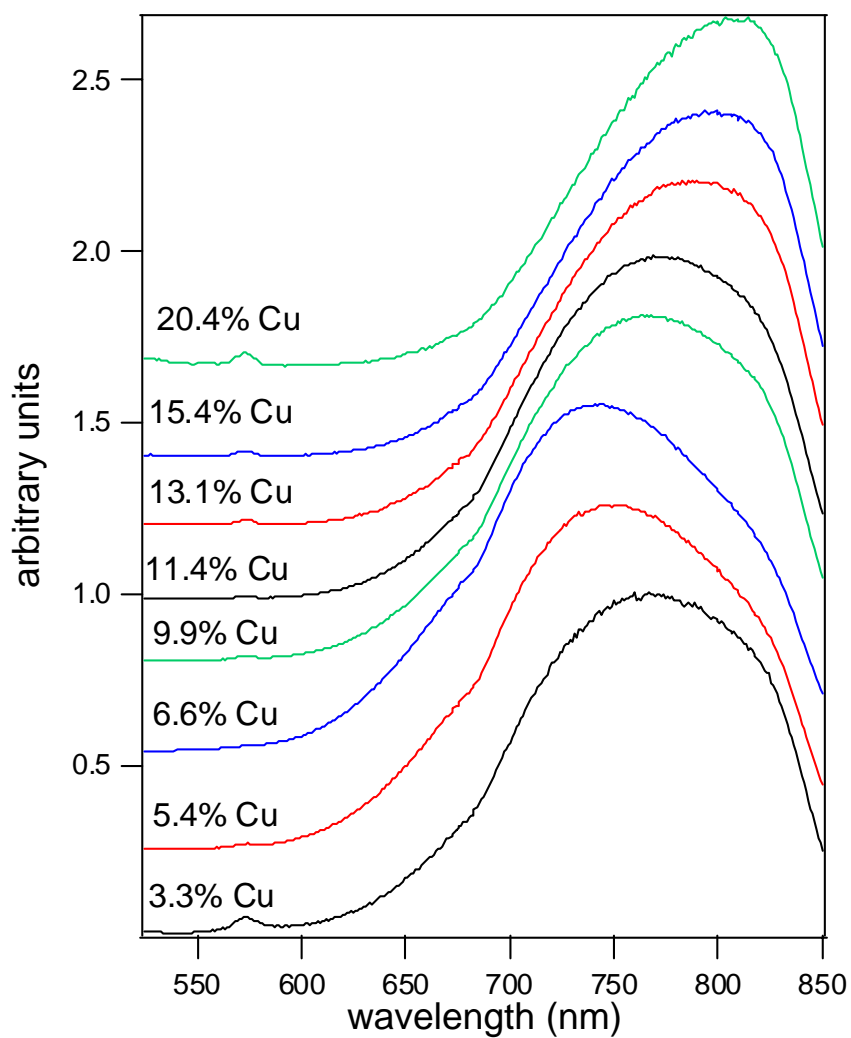


**Figure 4.5.** Photoluminescence spectra in toluene at RT of 8 different Cd<sub>1-x</sub>Cu<sub>x</sub>Se samples with the %Cu doping concentration indicated in the graph.

**4.3.2 Elemental Analysis of Nano-dot alloys by ICP-AE.** Elemental analysis of these materials was performed after the surface of the quantum dots had been stripped and recapped with pyridine to remove adventitious Cu ions from the surface of the nanodot alloy. This step ensures removal of any Cu that may be electrostatically attached to the surface of the particle or that may not have been removed during the isolation of the material from the hexadecylamine. Based on the ICP-AE measurements, doping levels as high as 20% were achieved for these samples using the single source precursor methodology. Elemental analysis prior and after recapping with pyridine revealed that there was essentially no difference in the amount of copper relative to cadmium in the samples (Table 1), confirming the effectiveness of the washing protocol for removal of surface bound Cu ions. The only samples that exhibited a change in copper concentration following stripping were the highest doped samples ( $x > 15\%$ ). Figure 4.6 shows the change in Cu doping concentration from quantum dots isolated from the mixture and after the QDs have been pyridine capped. The change in Cu concentration arising from removal of adventitious Cu ions is further verified by the observation of HDA signals in the pXRD data set.

%Cu doping in HDA capped QDs		%Cu doping after pyridine stripping	
3.3	±0.17	3.3	±0.17
5.4	±0.27	5.5	±0.27
6.6	±0.33	6.5	±0.33
9.9	±0.50	9.9	±0.50
11.3	±0.57	11.4	±0.57
13.2	±0.66	13.1	±0.66
15.2	±0.76	15.4	±0.76
22.3	±1.12	20.4	±1.02

**Table 1.** List of the %Cu doping determined by ICP-AE from samples out of batch and pyridine stripped (x2) samples.

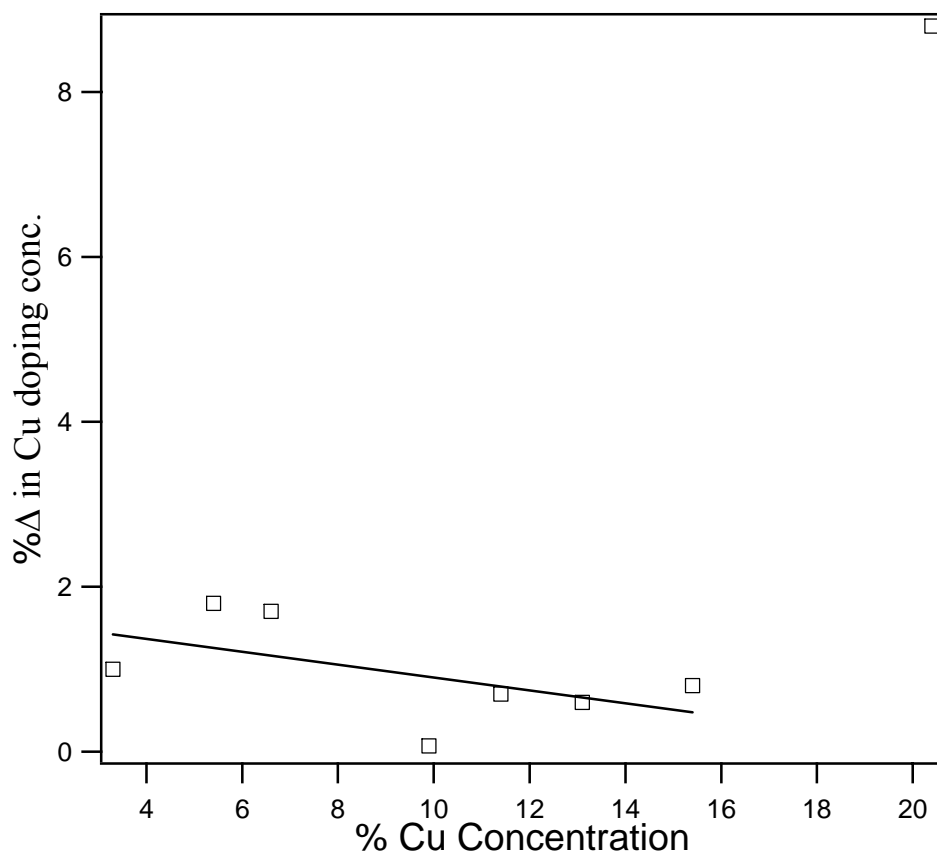


**Figure 4.6.** % change in Cu doping concentration between out of batch samples and pyridine stripped (x2) samples.

The samples synthesized in this study had doping levels of 3.3%, 5.4%, 6.6%, 9.9%, 11.4%, 13.1%, 15.4% 20.3% and 20.4% Cu. The doping percent can be correlated with the number of guest ions incorporated into the nano-dot. Assuming a spherical model for the 4 nm quantum dot, the material has approximately 1177 atoms of which 577 would be Cd atoms. Therefore the quantum dots would on average have 19 (3.3%), 31(5.4%), 38(6.6%) 57(9.9%), 66(11.4%), 89(13.1%), 117(15.4%), and 118(20.3-20.4%) Cu atoms randomly substituted between the core and surface within each dot.

It is not surprising that such high levels of core doping were accomplished in this paper using the  $[\text{Cd}_{10}\text{Se}_4(\text{SPh})_{16}]^{4-}$  single source precursor. Metal-thiolate clusters with adamantane like structures are known to readily exchange metal ions under solvothermal conditions. Holm, et al showed that clusters with the structure  $[\text{M}_4(\text{SPh})_{10}]^{2-}$  readily exchanged the following metal ions (Fe(II), Co(II), Zn(II), Cd(II)) to give the following structure  $[\text{M}_4\text{-nM}'_n(\text{SPh})_{10}]^{2-}$  when mixed together in  $\text{CD}_3\text{CN}$ .<sup>22</sup> Using ESI-MS techniques, Bowmaker demonstrated metal ion exchange occurs rapidly for Zn displacement of all the Cd ions in  $[\text{Cd}_{10}\text{Se}_4(\text{SPh})_{16}]^{4-}$ .<sup>23</sup> Recent ESI-MS measurements in our group on Co exchange into  $\text{Cd}_{10}$  have shown rapid (<20 min) exchange of Co for core Cd ions arise at room temperature in  $\text{CH}_3\text{CN}$ .

**4.3.3 Oxidation State of Cu in Cu:CdSe.** In the nanoalloy, the Cu ion can be incorporated as either Cu(I), Cu(II) or as a mixed valence species. Identification of the Cu oxidation state is critical in determining the properties of the alloy. XANES is a technique that is routinely applied for the determination of the oxidation state of atoms within solid-state compounds. Oxidation state changes in elements directly affect the binding energies of its core electrons. Figure 4.7 shows XANES data for a series of  $\text{Cd}_{1-x}\text{Cu}_x\text{Se}$  quantum dots. The spectra of this series was compared to that of the precursor cluster  $\text{TMA}_2[\text{Cu}_4(\text{SPh})_6]$  in which the Cu exists as Cu(I), Cu(II)Se and Cu(I)I. As can be seen in figure 4.7 the spectra of the quantum dots closely resembles that of the Cu(I) standards. This provides strong evidence for the existence of Cu(I) within the quantum dots. However at lower binding energy, trace Cu(II) can be observed to the lattice. The observation of Cu(I) doping within the nanoalloy indicates that Se vacancies must be present to accommodate the charge imbalance created by the presence of the Cu(I) on a Cd(II) site.

To address the possibility of Se vacancies, XPS is a useful technique that can provide qualitative information on the magnitude of vacancy formation in the lattice. Regional scans similar to the one on Figure 4.8 can be used to determine the concentration of different elements in the alloy samples. Table 2 shows the ratios of (Cd+Cu):Se as a function of doping concentration. The Cd  $3d_{5/2}$ , Cu  $2p_{3/2}$  and Se

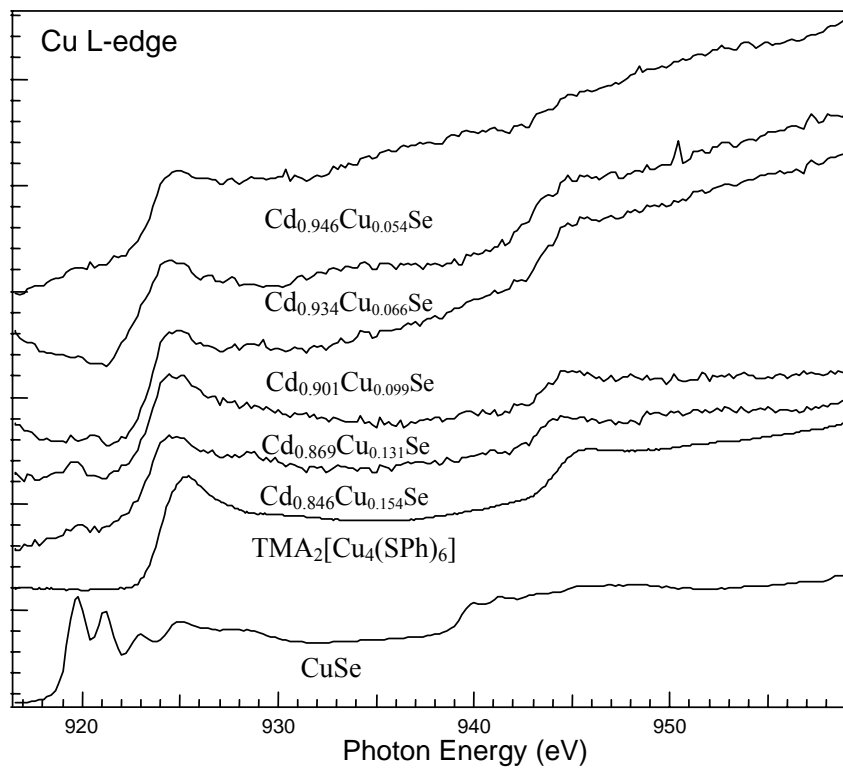


**Figure 4.7.** XANES spectra of 5 Cu:CdSe samples,  $\text{TMA}_2[\text{Cu}_4(\text{SPh})_6]$ , and CuSe.

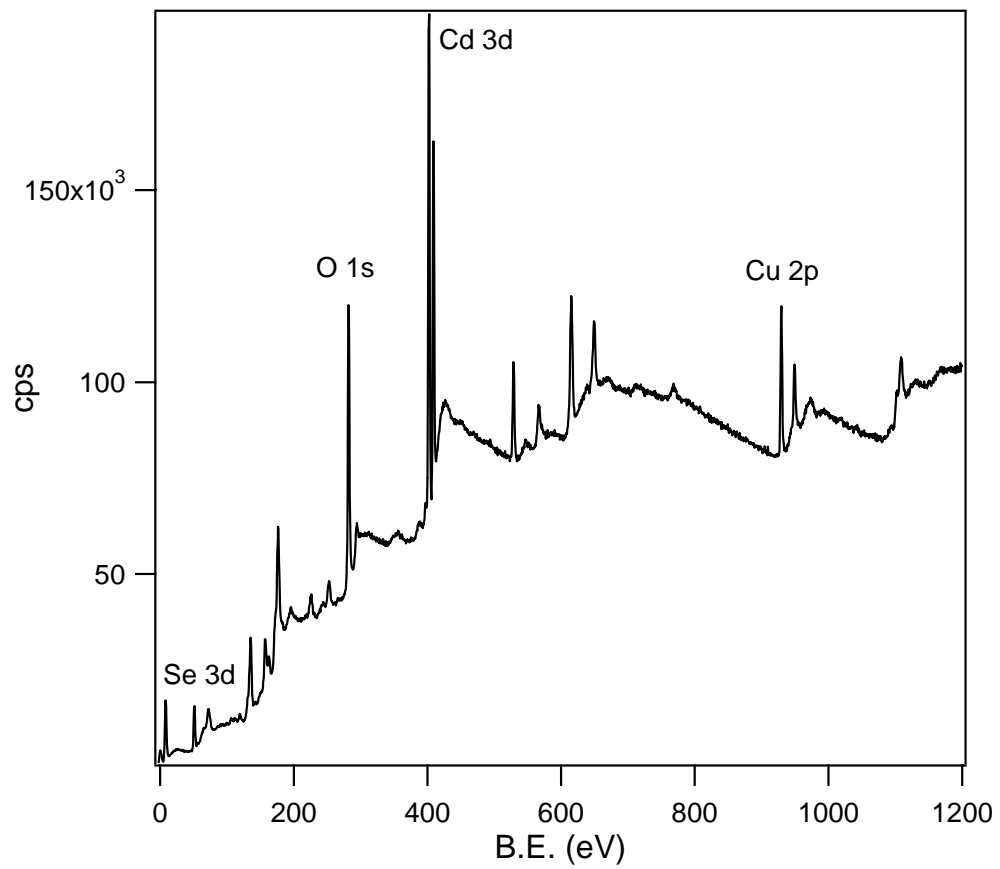


**Figure 4.8.** XPS survey scan of  $\text{Cd}_{0.967}\text{Cu}_{0.033}\text{Se}$ .

Sample	(Cd+Cu):Se Ratio
CdSe	1.35
Cd <sub>0.967</sub> Cu <sub>0.033</sub> Se	1.32
Cd <sub>0.945</sub> Cu <sub>0.055</sub> Se	1.49
Cd <sub>0.935</sub> Cu <sub>0.065</sub> Se	1.30
Cd <sub>0.901</sub> Cu <sub>0.099</sub> Se	1.34
Cd <sub>0.897</sub> Cu <sub>0.103</sub> Se	1.35
Cd <sub>0.868</sub> Cu <sub>0.132</sub> Se	1.50
Cd <sub>0.847</sub> Cu <sub>0.153</sub> Se	1.58
Cd <sub>0.777</sub> Cu <sub>0.223</sub> Se	1.89

**Table 2.** Values of (Cd+Cu):Se concentration for each of the Cu:CdSe samples.

$3d_{3/2}$  peaks were integrated and the appropriate sensitivity factors were used to determine the relative concentrations of the different elements. In the lower doped samples the ratio is very close to one.

The oxidation state assignment made using ZANES spectroscopy can be verified using XPS. A very common phenomenon in paramagnetic d- and f-transition metals is the observance of very intense shake-up peaks (satellite peaks) on the high binding energy side of the main photoelectron band in first row paramagnetic transition metals. Shake-up peaks are more intense for core electron ionizations than those of the valence electrons. Therefore, in the case of the Cu 2p photoelectron peak, the shake-up peaks can be as intense as the main photoelectron band. In elements such as Co(II) the difference between high spin and low spin Co(II) and Co(III) have been distinguished by observance of shake-up peaks and on the intensity of these peaks.<sup>24</sup> The lack of shake up peaks for the Cu  $2p_{3/2}$  and Cu  $2p_{1/2}$  lines confirm Cu(I) doping in these alloys (Fig. 4.9). This is consistent with the lack of shake-up peaks observed in the Cu cluster XPS data (Fig. 4.10).

In addition to the Cu oxidation state, a qualitative analysis of the Se concentration can be extracted from the XPS data. XPS analysis of concentration does possess a ~ 10% error in quantitative analysis, however the trend of Cu = Cd to Se in a series of alloy samples can provide indirect proof of Se loss with increasing Cu concentration. The data for the Cu:CdSe nanodot alloys shows a

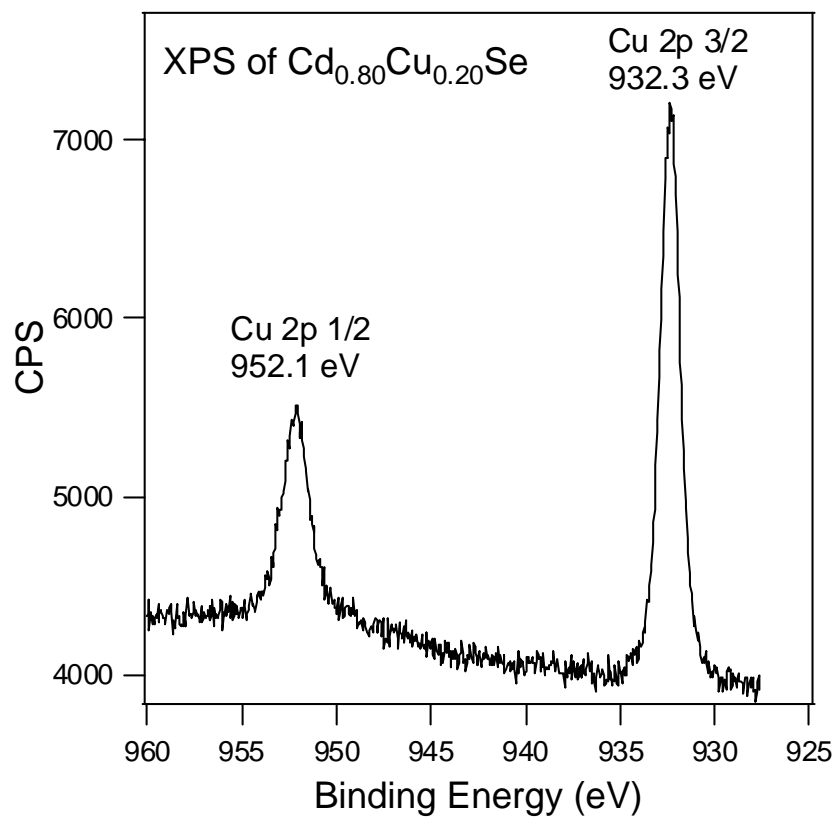


**Figure 4.9.** XPS regional scan of the Cu region for  $\text{Cd}_{0.796}\text{Cu}_{0.204}\text{Se}$ .

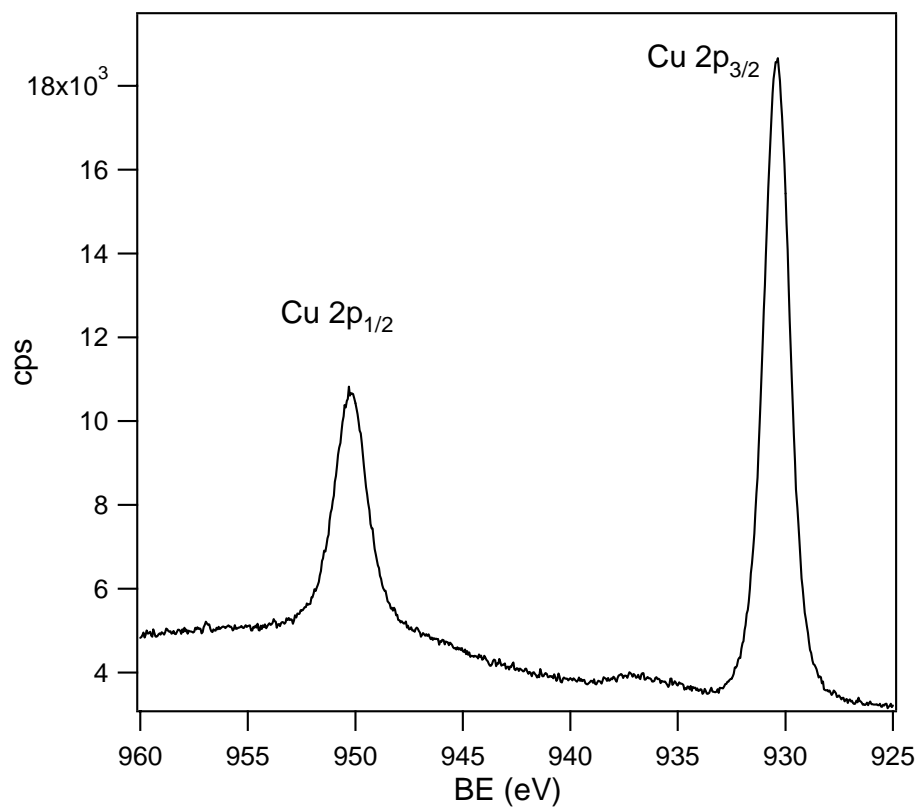


**Figure 4.10.** XPS Cu regional spectra of TMA<sub>2</sub>[Cu<sub>4</sub>(SPh)<sub>6</sub>].

definite decrease in Se concentration as the doping level increases in the QD samples verifying Se vacancy formation in the lattice to compensate the charge imbalance. The Se vacancies confirm the speculation that the lack of PL emission intensity arises from trap centers created within the lattice by Se vacancy formation. Selenium vacancies have been previously observed to form in bulk II-VI semiconductor when doping with Cu(I) consistent with these findings. A more quantitative analysis of Se would be better, however measurement of the Se concentration using analytical techniques such as ICP-AE and atomic absorption are not ideal due to the insensitivity of these methods towards the detection of selenium.

Another observation that has been made in these samples is the surprising lack of XPS signatures for  $\text{SeO}_2$  or  $\text{CdO}$  in the samples. In TOP/TOPO prepared CdSe quantum dots oxidation of the surface atoms was observed to occur within 24hrs of exposing the samples to air.<sup>25</sup> The alloy materials in this study had been isolated and stored in air for over a month, while the undoped CdSe quantum dot sample had been exposed to air for over a year prior to performing XPS measurements (Fig. 4.11 & 4.12). We believe the lack of oxidation in these materials is a result of thiophenol passivation on the nanomaterial surface grown by the single source precursor methodology. Based on recent NMR experiments in our laboratory, the thiophenol appears to occupy reactive vertex and edge sites which apparently limit the rate of oxidation in these samples.<sup>26</sup>

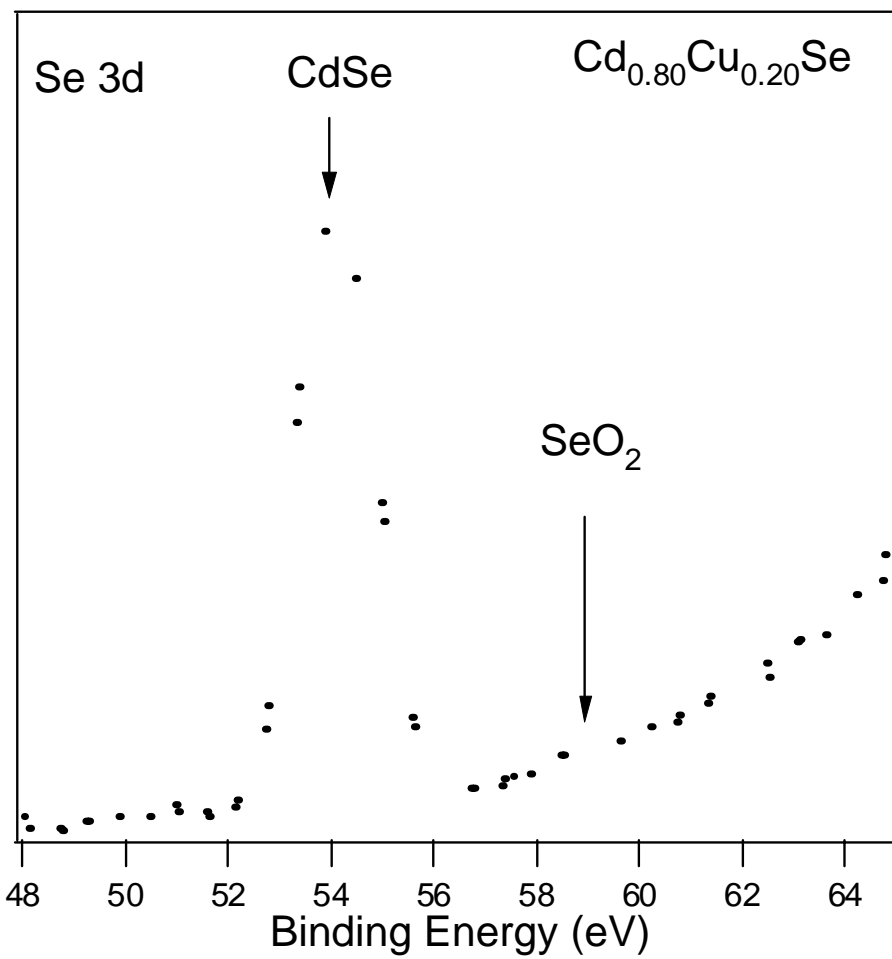


**Figure 4.11.** XPS of Se region for Cd<sub>0.80</sub>Cu<sub>0.20</sub>Se.

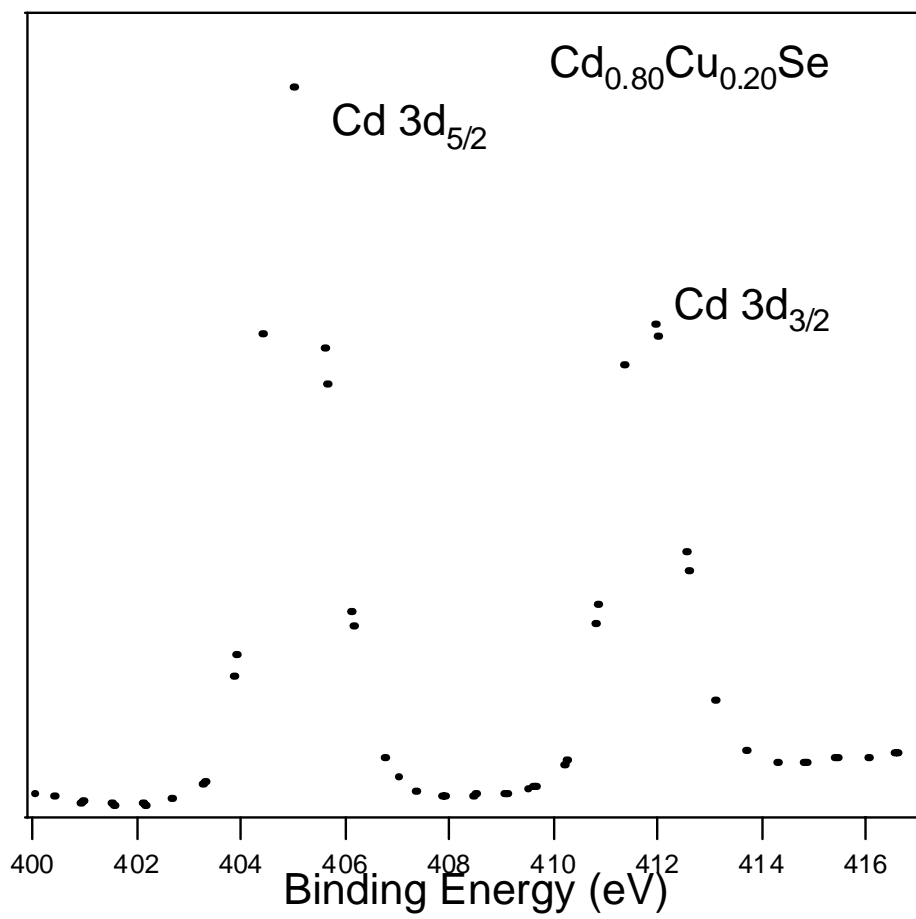


**Figure 4.12.** XPS spectra of Cd region for  $\text{Cd}_{0.80}\text{Cu}_{0.20}\text{Se}$ .

#### 4.3.4 X-ray Powder Diffraction (XRD):

As previously stated the location of the impurity is very important. The dopant can exist either in the core of the particle or on the surface. The ICP-AE measures the average Cu concentration and does not distinguish the site of occupation or whether it is random ions, phase segregation, or surface isolated. While ICP-AE cannot identify the nature of doping, p-XRD can be used to prove that the Cu ions exist randomly in the core of the CdSe quantum dots as substitutional lattice points using a Vegard law analysis of the lattice parameter shift with increased doping levels.

The powder diffraction of all nine of the  $\text{Cd}_{1-x}\text{Cu}_x\text{Se}$  nano-dot alloy samples exhibit three peaks that can be assigned to  $\langle 111 \rangle$ ,  $\langle 220 \rangle$  and  $\langle 311 \rangle$  reflections of the zinc blende structure. This is an uncommon lattice for CdSe quantum dots, which typically exhibit a wurtzite lattice. The presence of Cu(I) in the lattice creates enough of a driving force to form a zinc blende lattice, even at low doping levels. The peaks are broadened due to Scherrer broadening which result from the small size of the quantum dots. The p-XRD spectra in Figure 4.13 for these compounds exhibit a peaks shift to smaller d-spacing as the doping level is increased. This behavior is expected when the material core is doped with a smaller cation than the one it is replacing. Literature values of the tetrahedral covalent radii for both Cd and Cu are 1.48 and 1.38 Å respectively.<sup>27</sup> According to Vegard's law, the lattice spacing or unit cell parameters should

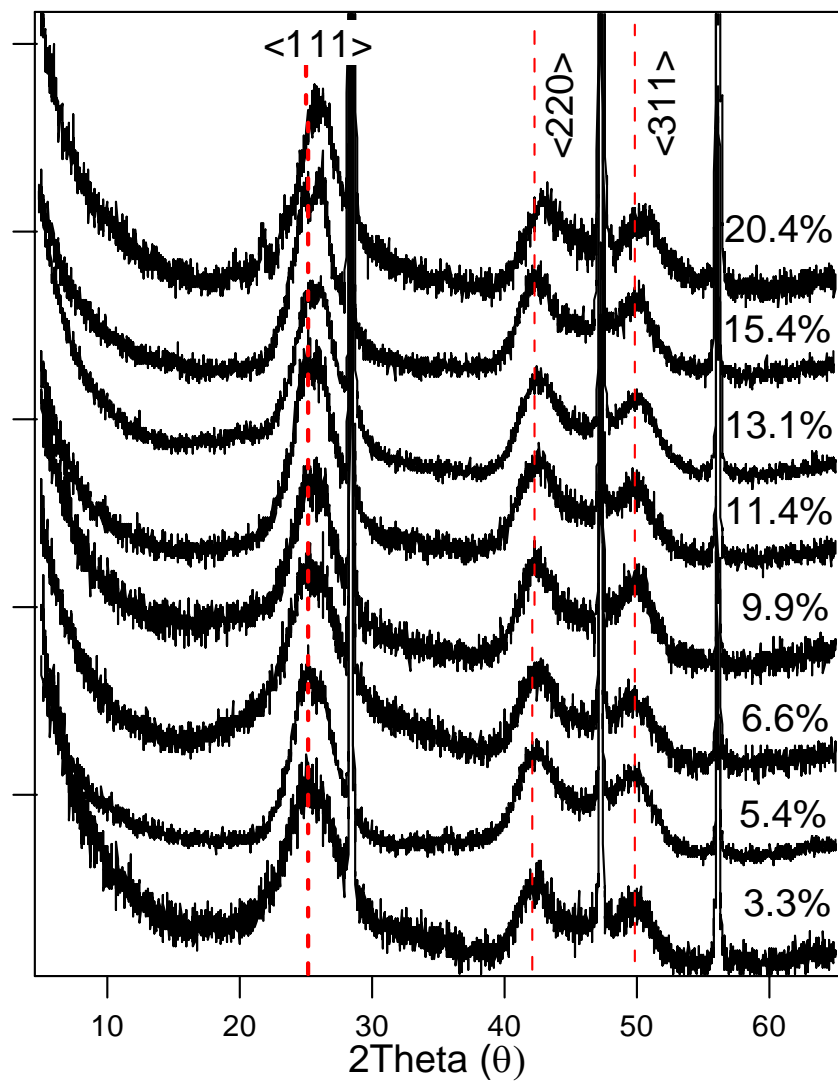


**Figure 4.13.** XRD spectra of 8 Cu:Cde samples. The sharp peaks are due to the Si standard, which was used as an internal standard.

shift linearly with doping concentration if the dopant is statistically distributed throughout the lattice.<sup>28</sup> Figure 4.14 shows a plot of the <111> reflection vs. %Cu doping. The shift in lattice spacing is linear with doping concentration in accordance to Vegard's law. The p-XRD data is consistent with increased levels of Cu<sup>+</sup> cations being incorporated within the lattice of the host material with increased amounts of dopant cluster being added to the reaction mixture.

#### **4.4 PART II: Cd<sub>1-x</sub>Cu<sub>x</sub>Se NanoRods**

In addition to nano-dots, nano-rod alloys can be prepared by the addition of octylamine to the reaction mixture. Several researchers have expressed the position that nanorods increase the optical cross-section of the materials, and if aligned can improve carrier injection into a backing electrode for a photovoltaic device.<sup>29</sup> The nano-rod alloys prepared by this method are uniform in width, but are not mono-disperse in length. They have a 7 nm width, as confirmed by TEM (figure 4.16) and absorption spectroscopy (figure 4.15). The average aspect ratio is ~ 1.7 for these materials.

The nano-rod alloys were recapped with pyridine three times to determine the Cu core doping levels. Elemental analysis using ICP-AE methods revealed that the doping levels of these dots were 1.1%, 4.2%, and 10.3%. Table 3 shows the concentration of Cu relative to Cd prior to and after the pyridine recapping

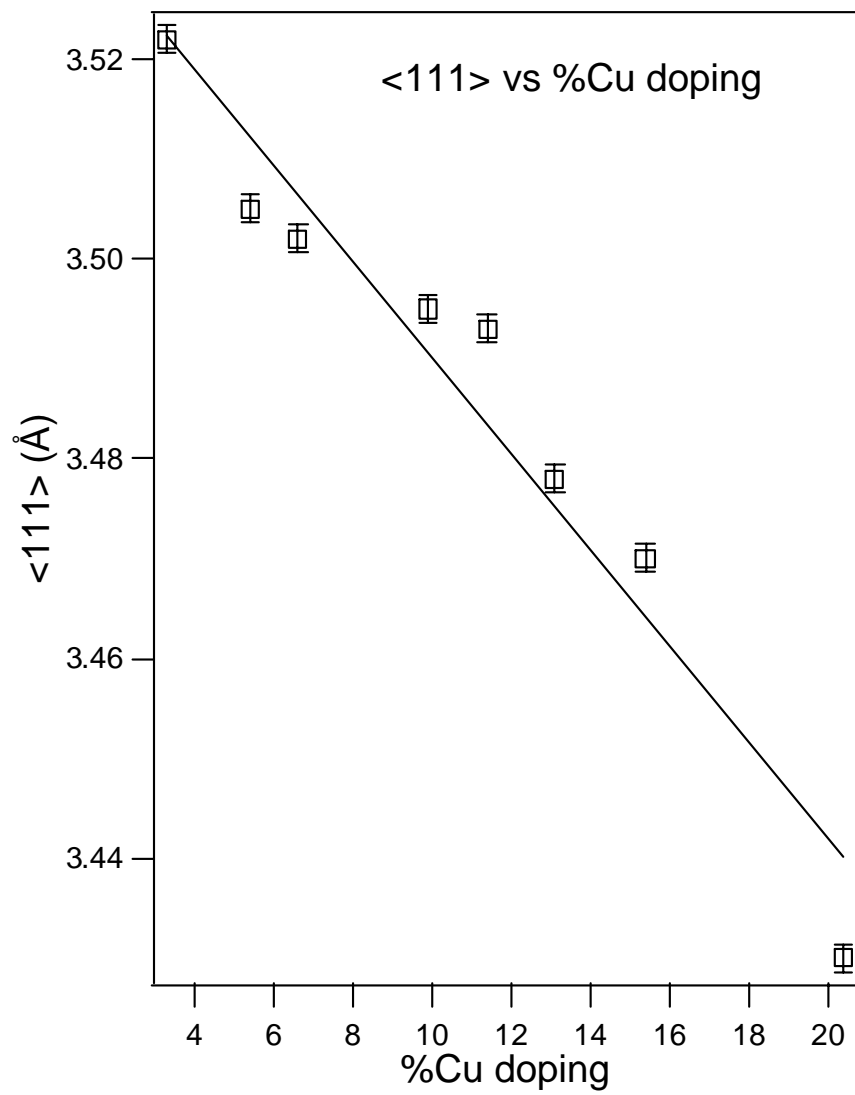
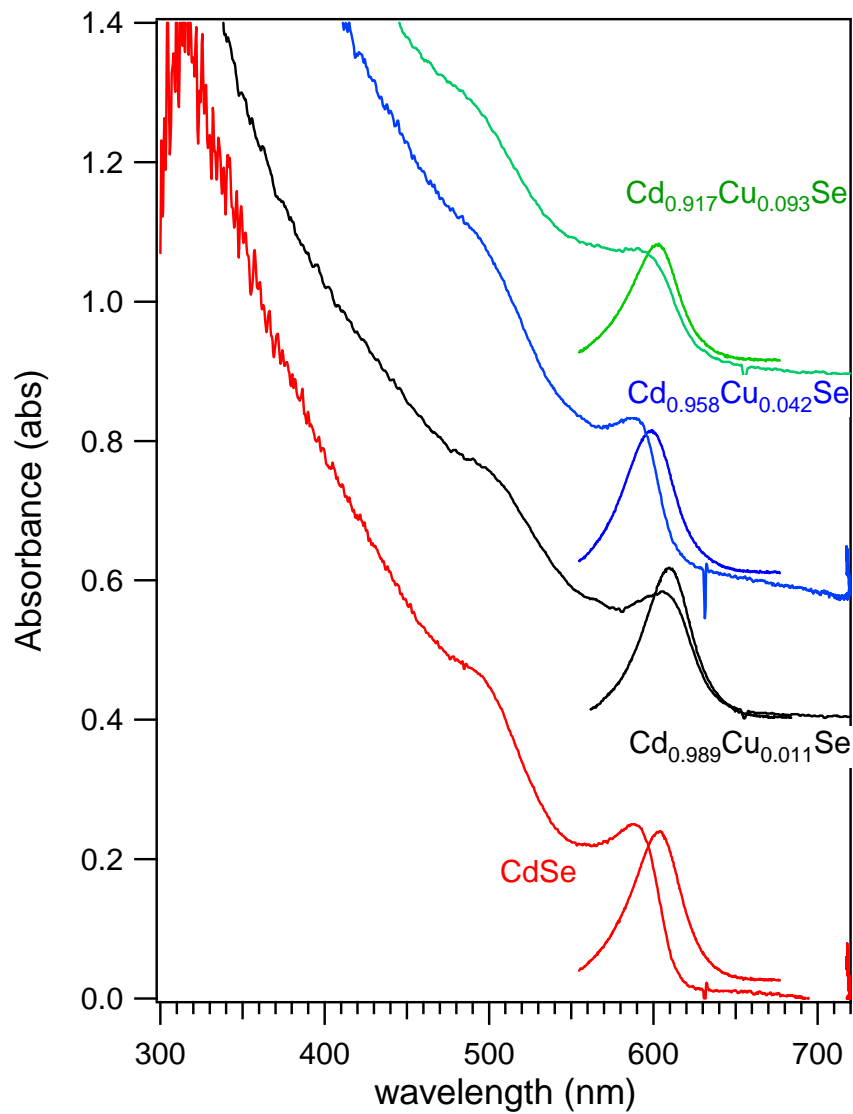
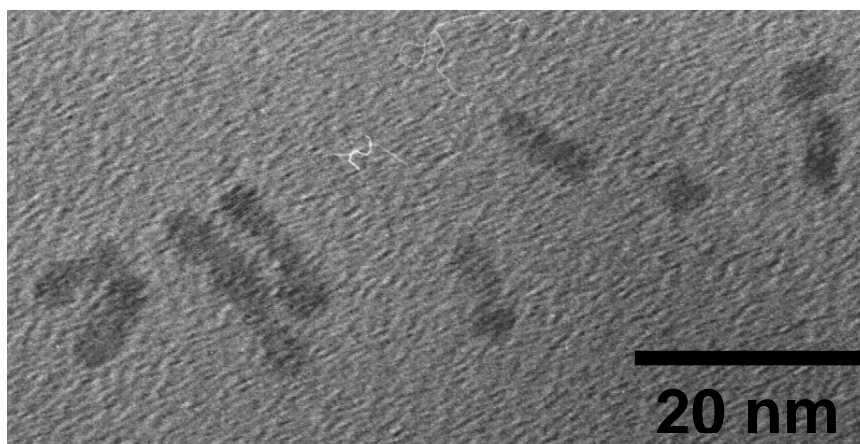


Figure 4.14. Plot of the <111> position vs Cu doping concentration.



**Figure 4.15.** Absorption spectra of 3 Cu:CdSe nanorod samples and one CdSe nanorod.



**Figure 4.16.** TEM image of Cd<sub>0.91</sub>Co<sub>0.09</sub>Se nanorods with an aspect ratio of ~ 1.7.

process. Unlike the nano-dot alloys, the nano-rods show a dramatic change in the doping concentration when recapped with pyridine. This suggests that the method employed in isolating these quantum rods is not effective in removing Cu that is not part of the particle or due to the higher surface area in nano-rods leading to a higher percentage of adventitious Cu in the rod structures. The nano-rod alloys have very low quantum yields as shown in Table 4. However, it is worthwhile to note that the intensity of emission in the rods is considerably stronger than in the dots (Fig. 4.15). This suggests that there may be a decrease in vacancy formation or trap localization in rods due to the increased surface area. However, emission in the red exists in the rods indicative of defects in the material. XRD powder patterns for these materials are shown in figure 4.17. The XRD spectra reveal that the structure of the rods is wurtzite rather than zinc blende. The difference in the nanodot and nanorod alloy lattice structure may be reflective of the lower plane concentration of Cu in a rod versus a dot. Assignment of a wurtzite structure is determined by the observation of the  $\langle 100 \rangle$ ,  $\langle 002 \rangle$ ,  $\langle 101 \rangle$ ,  $\langle 102 \rangle$ ,  $\langle 110 \rangle$ ,  $\langle 103 \rangle$  and  $\langle 112 \rangle$  peaks of the hexagonal wurtzite structure. The  $\langle 002 \rangle$  is sharper than the other peaks as expected for elongation of the rods along the  $\langle 002 \rangle$  axis (Figure 4.18). The peaks also shift to lower d-spacing as a function of doping concentration consistent with a random ion substitution process as observed in the nanodot samples. As mentioned before, this is due to the replacement of a Cd-T<sub>d</sub> site with a Cu atom.

%Cu doping out of batch	%Cu doping after pyridine stripping
4.78 ±0.24	1.06 ±0.05
7.67 ±0.38	4.24 ±0.21
14.02 ±0.70	9.27 ±0.46

**Table 3.** Table listing the %Cu doping measure by Atomic Absorbance spectroscopy out of batch and after pyridine stripping (x3).

---

Sample	Quantum Yield
$\text{Cd}_{0.99}\text{Co}_{0.01}\text{Se}$	0.94%
$\text{Cd}_{0.96}\text{Co}_{0.04}\text{Se}$	0.82%
$\text{Cd}_{0.91}\text{Co}_{0.09}\text{Se}$	1.19%

---

**Table 4.** Quantum yields of Cu: CdSe in toluene.  $\text{Ru}(\text{bpy})_3$  was used as a standard.

The lattice parameters shift linearly as a function of doping as can be seen in figure 4.18.

XPS data on the nano-rod alloys reveal that the dopant in the rod is also Cu(I) (Figure 4.19). This once again can be seen by the lack of satellite peaks in the Cu 2p region. The regional XPS scans of Cd and Se for our quantum rods in figure 4.20 and 4.21 show no evidence of oxidation of the Se or Cd in these samples, confirming the lack of oxidation due to reaction conditions.

#### **4.5 Conclusion.**

Although we have not measured carrier concentrations verifying p-doping in these nano-alloys, we have demonstrated a simple and effective synthetic technique that yields doped nano-dot and nano-rod materials with high levels of core doping. This is the first time that CdSe quantum dots and rods have been doped with Cu(I). Structural evidence was provided indicating that the core of these materials is statistically doped with Cu ions. XANES and XPS data confirm the presence of the Cu guest ion as Cu(I) producing Se vacancies to compensate for the resultant charge imbalance. The creation of Se vacancies results in a loss of band edge photoluminescence from CdSe due to trap site formation in the lattice.

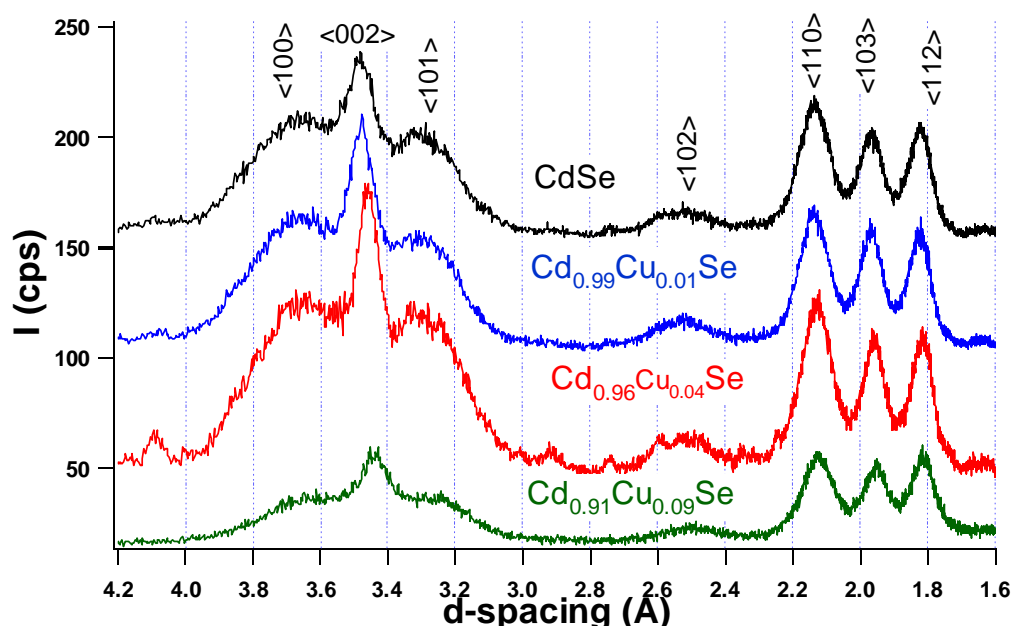


**Figure 4.17.** XRD spectra of Cu: CdSe and CdSe nanorods.

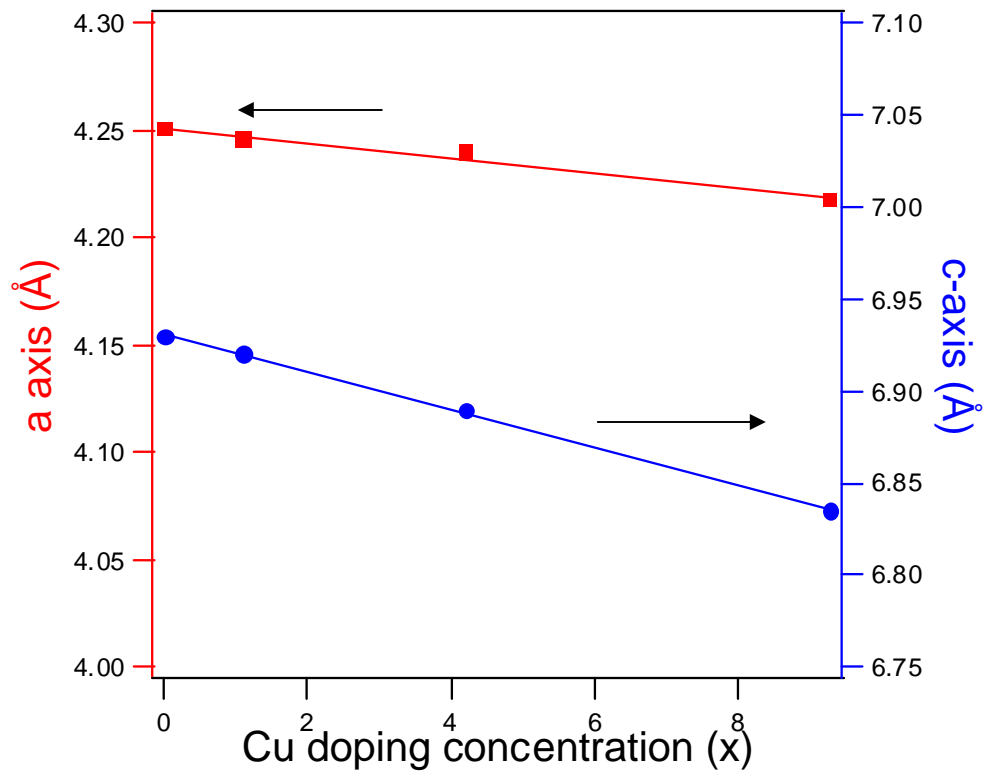


**Figure 4.18.** Plot of the  $a$  and  $c$  lattice parameters vs Cu doping concentration.

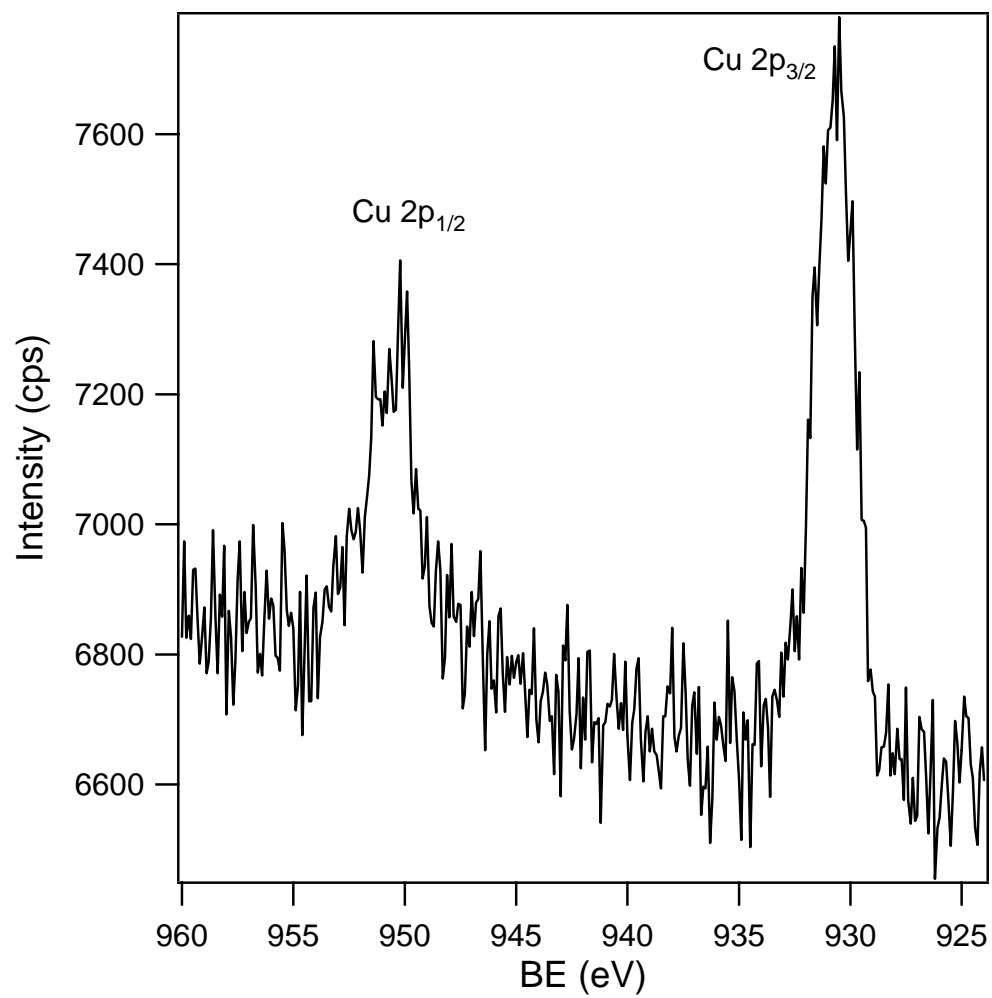


**Figure 4.19.** XPS Cu regional scan of  $\text{Cd}_{0.91}\text{Cu}_{0.09}\text{Se}$ .

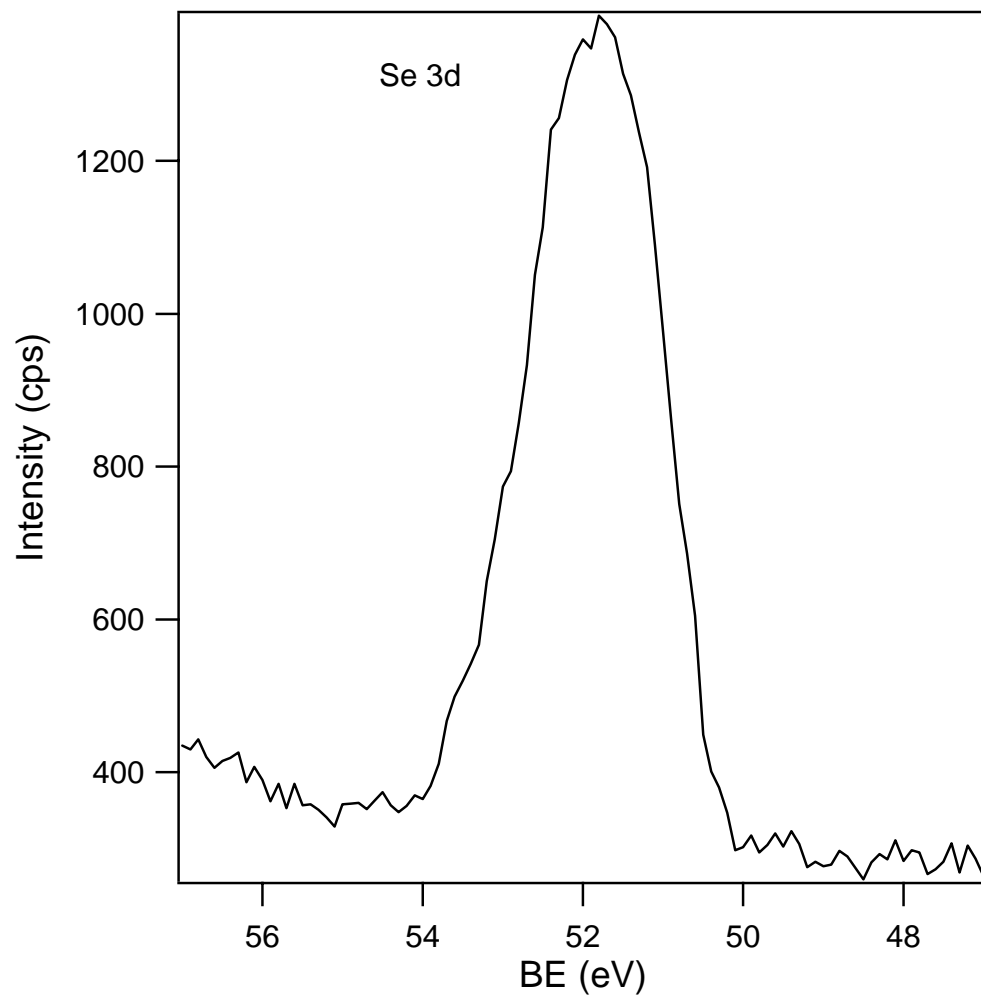


**Figure 4.20.** XPS Se regional scan of  $\text{Cd}_{0.91}\text{Cu}_{0.09}\text{Se}$ .

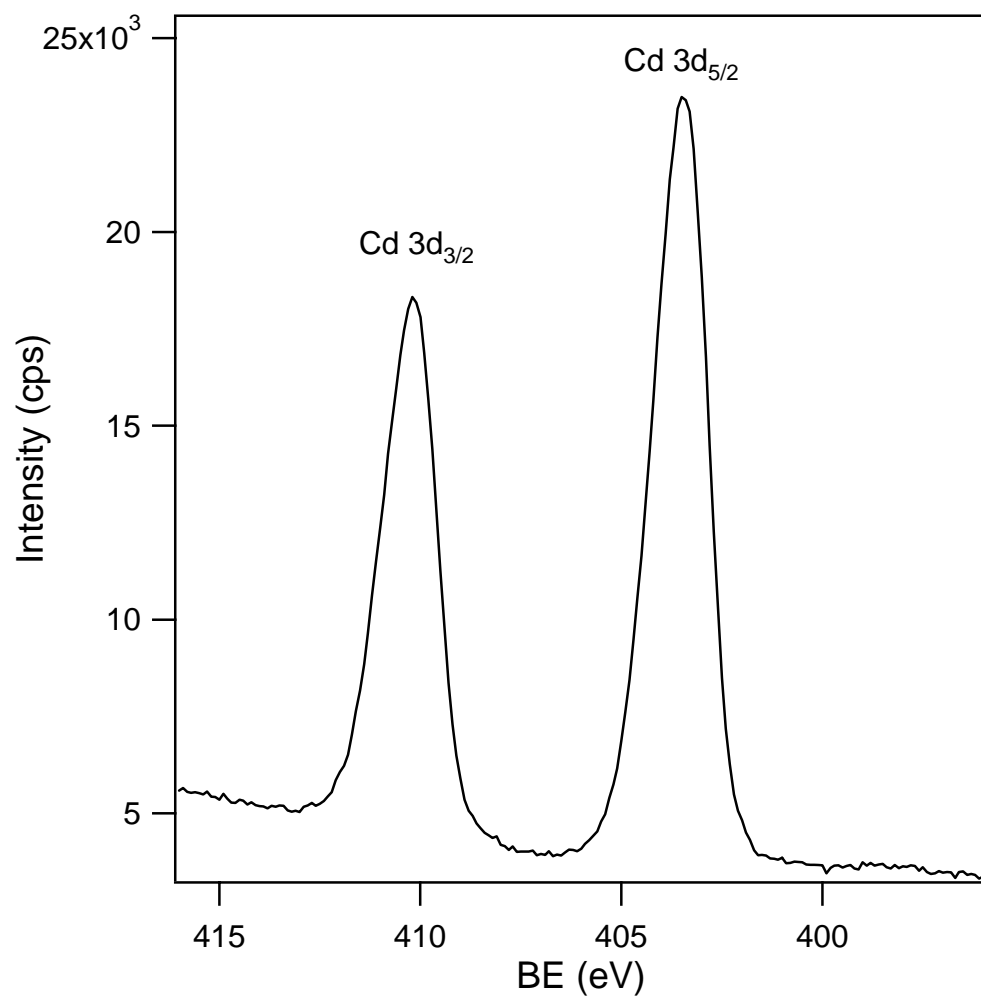


**Figure 4.20.** XPS Se regional scan of Cd<sub>0.91</sub>Cu<sub>0.09</sub>Se.

#### 4.6 REFERENCES

- (1) Green, M. A.; Emery, K.; King, D. L.; Igari, S.; Warta, W. *Prog Photovoltaics* **2001**, *9*, 287-293.
- (2) Han, S. J.; Song, J. W.; Yang, C. H.; Park, S. H.; Park, J. H.; Jeong, Y. H.; Rhie, K. W. *Applied Physics Letters* **2002**, *81*, 4212-4214.
- (3) Kashiwaba, Y.; Kanno, I.; Ikeda, T. *Jpn J Appl Phys I* **1992**, *31*, 1170-1175.
- (4) Murray, C. B.; Norris, D. J.; Bawendi, M. G. *Journal of the American Chemical Society* **1993**, *115*, 8706-8715.
- (5) Alivisatos, A. P. *Journal of Physical Chemistry* **1996**, *100*, 13226-13239.
- (6) Alivisatos, A. P. *Science* **1996**, *271*, 933-937.
- (7) Zhong, X. H.; Han, M. Y.; Dong, Z. L.; White, T. J.; Knoll, W. *Journal of the American Chemical Society* **2003**, *125*, 8589-8594.
- (8) Malik, M. A.; O'Brien, P.; Revaprasadu, N. *Adv Mater* **1999**, *11*, 1441-1444.
- (9) Haury, A.; Wasiele, A.; Arnoult, A.; Cibert, J.; Tatarenko, S.; Dietl, T.; dAubigne, Y. M. *Physical Review Letters* **1997**, *79*, 511-514.

- (10) Dietl, T.; Cibert, J.; Ferrand, D.; d'Aubigne, Y. M. *Materials Science and Engineering B-Solid State Materials for Advanced Technology* **1999**, *63*, 103-110.
- (11) Cibert, J.; Kossacki, P.; Haury, A.; Ferrand, D.; Wasiela, A.; d'Aubigne, Y. M.; Arnoult, A.; Tatarenko, S.; Dietl, T. *Journal of Crystal Growth* **1999**, *202*, 670-673.
- (12) Ramaiah, K. S.; Su, Y. K.; Chang, S. J.; Juang, F. S.; Ohdaira, K.; Shiraki, Y.; Liu, H. P.; Chen, I. G.; Bhatnagar, A. K. *Journal of Crystal Growth* **2001**, *224*, 74-82.
- (13) Kokubun, Y.; Hatano, H.; Wada, M. *Japanese Journal of Applied Physics* **1979**, *18*, 1947-1950.
- (14) Levy, L.; Hocheplied, J. F.; Pileni, M. P. *J Phys Chem-Us* **1996**, *100*, 18322-18326.
- (15) Norman, T. J.; Magana, D.; Wilson, T.; Burns, C.; Zhang, J. Z.; Cao, D.; Bridges, F. *Journal of Physical Chemistry B* **2003**, *107*, 6309-6317.
- (16) Norris, D. J.; Yao, N.; Charnock, F. T.; Kennedy, T. A. *Nanoletters* **2001**, *1*, 3-7.
- (17) Hanif, K. M.; Meulenberg, R. W.; Strouse, G. F. *Journal of the American Chemical Society* **2002**, *124*, 11495-11502.
- (18) Ji, T. H.; Jian, W. B.; Fang, J. Y. *Journal of the American Chemical Society* **2003**, *125*, 8448-8449.

- (19) Raola, O. E.; Strouse, G. F. *Nano Letters* **2002**, 2, 1443-1447.
- (20) Jun, Y. W.; Jung, Y. Y.; Cheon, J. *Journal of the American Chemical Society* **2002**, 124, 615-619.
- (21) Mikulec, F. V.; Kuno, M.; Bennati, M.; Hall, D. A.; Griffin, R. G.; Bawendi, M. G. *Journal of the American Chemical Society* **2000**, 122, 2532-2540.
- (22) Hagen, K. S.; Stephan, D. W.; Holm, R. H. *Inorg Chem* **1982**, 21, 3928-3936.
- (23) Lover, T.; Henderson, W.; Bowmaker, G. A.; Seakins, J. M.; Cooney, R. P. *Chem Mater* **1997**, 9, 1878-1886.
- (24) Briggs, D. *Handbook of x-ray and ultraviolet photoelectron spectroscopy*; Heyden & Son Ltd.: London, 1977.
- (25) Katari, J. E. B.; Colvin, V. L.; Alivisatos, A. P. *Journal of Physical Chemistry* **1994**, 98, 4109-4117.
- (26) Berrettini, M. G.; Braun, G.; Hu, J.; Strouse, G. F. *JACS* **2003**, accepted.
- (27) Suresh, C. H.; Koga, N. *Journal of Physical Chemistry A* **2001**, 105, 5940-5944.
- (28) Vegard, L.; Schjelderup, H. *Phys. Z.* **1917**, 18, 93-96.
- (29) Huynh, W. U.; Dittmer, J. J.; Alivisatos, A. P. *Science* **2002**, 295, 2425-2427.



**Chapter 5.** Structural determination and vibrational study for hexagonal  
elpasolites  $\text{Cs}_2\text{NaGaF}_6:\text{Cr}^{3+}$  and  $\text{Cs}_2\text{NaAlF}_6:\text{Cr}^{3+}$

The work in this chapter is based on the following two papers and it is being reproduced with permission from the publishers.

Bordallo, H.N.; Wang, X.; Hanif, K.M.; Strouse, G.F.; daFonseca, R.J.M.; Sosman, L.P.; Dias Tavares, A. *J. Phys. Condens. Matter*, **14**, 12383-12389 (2002)

[www.iop.org/journals/jpcm](http://www.iop.org/journals/jpcm)

Bordallo, H.N.; Henning, R.W.; Sosman, L.P.; daFonseca, R.J.M.; Dias Tavares, A.; Hanif, K.M.; Strouse, G.F.. *J. Chem. Phys.*, **115**, 4300-4305 (2001)

## 5.1: Introduction

$\text{Cr}^{3+}$  has been studied extensively in the field of inorganic spectroscopy. In fact, what makes  $\text{Cr}^{3+}$  containing materials of interest is their optical properties. A large number of  $\text{Cr}^{3+}$  complexes emit after photoexcitation, and it is this property in particular that has been the focus of many studies in photophysics and photochemistry.<sup>1</sup>

The extensive study in this area resulted in the use of ruby ( $\text{Cr}^{3+}:\text{Al}_2\text{O}_3$ ) for the first ever laser.<sup>2</sup> Since the discovery of ruby, considerable research has been conducted on the study of  $\text{Cr}^{3+}$  incorporated in oxide or fluoride hosts.<sup>3</sup> The optical properties of  $\text{Cr}^{3+}$  doped materials is dependent on its site symmetry and can be altered by changing the properties of the host lattice. Two examples of this are ruby ( $\text{Cr}^{3+}:\text{Al}_2\text{O}_3$ ) and alexandrite ( $\text{Cr}^{3+}:\text{BeAl}_2\text{O}_4$ ).  $\text{Cr}^{3+}$  experiences a stronger ligand field in  $\text{Al}_2\text{O}_3$  than  $\text{BeAl}_2\text{O}_4$ . As a result of the increased ligand field strength and the resultant increase in electron-phonon coupling the emission spectrum of  $\text{Cr}^{3+}$  in alexandrite is much broader (700-820 nm) making this material much more attractive for tuneable lasing applications.<sup>4,5</sup> Studies have shown that electron-phonon coupling in rare earth doped materials depend upon the host lattice. The degree of electron-phonon coupling is dependant upon the covalency of the host lattice.<sup>6</sup> Electron-phonon coupling is expected to be significantly stronger in transition metals, since the 3d orbitals of the transition metals are not shielded by filled outer shells as are those of the

f-orbitals. Stronger coupling is expected to result in greater line broadening, faster multi-phonon relaxation and more intense vibronic side bands.<sup>7</sup>

The sensitivity of Cr<sup>3+</sup> photoluminescence to its host lattice is surprising. It exhibits broader emission bands in fluoride and chloride hosts due to the weak crystal field of the hosts than in oxides. The emission is generally between 650-900nm in fluoride hosts and around 1  $\mu\text{m}$  in chloride hosts.<sup>5</sup> In these systems the electron-electron and electron-phonon couplings compete with one another. The electron-phonon coupling consists of interactions between the electronic states of the dopant ion with the phonon of the host lattice. A number of spectroscopic properties arise due to these interactions including non-radiative decay, increase in linewidth of photoluminescence (PL), line shifts with increasing temperature and vibronic wings on the zero phonon line.<sup>8</sup> Since these materials are of interest for possible laser applications, the main concern that arises with increased electron-phonon coupling is a decrease in quantum yield.

Detailed analysis of the degree of electron-phonon coupling in solid state lattices containing Cr<sup>3+</sup> and the spatial resolution of this interaction is important in order to understand the energy flow in electron dynamics involving the vibrational system. It is difficult to study the spatial extension of the electron-phonon coupling in most doped materials since the dopant ion has the same oxidation state as that of the host ion it replaces. This results in

similar vibronic properties as the host since the surrounding environment around the dopant is almost identical to that of the host ion it replaces. Exceptions to this rule are well defined compounds that contain molecular species. In  $(\text{NH}_4)_3\text{GdCl}_5$ ,  $\text{NH}_4^+$  is in the second coordination shell of  $\text{GdCl}_6$ . Electron-phonon coupling to the  $\text{NH}_4^+$  was observed by the occurrence of a phonon wing or sideband in the luminescence spectra.<sup>9</sup> Electron-phonon coupling of  $\text{Eu}^{3+}$  to  $\text{NH}_4^+$  vibrational modes in  $(\text{NH}_4)_3\text{YCl}_6:\text{Eu}^{3+}$  was concluded to be the cause of the observed low quantum yield for these materials.

In this chapter, we report the single crystal x-ray and neutron scattering measurements, along with single crystal Raman spectroscopy of two  $\text{Cr}^{3+}$  doped elpasolites:  $\text{Cs}_2\text{NaAlF}_6:\text{Cr}^{3+}$  and  $\text{Cs}_2\text{NaGaF}_6:\text{Cr}^{3+}$ . These  $\text{A}_2\text{BMF}_6$ , where A and B are alkali metals and M is Al or Ga, type elpasolite materials were prepared by hydrothermal methods by a collaborator. The  $\text{Cr}^{3+}$  was doped within the structure sitting on either the  $\text{Ga}^{3+}$  or  $\text{Al}^{3+}$ , cation sites depending on the host lattice. The four  $\text{Cs}_2\text{NaAlF}_6:\text{Cr}^{3+}$  samples that were studied had  $\text{Cr}^{3+}$  doping levels of 0.1%, 0.5%, 1% and 3%. The  $\text{Cs}_2\text{NaGaF}_6:\text{Cr}^{3+}$  sample was doped with 0.5%  $\text{Cr}^{3+}$ . Earlier PL measurements on the  $\text{Cs}_2\text{NaAlF}_6:\text{Cr}^{3+}$  sample indicated that these materials contain two different  $\text{Cr}^{3+}$  emitting sites that arise from differences in metal sites within the host lattice. It is important to understand the exact  $\text{MF}_6$  geometry in order to be able to draw a parallel between the structural and luminescent properties of these materials. Our x-ray

and neutron scattering data along with the Raman data provide strong evidence that the photoluminescence of these materials is inhibited by electron-phonon coupling.

## 5.2. Experimental

Hydrothermal methods were employed in the synthesis of the doped elpasolites.  $\text{Cs}_2\text{NaAlF}_6:\text{Cr}^{3+}$  single crystals with 0.1%, 0.5%, 1% and 3%  $\text{Cr}^{3+}$  doping concentrations were synthesized. The  $\text{Cs}_2\text{NaGaF}_6:\text{Cr}^{3+}$  with 0.5%  $\text{Cr}^{3+}$  doping concentration was also synthesized using hydrothermal methods. These samples were made at the Institute of General and Inorganic Chemistry in Moscow using literature methods.<sup>10</sup>

Single crystal x-ray diffraction measurements were performed on a Siemens SMART CCD area detector diffractometer at room temperature. Refinement of the  $\text{Cs}_2\text{NaAlF}_6:\text{Cr}^{3+}$  sample with 0.5% Cr was performed using Shelx-97 package to a GOF of 1.26. The related elpasolite structure was used as a starting point and it was assumed that the chromium substitute for aluminum atoms within the lattice.<sup>11</sup> Despite the large difference in scattering between that of aluminum and chromium, the low random ion substituted process and concentration of Cr did not allow refinement of specific  $\text{Cr}^{3+}$  positions in the lattice. It was therefore assumed that statistical doping as expected for a hydrothermal synthesis occurred within the structure. Attempts

to refine in lower space groups did not improve the analysis. In the  $\text{Cs}_2\text{NaGaF}_6:\text{Cr}^{3+}$  sample it was assumed that the  $\text{Cr}^{3+}$  would statistically replace the Ga through a random ion substitution process, which would not allow the  $\text{Cr}^{3+}$  site to be specifically identified. The model was also refined using Shelx-97 package to an R-value of 0.018.

Single crystal neutron diffraction measurements were performed at room temperature on the 0.5%  $\text{Cr}^{3+}$  doped  $\text{Cs}_2\text{NaAlF}_6:\text{Cr}^{3+}$  sample using a single crystal spectrometer SCD at the Intense Pulsed Neutron Source at Argonne National Laboratory. Time-of-flight diffraction peaks were measured using a position-sensitive  $^6\text{Li}$ -glass scintillation detector with an active area of 30x30 cm. Two different histograms were collected at different  $\chi$  and  $\phi$  settings and the initial orientation matrix was determined using an autoindexing routine.<sup>12</sup> In total, 38 histograms were collected covering  $-6 \leq h \leq 12$ ,  $-13 \leq k \leq 6$ ,  $-60 \leq l \leq 63$  of reciprocal space. Analysis of the neutron data was performed using GSAS.<sup>13</sup>

Polarized single crystal Raman scattering measurements were performed using a back-scattering configuration on a 0.5M ARC single spectrograph (1800 lines  $\text{mm}^{-1}/400$  blaze) coupled to a Princeton Instrument LN2 512x512 CCD array. Figure 5.1 provides a diagram of the Raman instrument. Notch filters (Kaiser Optical) were placed in front of the monochromator entrance slits in order to reject the laser light. Excitation

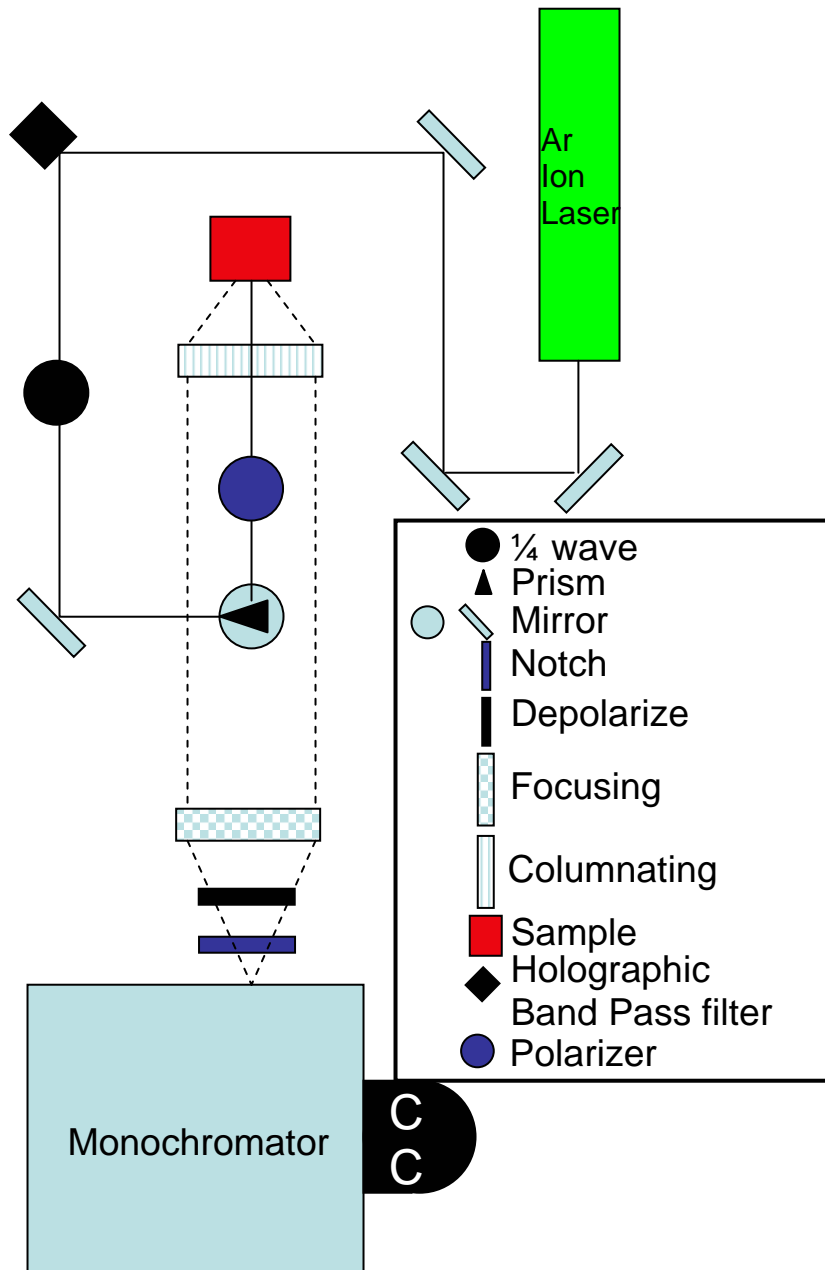


**Figure 5.1.** Raman configuration for polarized Raman data collection.

wavelengths of 488.0 and 514 nm with a power of 3.0 mW was provided by a 10W Spectra-Physics 2200 Ar<sup>+</sup> ion laser. A 5 nm bandpass filter (Kaiser Optical) was used in order to reduce contributions from plasma lines. The polarization measurements were carried by laser polarization rotation at a  $\lambda/4$  plate and collection of the scattered intensity through a calcite polarizer. In order to eliminate instrumental polarization dependencies, a depolarizer was placed prior to coupling in the spectrograph. An Argon lamp was used to make wavenumber calibrations. Temperature control of  $\pm 1.0\text{K}$  was achieved using a APD Heli-Tran cryostat controlled by a SI 9620-1 temperature controller.<sup>14</sup>

### 5.3. RESULTS

$\text{Cs}_2\text{NaAlF}_6:0.5\text{Cr}^{3+}$  and  $\text{Cs}_2\text{NaGaF}_6:0.5\text{Cr}^{3+}$  crystallize in a hexagonal structure with  $R3m$  symmetry, and have a framework of either  $\text{AlF}_6$  or  $\text{GaF}_6$  octahedra that are interconnected through face and corner sharing  $\text{NaF}_6$  octahedra (Fig. 5.2). The crystal structure of  $\text{Cs}_2\text{NaMF}_6:0.5\text{Cr}^{3+}$ , where  $M=\text{Al}$  or  $\text{Ga}$ , is shown in figure 5.2. The structure was solved by single crystal x-ray and neutron diffraction measurements, allowing unambiguous crystal structure determination. The collection parameters for the x-ray diffraction and neutron data set of  $\text{Cs}_2\text{NaAlF}_6:0.5\text{Cr}^{3+}$  and  $\text{Cs}_2\text{NaGaF}_6:0.5\text{Cr}^{3+}$  can be found in Table 5.1 and 5.2 respectively. Tables 5.3 – 5.5 provide the atomic positions,

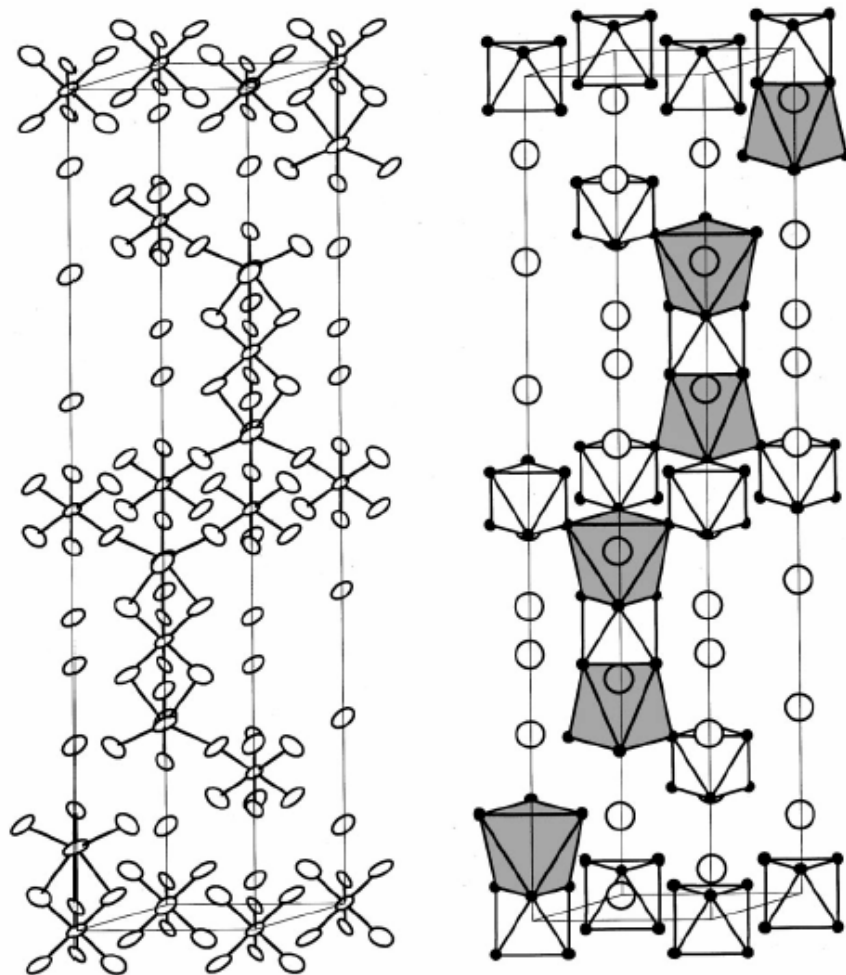


**Figure 5.2.** ORTEP view (left) and polyhedra representation (right) from neutron refinement showing the connectivity between  $\text{AlF}_6$  and  $\text{NaF}_6$  octahedra. In the right diagram the white and gray polyhedra represent  $\text{AlF}_6$  and  $\text{NaF}_6$ , respectively. White and black atoms correspond to cesium and fluorine. The ellipsoidal probabilities were drawn at 90%. Some of the octahedra have been removed for clarity.

---

Temperature(°C)	23°C	
Crystal Size (mm)	0.5x0.25x0.25	0.5x0.25x0.25
Space group	$R\bar{3}m$ (No. 166)	
a(Å)	6.1811(8)	6.244(1)
c(Å)	29.845(6)	30.270(4)
V(Å <sup>3</sup> )	987.5(2)	1022.1
Z	6	
Radiation	X-ray, $\lambda=0.71073$ Å	
Data collection technique	Siemens Smart CCD	
Extinction parameter	0.044	0.00557
No of reflections before averaging	2539	3553
No of unique reflections	214	357
Variables	27	28
Function minimized	$\sum w(F_0 - F_c)$	
Refinement type	F <sup>2</sup>	
R <sub>w</sub> (F <sup>2</sup> )/ $\omega$ R2	9.1	0.0434
R(F)/R1	3.2	0.0183
GOF	1.55	1.147

---

**Table 5.1.** X-ray collection parameters for Cs<sub>2</sub>NaAlF<sub>6</sub>:Cr<sup>3+</sup> and Cs<sub>2</sub>NaGaF<sub>6</sub>:Cr<sup>3+</sup>

---

Temperature(°C)	23°C
Crystal Size (mm)	5 x 5 x 1
Space group	$R\bar{3}m$ (No. 166)
a(Å)	6.1920(4)
c(Å)	29.839(4)
V(Å <sup>3</sup> )	990.8(2)
Z	6
Radiation	Neutrons, $\lambda=0.7 - 4.2$ Å
Data collection technique	ToF Laue with position sensitive area detector
$\mu(\lambda)$ , cm <sup>-1</sup>	$0.222 + 0.198 \cdot \lambda$
Extinction parameter	$1.36(3) \times 10^{-4}$ rad <sup>-1</sup>
No of reflections in final 1s with $F_0^2 > 3\sigma(F_0^2)$	2731
No of unique reflections	780
Variables	64
Function minimized	$\sum w(F_0 - F_c)$
Refinement type	F
$R_w(F^2)/\omega R^2$	9.1
$R(F^2)$	7.8
$R_w(F)$	4.6
R(F)/R1	4.9
GOF	1.55

---

**Table 5.2.** Neutron data collection parameters for Cs<sub>2</sub>NaAlF<sub>6</sub>:Cr<sup>3+</sup> and Cs<sub>2</sub>NaGaF<sub>6</sub>:Cr<sup>3+</sup>

Site symmetry	Atom	x	y	z	$U_{\text{eq}}$
$3a(3m) - D_{3d}$	Al(1)	0.0	0.0	0.0	0.90
		0.0	0.0	0.0	0.93
$3a(3m) - D_{3d}$	Al(2)	0.0	0.0	0.5	0.77
		0.0	0.0	0.5	0.54
$6c(3m) - C_{3v}$	Na	0.0	0.0	0.09844(5)	1.43
		0.0	0.0	0.0982(2)	1.26
$18h(m) - C_S$	F(1)	0.13627(4)	-0.13627(4)	0.96371(2)	1.45
		0.1360(5)	-0.1360(5)	0.9638(2)	1.54
$18h(m) - C_S$	F(2)	0.19289(5)	-0.19289(5)	0.13181(2)	1.62
		0.1941(5)	-0.1941(5)	0.1317(2)	1.63
$6c(3m) - C_{3v}$	Cs(1)	0.0	0.0	0.77992(3)	1.58
		0.0	0.0	0.78000(4)	1.65
$6c(3m) - C_{3v}$	Cs(2)	0.0	0.0	0.62811(3)	1.32
		0.0	0.0	0.62818(4)	1.43

**Table 5.3.** Atomic positions and isotropic equivalent thermal parameters for  $\text{Cd}_2\text{NaAlF}_6:\text{Cr}^{3+}$ . The neutron data is on the top line with the x-ray data beneath it.

Site symmetry	Atom	x	y	z	$U_{eq}$
$3a(3m) - D_{3d}$	Ga(1)	0.0	0.0	0.0	1.13
$3a(3m) - D_{3d}$	Ga(2)	0.0	0.0	0.5	0.93
$6c(3m) - C_{3v}$	Na	0.0	0.0	0.09768(10)	1.59
$18h(m) - C_S$	F(1)	0.1408(2)	-0.1408(2)	0.96239(8)	1.70
$18h(m) - C_S$	F(2)	0.1888(2)	-0.1888(2)	0.13085(8)	1.99
$6c(3m) - C_{3v}$	Cs(1)	0.0	0.0	0.780875(16)	1.81
$6c(3m) - C_{3v}$	Cs(2)	0.0	0.0	0.628079(15)	1.62

**Table 5.4.** Atomic positions and isotropic equivalent thermal parameters for  $Cs_2NaGaF_6:Cr^{3+}$  based on x-ray data.

Atom	U <sub>11</sub>	U <sub>22</sub>	U <sub>33</sub>	U <sub>12</sub>	U <sub>13</sub>	U <sub>23</sub>
Al(1)	0.0091(3) 0.005(2)	0.0091(3) 0.005(2)	0.0085(6) 0.017(3)	0.0046(1) 0.003(1)	0.0 0.0	0.0 0.0
Al(2)	0.0074(3) 0.002(2)	0.0074(3) 0.002(2)	0.0082(5) 0.013(3)	0.0037(1) 0.000(1)	0.0 0.0	0.0 0.0
Na	0.0155(3) 0.010(2)	0.0155(3) 0.010(2)	0.0118(5) 0.018(3)	0.0077(1) 0.005(1)	0.0 0.0	0.0 0.0
F(1)	0.0161(1) 0.011(2)	0.0161(1) 0.011(2)	0.0136(2) 0.025(3)	0.0101(1) 0.007(2)	0.00138(7) 0.000(1)	-0.00138(7) -0.000(1)
F(2)	0.0170(1) 0.017(2)	0.0170(1) 0.017(2)	0.0171(2) 0.020(3)	0.0105(2) 0.013(3)	-0.00273(7) -0.004(1)	0.00273(7) 0.004(1)
Cs(1)	0.0142(2) 0.0112(9)	0.0142(2) 0.0112(9)	0.0187(5) 0.027(1)	0.00708(9) 0.0056(4)	0.0 0.0	0.0 0.0
Cs(2)	0.0124(2) 0.0010(9)	0.0124(2) 0.0010(9)	0.0143(3) 0.023(1)	0.00622(9) 0.0050(4)	0.0 0.0	0.0 0.0

**Table 5.5** Anisotropic thermal parameters for Cs<sub>2</sub>NaAlF<sub>6</sub>:Cr<sup>3+</sup>. Neutron data is on the top line and the x-ray data is on the second line.

isotropic equivalent thermal parameters, and anisotropic parameters for the x-ray and neutron data for  $\text{Cs}_2\text{NaAlF}_6\cdot\text{Cr}^{3+}$  and  $\text{Cs}_2\text{NaGaF}_6\cdot\text{Cr}^{3+}$  respectively. Based on x-ray diffraction analysis it can be determined that the  $\text{Cr}^{3+}$  replaces the Al and Ga atoms statistically in the two samples. Further inspection into the atomic radii of  $\text{Ga}^{3+}$  (0.62Å),  $\text{Cr}^{3+}$  (0.615Å), and  $\text{Na}^+$ (0.97Å) reveals that  $\text{Cr}^{3+}$  most likely substitutes into a  $\text{Ga}^{3+}$  site in  $\text{Cs}_2\text{NaGaF}_6\cdot 0.5\text{Cr}^{3+}$ . Previous optical studies provide evidence further evidence for the existence of  $\text{Cr}^{3+}$  ions into an octahedral site which would eliminate the possibility of random doping of  $\text{Cr}^{3+}$  within the lattice.<sup>15</sup>

In el-pasolites there exists two M sites in the lattice.<sup>11,16,17</sup> The two crystallographically equivalent M positions in  $\text{Cs}_2\text{NaMF}_6$ , M(1) and M(2), are on high symmetry positions. Therefore the fluoride atoms form regular octahedra around the central M, although a slight elongation along the c axis reduces them to trigonal antiprisms (Fig. 5.1). The Al(1)-F(1) and Al(2)-F(2) bond distances from the neutron refinement are 1.8189(5) and 1.8304(5) Å. The sodium fluoride polyhedron ( $\text{NaF}_6$ ) is distorted with three Na-F distances of 2.361(1) Å [Na-F(1)] and three of 2.2958(8) Å [Na-F(2)] according to the neutron data. The structure of these el-pasolites is designated as 12L type, because of the 12 layers of Al and Na polyhedra stacked along the c-axis. The difference between the two aluminum sites is that the Al(1) containing

octahedral share two trigonal faces with Na polyhedra along the c axis while the Al(2) octahedra share corners with six Na polyhedra. The Cs atoms sit in the cavities formed by the 12 fluoride atoms.

Table 5.6 shows that the bond distances of  $\text{Cs}_2\text{NaAlF}_6:0.5\text{Cr}^{3+}$  and  $\text{Cs}_2\text{NaGaF}_6:0.5\text{Cr}^{3+}$  are comparable to each other and other similar compounds.<sup>11,18</sup> It can be seen that there is a larger variation in bond distances in the  $\text{Cs}_2\text{NaAlF}_6:0.5\text{Cr}^{3+}$  material with respect to the other 3 elpasolites in table 5.6. The ionic radii of  $\text{Al}^{3+}$  (0.53Å) is much smaller than that of  $\text{Ga}^{3+}$  (0.62Å) or  $\text{Cr}^{3+}$  (0.615Å), which would explain for the greater distortion in the lattice. Further support for this is seen in time-resolved-emission experiments which have shown sites occupied by  $\text{Al}^{3+}$  in the aluminate systems exhibit larger distortion.<sup>15</sup> As a result of the larger ionic radii mismatch between  $\text{Al}^{3+}$  and  $\text{Cr}^{3+}$ , in combination with the x-ray and optical studies done to date it can be stated that  $\text{Cr}^{3+}$  can be doped into a  $\text{Ga}^{3+}$  site with much more ease than that of an  $\text{Al}^{3+}$  site.

### 5.3.1. Vibrational Analysis

Factor group analysis of the Bravais cell yields the normal modes of vibration at the Brillouin zone, their symmetries, and the selection rules for infrared and Raman scattering. The space group for  $\text{Cs}_2\text{NaMF}_6:\text{Cr}^{3+}$  is  $D_{3d}^5$  ( $R3m$ ) and contains six formula units per unit cell. This unit cell is triply

Interatomic- distance (Å)	A <sup>18</sup>	B	C <sup>11</sup>	D <sup>11</sup>
M(1) - F(1)	1.813(5)	1.902(2)	1.906(5)	1.930(4)
M(2) - F(2)	1.820(5)	1.901(2)	1.913(6)	1.922(4)
Na - F(1)	2.361(1)	2.371(3)	2.370(6)	2.377(6)
Na - F(2)	2.2958(5)	2.275(3)	2.272(7)	2.266(6)

**Table 5.6.** Interatomic distances for isostructural (A) Cs<sub>2</sub>NaAlF<sub>6</sub>:0.5Cr<sup>3+</sup> (B) Cs<sub>2</sub>NaGaF<sub>6</sub>:0.5Cr<sup>3+</sup> (C) Cs<sub>2</sub>NaCrF<sub>6</sub> (D) Cs<sub>2</sub>NaFeF<sub>6</sub>

primitive, therefore at the  $\Gamma$  point in the Brillouin zone ( $q=0$ ), only one third of the 60 crystallographic vibrational modes are expected to be observed.

From a group theoretical analysis of the primitive cell, the phonons at the  $\Gamma$  point can be classified as follows:

$$\Gamma = 7A_{1g} + 2A_{1u} + 9A_{2u} + 2A_{2g} + 9E_g + 11E_u$$

The irreducible representations for the  $\Gamma$ -point normal modes give rise to  $16(7A_{1g}^{zz,xx,yy} + 9E_g^{xy,xz,yz})$  Raman active modes,  $18(8A_{2u} + 10E_u)$  IR-active modes,  $4(2A_{2g} + 2A_{1u})$  inactive modes and  $2(A_{2u}^z + E_u^{xy})$  acoustic modes.

The Raman measurements were obtained on single crystals, mounted in two different orientations as shown in Figure 5.3a and 5.3b. The Raman spectra for  $\text{Cs}_2\text{NaGaF}_6:\text{Cr}^{3+}$  and  $\text{Cs}_2\text{NaAlF}_6:\text{Cr}^{3+}$  are shown in Figure 5.4, 5.5a, and 5.5b and the observed modes are tentatively assigned in Table 5.7. The orientation shown in figure 5.3a,  $\langle xy||xy \rangle$ , the polarization vector  $\eta$  was perpendicular to the [001] crystallographic direction, and polarization rules impose that light is scattered mainly by the modes of  $A_{1g}(zz)$  and  $E_g(yz)$  symmetries. In the orientation of Fig. 5.3b,  $\langle z||z \rangle$ ,  $\eta$  was parallel to the [0,0,1] crystallographic direction, with light scattered by an  $E_g$  mode predominantly crossed polarized. Since the [0 1 0] in the single crystal direction forms a  $30^\circ$  angle with the XY plane, the  $A_{1g}$  and  $E_g$  raman lines are both observed in the polarized data in Figs. 5.5a and 5.5b.

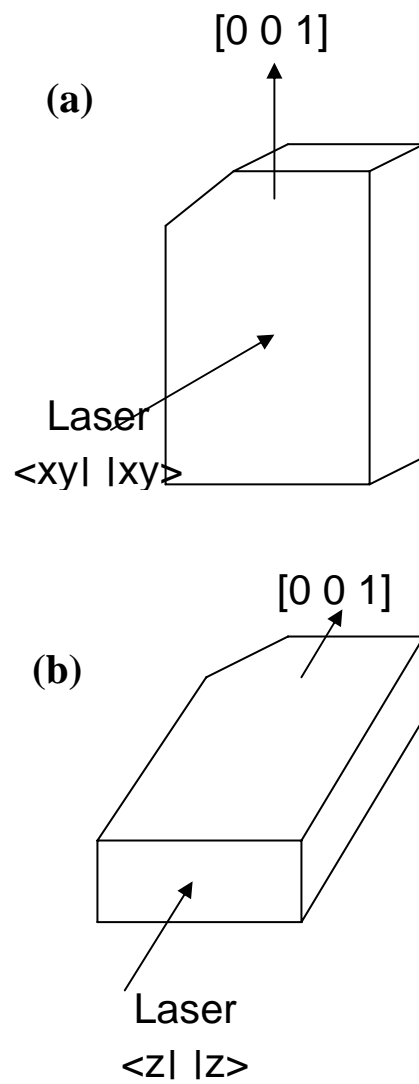


**Figure 5.3a and b:** Two orientations of elpasolite crystals used in polarized Raman measurements.

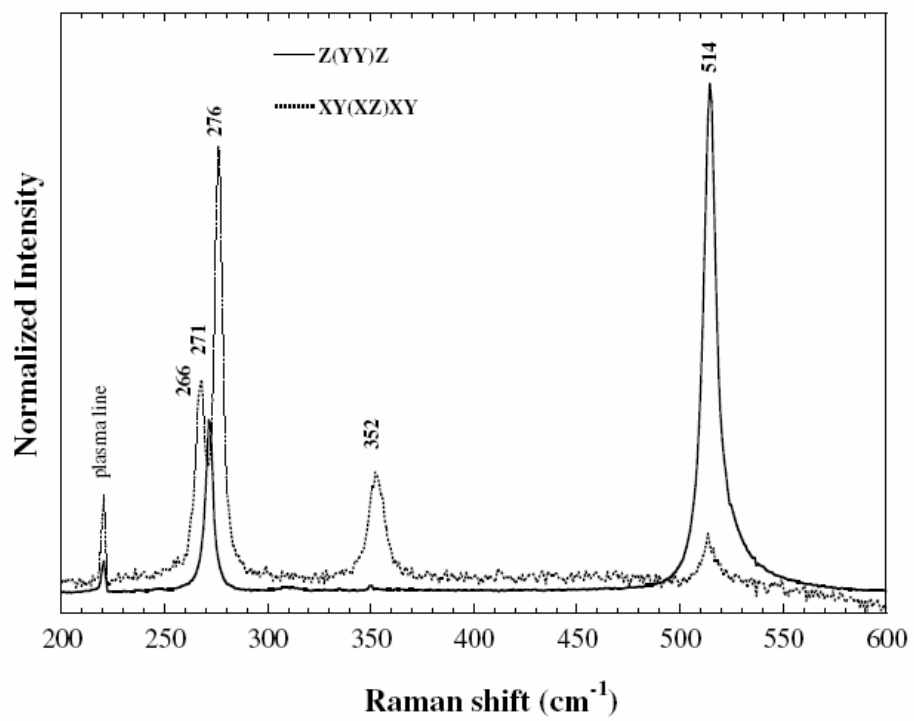


**Figure 5.4.** Polarized Raman spectra of Cs<sub>2</sub>NaGaF<sub>6</sub>:0.5Cr<sup>3+</sup>.

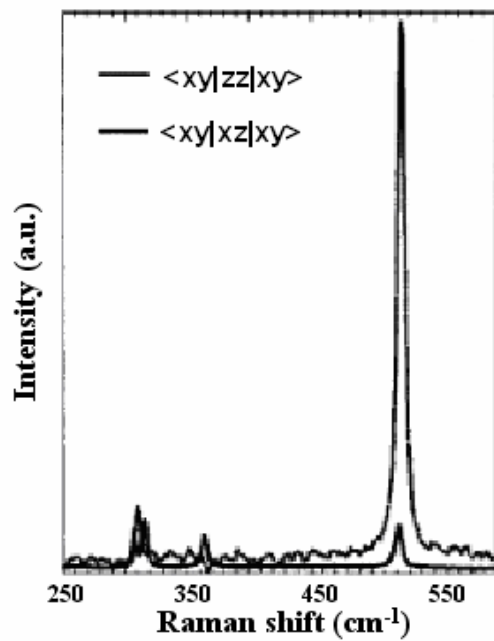


**Figure 5.5a.** Polarized RT Raman spectra of  $\text{Cs}_2\text{NaAlF}_6:0.5\text{Cr}^{3+}$  for orientation figure 3a.

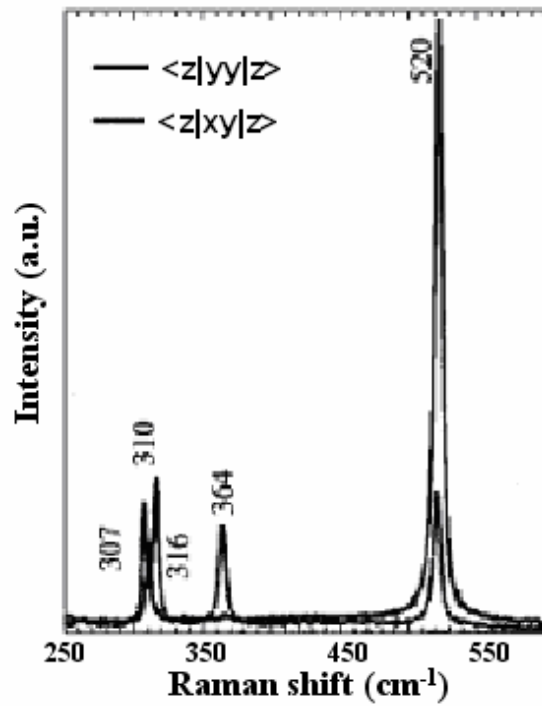


**Figure 5.5b.** Polarized RT Raman spectra of  $\text{Cs}_2\text{NaAlF}_6:0.5\text{Cr}^{3+}$  for orientation figure 3b.

Mode symmetry	Energy (cm <sup>-1</sup> )
$E_g$	307
$E_g$	316
$E_g$	364
$A_g$	310
$A_g$	520

**Table 5.7.** Phonon wave number (cm<sup>-1</sup>) of Raman active modes of vibration in Cs<sub>2</sub>NaAlF<sub>6</sub>:Cr<sup>3+</sup>.

The small sidebands of the  $A_{1g}$  mode at  $528\text{ cm}^{-1}$  can be attributed to a local mode associated with the  $\text{Cr}^{3+}$  impurity (See Fig. 5.6). The resolution of this mode is enhanced upon cooling. Based on the Raman data taken at 16K in figure 5.7, it can be determined that this sideband is impurity related. The sideband does not appear until a doping concentration of 3%  $\text{Cr}^{3+}$  has been achieved. Since the elpasolite crystal structure can accommodate a trivalent impurity without charge compensation, the point symmetry is unaffected by doping and only the translational symmetry is lost. As a result of this, the selection rules are preserved but not the restriction to zone-center phonons. In addition this assignment is validated on the frequency and intensity being consistent with an identified defect mode in the emission spectrum for the same material.<sup>19</sup>

#### 5.4. Discussion

The observed crystal structures for the elpasolites of the structure  $A_2\text{BMF}_6$  depend on the radius ratio of the ions in the lattice, as described by the Goldschmidt tolerance factor:

$$t = 2^{1/2}(r_A + r_F)/(r_M + r_B + 2r_F),$$

where,  $r_A$ ,  $r_B$ ,  $r_M$ , and  $r_F$  are the radius of the A, B, M, and F ions, respectively.<sup>20</sup>

The cubic perovskite superstructure is the ideal elpasolite structure. This structure has doubled cell edges which are derived from closest packed  $\text{AX}_3$  layers stacked in a hexagonal packing arranged along [001] direction. As has

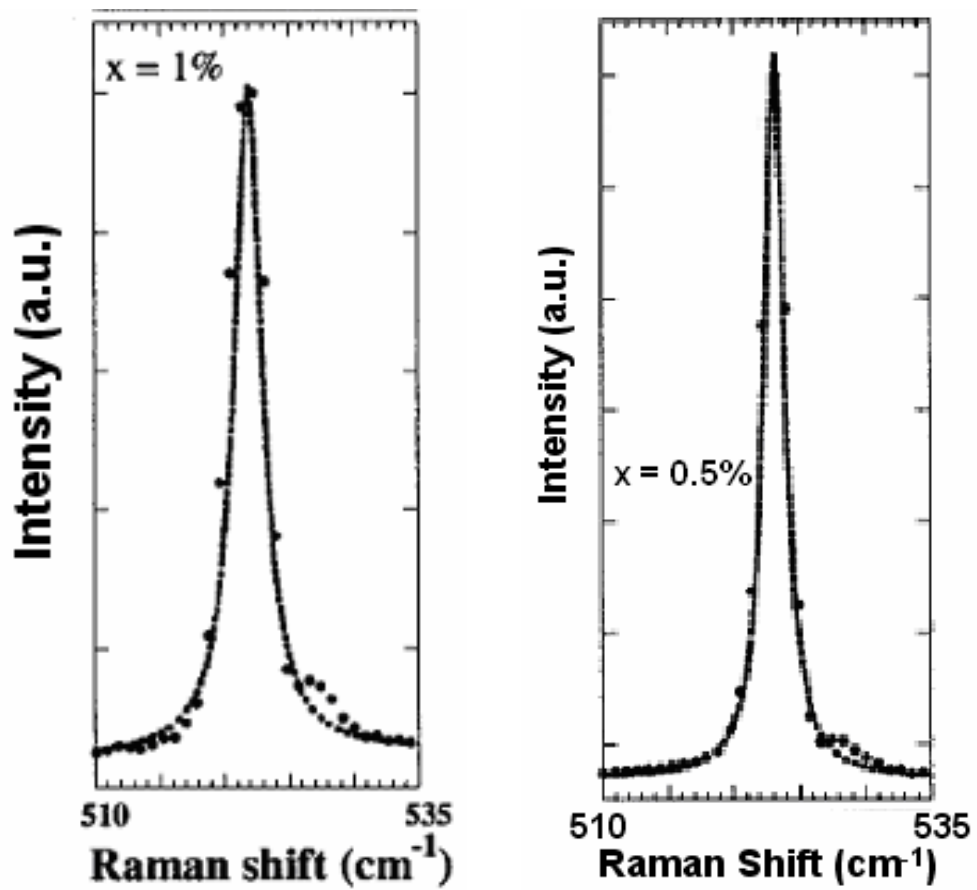


**Figure 5.6.** Evolution of side band as a function of concentration (1%, 0.5%) for  $\text{Cs}_2\text{NaAlF}_6\text{0.5Cr}^{3+}$  with polarization  $\langle z|xx|z \rangle$ .

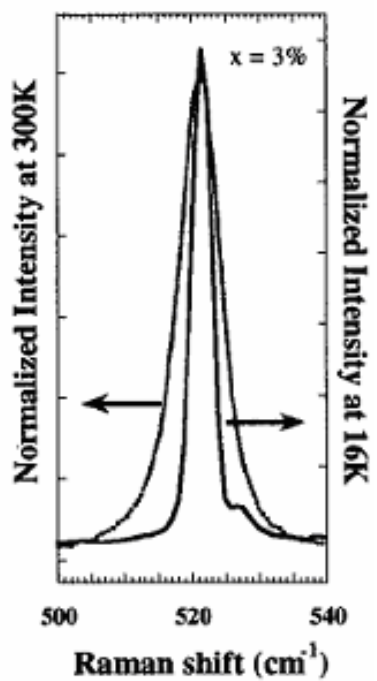


Figure 5.7. Evolution of side band as a function of temperature (300K & 16K) for  $\text{Cs}_2\text{NaAlF}_60.5\text{Cr}^{3+}$  with polarization  $\langle z|xx|z \rangle$ .

been observed in the  $\text{Cs}_2\text{NaYF}_6$ , the highest symmetry packing ( $Fm\bar{3}m$ ) is observed when the tolerance factor lies between  $0.88 \leq t \leq 1$ .<sup>21</sup> If  $t$  becomes below 0.88, deviations from the cubic structure result in distortion of the  $\text{MF}_6$  and  $\text{BF}_6$  octahedra, displacements of the  $\text{A}^+$  cation from its geometrical center, or tilts and rotations of the octahedral, as in the cryolite  $\text{Na}_3\text{AlF}_6$ .<sup>22</sup> If  $t$  exceed 1, then a hexagonal stacking dominates the structure, with the exhibition of face sharing of octahedral, similar to that observed in the simplest hexagonal 2L structure of  $\text{Cs}_2\text{LiGaF}_6$ .<sup>11</sup>

Based on the radius mismatch in  $\text{Cs}_2\text{NaGaF}_6$  and  $\text{Cs}_2\text{NaAlF}_6$  ( $t=1.052$ ) the observed  $R\bar{3}m$  structure is expected. This is in agreement with both the neutron and x-ray data which showed slight structural perturbation due to the incorporation of the  $\text{Cr}^{3+}$  ion into the host. The distortion from an ideal  $Fm\bar{3}m$  structure is due to octahedral tilting, and more interestingly a different stacking sequence of the  $\text{AX}_3$  layers, as observed in Fig. 5.2.

Due to the low level of  $\text{Cr}^{3+}$  doping the effect upon the structure of the elpasolite is minimal. Both x-ray and neutron diffraction measurements are used to study the ensemble of atoms and can not be used study local structure. Raman spectroscopy is used to study local structures it is ideal for the study of the  $\text{Cr}^{3+}$  site analysis. The crystallographic directions were determined prior to mounting the sample for Raman measurements. This allowed for unambiguous determination of the Raman modes.

The fundamental lines observed at room temperature in the first-order Raman spectra of  $\text{Cs}_2\text{NaAlF}_6:\text{Cr}^{3+}$  and  $\text{Cs}_2\text{NaGaF}_6:\text{Cr}^{3+}$  are attributed to the zone center normal modes of the host crystal. Only 5 ( $2A_{1g}$  and  $3E_g$ ) of the 16 Raman active modes can be observed in the wavenumber range of  $200\text{ cm}^{-1}$  to  $600\text{ cm}^{-1}$ . The lattice mode for the Cs ion is expected to be observed at  $\sim 80\text{ cm}^{-1}$ ,<sup>21</sup> and both the Al and Ga ions are only IR active. Both comparison with previously published results,<sup>21,23,24</sup> and taking into consideration that the intensity of the  $\text{XY}_6$  molecule normally follows the order  $I(A_{1g}) > I(E_g)$ ,<sup>25</sup> enable us to unambiguously assign the  $\text{Cs}_2\text{NaAlF}_6:\text{Cr}^{3+}$  modes at  $310\text{ cm}^{-1}$  and  $520\text{ cm}^{-1}$  and the  $\text{Cs}_2\text{NaGaF}_6:\text{Cr}^{3+}$  modes at  $271\text{ cm}^{-1}$  and  $514\text{ cm}^{-1}$  as  $A_{1g}$  modes. These modes arise predominantly from F ion stretching modes in the  $D_{3d}$  factor group for the crystal. Polarization data enables us to assign the modes at 307, 316, and  $364\text{ cm}^{-1}$  for  $\text{Cs}_2\text{NaAlF}_6:\text{Cr}^{3+}$  and the modes at  $266\text{ cm}^{-1}$ ,  $276\text{ cm}^{-1}$  and  $352\text{ cm}^{-1}$  for  $\text{Cs}_2\text{NaGaF}_6:\text{Cr}^{3+}$  as  $E_g$  modes arising from Na and F motions in the  $xy$  plane.

It can be concluded that the  $\text{Cr}^{3+}$  dopant did not perturb the lattice very much since weak diffraction peaks, IR modes in the Raman or formation of new modes as a function of temperature were not observed. There is some suggestion for electron-phonon coupling with the observation of a weak side band at  $\sim 528\text{ cm}^{-1}$ , associated with the bulk  $\nu_{A_{1g}}$ . This mode is believed to be associated with the substitution of an  $\text{Al}^{3+}$  ion with a  $\text{Cr}^{3+}$  ion. The side bands at

278  $\text{cm}^{-1}$  and 530  $\text{cm}^{-1}$  in the  $\text{Cs}_2\text{NaGaF}_6:\text{Cr}^{3+}$  spectra are attributed to  $[\text{CrF}_6]^{3-}$  modes in agreement with both the  $\text{Cs}_2\text{NaAlF}_6:\text{Cr}^{3+}$  system and also with values obtained in the literature for similar systems.<sup>15</sup> It is however important to note that the 530  $\text{cm}^{-1}$  mode lies above the cut off frequency of the system, therefore it can not be attributed to a true localized vibrational mode. The intensity of this mode is dependant upon the level of doping level further supporting our assignment of it. This type of behavior has been observed in other elpasolites, where local modes were observed due to electron-phonon coupling.<sup>21,23,26</sup> In the  $E_{0-0}$  luminescence spectra of the material a phonon wing is observed, supporting the assignment of the local mode as a defect mode.<sup>19</sup> This phonon wing has been assigned as a Cr site coupling to the Al-F lattice, which supports the possible assignment of the sideband at 528  $\text{cm}^{-1}$  to a local defect ion perturbation.

Raman spectroscopy is an excellent tool for probing the level of distortion that arises within a lattice due to a defect ion.<sup>27</sup> In the  $\text{Cs}_2\text{NaAlF}_6:\text{Cr}^{3+}$  samples only a slight shift of the  $A_{1g}$  mode (3-5  $\text{cm}^{-1}$ ) was observed which is consistent with our assumption that very slight perturbations of the lattice occur due to the  $\text{Cr}^{3+}$  doping. The reason that such a small perturbation was observed by doping  $\text{Cr}^{3+}$  is most like due to the small difference in ionic radii between the guest:host ion. In other materials such as  $\text{CsCdBr}:\text{Y}^{3+}$  and  $\text{K}_2\text{NaScF}_6:\text{Cr}^{3+}$ , large shifts in both the Yb-Br and F stretching

modes were observed and were attributed to the large difference in ionic radii between the guest:host ion.<sup>9,23</sup>

Lattice distortions and el-ph coupling are known to affect the quantum yield ( $\eta$ ) of a system.<sup>5,9</sup> The vibrational spectra of  $\text{Cs}_2\text{NaAlF}_6:\text{Cr}^{3+}$  and  $\text{Cs}_2\text{NaGaF}_6:\text{Cr}^{3+}$  show large shifts ( $16\text{ cm}^{-1}$ ) between the bulk and local mode frequency of  $[\text{CrF}_6]^{-3}$  which provides evidence for strong el-ph coupling in these systems. This is not surprising due to the large degree of covalency in Ga compounds.<sup>28</sup> Based on this it would be expected for the  $\text{Cs}_2\text{NaAlF}_6:\text{Cr}^{3+}$  to have a greater quantum yield than that of  $\text{Cs}_2\text{NaGaF}_6:\text{Cr}^{3+}$ . It is advantageous for  $\text{Cr}^{3+}$  to dope into a lattice with a small host ion, since this will allow the  $\text{CrF}_6^{-3}$  unit to expand with greater ease upon photoexcitation. The displacement of the  $^4\text{T}_2$  excited state is smaller and more competitive with radiative emission than the displacement of multiphonon relaxation.<sup>5</sup> Based upon the above arguments the room temperature quantum yields for three  $\text{Cr}^{3+}$  doped elpasolites should follow the trend below in agreement with experimental results.<sup>19,29,30</sup>

$$\eta_{\text{Cs}_2\text{NaAlF}_6:\text{Cr}^{3+}} (r_{\text{Al}^{3+}} = 0.53) > \eta_{\text{Cs}_2\text{NaGaF}_6:\text{Cr}^{3+}} (r_{\text{Ga}^{3+}} = 0.62) > \eta_{\text{Cs}_2\text{NaYF}_6:\text{Cr}^{3+}} (r_{\text{Y}^{3+}} = 0.9)$$

Measured values of  $\eta$  for  $\text{Cs}_2\text{NaAlF}_6:\text{Cr}^{3+}$ ,  $\text{Cs}_2\text{NaGaF}_6:\text{Cr}^{3+}$  and  $\text{Cs}_2\text{NaYF}_6:\text{Cr}^{3+}$  are approximately 0.4, 0.3 and 0.15 respectively.

## 5.5. CONCLUSION

These materials were studied using both optical and structural analysis. The optical analysis was essential to providing evidence that the dopant did truly lie in an Al or Ga site within the elpasolite structure. The x-ray and neutron diffraction data revealed that the  $\text{Cs}_2\text{NaAlF}_6:\text{Cr}^{3+}$  and  $\text{Cs}_2\text{NaGaF}_6:\text{Cr}^{3+}$  materials crystallize in a distorted  $Fm\bar{3}m$  structure which lowers the symmetry to  $R\bar{3}m$  resulting from a unique stacking interaction. The sideband that is associated with the  $A_{1g}$  mode suggests that the  $\text{Cr}^{3+}$  ion is coupled to the lattice within the first coordination sphere by electron-phonon coupling. If the  $\text{Cr}^{3+}$  ion had perturbed the lattice greatly then a breakage of symmetry would be expected with the observation of new modes in the Raman spectra. This is not the case in  $\text{Cs}_2\text{NaAlF}_6:\text{Cr}^{3+}$  therefore it can be concluded that the  $\text{Cr}^{3+}$  ion does not perturb the lattice to an appreciable extent. The argument that electron-phonon coupling decreased guest ion emission has been used in both  $\text{Er}^{3+}$  and  $\text{Yb}^{3+}$  doped materials.

Room temperature quantum yields in the neighborhood of 0.7 have been reported in  $\text{Cs}_2\text{NaInCl}_6:\text{Cr}^{3+}$  and  $\text{Cs}_2\text{NaScCl}_6:\text{Cr}^{3+}$ .<sup>5</sup> However in the case of  $\text{Cs}_2\text{NaAlF}_6:\text{Cr}^{3+}$  the measured quantum yield is  $\sim 0.4$ . The lower quantum yield in  $\text{Cs}_2\text{NaAlF}_6:\text{Cr}^{3+}$  compared to analogous materials can be attributed to the lowering of the  $O_h$  symmetry. Despite the room temperature quantum yield

$\text{Cs}_2\text{NaAlF}_6:\text{Cr}^{3+}$  it is still a good candidate for laser tuneable solid state laser applications due to the intense fluorescence observed for this material.

## 5.6 REFERENCES:

- (1) Lever, A. B. P. *Inorganic Electronic Spectroscopy*; 2nd ed.; Elsevier: Amsterdam, 1984.
- (2) Maiman, T. H. *Nature* **1960**, *187*, 493-494.
- (3) Kaminskii, A. A. *Crystalline Lasers*; CRC Press: New York, 1996.
- (4) Walling, J. C.; Peterson, O. G.; Morris, R. C. *Ieee J Quantum Elect* **1980**, *16*, 120-121.
- (5) Wenger, O. S.; Gudel, H. U. *J Chem Phys* **2001**, *114*, 5832-5841.
- (6) Meijerink, A.; Blasse, G.; Sytsma, J.; Donega, C. D.; Ellens, A. *Acta Phys Pol A* **1996**, *90*, 109-119.
- (7) Vink, A. P.; de Bruin, M. A.; Meijerink, A. *J Phys-Condens Mat* **2000**, *12*, 8607-8615.
- (8) Ellens, A.; Andres, H.; Meijerink, A.; Blasse, G. *Phys Rev B* **1997**, *55*, 173-179.
- (9) Hehlen, M. P.; Kuditcher, A.; Rand, S. C.; Tischler, M. A. *J Chem Phys* **1997**, *107*, 4886-4892.
- (10) Goryunov, A. V.; Popov, A. I.; Khajdukov, N. M.; Fedorov, P. *P. Mater Res Bull* **1992**, *27*, 213-220.

- (11) Babel, D.; Haegele, R. *J Solid State Chem* **1976**, *18*, 39-50.
- (12) Jacobson, R. A. *J Appl Crystallogr* **1986**, *19*, 283-286.
- (13) Larson, A. C.; von Dreele, R. B. LANL-Report LA-UR-86-748.
- (14) Cryostat pin configuration. Heater 9 - 11 (Blue-Brown),  
Thermocouple 12-5 or 4-6 (Yellow-White).
- (15) de Fonseca, R. J. M.; Sosman, L. P.; Dias avarés, A. J.; Bordallo, H. N. *J. Fluorescence* **2000**, *10*, 375.
- (16) Fargin, E.; Lestienne, B.; Dance, J. M. *Solid State Commun* **1990**, *75*, 769-771.
- (17) Wingefeld, G.; Hoppe, R. *Z Anorg Allg Chem* **1984**, *516*, 223-228.
- (18) Bordallo, H. N.; Henning, R. W.; Sosman, L. P.; da Fonseca, R. J. M.; Tavares, A. D.; Hanif, K. M.; Strouse, G. F. *J. Chem. Phys.* **2001**, *115*, 4300.
- (19) Sosman, L. P.; Tavares, A. D.; da Fonseca, R. J. M.; Abritta, T.; Khaidukov, N. M. *Solid State Commun* **2000**, *114*, 661-665.
- (20) Babel, D.; Haegele, R.; Pausewan, G.; Wall, F. *Mater Res Bull* **1973**, *8*, 1371-1382.
- (21) Tanner, P. A.; Liu, Y. L.; Edelstein, N. M.; Murdoch, K. M.; Khaidukov, N. M. *J Phys-Condens Mat* **1997**, *9*, 7817-7836.

- (22) Babel, D.; Tressaud, A. *Inorganic Solids Fluorides*; Academic: New York, 1985.
- (23) Sliwczuk, U.; Bartram, R. H.; Gabbe, D. R.; Mccollum, B. C. *J Phys Chem Solids* **1991**, *52*, 357-361.
- (24) Couzi, M.; Khairoun, S.; Tressaud, A. *Phys Status Solidi A* **1986**, *98*, 423-434.
- (25) *Infrared and Raman Spectra of Inorganic and Coordination Compounds*; Wiley: New York, 1978.
- (26) Tanner, P. *J. Mol. Struc.* **1997**, *405*.
- (27) Hanif, K. M.; Meulenberg, R. W.; Strouse, G. F. *J Am Chem Soc* **2002**, *124*, 11495-11502.
- (28) Vink, A. P.; Meijerink, A. *J Lumin* **2000**, *87-9*, 601-604.
- (29) Blasse, G.; Dirksen, G. J. *J Solid State Chem* **1992**, *96*, 258-262.
- (30) Knochenmuss, R.; Reber, C.; Rajasekharan, M. V.; Gudel, H. U. *J Chem Phys* **1986**, *85*, 4280-4289.

## APENDIX I.

This appendix will describe how the irreducible representation for  $\text{Cs}_2\text{NaAlF}_6:\text{Cr}^{3+}$  were determined. The irreducible representations were determined using the procedures defined by the following article:

Rousseau, D.L.; Bauman, R.P.; Porto, S.P.S.; *Journal of Raman Spectroscopy*, 10, 253-289 (1981)

Table 1 list the symmetry and Wyckov sites of each of each of the atoms in the crystal. Based on single crystal diffraction the structure can be indexed as  $R\bar{3}m$ ,  $D_{3d}^5$  space group. Table 2 shows the irreducible representation for atoms in with site symmetry of  $C_S$ ,  $C_{3v}$ , and  $D_{3d}$  in a crystal with a space group of  $R\bar{3}m$ .

Since there are 2 atoms with  $C_S$  and  $D_{3d}$  symmetry then the number of irreducible representation of these can be determine by multiplying each of the modes listed for these atomic position in table 2 by 2. Since there are three atoms with  $C_{3v}$  symmetry the modes for  $C_{3v}$  symmetry in table 2 need to be multiplied by 3. This will give a total of 60 modes:

$$\Gamma = 7 A_{1g} + 2A_{1u} + 9A_{2u} + 2A_{2g} + 9E_g + 11E_u$$

---

<u>Atom</u>	<u>Wyckov Site</u>	<u>Symmetry</u>
Al(1)	3a	$D_{3d}$
Al(2)	3b	$D_{3d}$
Na	6c	$C_{3v}$
F(1)	18h	$C_s$
F(2)	18h	$C_s$
Cs(1)	6c	$C_{3v}$
Cs(2)	6c	$C_{3v}$

---

Table 1. Wyckov sites and symmetry of the atoms in  $Cs_2NaAlF_6$ .

Site symmetry	Irreducible Representations
$C_S$	$2A_{1g} + A_{1u} + A_{2g} + 2A_{2u} + 3E_g + 3E_U$
$C_{3v}$	$A_{1g} + A_{2u} + E_g + E_U$
$D_{3d}$	$A_{2u} + E_U$

Table 2. Irreducible representation for three of the atomic position in a crystal with a space group of  $R\bar{3}m$ .